On the Effect of Large-Scale Patterned Wettability on Contact Line Hydrodynamics

Thesis by
Morgane Anne Marie Grivel

In Partial Fulfillment of the Requirements for the
degree of
Doctor of Philosophy

Caltech

CALIFORNIA INSTITUTE OF TECHNOLOGY
Pasadena, California

2018
Defended June 20, 2017

To Marie-Claude, Jean-Charles, Margaux, Médérick,
Manon, and Hugo for always being by my side despite the
thousands of miles between us. Thank you.

ACKNOWLEDGEMENTS

I would like to begin by thanking my advisor, Mory Gharib, for his support over the last four years. In particular, I want to thank him for allowing me to travel and work from afar in order to sustain my personal relationships. I am extremely grateful for his understanding with regards to this aspect of my life.

I would also like to thank my committee members, Professors Tim Colonius and Ravi Ravichandran, for their input and insightful questions, and Professor Beverley McKeon for the constant support and encouragement during my time at Caltech.

My group members, present and past, also deserve much thanks, in particular Chris for always lending an ear and being eternally optimistic; Nathan, Cecilia, and Remi for enlivening my days in the office; Cong for his willingness to help me whenever I asked; and Martha for answering all my administrative needs. I also cannot thank all of them, including Damian, Jinglin, and Manu, enough for the fond memories made during our annual APS trips.

Manu also deserves thanks for his invaluable help with my pet project: creating an entirely new website for the group. I am proud of what we accomplished.

I am tremendously grateful to David Jeon for the hours spent in the lab troubleshooting setups as well as for always being available to discuss my questions. His advice with regards to this thesis has been invaluable. Thank you for being a constant presence during my time here. And, thank you for the countless treats. They were truly delicious.

I would also like to thank the GALCIT staff, especially Dimity, Christine, Peggy, and Cheryl, for all the work they put in to making our department run smoothly and for all the help they have given me over the years. Furthermore, I would like to recognize Jackie Gish for always checking in and leaving her door open to me. I have throughly enjoyed our conversations.

I am also indebted to the Aero Machine Shop staff: Joe, Ali, Matavos, and Brad. Thank you for the impeccable work and for always accommodating me. I also cannot thank you enough for greeting me every morning when I was slaving away in the lab and for asking how I was doing. I appreciated it enormously.

I would also like to acknowledge Professors Dan Meiron and Joe Shepard for reworking the GALCIT- Ecole Polytechnique exchange so I could partake in it without

loosing my fellowship. I had an amazing year studying in Paris and am grateful for the experience. That said, I am also grateful for the National Science Foundation, which granted me a GRFP fellowship, allowing me to pursue my PhD without financial worry, and to the Aerospace Historical Society for honoring me with the Shirley Thomas award.

Last, but certainly not least: I am enormously thankful for my friends and family. To my friends, in particular Marcello, Gita, Kirsten, Lee, Pablo, Federico, and Jonathan: thank you for the laughs, the memories, and all around good times. To my rugby teammates and coaches: thank you for reminding me to enjoy my time here and for giving me the space to be more than a grad student. I cherish the friendships I have made on this team and cannot wait to see the Pasadena Royals keep turning heads.

And finally, to my family. To my parents, Marie-Claude and Jean-Charles, whose faith in me has never faltered: thank you for pushing me onwards. Thank you for the guidance and loving words. I am also extremely touched that you are for making the trek from Qatar and the East Coast to see me deliver my thesis presentation. This thesis is as much for you as it is for me. Thank you for not letting me give up.

To my siblings, Margaux, Médérick, and Manon: thank you for the thoughtful letters and notes, for the kind words when I needed them most. I am incredibly proud of you, of your kindness, strength, intelligence, and accomplishments. I will support you in all your endeavors the way you have supported me in mine.

And, to Hugo: thank you for brightening my days. Thank you for your unwavering support and encouragement and for understanding why I needed to do this even though it meant being apart for four years. I will not miss the endless trips across continents and oceans, but I am grateful we were able to share our parts of the world with each other. You have been my rock, the constant in my life: there are not enough words to thank you for it.

ABSTRACT

Numerous studies have investigated how liquid water behaves on solid surfaces with uniformly hydrophilic or uniformly hydrophobic wetting properties. In particular, uniformly hydrophobic surfaces have been widely studied for modifying flow behavior of rivulets and drops at smaller scales, as well as for drag reduction on ships or other free-surface-piercing bodies at larger scales. Despite the extensive body of work on surfaces with uniform wetting properties, minimal work has been done to investigate how combining hydrophilic and hydrophobic regions onto a single surface to create macroscopic non-uniform wetting properties affects flows. Research in this vein has predominantly focused on low Reynolds number flows, such as in microfluidic channels or droplet impacts.

This thesis expands on the current literature by investigating contact line dynamics and global flow behavior on surfaces with larger-scale non-uniform wetting properties. Experiments were first carried out to study thin sheet flow down an inclined plate at $Re \sim 50 - 1200$. The plate's wetting condition was changed by introducing alternating hydrophilic and hydrophobic bands 2-25 mm wide oriented at different angles with respect to the flow direction. Results show that the contact line of such flows is heavily modified compared to the uniform cases. At low Reynolds numbers, large-scale wettability heterogeneities are observed to tune the fingering instability wavelength if the bands are parallel to the flow direction and to dampen finger oscillations if the bands are perpendicular to the flow direction. At higher Reynolds numbers, roller structures are introduced at every hydrophilic-to-hydrophobic junction, modifying the global flow morphology. Entrained air bubbles are also captured and observed to coalesce if the bands are perpendicular to the flow direction.

These experiments were then extended to a surface-piercing hydrofoil coated with alternating hydrophilic and hydrophobic bands. Experiments were run in Caltech's Free Surface Laboratory water tunnel for Re on the order of 10^4 to 10^5. The experiments demonstrate that the contact line is modulated in this context, alternating from concave to convex over the different wettability regions. The modulation of the contact line propagates to the rest of the water free-surface via the generation of standing waves and further modifies the free-surface separation point's location and steadiness. In addition, changes in wettability are observed to generate side force, which is of interest for vessel maneuvers in naval applications.

TABLE OF CONTENTS

C h a p t e r   1

INTRODUCTION

The contact line, or triple-phase line, is the intersection between three phases: generally a solid, a liquid, and a gas. The contact line's dynamics play a role in many processes and affect an enormous range of flow regimes: from inkjet printing to thin film coating (e.g., paint or spin coated materials); from flow control in microfluidic devices for use in biological and chemical applications to flow manipulation in porous materials (e.g., the creation of waterproof fabrics and surfaces); and, from bubble and drop evolution to spray generation and bow wave formation in large-scale naval flows.

This body of work focuses on contact line dynamics in the presence of large-scale surface inhomogeneities. These inhomogeneities are introduced as changes in the solid's wettability (i.e., its affinity to the liquid phase). Their effect on contact line dynamics is studied in thin films flowing down inclined planes as well as over surface-piercing bodies.

1.1   Surface Tension, Contact Lines, and Wettability

Consider a drop of liquid in air. A molecule in the bulk of the liquid interacts with its neighboring molecules. This interaction results in a cohesive force between the molecules. The stronger the cohesive force, the stronger the attractive forces between like molecules. In the case of water, the cohesive force is due to the polarity of water, which results in hydrogen bonds forming between neighboring molecules (i.e., an electrostatic attraction).

In addition to these cohesive forces, the outer molecules of the liquid drop will also experience adhesive forces due to interactions with air molecules. The stronger the adhesion, the greater the affinity between the different types of molecules. In the case of liquids and air, cohesion dominates, causing liquid molecules to feel a net inward pull by bulk molecules. The result is a spherical drop.

The comparative measure of the cohesive forces within the liquid to the adhesive forces between the liquid and gas is referred to as surface tension: the greater the surface tension, the more difficult it is to penetrate or deform the liquid. Surface tension can thus be viewed as the amount of force necessary to deform a liquid by a

unit length while it is surrounded by a given gas (or other fluid).

Surface tension, which is often mistakenly introduced as an inherent property of a fluid, is, therefore, actually a property of the interface between two mediums. The interchangeably-used term "interfacial tension" more appropriately captures the essence of this phenomenon. Surface tensions can also be defined between solids and liquids and between solids and gases, although this last surface tension is commonly called "surface free energy," highlighting the fact that surface tension can also be viewed in terms of energy. In this context, surface tension is the amount of work required to increase the surface area of a medium in contact with another medium by one unit area. Surface tension thus has units of J/m^2 or, equivalently, N/m in SI units.

When a liquid is in contact with both a gas and a solid, three surface tensions are present: the surface tension between the liquid and gas (γ_{lg}), the surface tension between the solid and the liquid (γ_{sl}), and the surface tension between the solid and the gas (γ_{sg}). These surface tensions, shown in figure 1.1, effectively point forces, must balance at the intersection between the three phases. This intersection is called the triple-phase line or the contact line. For a drop deposited on a surface, it is the line defining the perimeter of the drop in contact with the solid substrate.

Side view   Top view
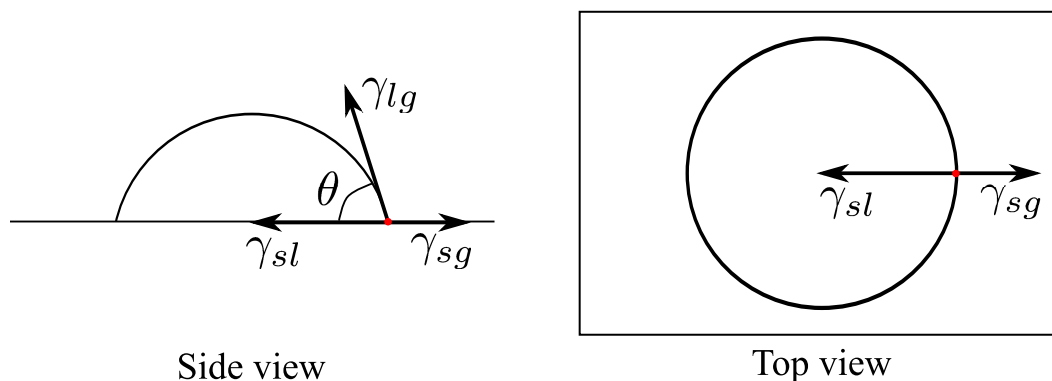
Figure 1.1: Schematic of the contact angle (a) and contact line (b) made by a drop sitting on a solid surface as well as the surface tensions involved.

The balance between the three interfacial point forces determines the equilibrium contact angle θ, as shown in figure 1.1, yielding the Young-Dupré relation:

$$\cos\theta = \frac{\gamma_{sg} - \gamma_{sl}}{\gamma_{lg}}. \tag{1.1}$$

Measuring the contact angle that a liquid makes on a surface is thus a way of measuring the relative importance of the different surface tensions (or energies) in the system. The contact angle equals zero when the energy reduction from the drop spreading on the surface ($\gamma_{sg} - \gamma_{sl}$) is greater than or equal to the energy required to deform the liquid-gas interface (γ_{lg}). That is, if the energy of the wetted solid surface is lower than the energy of the dry solid surface, the drop will spread and wet the solid in order to minimize the system's energy. On the other hand, the contact angle equals 180° when the solid's dry energy is much lower than its wetted energy. That is, the energy gained from increasing the solid-gas interface and decreasing the liquid-solid interface ($\gamma_{sl} - \gamma_{sg}$) is greater than or equal to the energy required to deform the liquid-gas interface. The drop therefore forms a sphere on the solid.

For intermediate contact angles, drops are observed to have flattened, pancake-like shapes when $\theta < 90°$ and spherical-like shapes when $\theta > 90°$. Surfaces on which water drops have $\theta < 90°$ are "hydrophilic", while surfaces where $\theta > 90°$ are "hydrophobic".
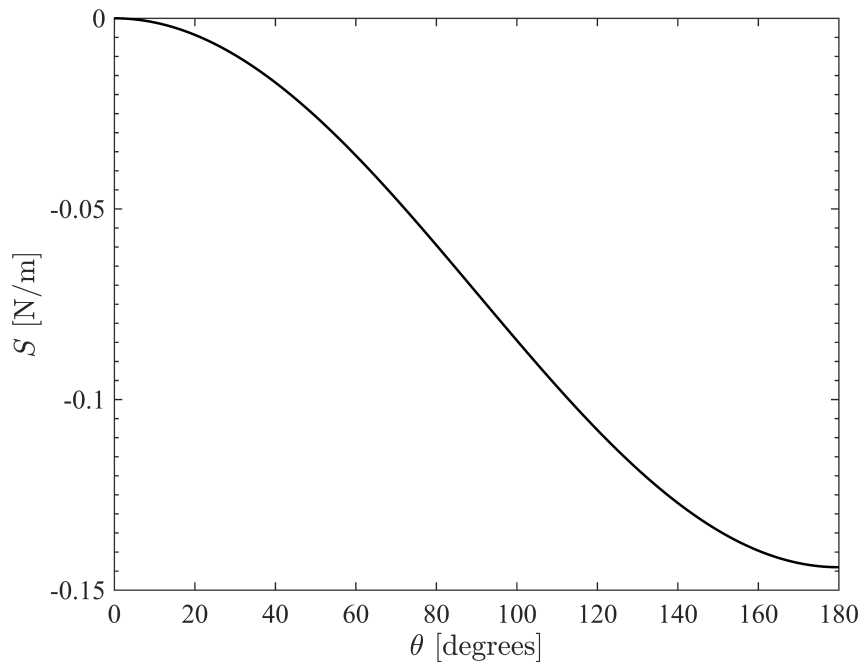
Figure 1.2: The spreading parameter S as a function of the contact angle θ for a drop of water ($\gamma_{lg} = 72 \times 10^{-3}$N/m).

The spreading parameter $S = \gamma_{sg} - \gamma_{sl} + \gamma_{lg}$ can also be used to define how much a drop wets (or spreads on) the solid surface. When $S \geq 0$, total wetting occurs as the solid surface's dry condition is less energetically favorable than its wetted

condition. When $S > 0$, partial wetting occurs. In this case, the drop does not spread completely but rather reaches an equilibrium as set by θ.

S can be re-written using the Young-Dupré equation as $S = \gamma_{lg}(\cos\theta - 1)$. Thus, total wetting occurs for $\theta = 0°$, while partial wetting occurs for all other θ. Furthermore, hydrophilic surfaces are said to be mostly wetting surfaces as S is only slightly negative (see figure 1.2). Hydrophobic surfaces, on the other hand, are mostly non-wetting as they are associated with large negative values of S.

So far, only smooth, homogeneous solid surfaces have been considered. However, introducing roughness affects the contact angle of the system. Consider the rough surfaces in figure 1.3. The roughness is characterized by

$$r = \frac{\text{total solid area}}{\text{geometric area}} = \frac{A_t}{A}. \tag{1.2}$$
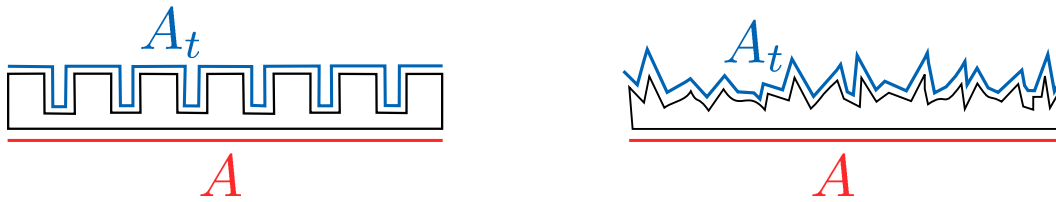
Figure 1.3: Schematic of surface roughness: (a) idealized patterned roughness and (b) random roughness

When a drop is deposited on the surface, several types of wetting can occur depending on if the liquid penetrates the roughness or air gets trapped in the roughness. In either case, the new apparent contact angle θ^* is given by

$$\cos\theta^* = f_1 \cos\theta_1 + f_2 \cos\theta_2, \tag{1.3}$$

where f_1 and f_2 are the fractions of the two phases below the drop ($f_1 + f_2 = 1$), and θ_1 and θ_2 are the equilibrium contact angles the drop makes with each individual phase. This expression is a generalized version of the contact angle relation developed by Cassie and Baxter (1944).

For a hydrophilic surface, the drop of water will fill the roughness, as shown in figure 1.4. The extent to which the roughness is filled, however, depends on the equilibrium contact angle water makes with the solid surface (as given by θ from the Young-Dupré relation for a smooth surface).

Figure 1.4: Schematic of wetting on a rough, hydrophilic surface.

If the equilibrium contact angle θ is less than a critical value, the water will fill the roughness ahead of the drop (Bico, Tordeux, and Quéré, 2001). Although the volume of water in the roughness is generally negligible (Gennes, Brochard Wyart, and Quéré, 2004), the result is that the drop is deposited on an effectively "smooth" heterogeneous surface made up of two phases: a solid phase and a water phase. In this case, $\theta_1 = \theta$, $f_1 = \phi_s$, $\theta_2 = 0$ (as water forms no contact angle with itself), and $f_2 = 1 - \phi_s$. Here, ϕ_s is the fraction of the drop in contact with the solid surface and $(1 - \phi_s)$ is the fraction of the drop in contact with the water filling the roughness. This type of wetting is often referred to as Cassie-Baxter-type wetting.

If θ is greater than a critical value, the water only fills the roughness directly beneath the drop. Therefore, $f_1 = r$, $\theta_1 = \theta$, and $f_2 = 0$, which results in Wenzel-type wetting (Wenzel, 1936).

The critical contact angle is found by considering the energy change (dE) resulting for the drop's contact line advancing a distance dx:

$$\frac{dE}{dx} = (r - \phi_s)(\gamma_{sl} - \gamma_{sg}) + (1 - \phi_s)\gamma_{lg}. \tag{1.4}$$

This expression can be re-written as $dE/dx = \gamma_{lg}[(1 - \phi_s) - (r - \phi_s)\cos\theta]$ using the Young-Dupré relation. The critical contact angle θ_c occurs when $dE/dx = 0$. Thus,

$$\cos\theta_c = \frac{1 - \phi_s}{r - \phi_s}. \tag{1.5}$$

Note that $\theta_c < 90°$. In order for the contact line to advance and for the water to impregnate the roughness ahead of the drop, we must have $dE/dx < 0$. That is, wetting more of the solid lowers the system's energy. Therefore, $\theta < \theta_c$ for impregnation. The Wenzel-type wetting regime is recovered if $\theta > \theta_c$ for the hydrophilic surface.

For a hydrophobic surface, the size of the roughness determines whether the drop conforms to the surface or air gets trapped in the roughness pockets, as seen in figure 1.5. Below a critical roughness (r^*), the Wenzel type wetting is recovered with $f_1 = r$, $\theta_1 = \theta$, and $f_2 = 0$ (Gennes, Brochard Wyart, and Quéré, 2004; Bico, Marzolin, and Quéré, 1999).
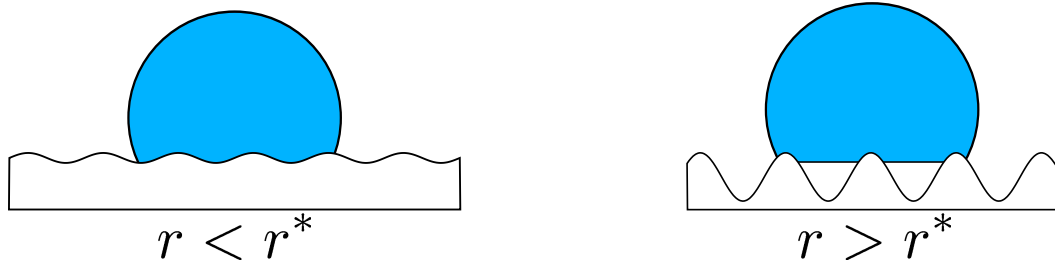

$$r < r^* \qquad\qquad r > r^*$$

Figure 1.5: Schematic of wetting on a rough, hydrophobic surface.

However, if $r > r^*$, air pockets get trapped beneath the drop in the roughness crevices. In this case, $f_1 = \phi_s$, $\theta_1 = \theta$, $f_2 = 1 - \phi_s$, and $\theta_2 = 180°$ (as drop of water will form a perfect sphere in air).

The wetting regimes are thus:

$$\cos\theta^* = \begin{cases} 1 + \phi_s(\cos\theta - 1), & \text{if } 0° \leq \theta < \theta_c < 90° \\ r\cos\theta, & \text{if } \theta_c < \theta < 90° \text{ or } \theta > 90°, r < r^* \\ \phi_s(\cos\theta + 1) - 1, & \text{if } \theta > 90°, r > r^* \end{cases} \tag{1.6}$$

As can be seen in figure 1.6, roughness amplifies the solid substrates's natural condition. That is, hydrophilic substrates become more hydrophilic ($\theta^* < \theta$) and hydrophobic substrates become more hydrophobic ($\theta^* > \theta$). The mechanism for this amplification is (i) increasing the contact area between the drop and substrate, which makes the surface a rough, chemically homogeneous surface and results in a Wenzel-type wetting state; or (ii) impregnating the roughness with a second phase (water for hydrophilic substrates or air for hydrophobic substrates), which turns the substrate into a smooth, chemically heterogeneous surface and results in a Cassie-Baxter-type wetting state. This second state amounts to introducing small, local changes in wettability.
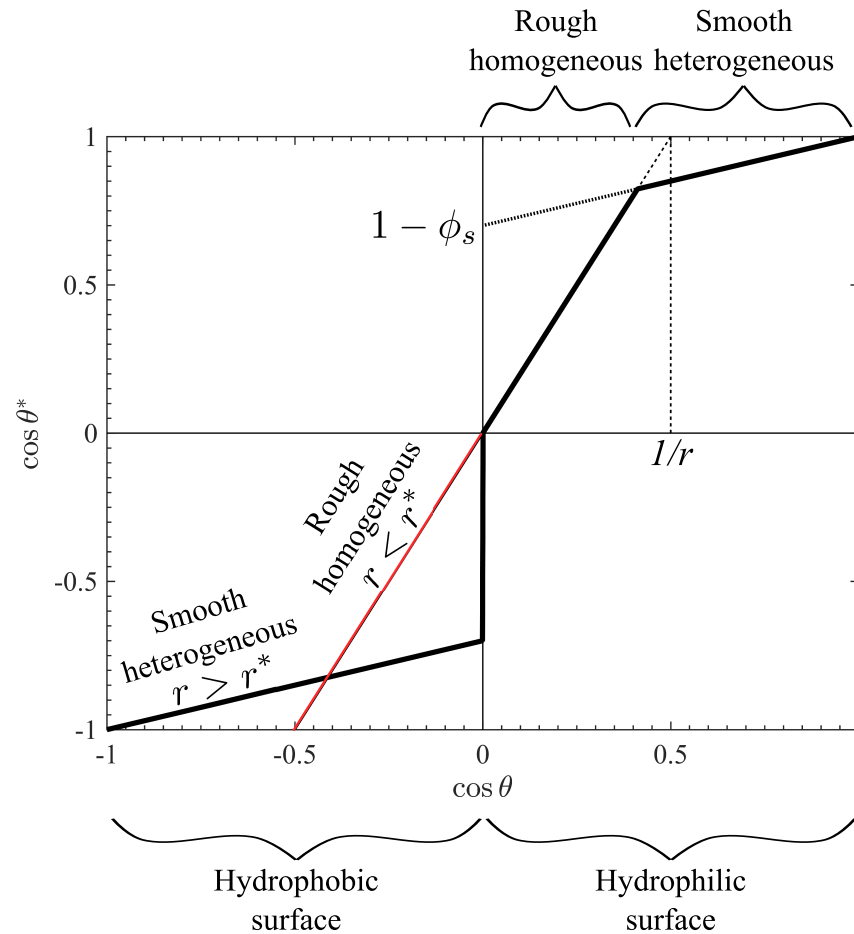
Figure 1.6: The apparent contact angle θ^* on a rough surface as a function of the equilibrium contact θ on a smooth, chemically homogeneous surface.

(Note that the above expressions are functions of the *contact area* between a drop and solid substrate. Gao and McCarthy (2007) argue that the *contact line* is responsible for changes in the apparent contact angle. Thus, only what occurs in the vicinity of this triple-phase line is of importance. Regardless of whether the contact area or contact line is of import, roughness and local changes in wettability are still seen to affect the contact angle and therefore drop behavior and morphology.)

1.2 Objectives and Outline

The vast majority of the literature concerning contact line dynamics is devoted to flow over surfaces with homogenous wettability or local wettability heterogeneities (microscopic scale), as discussed above. Having observed that local changes in wettability affect the contact angle, and therefore the associated contact line, the major hypothesis of this work is that introducing large-scale changes in wettability will likewise impact contact line dynamics.

The primary objective of this thesis is thus to expand current knowledge and demonstrate that large, distinct ($\sim 2 - 25$ mm wide by 10 cm long) heterogeneities in wettability have an observable effect on the contact line dynamics. To this end, experiments are conducted using a thin film (1.6mm thick) flowing down an inclined plane whose wettability is altered by introducing alternating hydrophilic and hydrophobic bands. This fundamental investigation is discussed in chapter 2.

The present work is also motivated by naval applications, in which the contact line acts along the entire perimeter of the ship ($O(10^3)$m). As such, contact dynamics are an important aspect of the flow around the ship. Finding ways to modify contact line dynamics therefore presents a method for altering the forces and flow features around a vessel. For example, most ships cannot generate direct transverse (or lateral) forces, which are necessary to counter oblique seas or to maneuver in port, as their thrusters are located near the stern of the vessel. Instead, they generate a yaw moment, which forces them to zig-zag at sea in order to maintain heading and track. The result is a loss of speed and an increased drag on the ship. There is therefore a need to reduce zig-zagging motions as well as improve maneuverability at port.

The secondary hypothesis of this work is that transverse forces can directly be generated by introducing large scale wettability modifications on a surface-piercing body. This hypothesis is tested by conducting experiments with a surface-piercing hydrofoil whose wettability is modified via alternating hydrophilic and hydrophobic bands, as discussed in chapter 3.

The principal objectives of the present work are thus:

1. To explore the effects of large scale heterogeneities on the contact line dynamics and global flow behavior of thin film flows down inclined planes.

2. To investigate how modifying flow conditions (the flow rate and the plane inclination angle) and surface conditions (the size and orientation of wettability patterns introduced) affects thin film flows.

3. To demonstrate the applicability of large scale wettability modifications in naval contexts by generating direct transverse forces on a surface-piercing body.

Results are summarized in chapter 4.

Chapter 2

FUNDAMENTAL INVESTIGATION: THIN FILM EXPERIMENTS

2.1 Background and Objectives

The vast majority of literature regarding the effect of wetting properties on flows looks at surfaces with uniform wettability or with very fine heterogeneities in chemical or surface composition. These fine heterogeneities in surface composition (in the form of patches that are about 100 microns wide and have asperities a few microns high) have been linked to increased contact angle hysteresis and non-repeatability of contact angle measurements (Dettre and Johnson, 1965; Drelich, Miller, and Good, 1996). Rivulet stability is also found to depend on microscopic surface defects and wettability irregularities, resulting in a perturbed contact line that predisposes the flow to meandering instabilities (Le Grand-Piteira, Daerr, and Limat, 2006; Couvreur and Daerr, 2012).

At the nano-scale, molecular dynamics simulations conducted by Karakare et al. (2010) have shown that nano-fluidic cells with patterned wettability in the form of approximately 1 nm^2 checkerboard patches results in toroidal nanoscale vortices at very low Reynolds numbers. These nanoscale vortices can be used to enhance mixing and facilitate molecular transport in nanochannels, which is of interest in chemical as well as biological applications. Molecular dynamics simulations were also used by Priezjev, Darhuber, and Troian (2005) to investigate slip of Stokes flow (*Re* $<<$ 1) in a small Couette cell (gap on the order of 10^{-9} m) with hydrophilic and hydrophobic wettability regions. The slip length (on the order of $10^{-10} - 10^{-8}$ m) was found to vary with the wettability regions' size ($\leq 10^{-8}$ m wide), the pattern wavelength, and the orientation of the patterns with respect to the flow direction.

Studies into larger scale wettability heterogeneities have been largely confined to microfluidics or droplet studies. These large scale heterogeneities, introduced as neighboring regions of different wetting properties with micron-sized roughness and widths ranging from several microns to a few millimeters, have been shown to affect the morphology of drops deposited on the surface, deform the contact line, and also result in the formation of liquid bridges (Jokinen, Sainiemi, and Franssila, 2008; Brinkmann and Lipowsky, 2002; Lipowsky, 2001; Paterson and Fermigier,

1997; Cubaud and Fermigier, 2004). Furthermore, the size, geometry, and degree of hydrophilicity or hydrophobicity of patterns have been shown to affect droplet impact, altering the shape of the liquid deposit as well as its dynamics (Kim, Moon, and Kim, 2013). Patterned wettability was observed to cause film rupture, fluid ejection, and bouncing drops under different conditions in these experiments. Air entrainment was also observed at the unstable contact line (the interface between the surrounding air, the liquid drop, and the solid surface) created when the fluid advances on a hydrophobic surface and then abruptly encounters a hydrophilic region, transitioning from Cassie-Baxter type wetting to Wenzel type wetting. These studies have practical implications for inkjet printing, where drop morphology and impact dynamics affect printing quality.

Experiments have also shown that non-uniform wetting properties can be used for pumpless fluid transport of liquid volumes on the order of 1-500 μL in open air microfluidic platforms (Ghosh et al., 2014; Schutzius et al., 2012). Hydrophilic rails or tracks on a superhydrophobic background can also act as guides for water moving on a substrate (Seo et al., 2011). Similarly, hydrophobic tracks on a hydrophilic background can be used to slow down capillary flows at precise locations in microfluidic channels (Suk and Cho, 2007). These observations have broad implications for the design of novel microfluidic devices in biological and chemical applications.

Studies have additionally been conducted to demonstrate the use of patterned wettability for water harvesting (Zhai et al., 2006; Garrod et al., 2007). These microcondenser surfaces are inspired by the Namib Stenocara desert beetle, whose body is covered in non-waxy hydrophilic bumps surrounded by waxy hydrophobic tracks (Parker and Lawrence, 2001). Water particles in the air collect on the hydrophilic bumps where they grow until they are too big to remain attached to the bump. The drops then roll on the hydrophobic tracks which lead them to the beetle's mouth.

With regards to thin film flows, Kataoka and Troian (1999) investigated combining thermal gradients and patterned wettability to manipulate the flow of one micron thick films at capillary numbers on the order of 10^{-6}, which are susceptible to the fingering instability when undergoing thermocapillary spreading. The natural wavelength of the fingers is superseded by the wettability pattern, composed of alternating 200 micron-wide hydrophilic and hydrophobic stripes aligned to the flow direction. Ledesma-Aguilar, Hernández-Machado, and Pagonabarraga (2010) found similar results in numerical simulations of gravity-driven thin film flow at a capillary

number of 0.41 and Reynolds number of 0.21, which are also susceptible to the fingering instability. In addition, they determined that the flow pattern (checkerboard or stripes) can be used to tune the width and growth rate of the fingers.

As there has been little work done to experimentally study the effects of large, distinct wettability heterogeneities outside of microfluidic or droplet applications, the objective of the present work is to first and foremost demonstrate their effect on contact line dynamics in other contexts and, secondly, to observe how these changes affect the flow behavior globally. In addition, the work in this chapter aims to demonstrate whether these large-scale wettability heterogeneities affect higher Reynolds number flows for later application to naval contexts (where *Re* is on the order of 10^9).

The investigation into the effects of large-scale non-uniform wetting properties on flows is conducted using a thin water sheet flowing over an inclined, flat plate. The contact line, or triple-phase line, in this scenario is the intersection between the surrounding air, the sheet of water, and the plate's surface.

Experiments are carried out to characterize how the observed effects depend on the flow rate, the plate inclination angle, and the manner in which non-uniform wetting properties are introduced. As this work is largely motivated by naval applications, particular attention is paid to the high flow rate (or equivalently high Reynolds and Froude number) regime. Observing contact line modification at these higher Reynolds numbers is favorable for application of non-uniform wetting properties in naval contexts, which is one of the overarching objectives of this thesis.

2.2 Physical Setup

The experiments in this section consist of a thin water sheet issued from a rectangular jet nozzle that is 10.2 cm wide by 1.6 mm high (i.e., the jet is initially 64 times thinner than it is wide). This thin sheet of water flows over a 10.2 cm wide by 30.5 cm long plate inclined at angle α with the horizontal. The sheet impinges the plate at an angle of 0° with respect to the plate's surface. A schematic of the experimental setup is presented in figure 2.1 along with images in figure 2.2.

The jet is run by a Lifegard Aquarium Model 6000 pump, which is placed in a tank that collects water flowing off the plate. The pump therefore recirculates the flow through the system.

Four surface conditions are studied: two uniform plates (one hydrophilic and one hydrophobic), which serve as the two control cases, and two heterogeneous plates.

The heterogenous plates are patterned with alternating hydrophilic and hydrophobic bands oriented at angle β with respect to the flow direction (the y-axis). Two orientations are considered: $\beta = 0°$ (bands parallel to the flow direction) and $\beta = 90°$ (bands perpendicular to the flow direction). In addition, the width d of the bands is varied between 1.6 mm and 25.4 mm. In all cases, the hydrophilic and hydrophobic bands have the same width.
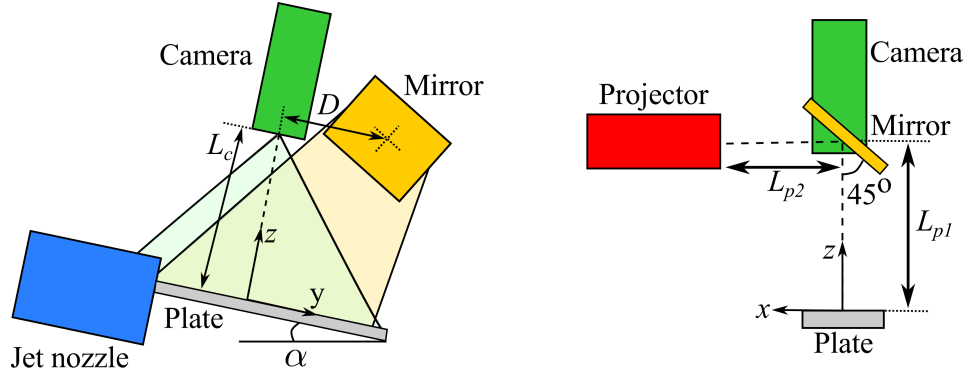

Figure 2.1: Schematic of the experimental setup.

The jet flow rate is also varied, ranging from 4 cm³/s to 110 cm³/s, as is the plate inclination angle ($\alpha = 9°, 10°, 25°$). The patterned plates, however, are not tested at $\alpha = 9°$.

A list of the relevant non-dimensional numbers can be found in table 2.1. Note that, for reasons discussed in later sections, the working fluid in these experiments is a 0.5% (by volume) titanium-dioxide dispersion in deionized water. As the titanium-dioxide is a small fraction of the working fluid, the working fluid properties are not expected to significantly differ from that of pure deionized water. Thus, the properties of deionized water are used in calculating non-dimensional numbers.

Definition	Relation	Values
$Ca = \mu Q/(h_{jet}w_{jet}\gamma)$	Viscosity/surface tension	3.5×10^{-4} - 8.5×10^{-3}
$Fr = Q/(w_{jet}\sqrt{h_{jet}^3 g \sin \alpha})$	Inertia/gravity	0.34 - 14
$Re = \rho Q/(\mu w_{jet})$	Inertia/ viscosity	50 - 1200
$We = \rho Q^2/(h_{jet}w_{jet}^2\gamma)$	Inertia/ surface tension	1.73×10^{-2} - 10.4
d/h_{jet}	Ratio of characteristic lengths	1-16

Table 2.1: Parameter space for the thin film experiments based on jet nozzle conditions (h_{jet} = 1.6 mm, w_{jet} = 10.2 cm) with ρ = 1000 kg/m³, μ = 8.94×10^{-4} Pa s, and $\gamma = 72 \times 10^{-3}$ N/m for water. $Q = Uw_{jet}h_{jet}$ is the jet flow rate where U is the average jet velocity.
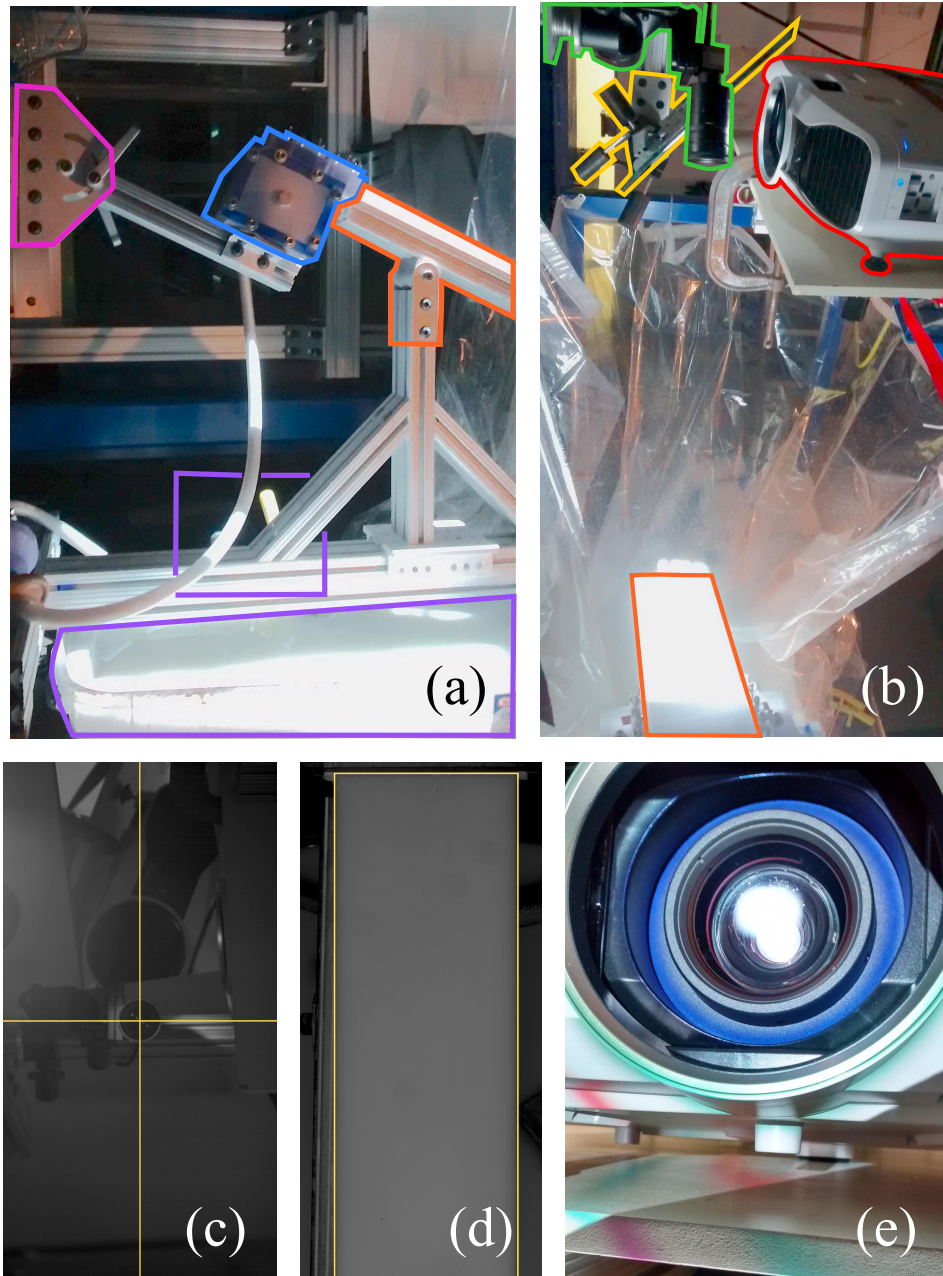
Figure 2.2: The experimental setup for the wall jet experiments. (a): side view of the jet nozzle (blue) and its pivot mechanism (pink) along with the plate and its pivot mechanism (orange). The tank containing the titanium-dioxide dispersion and the pump feeding the jet nozzle are shown in purple. (b): The flow visualization equipment (camera in green, projector in red, and mirror in yellow) located above the plate (orange). (c): Aligning the camera by placing a mirror over the plate surface and adjusting the camera's position until its optical opening is centered on the image plane (as indicated by the yellow crosshairs). (d): Adjusting the camera's tilt so that the plate (white) is square to the image plane, as determined by drawing a (yellow) rectangle in the uEye Cockpit image capturing software. (e): Aligning the projector by projecting concentric rings and then moving the projector until the (blue, green, and red) rings are centered about its optical opening.

2.2.1 Fourier Transform Profilometry

Fourier transform profilometry (FTP) is performed to capture the flow's surface deformations over the plates. This method requires projecting a sinusoidal fringe pattern onto the fluid's free surface. These fringes are deformed when water flows over the plate. The resulting phase shift in the fringes is related to the height of the flow features as given by

$$h(x', y') = \frac{L_c L_p \Delta\varphi(x, y)}{L_c \left[\Delta\varphi(x, y) - \omega_o (D + y)\right] + L_p \omega_o y},$$
(2.1)

where ω_o is the spatial frequency of the sinusoidal fringe pattern, and L_c, L_p, and D are geometric parameters. (For a detailed description, see appendix A.)

In order to perform FTP, a camera (iDS UI 336xCP-M-ID:1 with a 1:1.4, 25 mm FujiFilm lens and polarizer attached run via the uEye Cockpit 4.31.0 software at 45 frames per second) is placed at a height L_c above the plate. The camera's optical axis is aligned at angle α with the vertical such that the camera's field of view (FOV) is coincident with the plate's surface. An Epson 5030UB LCD projector, with a brightness of 2400 lumens and a resolution of 1080p, is used to project the fringe pattern. The projector is too heavy to be placed directly above the jet setup as is usually done for the FTP technique. Because it must be located on a separate platform off to the side, a mirror must be added to the FTP setup. The mirror is placed downstream of the camera at a height L_{p1} above the plate's surface, as shown in figure 2.1. The projector projects a fringe pattern onto this mirror, which then reflects the fringes down onto the plate's surface. The projector's optical axis is a distance D from of the camera's optical axis, and its optical opening is a total distance $L_p = L_{p1} + L_{p2}$ from the plate's surface, with L_{p2} being the horizontal distance between the mirror and the projector. The fringes are rotated η degrees in the projector, such that they are aligned with the x-axis in the camera's field of view, resulting in an equivalent FTP setup as seen in figure 2.3.

Because fringes must be projected onto the working fluid, the fluid must be opaque. The experiments conducted thus used a 0.5% TiO_2 (by volume) dispersion in deionized water. Properties of this mixture are discussed in section 2.2.3.
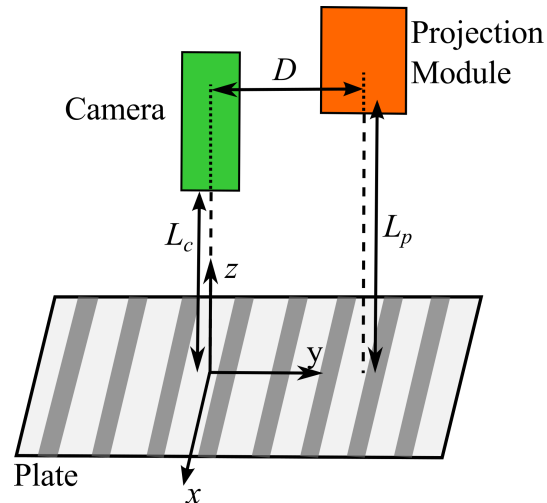
Figure 2.3: Schematic of equivalent parallel-optical-axes setup.

Alignment

Proper alignment of the camera, projector, and mirror are essential for accurate Fourier transform profilometry results.

To align the camera's optical axis to the z-axis (at an angle α with the vertical), a second mirror is placed on top of the plate's surface. The image captured by the camera thus shows the camera itself. When the camera is properly aligned, its optical opening, as seen in the reflection on the mirror, is at the center of the recorded image. The camera's position is thus adjusted until this is the case (figure 2.2c). The mirror in the camera's field of view is then removed and the camera's tilt in the $xy-$ plane is adjusted until the edges of the FOV are aligned to the plate's edges (figure 2.2d). This adjustment effectively changes the orientation of the camera's ccd sensor so that the region of interest is properly captured. The final step is to focus the camera. This is achieved by placing a sheet of paper with printed text onto the plate's surface and adjusting the camera's settings until the recorded image is in focus and the text is sharp.

The projector-mirror system is aligned next. The mirror is rotated about the x- and z- axes such that projections cover the entire plate surface with minimal zooming out on the projector. It is tilted approximately $45°$ about the y- axis to reduce distortions in projections. Rings of concentric circles centered about the projector's optical axis are then projected onto a mirror placed on the plate's surface. The rings are thus reflected back up to the projector. The projector's position is adjusted until these reflected rings are centered about its optical opening (figure 2.2e), as is

expected if the projector-mirror system's optical axes is aligned to the z-axis and perpendicular to the plate's surface. Once aligned, the projector is set to project text. The projector's focus is adjusted until the text is clear and sharp on the plate's surface.

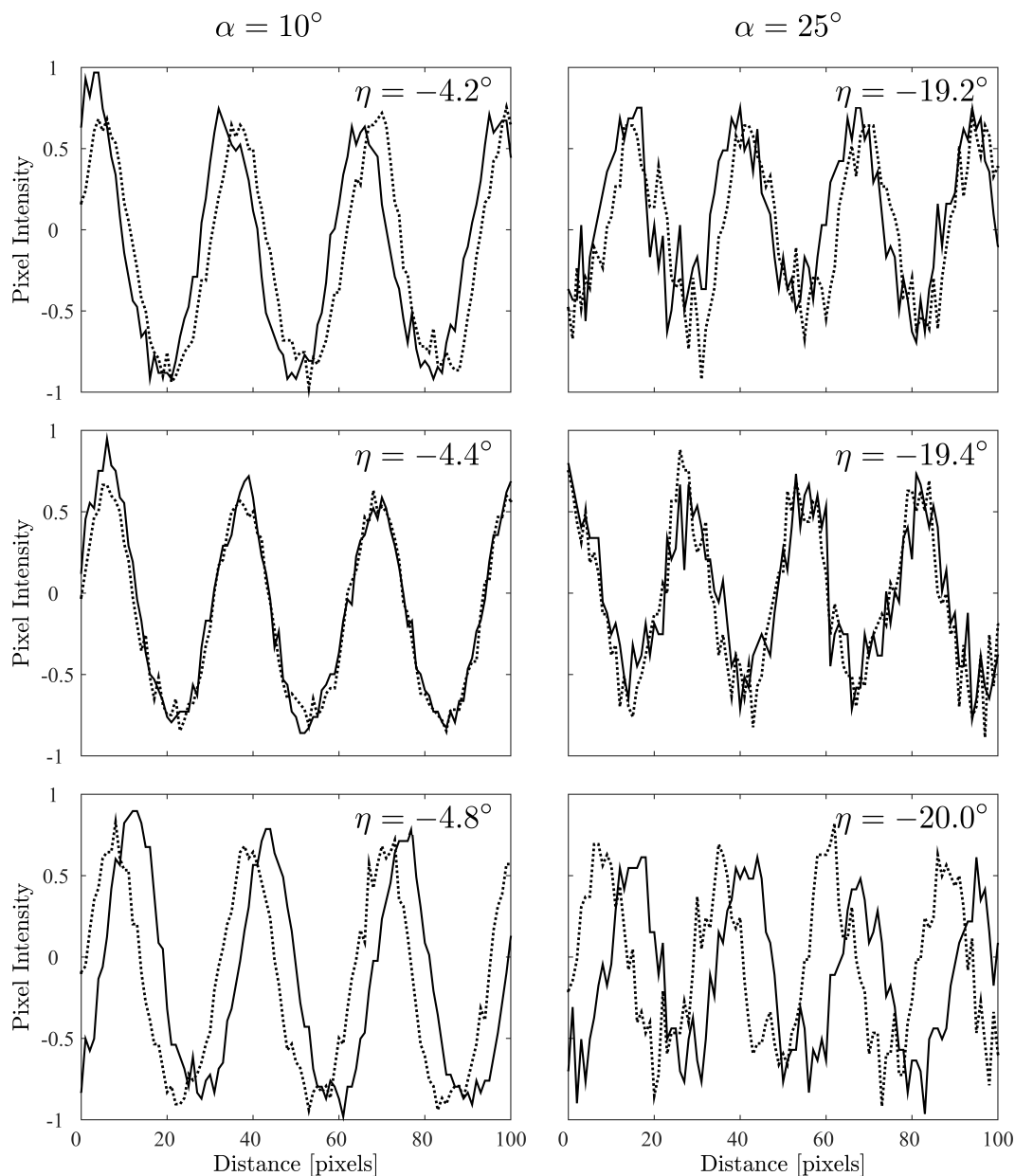**Figure 2.4:** The projected fringe pattern must be rotated in the projector in order to be aligned to the x-axis on the camera's FOV. When the fringe pattern is properly aligned, the intensity profile of the pattern at the downstream and upstream edges of the plate (solid and dashed lines, respectively) will be in phase and have the same frequency. The middle row shows properly aligned cases.

The final step is the alignment of the fringes with the x-axis of the camera's field of view. Because the mirror reflecting the fringes down to the camera's FOV is rotated about the x- and z- axes, the fringes must be rotated in the projector in order to properly align them with the x-axis. A sinusoidal fringe pattern is projected onto the plate's surface at different angles η with respect to the projector's optical axis. Images of the fringes are taken for each angle. The images are loaded into ImageJ, where the greyscale intensity profile of the downstream and upstream edges of the plate are taken (seen in figure 2.4). These two profiles are compared to one another: if a phase shift is present, the fringes are not correctly aligned to the x-axis and the fringe angle in the projector must be modified; if the two signals do not have the same frequency, then either the projector-mirror or the camera systems are not properly aligned.

Calibration

Calibration is conducted prior to experiments by offsetting the plate's surface by known heights and fitting L_c, L_p, and D such that FTP correctly predicts the surface heights. The surface is raised by stacking high tolerance plates of different thicknesses beneath the original surface plate. Initial estimates for L_c and L_p can be found by measuring the approximate camera-to-plate and projector-to-mirror-to-plate distances before raising the surface. D can be approximated by projecting crosshairs (centered in the projector) onto the plate's surface and taking an image. The distance between the crosshairs and the center of the image (i.e. the camera's optical axis) estimates D.

The calibration process must be repeated every time the inclination angle α is changed, the results of which are presented in figures 2.5a and 2.5b. (Note that FTP was not performed at the $\alpha = 9°$ case.) The dashed lines in the plots are the tolerances on the heights, as given by the manufacturers' specifications for the stacking plates. The goal is to have the solid lines from FTP fall within the dashed lines. Note that there are edge effects present in the FTP reconstruction of the height profiles. However, the features of interest in the experiments are located away from the edges of the image, thus edge effects are not a hindrance.

Error analysis of the FTP process is obtained by reconstructing the profile of a wedge of known dimensions at different y-locations. The reconstructed FTP wedge profile is plotted as a solid line in figures 2.5c and 2.5d for three y-locations. The dashed line is the actual wedge profile. The wedge is fabricated with an Objet500 Connex1

3D printer with a tolerance of 200 microns (profile tolerance not shown in plots). Comparing the reconstructed FTP profiles to the actual profile yields the error in the FTP results. For the $\alpha = 10°$ case, however, the reconstructed wedges have lower error than the plate calibration results (FTP overestimates the height for the 3.175 mm thick plate whereas it obtains the height correctly for the other thickness plates). For this case, the error associated with the plate calibration is therefore used as the overall expected FTP error. Because of the edge effects present in the FTP results, the first and last hundred data points are discarded in error analysis.
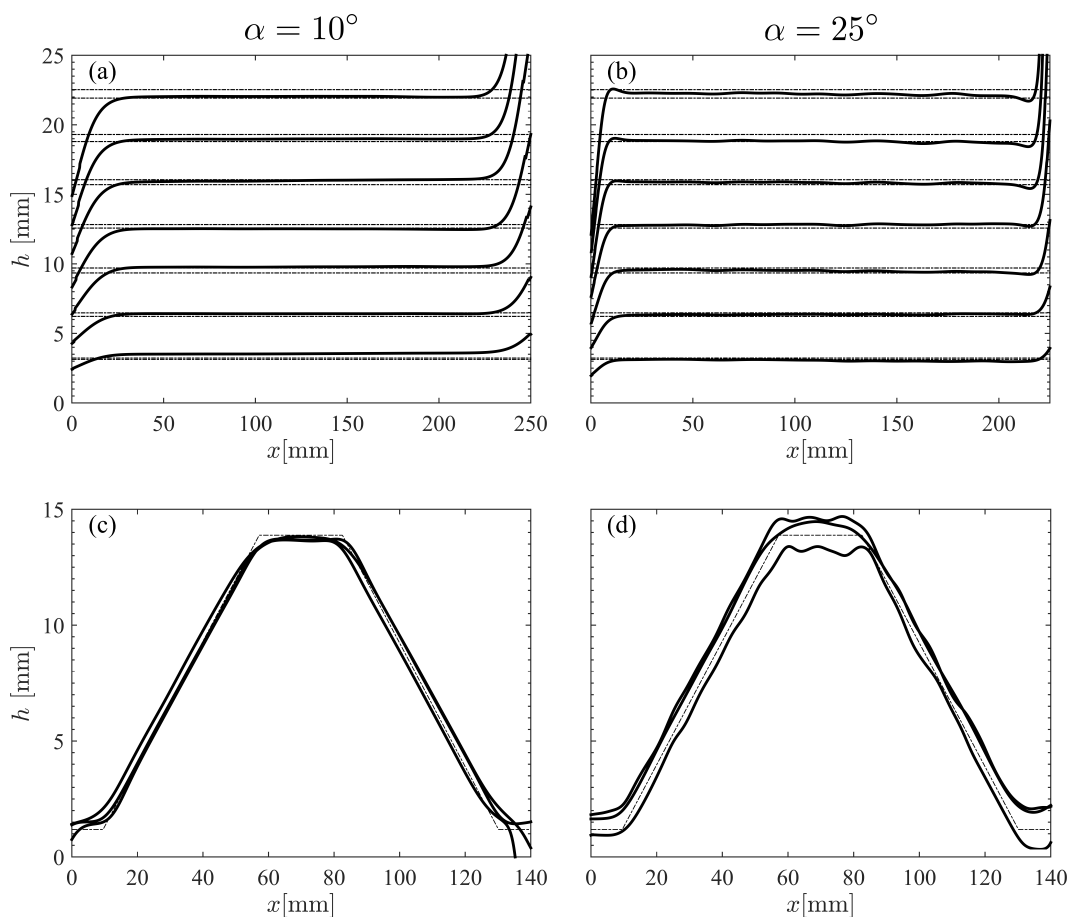

Figure 2.5: Calibration for FTP as obtained by raising the surface plate by known heights for $\alpha = 10°$ (a) and $\alpha = 25°$ (b) . Dashed lines are the tolerances on the heights, as given by the manufacturers. Solid black lines are the FTP results. Error analysis for FTP is conducted by reconstructing a known wedge profile (insets c and d). The dashed line is the actual wedge profile. Solid lines are the FTP reconstruction at three y-locations.

The maximum expected flow feature height in experiments is around 14 mm (or about ten times the initial sheet thickness). Calibration plates were stacked to heights

greater than this when fitting L_c, L_p, and D in order to ensure the full range of height features were properly resolved with the chosen parameters. The wedge used in error analysis has a maximum height of 13.88 mm, which also spans the range of expected flow feature heights.

The values for L_c, L_p, D, and the FTP errors are recorded in table 2.2. The errors that are reported are errors above or below the tolerances for the actual wedge profile or plate heights.

Case	L_c [mm]	L_p [mm]	D [mm]	Error [mm (pixels)]
Expected	546 - 648	724 - 826	102	-
$\alpha = 10°$	555	715	105	± 0.21 (1.6)
$\alpha = 25°$	655	850	98	± 0.68 (4.6)

Table 2.2: Calibration parameters and error values for FTP

2.2.2 Surface Properties

The plates used in these experiments are made of delrin. They are polished using sandpaper with progressively finer grit ratings, until a final 1200 grit sandpaper is used. The polished delrin is naturally hydrophilic, as can be observed in figure 2.7a.

In order to introduce hydrophobic properties, the plates are coated with Rust-Oleum's commercially available NeverWet Multi-Surface hydrophobic coating. To create the non-uniform wetting properties, masks of the desired band pattern are drawn in SolidWorks and saved as .dxf files. The masks are then imported into the Cricut Design Space program, which runs a Cricut Explore One cutting machine. The machine cuts the masks into adhesive vinyl sheets, which are then applied to the delrin plate. The plate is then coated with the hydrophobic coating, which consists of two layers: the first introduces micron-sized roughness on the surface to amplify the surface properties; and, the second provides the chemical treatment to render the surface hydrophobic. Once the hydrophobic coating has cured, the vinyl mask is peeled off. The result is a plate with alternating hydrophobic and hydrophilic bands.

Contact Angle Measurements

The contact angle associated with the hydrophilic and hydrophobic surfaces is measured using the setup show in figure 2.6. A sample is placed on an optical table whose tilt angle is adjusted until the table lies perfectly flat. A Harvard Pico Plus Elite pump dispenses a $10\mu L$ drop of either deionized water or 0.5%v/v titanium-dioxide-water dispersion onto the sample's surface. The drop is backlit by an LED

light source, and a iDS UI 336xCP-C-ID:1 camera with a Edmund Optics 0.5x
telecentric lens is used to capture images. The camera, run via the uEye Cockpit
4.31.0 software, is mounted onto a vertical rail in order to adjust its vertical position
such that the drop is imaged straight on. The DropSnake plugin in ImageJ 1.47v
(developed by Stalder et al. in their 2006 paper) is used to measure the contact angles
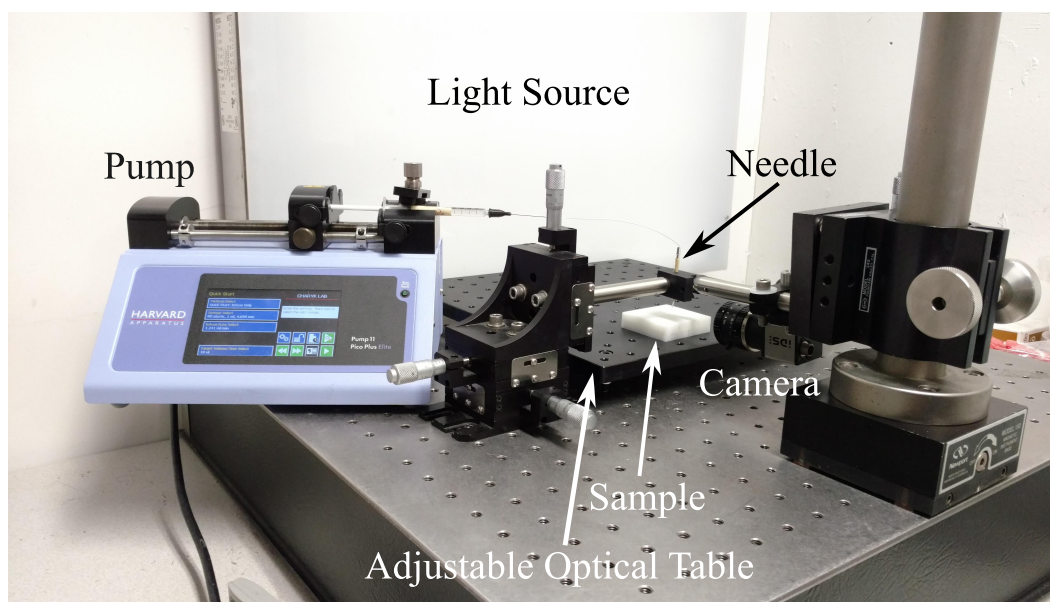from the resulting images.

Figure 2.6: Setup for contact angle measurements.

The contact angles are found to be $\theta = 96° \pm 2°$ ($93° \pm 2°$) on the hydrophilic
surface and $\theta = 157° \pm 1°$ ($158° \pm 1°$) for the hydrophobic surface using deionized
water (0.5%v/v titanium-dioxide dispersion). These values, however, correspond
to instantaneous measurements of the contact angle taken as soon as the drop is
deposited on the surface. As can be seen in figure 2.7, the hydrophilic surface's
contact angle decreases significantly with time (to a value of $73° \pm 3°$ ten minutes
after deposition).

As described by Ruijter et al. (2000), if a drop is deposited in a non-equilibrium
configuration on a hydrophilic surface, it will spread. Furthermore, two spreading
regimes exist: a molecular-kinetic regime, by which energy is dissipated in the vicin-
ity of the contact line due to physicochemical processes promoting the attachment
of water molecules to the surface, and a hydrodynamic regime. The contact angle's
time-dependence in these regimes goes like $\theta \sim t^{-3/7}$ and $\theta \sim t^{-3/10}$, respectively.
Thus, regardless of the regime of spreading, the contact angle will have largely

stabilized and reached equilibrium at the ten minute mark. The equilibrium contact angle is therefore $\theta = 73° \pm 3°$ for the hydrophilic surface. The contact angle on the hydrophobic surface does not change significantly with time and remains around 157°.
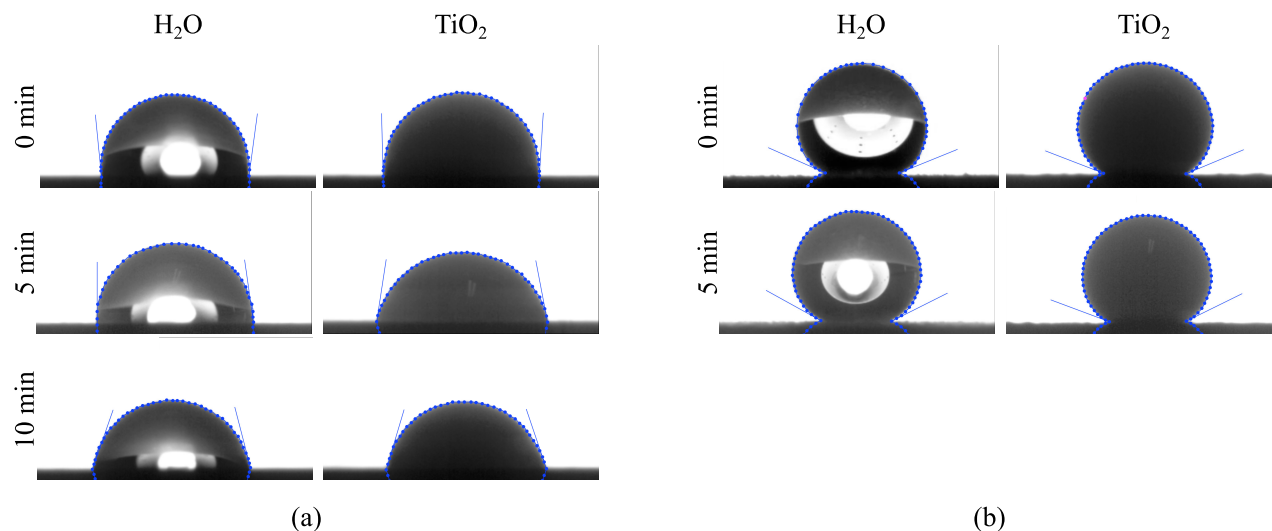

Figure 2.7: Contact angle measurements on the hydrophilic (a) and hydrophobic (b) surfaces using $10\mu L$ drops of water or 0.5%v/v titanium-dioxide dispersion, as indicated. Blue dotted curves are outlines of the drop used to compute the contact angle in ImageJ's DropSnake plugin (developed by the Biomedical Imaging Group at EPFL. See Stalder, Kulik, Sage, Barbieri, and Hoffmann (2006)).

In addition to the equilibrium contact angle being measured, the contact angle hysteresis is measured. The contact angle hysteresis is found one of two ways: for hydrophobic surfaces, the tilting plate method is used (Eral, Mannetje, and Oh, 2013). In this method, the sample is placed on a tilting plate, which is originally horizontal. As its tilt angle is increased, the drop on the sample begins to deform under gravitation pull. The contact angle increases on the downhill side of the drop while decreasing on the uphill side, as shown in the schematic of figure 2.8. The value of these two angles is measured when the drop finally unpins from the surfaces and rolls down the sample. They define the advancing and receding contact angles, respectively, which represent the maximum and minimum contact angles possible before contact line unpinning for the specific liquid-solid-gas combination. The advancing and receding contact angles are measured as $\theta_a \approx 160°$ and $\theta_r \approx 152°$ for the hydrophobic surface, resulting in a contact angle hysteresis of around 8°. These measurements are the same for both deionized water and the titanium-dioxide dispersion.
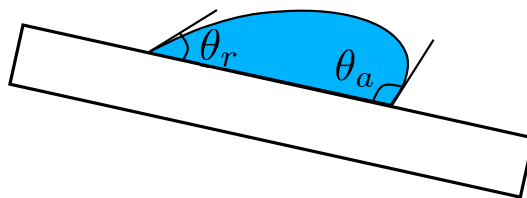
Figure 2.8: Schematic of contact angle hysteresis as measured in the tilting plate method. The contact angle of the drop increases on the downhill side of the drop (setting the advancing contact angle) while decreasing on the uphill side (setting the receding contact angle).

For hydrophilic surfaces, however, the tilting plate method is not practical as the contact angle hysteresis is large. Instead, a second method is used whereby additional water is added to the drop in 1μL increments. The contact angle at which the contact line suddenly unpins and jumps is the advancing contact angle. Fluid is then removed from the drop by running the pump in reverse. The contact angle at which the contact line suddenly retracts is the receding contact angle. This method is commonly referred to as the sessile drop method (Eral, Mannetje, and Oh, 2013). Using this method the contact hysteresis is found to be around $54°$ ($\theta_a \approx 110°$, $\theta_r \approx 56°$) for the hydrophilic surface. These measurements are only a couple of degrees different between the deionized water and titanium-dioxide dispersion, which is within the measurement uncertainty (typically $1° - 5°$).

The contact angle measurements are summarized in table 2.3.

Wetting condition	θ	θ_a	θ_r
Hydrophilic	73°	110°	56°
Hydrophobic	157°	160°	152°

Table 2.3: Contact angle measurements for the thin film experiments.

Coating Thickness Characterization

As hydrophobic wetting properties are introduced via an added coating, the heterogenous plates will have protrusions wherever there are hydrophobic bands. The thickness of these bands is measured using a Bruker DekTakXT stylus profilometer (1Å resolution reported) at Caltech's Molecular Materials Research Center.

The coating is 9 - 14 μm thick on average, with an increased thickness ($< 40\mu$m) at the edges of the band. This increased thickness at the edges is due to particles building up at the edge of the vinyl mask during the coating process. The coating is

less than 3% of the jet nozzle height h_{jet} at the band edges and less than 0.9% of h_{jet} away from the band edges. The roughness is also two orders of magnitude smaller than the band widths (d) studied.

The effects of the coating thickness are discussed further in appendix C.

2.2.3 Working Fluid Properties

Fourier Transform Profilometry requires that the fluid be opaque with a high reflectance. Because the working fluid is deionized water, particles must be added to the water in order to render it opaque. The ideal particles should provide the fluid surface with a high reflectance so that FTP fringes can be well contrasted and sharply defined. The particles should also disperse in water so that no aggregation of particles is present. In addition, the particles should not change the working fluid's properties, which could affect surface tension phenomena that the experiments are quantifying.

Titanium dioxide particles from Spectrum (type T1081, CAS no. 13463-67-7) were selected for the current experiments. The powder is a water dispersible anatase, which, although not water soluble, provides a well-mixed homogenous dispersion for experiments. The titanium dioxide particles have a specific gravity of 4.26 (using water as the reference substance). Thus, the particles tend to sink over time, which can cause the fluid surface reflectance to decrease and FTP to give a lowered surface height if not constantly mixed.

The average particle size is 300 nm (with a maximum of 1 micron), as reported by the manufacturer. This particle size is at the low-end of the range of optimal particle sizes (300 to 400 nm) for slow sedimentation as found by Przadka et al. (2012). The sedimentation speed they computed (and confirmed experimentally) for their titanium dioxide anatase particles is around 250 nm/s. Using the same equation for sedimentation speed (below), a sedimentation speed of about 160 nm/s is obtained for the particles used in the current work. The sedimentation speed equation is found by balancing the gravity force on particles and the viscous resistance of water,

$$v = \frac{2}{9}\frac{\Delta\rho g}{\mu}r^2, \tag{2.2}$$

where g is the gravitational acceleration of 9.81 m/s^2, μ is the dynamic viscosity of water of around 10^{-4} Pa s, and $\Delta\rho$ is the density difference between the titanium dioxide particles and water.

Experimental runs last less than five minutes each. The expected sedimentation without agitating the water would be less than 50 nm. However, by the very nature of the current experiments, the fluid is constantly agitated during testing: the dispersion is continuously circulating in a closed loop between the tank, the pump, and the jet. The jet speed is also orders of magnitude greater than the sedimentation speed in all experimental cases; thus, the jet should amply agitate the dispersion to prevent sedimentation during experiments. The dispersion in the tank is also mixed before every experiment to ensure any particles that have accumulated at the bottom of the tank between tests are thoroughly stirred up.

A dispersion of 0.5 % v/v TiO_2-to-H_2O was used in the current experiments (roughly a 20 g/L TiO_2 concentration), matching the concentration used by Cobelli et al. (2009) in their experiments. They reported a Michelson luminance contrast greater than 0.85, allowing for good contrast of the FTP fringes.

To further understand the effects of the anatase pigment on the experiments conducted, some simple tests were run. In the first set of tests, samples of the hydrophilic and hydrophobic surfaces used during experiments were placed in petri dishes and covered with the 0.5% v/v TiO_2-to-H_2O dispersion. The contact angle made by a 10 μL drop of deionized water deposited on the sample was measured on each surface before testing and then after the sample had soaked in the liquid for 5 minutes, 10 minutes, 30 minutes, 1 hour, and 24 hours. The samples were dried in a dehydrator for 10 minutes with the fan running and heat off before contact angle measurements were taken. The contact angle was measured instantly after the drop was deposited on the surface and five minutes later. For comparison, the test was repeated with pure deionized (DI) water.

In the second set of tests, the jet flowed over a half-hydrophilic, half-hydrophobic plate at maximum flow rate. The contact angle made by a 10 μL drop of deionized water was measured on each region before testing and then after 5, 10, and 30 minutes of being under the jet. The samples were again dried in a dehydrator for 10 minutes with the fan running and heat off before contact angle measurements were taken. As before, the contact angle was measured instantly after the drop was deposited on the surface and five minutes later. Results are presented in figure 2.9.

The results of these tests show that TiO_2 deposits decrease the contact angle for both the hydrophilic and hydrophobic surfaces (as shown by the grey curves in the top row), even going so far as to render the hydrophobic surface hydrophilic. However, whereas soaking the delrin plastic in pure DI water did not result in as large an

effect for the hydrophilic surfaces (the measured contact angles, shown in black, still fall within the contact angle hysteresis), the effect is more pronounced for the hydrophobic surfaces. In this case, the measured contact angles fall outside the equilibrium contact angle hysteresis. Thus, water absorption by the plastic lowers the hydrophobicity of the surface.
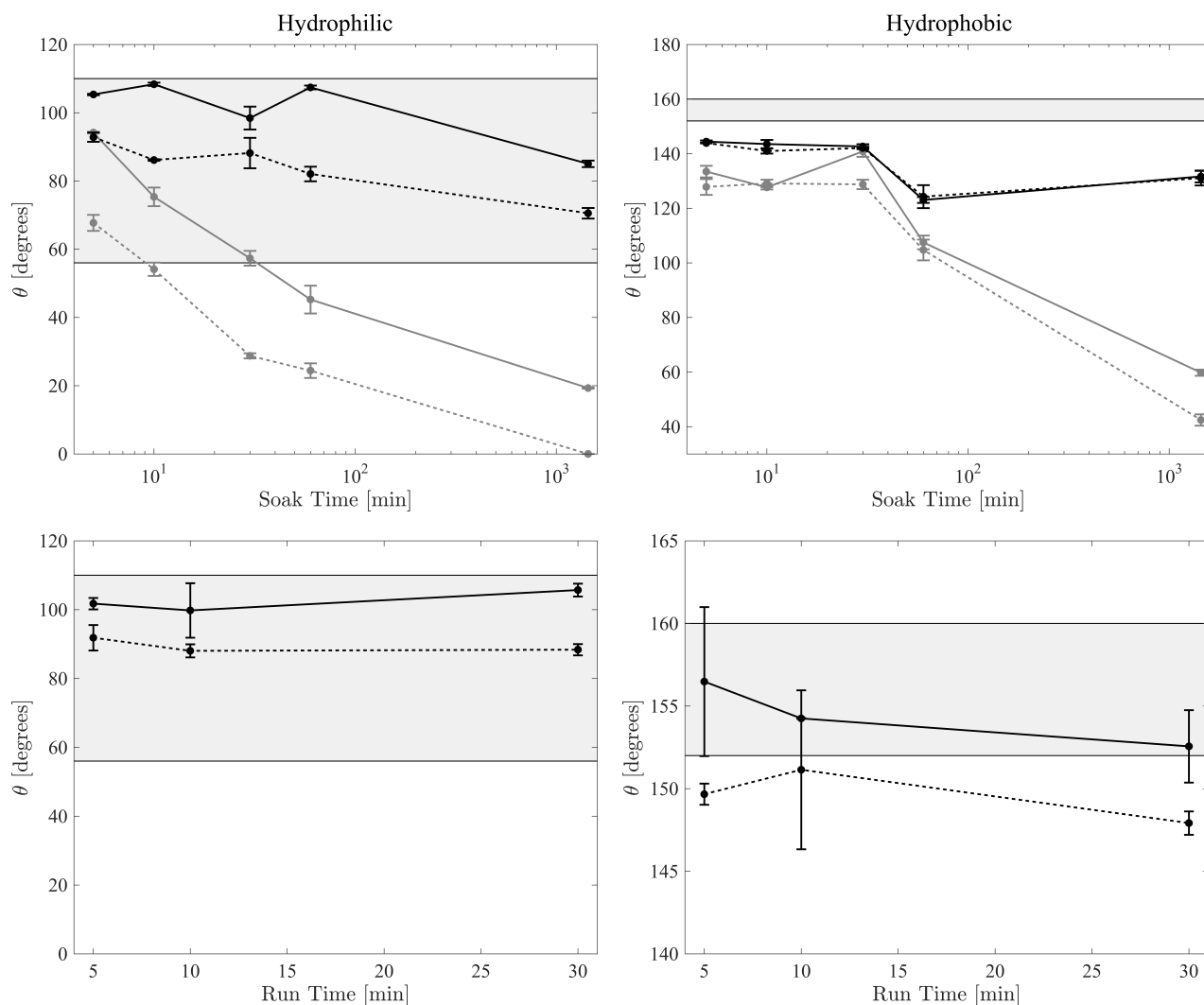

Figure 2.9: Quantifying the effects of titanium-dioxide on contact angle. Top row: samples are soaked in deionized water (black curves) or the titanium-dioxide dispersion (grey curves) for varying amounts of time. Bottom row: high flow rate titanium-dioxide dispersion flows over the samples for varying run times. Contact angle measurements are made with 10 μL drops of deionized water and are recorded instantly (solid lines) or five minutes after drop deposition (dashed lines). Light grey regions indicate the contact angle hysteresis range as determined in section 2.2.2.

When tested in experiment-like conditions (bottom row), the titanium-dioxide dispersion does not greatly affect the hydrophilic surface. The contact angle measurements all fall within the hysteresis region. Likewise, the hydrophobic surface is less affected, its contact angle only falling slightly lower than the hysteresis region when measured five minutes after drop deposition.

As a result of these tests, the present experiments were run for a maximum of five minutes before the plates were gently rinsed in deionized water and dried in a dehydrator (fan on only, no heat) for at least 10 minutes before continuing experiments. Due to these testing procedures, only one flow rate is tested at a time. That is, the plate is tested at a given flow rate, then removed from the setup, rinsed, and thoroughly dried before continuing to the next flow rate of interest.

By limiting the run time, titanium dioxide depositions are limited and thus should not affect the surface-liquid interactions during testing. Rinsing the plate and drying it thoroughly before re-testing further removes any titanium dioxide deposition that may have accumulated during testing and ensures that hydrophobic surfaces do not lose hydrophobicity due to water absorption.

2.2.4 Jet Characterization

The jet's flow rate is controlled by the adjustment knob of a needle valve connected to the flow pump. The flow rate's dependence on the needle valve setting is determined by collecting water exiting the jet in a beaker. A timer is simultaneously used to record the time taken to collect a given volume of water. Data is collected for valve settings ranging from 5 turns of the knob to the fully-open setting corresponding to 90 turns of the knob. The jet is also characterized at each of the three plate inclinations of interest as the jet nozzle is inclined at angle α with respect to the horizontal in order to ensure that the jet impinges the plate at zero-angle. As the inclination angle of the plate is set by rotating the plate about its center (as seen in orange in the top right of figure 2.2), the height of the plate at the leading edge increases with increasing α. The jet nozzle must likewise be moved vertically to remain flush with the plate's leading edge. Thus, the potential energy of the system increases, which affects the flow rate measured.

Each (α, valve setting) combination is repeated a minimum of three times. Results are shown in figure 2.10 along with data fits, which are fourth-order polynomials for all inclination angles. The flow rates reported in the remainder of this chapter are determined using the curve fit value for the given (α, valve setting) combination.
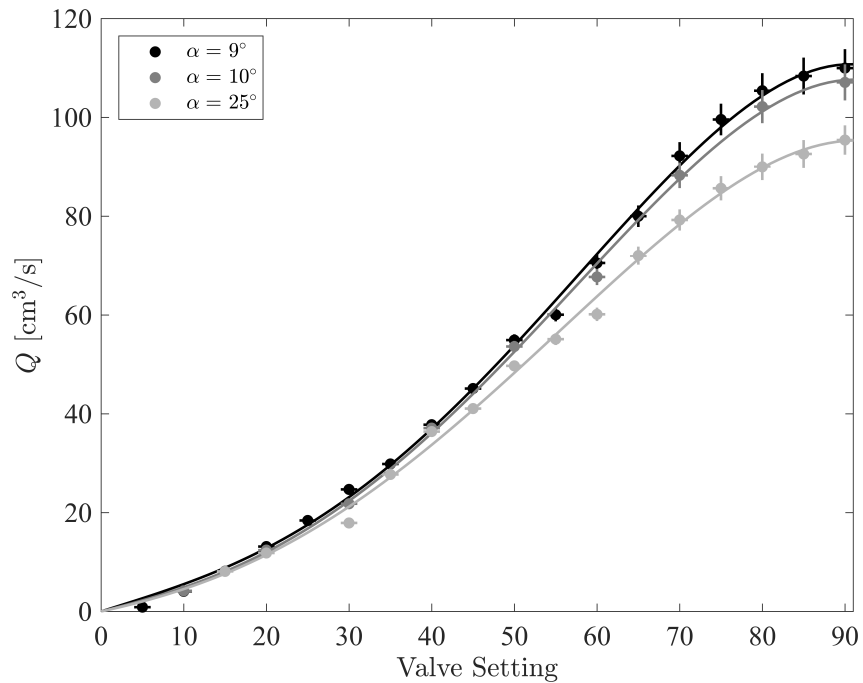
Figure 2.10: Jet flow rate as a function of the needle valve setting (90 turns is fully opened) for the plate inclination angles studied. Symbols represent the experimental data along with the measurement uncertainties. Solid lines are polynomial fits.

2.3 Results

Videos of the flow field over plates with different wetting conditions were taken at various flow rates and plate inclination angles. Still frames of some of the experimental videos are presented in figures 2.11 to 2.16. As can be seen from the figures, many flow regimes arise over the range of flow and surface conditions considered.
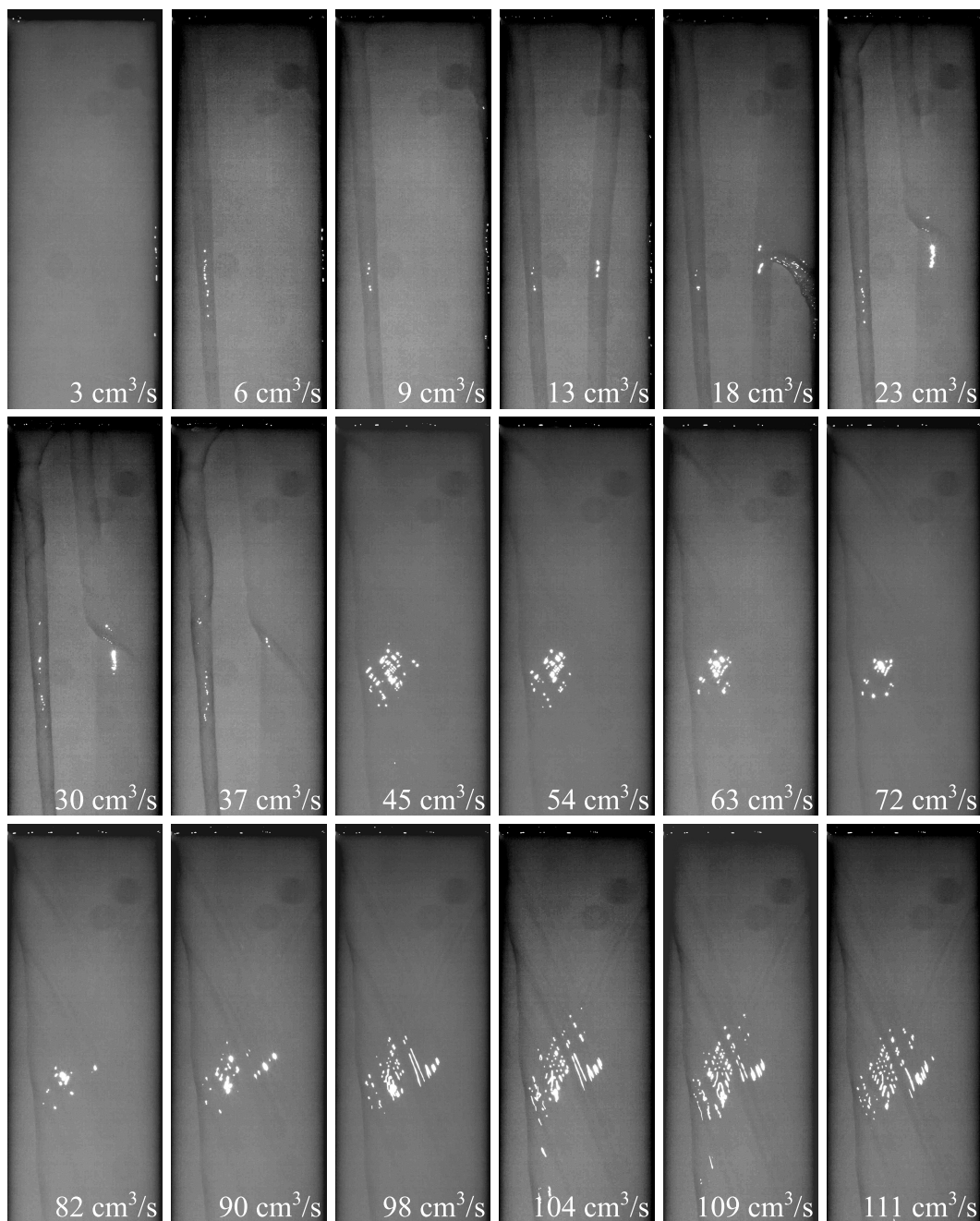
Figure 2.11: Flow over a uniformly hydrophilic plate inclined at $\alpha = 9°$ with respect to the horizontal. Flow is top to bottom. Three flow regimes occur: linear rivulets ($Q \leq 18$ cm^3/s, with two rivulets merging together to form a sheet on the righthand side of $Q = 18$ cm^3/s), meanders (second rivulet for 23 cm^3/s $\leq Q \leq 30$ cm^3/s and first rivulet of $Q = 37$ cm^3/s), and film flow ($Q \geq 45$ cm^3/s).

Figure 2.12: Flow over a uniformly hydrophilic plate inclined at $\alpha = 10°$ with respect to the horizontal. Flow is top to bottom. Three flow regimes occur: linear rivulets ($Q = 5$ cm^3/s), meanders (first rivulet in $Q = 17$ cm^3/s, which then merges with the wide finger in the center of the plate), and film flow ($Q \geq 29$ cm^3/s).

Figure 2.13: Flow over a uniformly hydrophobic plate inclined at $\alpha = 9°$ with respect to the horizontal. Flow is top to bottom. Several flow regimes occur: drops (in the dripping faucet mode for $Q = 3$ cm^3/s and for the second finger in $Q = 6$ cm^3/s; in the jetting mode for the first finger in $Q = 6$cm^3/s as well as for $Q = 9$ cm^3/s), pendulums (13 cm$^3 \leq Q \leq 45$ cm^3/s), and braiding ($Q \geq 54$ cm^3/s).
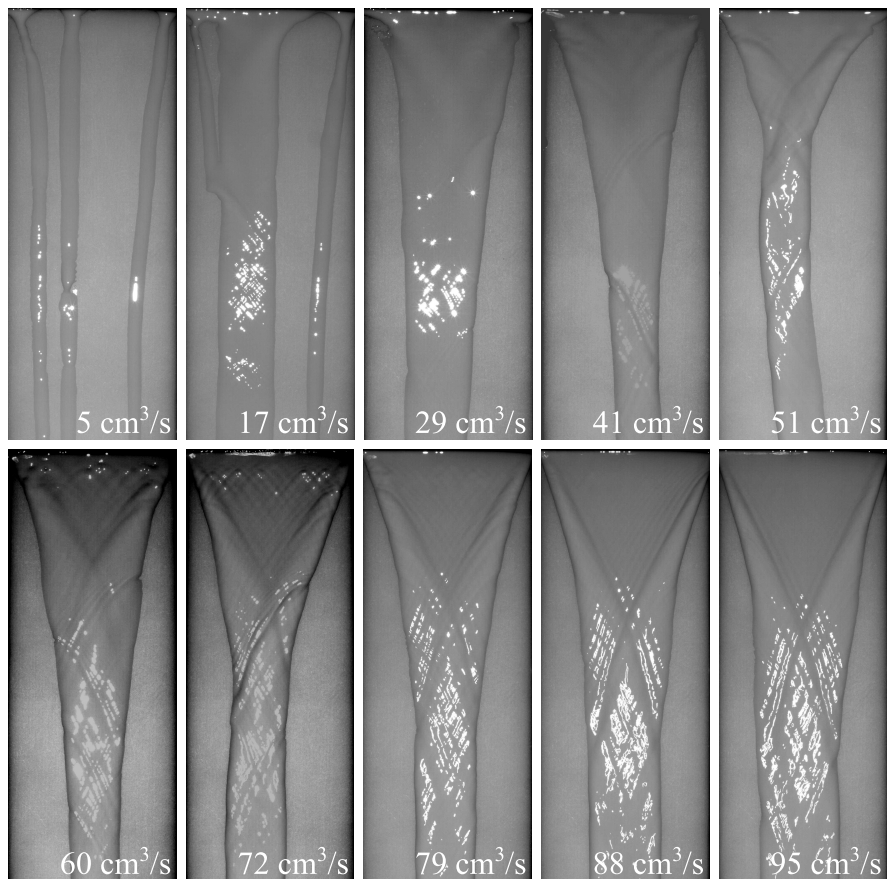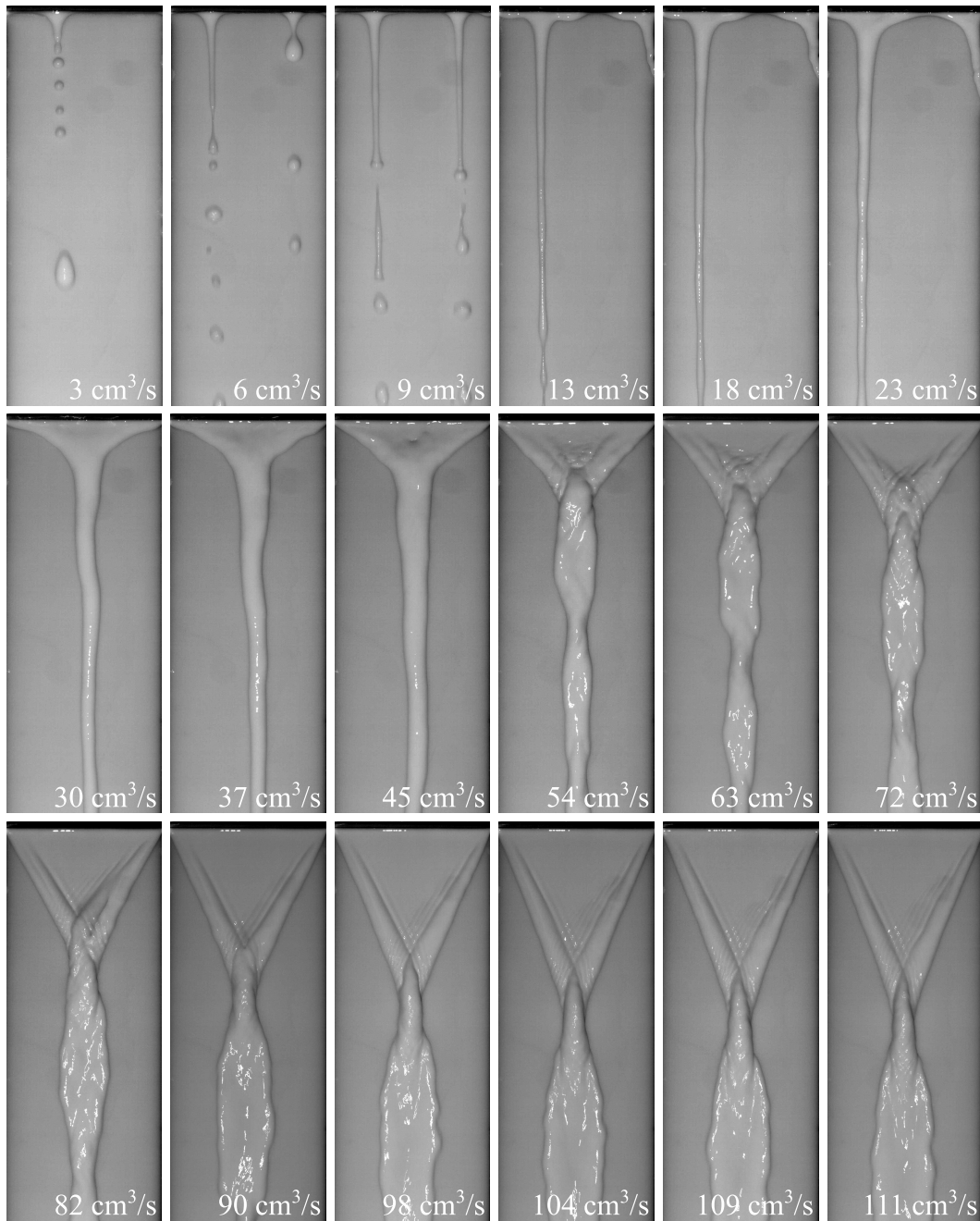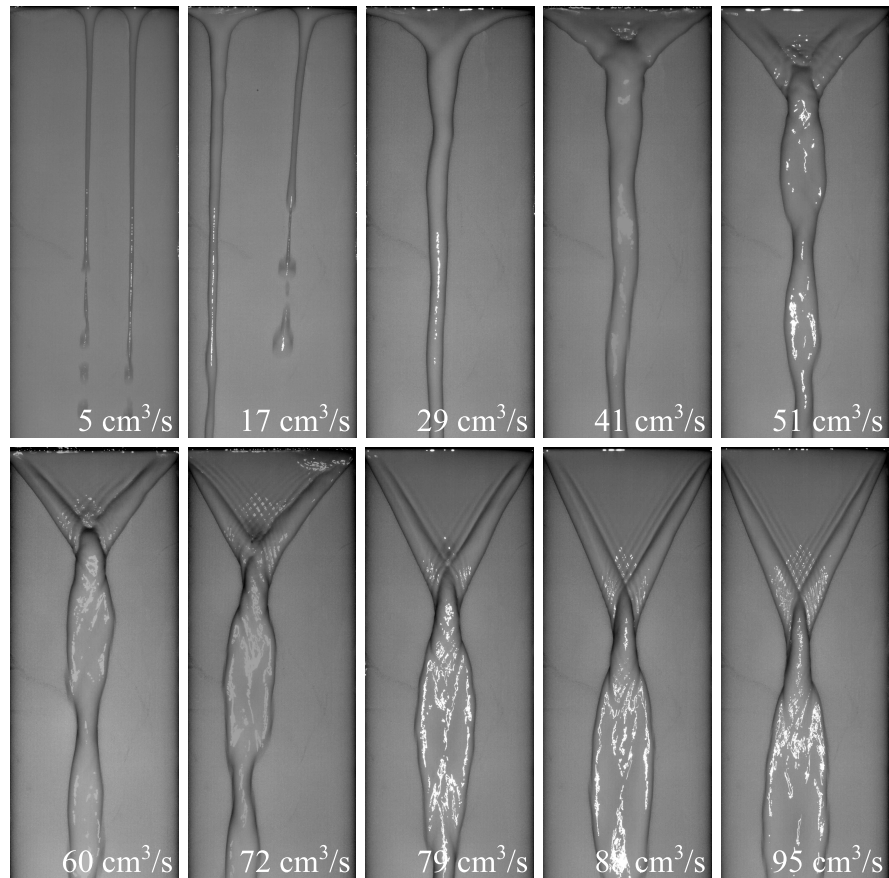
Figure 2.14: Flow over a uniformly hydrophobic plate inclined at $\alpha = 10°$ with respect to the horizontal. Flow is top to bottom. Several flow regimes occur: drops in the jetting regimes ($Q \leq 17$ cm³/s), pendulums (29 cm³/s $\leq Q \leq 41$ cm³/s), and braiding ($Q \geq 51$ cm³/s).
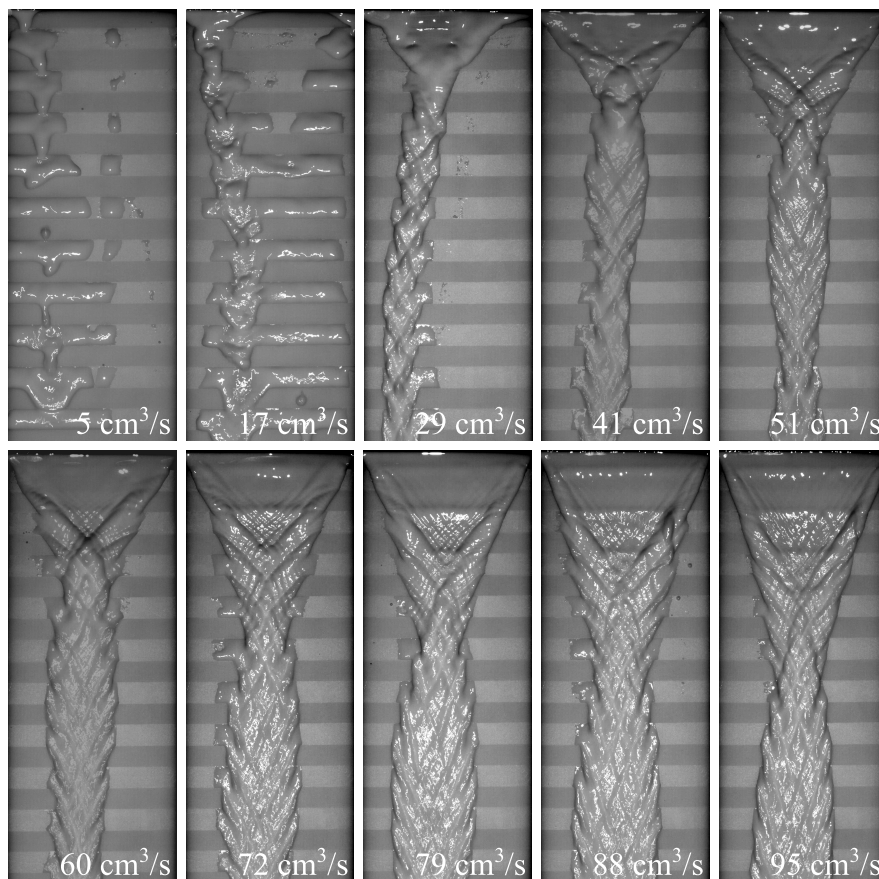
Figure 2.15: Flow over a patterned plate inclined at $\alpha = 10°$ with respect to the horizontal. The plate is patterned with 12.7 mm wide alternating hydrophilic (light gray) and hydrophobic (dark gray) bands oriented perpendicular to the flow direction. Flow is top to bottom. Three flow regimes occur: drop-like regime for $Q = 5$ cm^3/s, meanders (17 cm^3/s $\leq Q \leq$ 29 cm^3/s), and braiding ($Q \geq 41$ cm^3/s).
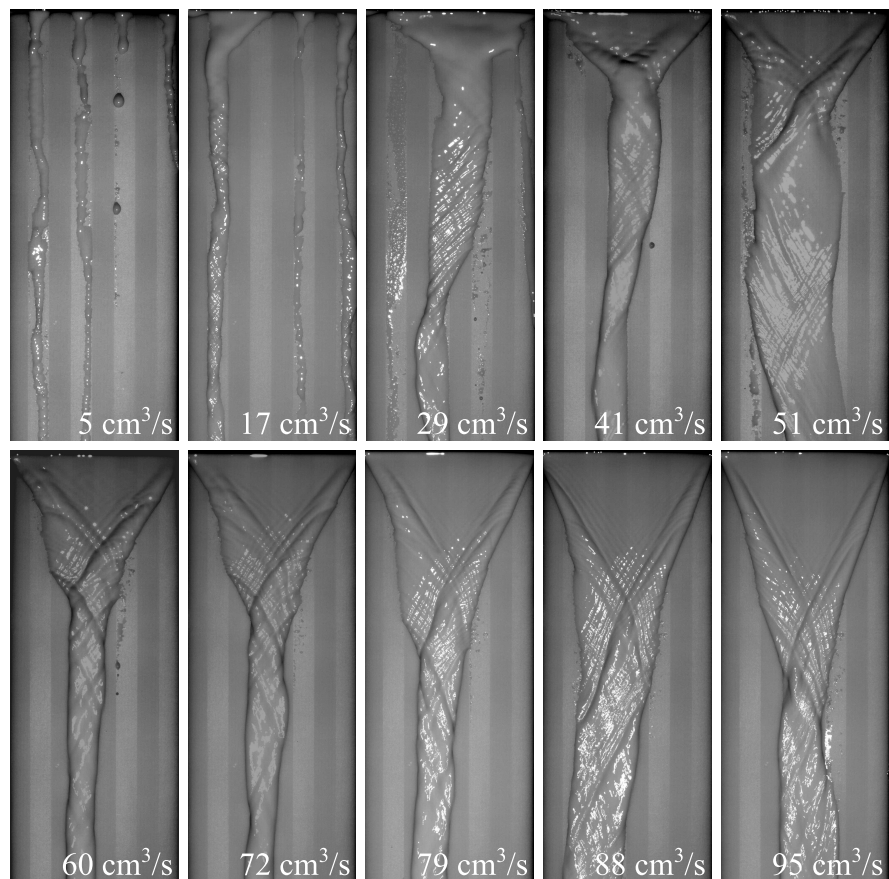
Figure 2.16: Flow over a patterned plate inclined at $\alpha = 10°$ with respect to the horizontal. The plate is patterned with 12.7 mm wide alternating hydrophilic (light gray) and hydrophobic (dark gray) bands oriented parallel to the flow direction. Flow is top to bottom. Three flow regimes occur: stationary rivulets (5 cm^3/s $\leq Q \leq$ 17 cm^3/s), meander-like regime (29 cm^3/s $\leq Q \leq$ 41 cm^3/s), and perturbed sheets or rivulets ($Q \geq$ 51 cm^3/s).

2.3.1 Fingering Instability

At very low flow rates, the sheet is susceptible to fingering instabilities irrespective of the plate's wetting condition.

Fingering instabilities may be gravity-driven (Rayleigh-Taylor instability) or viscous-driven, as depicted in figures 2.17a and 2.17b, respectively.

(a)   (b)   (c)
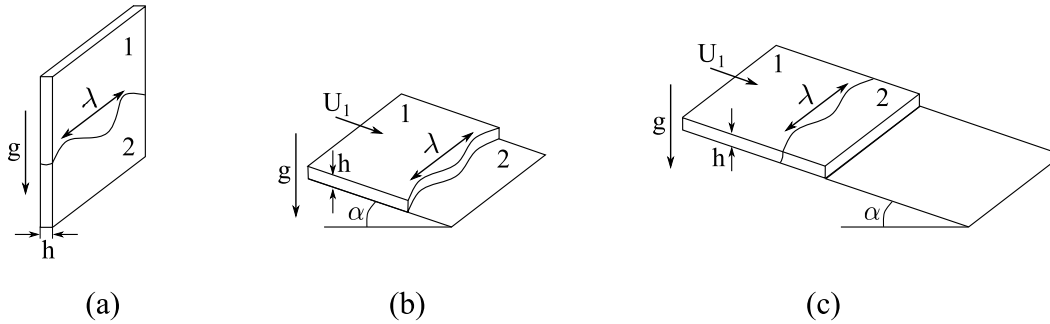
Figure 2.17: Schematic of the fingering instability. (a) The gravity-driven Rayleigh-Taylor instability in a Hele-Shaw cell with thickness h much smaller than its width. (b) The viscosity-driven fingering instability for a viscous fluid flowing down an inclined plane in ambient air. (c) Schematic of the current experimental setup with water flowing from the Hele-Shaw cell-like jet nozzle ($w = 64h$) onto an inclined plane.

The Rayleigh-Taylor instability is often studied in Hele-Shaw cells (i.e., two parallel plates separated by a small gap) with dense fluid 1 on top of less dense fluid 2 and accelerating due to gravity. In this scenario, the buoyancy forces caused by the pressure gradient being opposite the direction of gravity are counterbalanced by the friction between the fluids and the cell walls. This force balance gives rise to a velocity scale, defined by Saffman (1986) as

$$U^* = \frac{h^2}{12\mu}\nabla p, \tag{2.3}$$

where h is the gap size between the two cell plates, μ is the viscosity of the more viscous fluid (the less viscous fluid is assumed to have zero-viscosity here), and ∇p is the pressure gradient across the interface. This expression is identical to Darcy's law for flow through a porous material with permeability of $h^2/12$. In Saffman's studies, the pressure gradient was caused solely by buoyancy effects from the density gradient being opposite the direction of gravity. Thus, $\nabla p = -\Delta \rho g$, where g is the gravitational acceleration and $\Delta \rho = \rho_1 - \rho_2$ is the density difference between the two fluids.

Note that the Laplace pressure term, which is pressure jump between the two fluids due to the curvature of the interface, is neglected in the pressure gradient term above. The Laplace pressure is given by

$$\Delta P_L = \gamma \left(\frac{1}{R_1} + \frac{1}{R_2} \right),$$
(2.4)

where R_1 and R_2 are the two radii of curvature of the fluid 1-fluid 2 interface. The interface between the two fluids is initially assumed to be flat, and thus the curvature-related pressure jump is zero.

More recently, Fernandez et al. (2001) derived a dispersion relation for immiscible fluids ($\gamma \neq 0$) of the same viscosity ($\mu = \mu_1 = \mu_2$). Assuming an initially flat interface and applying linear stability analysis to the flow solution obtained using the Brinkman equations, Fernandez et al. (2001) obtained the following expression for the growth rate of the instability:

$$\Sigma = \frac{1}{2} \left(q - \frac{q^3}{12Ca} \right) \left(1 - \frac{q}{\sqrt{q^2 + 12}} \right),$$
(2.5)

where $\Sigma = 12\mu\omega/g\Delta\rho h$ is the reduced growth rate, $q = 2\pi h/|\lambda|$ is the reduced wave vector, and $Ca = \mu U^*/\gamma$. Here, ω gives the dimensional instability growth rate, and λ is the dimensional instability wavelength. This expression can be used to find the most amplified wavelengths at which the maximum growth rate is obtained for the Rayleigh-Taylor instability. Note that the Laplace pressure jump is incorporated in the derivation of the dispersion relation above. U^*, however, is still computed by assuming an initially flat interface such that the Laplace pressure term is zero when computing ∇p.

In 2006, Carlès et al., expanded the dispersion relation to immiscible fluids of different viscosities and obtained:

$$\Sigma = \frac{B\left[q - q^3/(12Ca)\right]}{2\left(\sqrt{q^2 + 12} - A_\mu^2 q\right) + A_\mu^2 B\left[2q^2/3 - Bq^3 - 18\right]},$$
(2.6)

where $B = \sqrt{q^2 + 12} - q$ and $A_\mu = (\mu_1 - \mu_2)/(\mu_1 + \mu_2)$, which can be thought of as a viscosity Atwood number. Due to the different viscosities, a modified velocity

U^* and capillary number are introduced:

$$U^* = -\frac{h^2}{6(\mu_1 + \mu_2)}\nabla p \tag{2.7a}$$

$$Ca = \frac{(\mu_1 + \mu_2)}{2\gamma}U^*. \tag{2.7b}$$

These expressions make evident that a system with two immiscible fluids of different viscosities (μ_1, μ_2) behaves similarly to a system with two immiscible fluids of the same viscosity $\mu = (\mu_1 + \mu_2)/2$. Furthermore, letting $\mu_1 = \mu_2$, results in Fernandez et al.'s dispersion relation for the Rayleigh-Taylor fingering instability.

While the gravity-driven Rayleigh-Taylor instability has been mainly studied in Hele-Shaw cells, the viscosity-driven instability, on the other hand, has been extensively studied for viscous thin film flows down inclined planes. In this scenario, the second fluid, usually air, is less viscous than the thin film. The instability in this case is caused by growing lateral (x-direction) perturbations in the thin liquid sheet which result in the thicker regions of the film front moving forward faster than the thinner regions (Marshall and Wang, 2005; Diez and Kondic, 2001; Lopez, Miksis, and Bankoff, 1997). The result is either sawtooth-shaped rivulets, where the root of the rivulet moves more slowly than the tip but full wetting of the plate occurs over time, or finger-like rivulets, where the root is stationary and full wetting of the plate never occurs.

The instability is dependent on the plate inclination angle. As the plate inclination angle increases, the rivulet spacing decreases (i.e., the most unstable wavelength decreases). Johnson et al. (1999), Huppert (1982), Silvi and Dussan V (1985), and Troian et al. (1989) report that the most unstable wavelength is given by

$$\lambda_{max} = K\frac{h_o}{(3Ca)^{1/3}}, \tag{2.8}$$

where h_o is the rivulet depth, $Ca = Q_w\rho\nu/h_o\gamma$ is the capillary number based off the flow rate per unit width Q_w, and K is a constant ranging from 13.9 to 18 in the literature. The fit was theoretically developed by Huppert in 1982 via the lubrication approximation and has since then been widely used to fit experimental and numerical data. Interestingly, Johnson et al. (1999) noticed that a fit using $Ca^{-0.45}$ (with $K = 9.2$) was better for their experimental data than the fit using $Ca^{-1/3}$; however, they did not given an explanation for it nor expand on it.

The theoretical fingering wavelength can be compared to those obtained in the current experiments, but first note that the fingers observed in experiments are formed as soon as the flow touches the plate. While care was taken to align the inclined plate flush to the jet nozzle, any small remaining lip may affect the flow and contribute to the observed flow behavior. However, as other notable experiments (see Huppert, 1982) have had similar setups and nonetheless observed the formation of a long, thin film before the fingering instability occurred, it seems unlikely that a small lip would so drastically affect the current results.

Furthermore, note that the jet nozzle is similar to a Hele-Shaw cell as the gap between the plates is small compared to the width of the nozzle ($w_{jet}/h_{jet} = 64$). However, the Hele-Shaw cell is inclined with respect to the horizontal and open to the atmosphere on one end. As the jet is inclined, air fills the nozzle when the jet is turned off. Thus, whenever the jet is turned on for future experiments, the heavier, viscous fluid (water, $\mu_1 = 8.90 \times 10^{-4}$ Pa·s, $\rho_1 = 1000$ kg m^{-3}), with an incoming average velocity $U = Q/(w_{jet}h_{jet})$, must push out the lighter, less viscous fluid (air, $\mu_2 = 1.86 \times 10^{-5}$ Pa·s, $\rho_1 = 1.23$ kg m^{-3}). (No air is ingested into the reservoir as the reservoir is below the jet nozzle.)

Therefore, the two mechanisms driving the fingering instability are present inside the jet nozzle: a viscous fluid accelerating into a less viscous fluid down an incline for the viscosity-driven fingering instability and a dense fluid atop a lighter fluid flowing between two parallel walls in the presence of gravity for the Rayleigh-Taylor fingering instability. As fingering is not observed within the jet nozzle, it would seem that the fingering instability is precipitated by the sudden removal of one cell wall (i.e., the top wall of the jet nozzle is replaced by a free surface at the nozzle exit).

As these experiments were not conducted with the express intention of studying this flow regime, this explanation is speculative. However, the observed rivulet wavelength (that is, the x-distance between rivulets on the plate) can nonetheless be measured and compared to the most unstable wavelengths given by equations 2.6 and 2.8. For the Rayleigh-Taylor instability comparison, the velocity scale of the finger instability must first be computed using equation 2.7a.

The pressure gradient is approximated by using Bernoulli's principle for incompressible, steady flow and by noting that $\nabla p \sim p/h_{jet}$. Thus,

$$\nabla p \sim -\Delta\rho g \sin\alpha - \frac{1}{2}\Delta\rho\frac{U^2}{h_{\text{jet}}}, \tag{2.9}$$

where $U = Q/(w_{\text{jet}}h_{\text{jet}})$ is the average velocity of the water sheet. The pressure term includes a hydrostatic (or buoyancy) term, as used by Saffman (1986), Fernandez et al. (2001), and Carlès et al. (2006), and others, plus a dynamic pressure term due to the imposed velocity of the water sheet. Thus,

$$U^* = \frac{\Delta\rho}{6(\mu_1 + \mu_2)}\left(h_{\text{jet}}^2 g \sin\alpha + \frac{U^2 h_{\text{jet}}}{2}\right). \tag{2.10}$$

The experimental values are plotted in figure 2.19 along with the most amplified wavelengths associated with the greatest growth rate (the peaks of figure 2.18) as given by equation 2.6. The experimental values have a bit of spread, though most of the data points fall within ±20% of the fit, which represents the typical standard deviation in the wavelength measurements. In general, the uniformly hydrophilic and uniformly hydrophobic plates have wavelengths that are around those predicted by theory, which gives $\lambda \sim hCa^{-1/2}$ in the long wavelength (low q) regime.
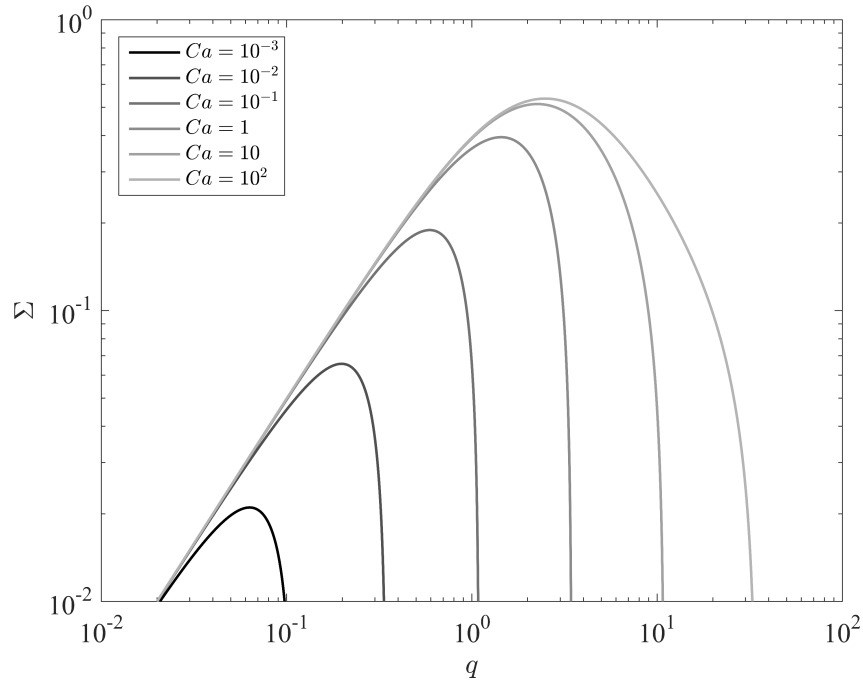

Figure 2.18: Non-dimensionalized growth rate of the Rayleigh-Taylor finger instability as a function of the non-dimensionalized wavenumber.
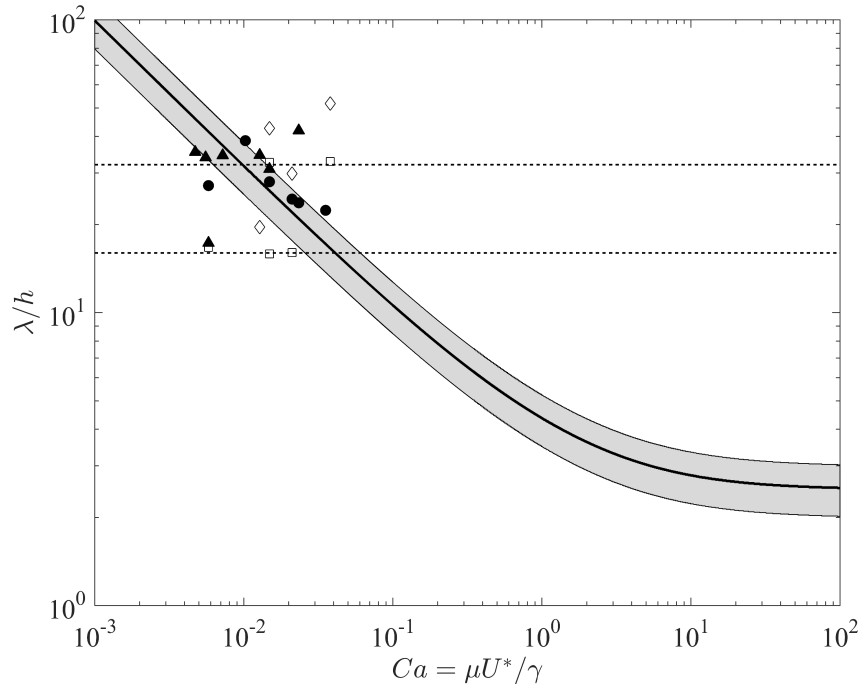
Figure 2.19: The Rayleigh-Taylor finger wavelength as a function of the capillary number. Symbols correspond to experiments: uniformly hydrophilic (●), uniformly hydrophobic (▲), $\beta = 0°, d = 12.7$ mm pattern (□), and $\beta = 90°, d = 12.7$ mm pattern (◇). Solid line represents theoretical fit given by equation 2.6 with ±20% of the fit indicated by the grey region. Dashed line corresponds to fit of $\lambda \sim ch$, where $c = 16$ and 32.

The plates with non-uniform wetting conditions (only $d = 12.7$ mm is used in the current analysis) have greater spread, falling outside the typical standard deviation limit. In addition, the plate with alternating hydrophobic and hydrophilic bands parallel to the flow direction has a relationship that is better described by $\lambda \sim ch$, as shown by the dashed lines in figure 2.19. The constant c equals 16 or 32, which are multiples of the pattern wavelength-to-nozzle height ratio ($2d/h_{\text{jet}} = 16$). Thus, the parallel bands appear to select the wavelength of the instability. This observation is also evident in figure 2.16 where the rivulets are found on the hydrophilic bands and are thus separated from one another (measured center-to-center) by multiples of $2d = 25.4$ mm.

Introducing alternating hydrophilic and hydrophobic bands perpendicular to the flow direction does not seem to affect the general relationship between λ, h, and Ca other than introducing greater spread in the data. This pattern does, however, greatly affect the shape of the resulting rivulet, causing it to spread and flatten on hydrophilic bands and become narrow and raised on hydrophobic bands (as seen in

figure 2.15).

For the viscosity-driven fingering instability analysis, it is assumed that the rivulet depth h_o is approximately the initial sheet thickness h_{jet}. The capillary number for this analysis is given by $Ca = \mu Q/(w_{\text{jet}} h_{\text{jet}} \gamma)$ based on the jet nozzle conditions. The experimental data is plotted in figure 2.20. $K = 3.9$ for the theoretical $Ca^{-1/3}$ fit (solid line), which is lower than the values given in the literature. The data has a lot of spread as in the previous analysis, but most of it falls within ±20% of the fit (grey, shaded region). In addition, the rivulet wavelength's dependence on the plate's pattern wavelength-to-nozzle height ratio is again evident for bands parallel to the flow direction (i.e., square symbols fall on the dashed lines corresponding to $2d/h_{\text{jet}} = 16, 32$).
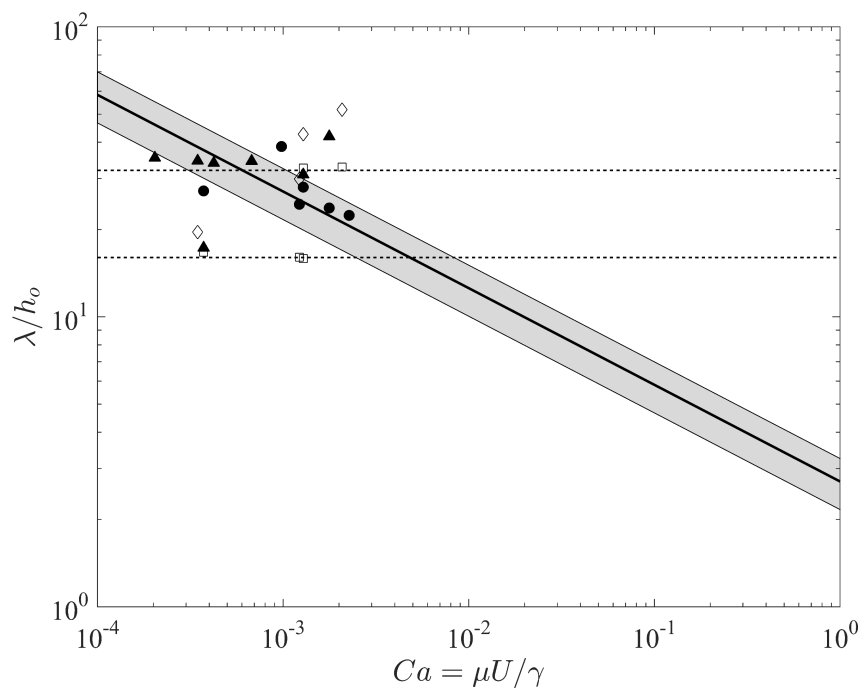
Figure 2.20: Observed rivulet wavelength as a function of the capillary number. Data points correspond to experimental values: uniformly hydrophilic (●), uniformly hydrophobic (▲), 12.7 mm wide alternating bands parallel to the flow direction (□), and 12.7 mm wide alternating bands perpendicular to the flow direction (◇). Solid line represents the theoretical fit based on the viscosity-driven fingering instability analysis, obtained via equation 2.8 with $K = 20.5$. The dashed line corresponds to a $Ca^{-0.56}$ fit with the corresponding ±20% region shown in grey.

From these two analyses, it appears that the rivulet wavelength goes like $\lambda \sim hCa^{-a}$, where $1/3 < a < 1/2$, for the uniformly coated plates. Thus, it remains unclear which of the two driving mechanisms for the fingering instability is most important in the current experiments.

The analyses also show that introducing alternating hydrophilic and hydrophobic bands parallel to the flow direction tunes the instability's wavelength, while bands perpendicular to the flow direction affects the finger's resulting form. These observations are in line with those made by Ledesma-Aguilar, Hernández-Machado, and Pagonabarraga (2010) in their numerical study on the effects of heterogenous wetting properties on the fingering instability. They found that bands parallel to the flow direction help select the instability wavelength, as the thin film flows preferentially on hydrophilic bands. In addition, they studied the effect of checkerboard patterns on the fingering instability, which is in the same vein as the $\beta = 90°$ patterns in the current experiments. They found that the contact line grows as a finger on the hydrophobic bands but then spreads out on the hydrophilic region, which is also as found in the current experiments. The contact line's growth rate (or the finger growth rate) is therefore reduced.

2.3.2 Drop Formation

At very low flow rates the individual fingers break up into droplets on the hydrophobic surface, as seen in figure 2.13 for $Q \leq 9\,\text{cm}^3/\text{s}$ and figure 2.14 for $Q \leq 17\,\text{cm}^3/\text{s}$. This instability is reminiscent of the Rayleigh-Plateau instability in which a falling liquid stream surrounded by an inviscid fluid will pinch off into drops.

The driving force behind the Rayleigh-Plateau instability is surface tension, which causes liquids to minimize their surface area. The instability is brought on by tiny varicose perturbations inherent in a falling stream of liquid, some of which grow with time. The nature of the instability is dependent on the Weber number (Clanet and Lasheras, 1999). At low $We = \rho Q^2/(h_{\text{jet}} w_{\text{jet}}^2 \gamma)$, drops of constant mass form at constant frequency near the top of the liquid column. This regime is referred to as periodic dripping. As Weber number increases, the drops start to vary in size and mass, usually with one large drop being followed by several smaller drops. In addition, droplet formation, which still occurs near the top of the liquid column, becomes quasi-periodic. This regime is referred to as the dripping faucet mode. As Weber number increases further, droplet break-off suddenly moves downstream. Droplet formation continues to move further downstream with increasing We until

a continuous jet is formed. This regime is termed the jetting regime.

Recall that the hydrophobic surfaces used in the current experiments utilize chemistry as well as roughness to repel water (corresponding to the two layers comprising the hydrophobic coating). The combination of the two results in Cassie-Baxter type wetting where air pockets form in the roughness grooves. Thus, the water now flows over air rather than the just the solid surface. The situation in the current experiments is therefore similar to a water column falling through air, with surface tension causing the rivulets to minimize their surface area over the hydrophobic surface to the point of breaking the rivulet up into drops. For similar reasons, droplet formation is not expected on hydrophilic surfaces as the cohesion between the water and the solid surface is much larger.

Flow over the uniformly hydrophilic plate indeed does not exhibit droplet formation, as seen in figures 2.11 and 2.12. Neither does flow over the plate with alternating hydrophilic and hydrophobic bands parallel to the flow direction as the water preferentially flows over the hydrophilic regions (figure 2.16. On the other hand, the dripping faucet, and jetting regimes can be observed in the uniformly hydrophobic case in figures 2.13 and 2.14, where the Weber number is changed by changing the flow rate in the present experiments ($We \propto Q^2$). The plate with alternating hydrophilic and hydrophobic bands perpendicular to the flow direction exhibits drop-like behavior without individual drops ever forming. Instead, the rivulet feeds large volumes of water which accumulate on hydrophilic bands. When the volume of water gets too large, it is shed downstream (see figure 2.21).
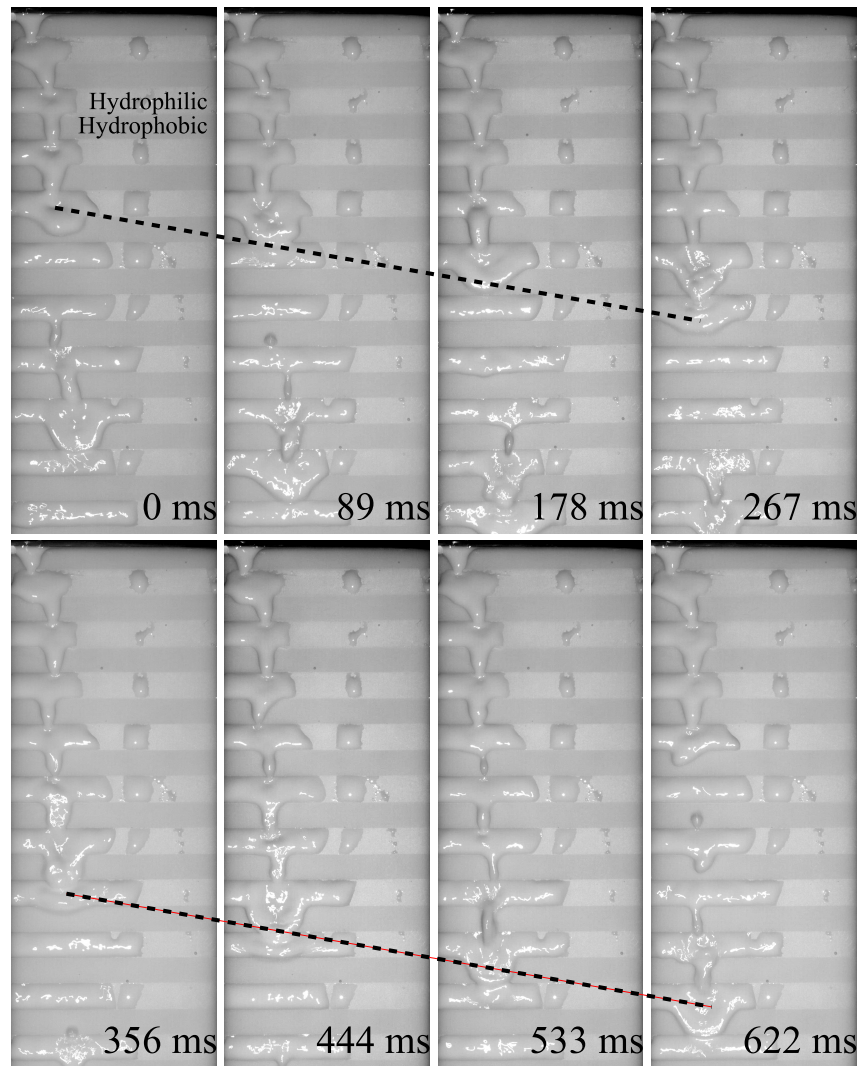
Figure 2.21: The modified droplet regime for the $\beta = 90°$ patterned plate at $\alpha = 10°$ and $Q = 5$ cm^3/s. Black lines serve as guides for the eyes, highlighting the large volume of water propagating downstream.

2.3.3 Meanders and Pendulums

As the flow rate increases, the distance between successive drops decreases until they eventually touch and straight, linear rivulets are formed (as seen in figure 2.13 for $Q = 13$ cm^3/s, for example). In the uniformly hydrophilic case, the fingers never enter the droplet regime but rather stay in the linear rivulet regime for all lower flow rates.

Increasing the flow rate further can lead to meandering rivulets, which have bends but are nonetheless stationary in time (as seen for the first rivulet in figure 2.11 for $Q = 37$ cm^3/s, for example). While meanders are observed on the uniformly

hydrophilic plate in the present experiments, they are not observed on the uniformly hydrophobic plates. The $\beta = 0°$ patterned plate also exhibits meandering in some cases (e.g., $Q = 5$ cm^3/s in figure 2.16) as does the $\beta = 90°$ patterned plate (e.g., $Q = 17$ cm^3/s in figure 2.15).

The cause of meanders is debated. Birnir et al. (2008) report that meanders are caused by flow fluctuations or by sedimentation of particles on the surface only. They find that if the surface is thoroughly cleaned and the flow rate is constant, meanders do not occur. Only the straight rivulets are observed. Hence, they conclude that meanders are not inherent to the flow. On the other hand, Le Grand-Piteira, Daerr, and Limat (2006), Nakagawa (1992), and Nakagawa and Scott (1982) find that the interplay between the inertial force, the surface tension force, and the pinning force at the contact line (which is a function of the contact angle hysteresis) determines the onset of the meanders. Small perturbations in the contact line (caused, for example, by surface defects, injection noise, small flow rate fluctuations, or air movement) cause small bends in the rivulet contact line. Inertial forces along these bends lead to a centrifugal force which acts to destabilize the rivulet. The surface tension force straightens the rivulet while the pinning forces at the contact line stabilize the rivulet, resisting movement. Thus, meandering only occurs when the centrifugal force is high enough to overcome the surface tension and pinning forces, causing the contact line to move. Couvreur and Daerr (2012) further find that the initial conditions, particularly the initial rivulet width and the extent of the contact lines perturbations, are critical to determining when transition between regimes occurs.

For stationary meanders, the contact line then re-stabilizes and pinning forces keep it stationary. As the inertial force (i.e. flow rate) continues to increase, however, the pinning force can no longer keep up and the contact line becomes fully destabilized. The rivulet then begins to oscillate on the surface and may even breakup into sub-rivulets (which themselves meander or oscillate). This oscillating behavior at higher flow rates defines the pendulum regime (Schmuki and Laso, 1990), which can be observed on the uniformly hydrophobic surface (see figure 2.22). As the uniformly hydrophobic surface has a low contact angle hysteresis, the pinning forces acting on the contact line are small, making it more susceptible to destabilization than the hydrophilic surface, which has a large contact angle hysteresis. In fact, the pendulum regime is not observed on the hydrophilic surface. Likewise, the pendulum regime is not observed for the $\beta = 0°$ patterned plate as the flow preferentially flows on the hydrophilic bands.

The $\beta = 90°$ pattern damps the oscillations, largely suppressing them, as presented at the bottom of figure 2.22. However, in some instances, meanders are observed to undergo the Rayleigh-Plateau-like instability discussed in the previous section. In this case, the meander can oscillate due to large volumes of water being shed at its tail-end (as in the jetting regime). This phenomenon is shown in figure 2.23. As the oscillations are due to "drop" formation, which affects the meander's dynamics, rather than simply contact line unpinning as for the pendulum regime, cases such as this are classified as transitions between the drop-like regime and the meandering regime rather than being classified as pendulum flow.

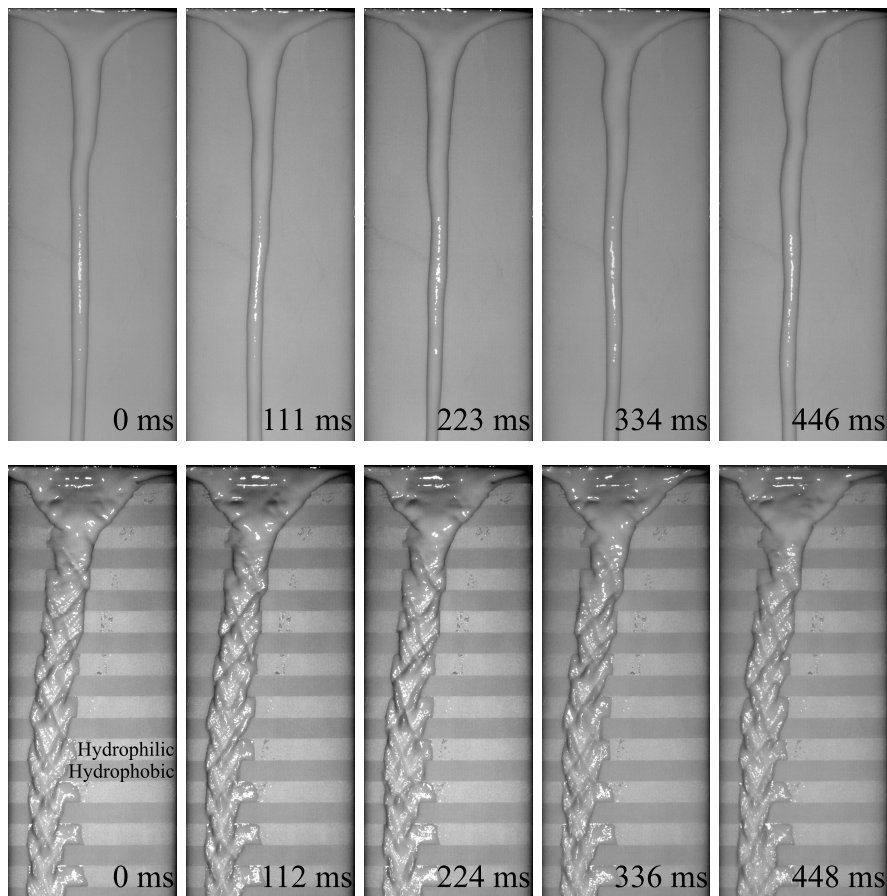**Figure 2.22:** The pendulum regime for $\alpha = 10°$ and $Q = 29$ cm^3/s as observed on the uniformly hydrophobic plate (top) and the suppressed pendulum regime on the $\beta = 90°, d = 12.7$ mm patterned plate under the same flow conditions (bottom).
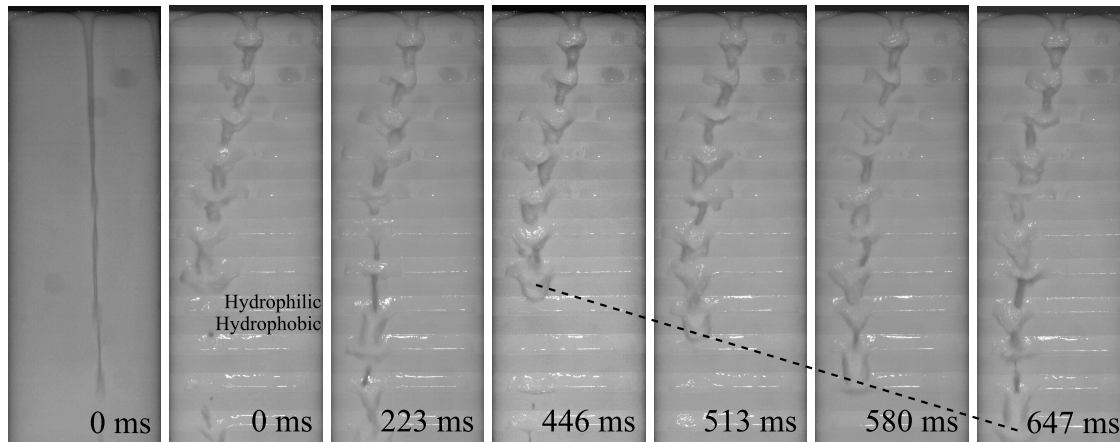
Figure 2.23: The jetting-meandering transition as observed on the $\beta = 90°, d = 12.7$ mm patterned plate for $\alpha = 25°$ and $Q = 16$ cm^3/s. Black lines serve as guides for the eyes, highlighting the large volume of water being shed downstream. Jetting flow over the uniformly hydrophobic case under the same flow conditions is presented on the left for comparison.

2.3.4   Braids

Finally, at high enough flow rates, the rivulet enters a stable regime whereupon a stationary braiding pattern is formed. At these higher flow rates, inertial effects are strong enough to briefly overcome the surface tension effects, causing the liquid to spread on the surface. This spreading creates thick outer rims, carrying most of the fluid, with a thin sheet in the middle (reminiscent of a hydraulic jump). However, inertia is not large enough to fully overcome surface tension. Therefore, surface tension manages to pull the liquid back inward. Thus, the rims first expand due to inertia and then come back together due to surface tension, creating a braid. When the rims collide together once again, the process repeats. Viscous dissipation dampens the motion, causing subsequent braids to be smaller in width until no braids are left, just a cylindrical stream of water.

The height profiles of the outer rims for two test cases are plotted in figure 2.24, along with the profiles at the first rim convergence point.

Braiding was first reported by Nakagawa in the early 1990s for jets emitted from round orifices. They noted in their later paper that braiding on a surface resembles the fluidic chains formed when a sheet of water falls in air (Nakagawa and Nakagawa, 1992). These fluidic chains can also be obtained when two circular jets falling in air collide at an angle (Bush and Hasha, 2004). The chains are symmetric about the xy and yz planes, whereas braids are symmetric about the yz plane only (the solid surface effectively acts as the xy symmetry plane).

The braiding regime has also garnered attention from Kibar et al. (2010), who investigated the effects of Weber number and contact angle ($\theta > 90°$) on the resulting braid patterns of round jets impinging on a vertical plate. They found that as Weber number increases (i.e., the relative importance of inertial forces increases), the braid width and length increases, with the length increasing more than the width. As a result, the surface area of the braid increases with Weber number. The surface area and its increase with *We* are also found to be greater for lower contact angles where the water has a greater adhesion to the surface. Interestingly, Kibar et al. (2010) also noticed that the braid lifts off the surface when the two outer rims collide at high enough Weber numbers and surface hydrophobicity. They referred to this phenomenon as "reflection."

The increase in braid width and length with *We* is observed in the current experiments for the uniformly hydrophobic case, as evident in figures 2.13 and 2.14. In fact, the braid becomes so large that it no longer fits on the plate at the highest flow rates studied. Braiding, however, is not observed on the uniformly hydrophilic plate. Instead, film flow (or sheet-like flow) is observed due to the increased adhesion between the plate and the water.

Mertens, Putkaradze, and Vorobieff (2005) also studied braiding, conducting experiments with a water-glycerin mixture round jet flowing over an inclined acrylic plate at low flow rates (order of $10 \text{ cm}^3/\text{s}$). The water-glycerin mixture is reported to form a contact angle between $50° - 60°$ on the acrylic plate used. Thus, braiding can also be observed on hydrophilic surfaces under the right conditions.

Note that all previous experiments and observations on braiding concern flows issued from round jets impinging on a surface. In this case, the jet immediately spreads on the surface due to inertial forces from impingement. In the current experiments, however, braiding is observed for a thin sheet of water with a zero-degree impingement angle. Rather than initially spreading on the surface, the sheet instead initially converges due to surface tension. Large outer rims, which appear to be large roller structures and carry most of the fluid, develop due to this convergence. Once these outer rims fully converge, braiding resumes as if emitted from a round jet of diameter equal to the width of the flow at convergence. The initial sheet convergence can be thought of as an exceptionally wide braid (with width equal to w_{jet}). As the flow rate increases, the first point at which the outer rims collide occurs further downstream and the large roller structures become more pronounced, as seen in figures 2.13 and 2.14.

Having considered braiding on the uniformly hydrophobic surface in the current experiments, the effects of patterned wettability on this flow regime can now be more closely examined.

Perpendicular bands ($\beta = 90°$)

From figure 2.24, it is observed that while the flow's envelope (dashed white line) at high flow rates is braided over patterned plates with bands perpendicular to the flow direction, the contact line is now modulated. The result of the modulated contact line is scale-like structures (outlined by the solid white line). These scale-like structures are caused by the flow contracting more on hydrophobic bands than on hydrophilic bands. As such, water appears to spread on the hydrophilic surface, reaching a local maximum right before flowing over the next hydrophobic band, whereupon it begins to contract (and reaches a local minimum just before flowing over the next hydrophilic band).
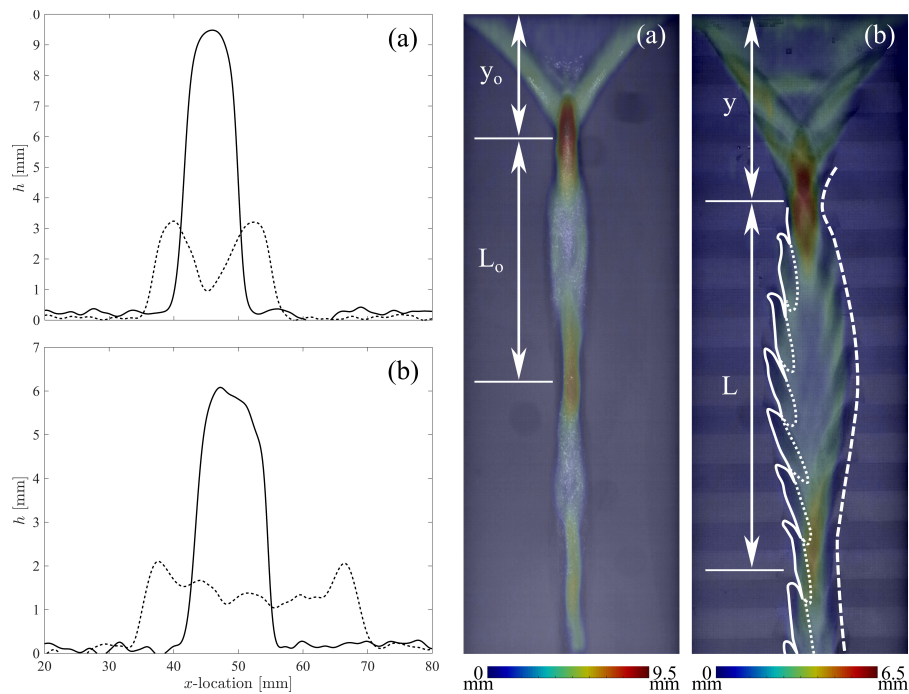
Figure 2.24: Flow over plates inclined at $\alpha = 25°$ for $Q = 41$ cm^3/s. Height profiles at the first rim collision point (y and y_o) and mid-way through the first braid are plotted to the left. The corresponding surface plots are to the right. Flow is top to bottom in the surface plots, with the uniformly hydrophobic plate to the left and the ($d = 12.7$ mm, $\beta = 90°$) patterned plate to the right. For the patterned case, darker bands are hydrophobic while lighter bands are hydrophilic. Colors represent the height of the flow at each location as obtained by Fourier transform profilometry. The braid length is given by L and L_o.

The Fourier transform profilometry (FTP) data in figure 2.24 also shows that the scale structures are associated with raised heights (ranging from 2.5-4.5 mm, depending on the flow rate and plate inclination angle) on the hydrophobic bands. A zoomed in image of the modulated contact line as seen from the side is presented in figure 2.25. The contact line is pinned to the hydrophilic surface but rolls over (i.e. lifts off) the hydrophobic surfaces, resulting in small scale roller structures with increased heights as seen in the FTP data. This lift-off is much like the lift-off or reflection that Kibar et al. (2010) observed during their experiments on vertical plates. As the plates are inclined at small angles with respect to the horizontal in the current experiments, the gravitational force is quite large and prevents complete lift-off as observed in Kibar et al.'s experiments. In addition, Kibar et al. studied small diameter rivulet flow ($d = 1.75 - 4$ mm). Reflection in their experiments occurs when the two outer rims collide, resulting in a reflected rivulet whose diameter is around that of the initial rivulet diameter. The reflection observed in current experiments occurs when the outer rims contact hydrophobic bands. These thick outer rims have a width that varies from 4 to 10 mm. They are also connected to the thin inner sheet at the center of the braid. Thus, complete lift-off of the entire sheet plus rim structure would require a much greater repulsive force than provided by the hydrophobic bands. These two observations combine to result in the small roller structures or scale-like structures observed. (These scale-like structures are also present for large rivulets, though they are not as pronounced.)
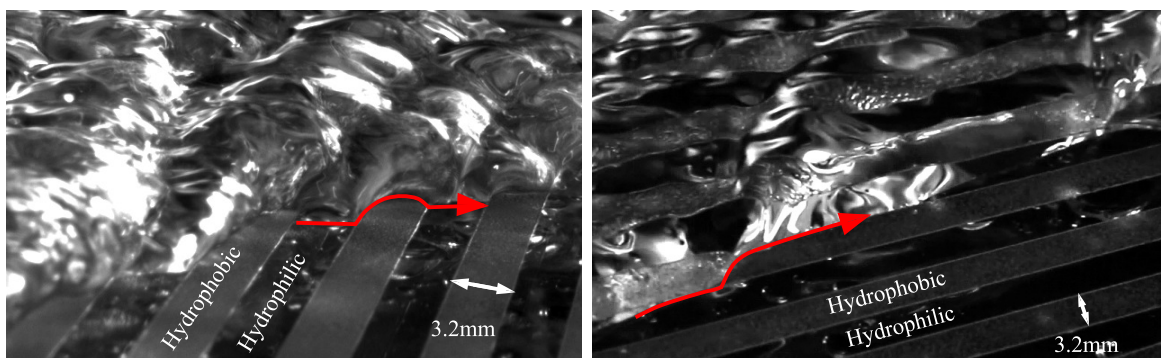
Figure 2.25: Side view of the modulated contact line over non-uniform plates inclined at $\alpha = 9°$. Surfaces are patterned with alternating 3.2 mm hydrophilic and hydrophobic bands. Flow is left to right.

In addition, these small roller and scale-like structures resulting from the modulated contact line are associated with capillary waves, which propagate into the bulk of the braid, as shown in figure 2.26. These capillary waves are caused in part by the

small step created by the hydrophobic coating thickness but are exacerbated by the roller structures caused by wettability changes. (Appendix C provides details on the effect of a step height equivalent to that introduced by the coating thickness in the absence of a change in wettability.) As these capillary waves originate at the contact line and there are two contact lines at each edge of the flow pattern (one to the left and one to the right), the waves criss-cross each other, resulting in diamond patterns in the bulk flow.

Note that small capillary waves also originate in other locations of the flow (as is observed in the inner sheet towards the top of the plates). These capillary waves signal small defects in the surface, which could be due to polishing for the hydrophilic regions or increased roughness for the hydrophobic regions.
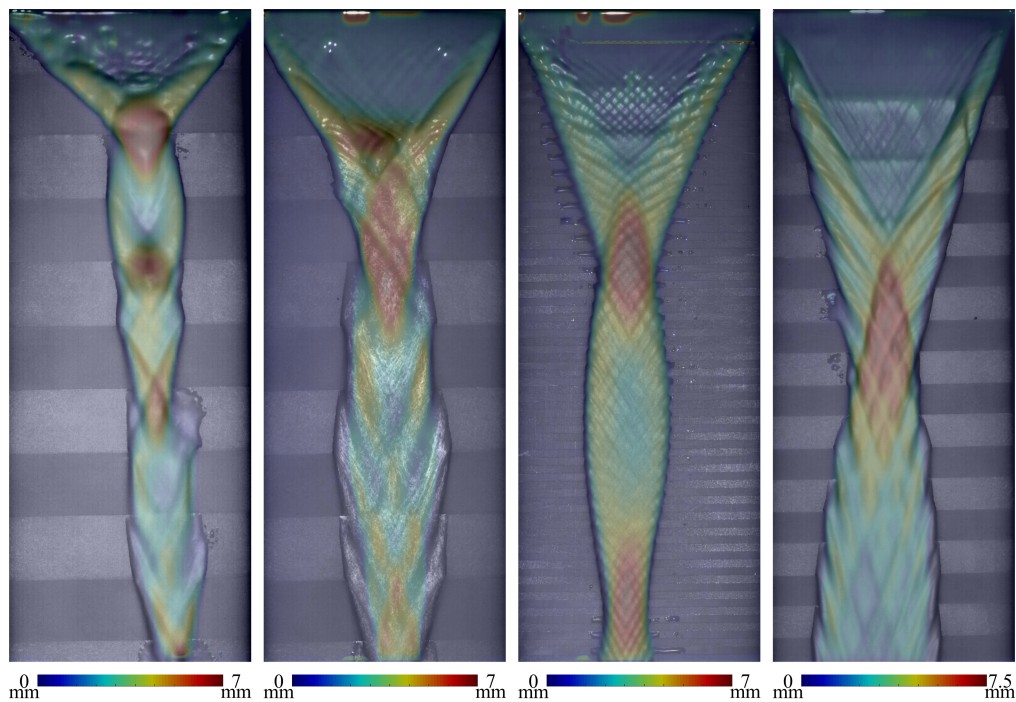
Figure 2.26: Flow over patterned plates with $\beta = 90°$, $\alpha = 10°$ and, going left to right: ($d = 25.4$ mm, $Q = 41$ cm^3/s), ($d = 25.4$ mm, $Q = 72$ cm^3/s), ($d = 3.2$ mm, $Q = 72$ cm^3/s), and ($d = 12.7$ mm, $Q = 108$ cm^3/s). Darker bands are hydrophobic while lighter bands are hydrophilic. Flow is top to bottom. Colors represent the height of the flow at each location as obtained by Fourier transform profilometry.

Returning to the envelope of the flow pattern in figure 2.24, non-uniform wetting properties are observed to elongate the braid when compared to the uniformly hydrophobic plate. In addition, the location of the start of the braid (i.e., the

location when the outer rims first collide) occurs further downstream. These effects become much clearer in figure 2.27. The first five columns correspond to decreasing band width, with the last column corresponding to the uniformly hydrophobic case. A total of five band widths are studied: 25.4 mm, 12.7 mm (as discussed previously), 6.4 mm, 3.2 mm, and 1.6 mm. In all cases, the hydrophilic and hydrophobic bands have the same width. Three flow rates are studied: $Q = 41, 72, 108$ cm^3/s, with the lowest flow rate approximately corresponding to the transition from the pendulum regime to the braiding regime in the uniformly hydrophobic case. Results presented are for a plate inclination of 10°.

The braid elongation and delayed start can be quantified by finding the points of maximum height in the FTP data. The first peak corresponds to the onset of braiding (when the outer rims first collide and the flow begins to spread again). The braid length is the distance between the first peak and the second peak (when the outer rims collide once again), as denoted in figure 2.24. As some braids are so long as to not fit on the plate, an ellipse is fit to the braid with its apex corresponding to the first peak in height. The length of this ellipse gives the length of the braid.

The onset of braiding y and braid length L for the ($\beta = 90°$, $d = 12.7$) patterned case is compared to the onset of braiding y_o and braid length L_o for the uniformly hydrophobic case at every (α, Re) flow condition. As can be seen in figure 2.28, the effects of the pattern on the location of the braid (shown at the top) and the braid length (shown at the bottom) decreases as Re increases (or equivalently as flow rate increases). This observation is intuitive: the surface tension effects introduced by the patterns are fixed. Thus, as inertial forces increase, the relative importance of these effects decrease and become less pronounced.

Looking at figures 2.27, the flow patterns are also found to approach the uniformly hydrophobic case (last column of the figure) as the band width decreases. That is, as the scales become smaller, the flow resembles the no-scale case corresponding to flow over the uniformly hydrophobic plate. The flow pattern is expected to approach either that of the uniformly hydrophilic (hydrophobic) plate as the band width becomes increasingly large if the first band is hydrophilic (hydrophobic). However, the largest band width studied in these experiments does not appear to have reached this hypothetical limit. Further experiments are therefore necessary to elucidate this observed trend for small band wavelengths and the expected trend for large band wavelengths.
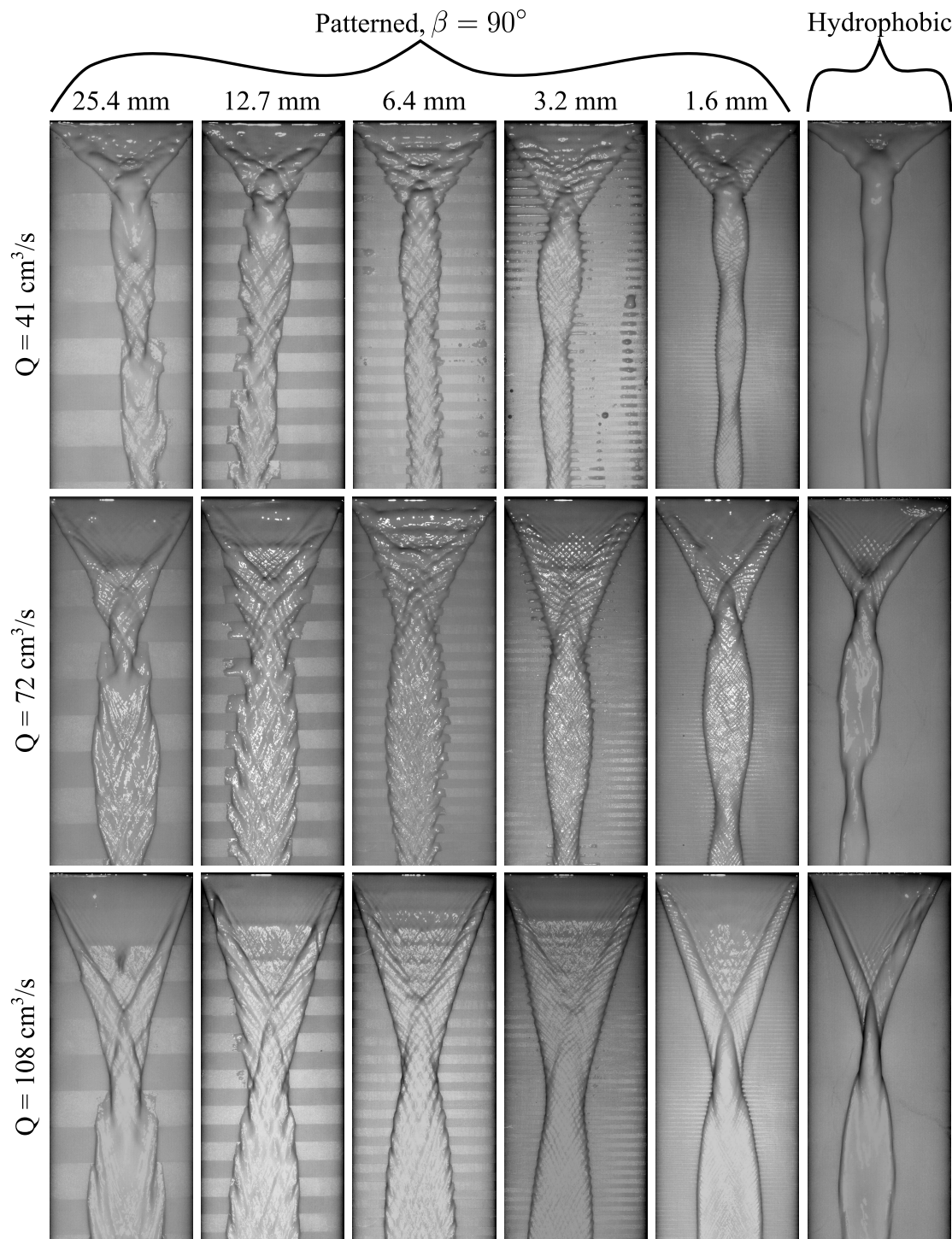
Figure 2.27: Flow over patterned plates inclined at $\alpha = 10°$ with respect to the horizontal for three flow rates (rows). The plates are patterned with alternating hydrophilic (light gray) and hydrophobic (dark gray) bands oriented perpendicular to the flow direction. Columns correspond to decreasing band width, with the last column corresponding to the uniformly hydrophobic plate for comparison. Flow is top to bottom.
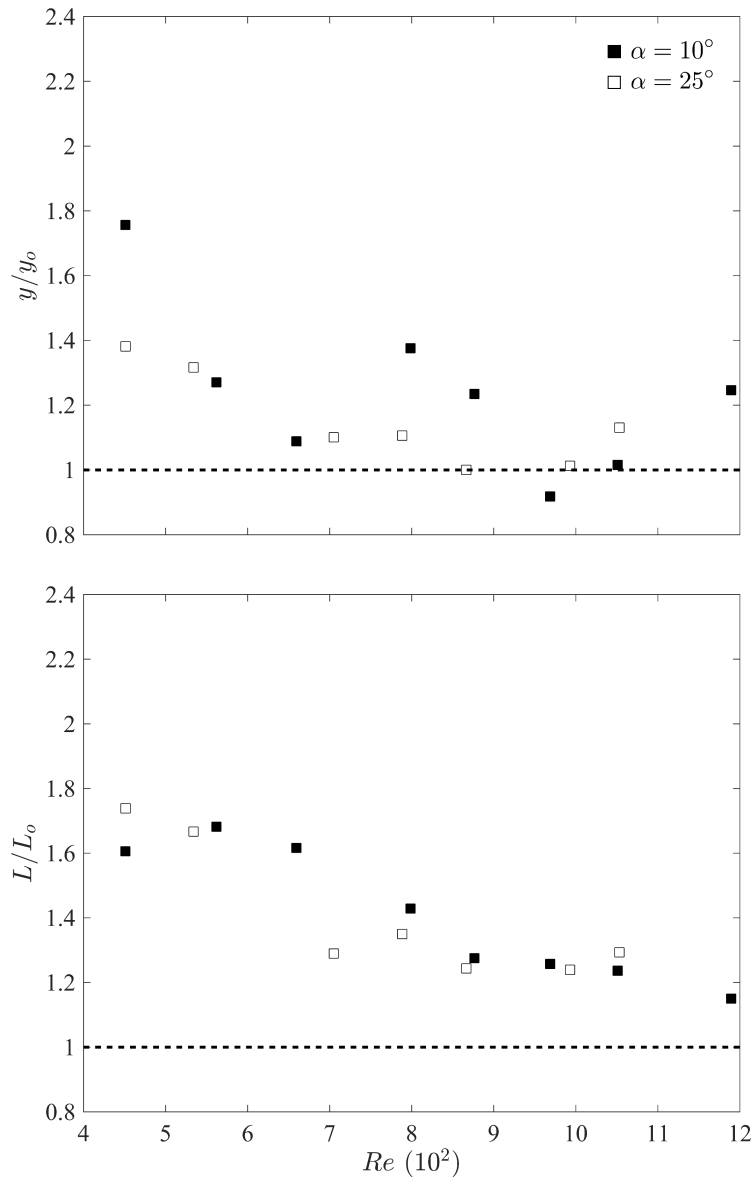
Figure 2.28: Delayed start and elongation of braids on the $\beta = 90°$ patterned plate with $d = 12.7$ mm. Filled and open symbols correspond to $\alpha = 10°$ and $25°$, respectively.

Another observation made during these experiments is the growth of captured air bubbles. As shown in figure 2.29, small air bubbles are entrained by the large roller structures in the uniformly hydrophobic case. These bubbles are extremely fine and get immediately swept downstream, making them unobservable in FTP data. For this reason, the images shown are taken using pure deionized water as the opacity of the titanium-dioxide dispersion does not allow for visualization.
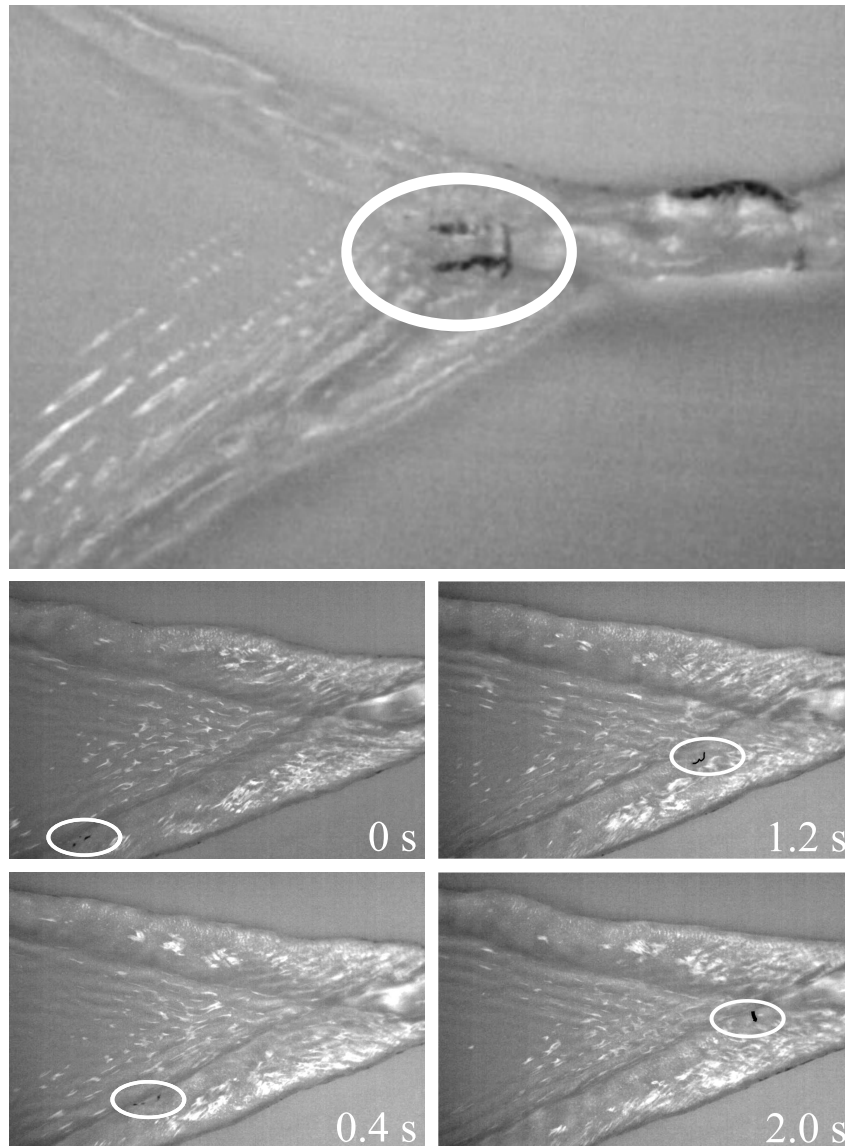
Figure 2.29: Air entrainment by the braid's outer rims on a uniformly hydrophobic plate. Air bubbles are highlighted by the white circle. Pure deionized water is used for visualization purposes.

However, as can be seen in figure 2.30, when alternating hydrophilic and hydrophobic bands perpendicular to the flow direction are introduced on the surface, the air bubbles entrained by the large rollers are observed grow to large sizes. The air bubbles grow on top of hydrophobic bands, near where the thick outer rims first collide. This adherence and growth on hydrophobic bands is due to water's repulsion of the hydrophobic surface. Thus, collecting air pockets on these bands allows the water to flow over air rather than the repulsive surface, lowering the energy of the system. As the following band is hydrophilic, the air preferentially stays on the hydrophobic

surface and collects there. However, the bubbles cannot grow indefinitely. At a certain size, the pressure drag on the bubbles overcomes the adherence force at the surface. The bubbles then get swept downstream. This cycle is illustrated in figure 2.30.
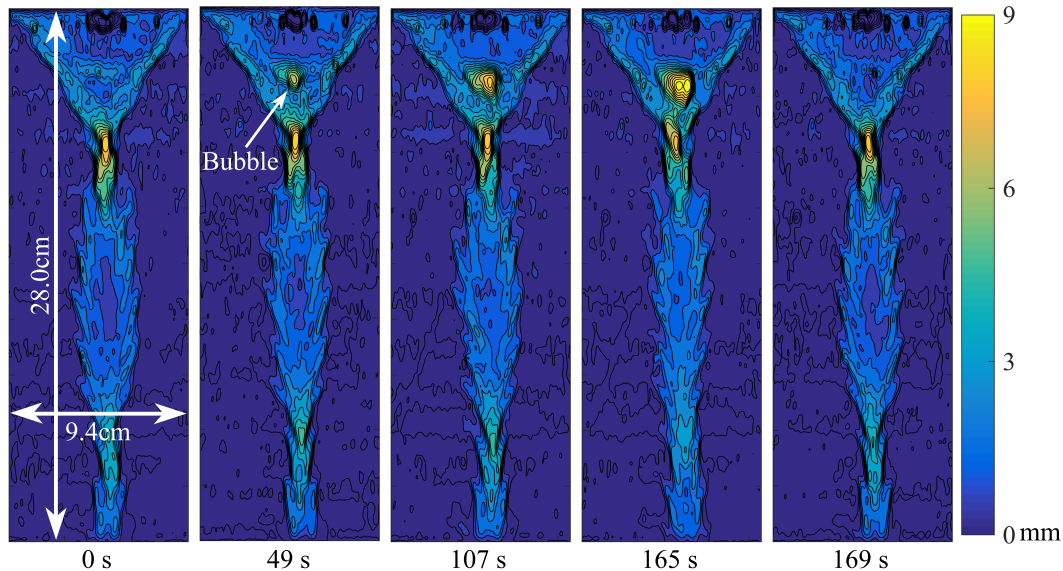
Figure 2.30: Bubble growth cycle over the ($\beta = 90°$, $d = 12.7$ mm) patterned plate inclined at $\alpha = 25°$ for a flow rate of 41 cm^3/s. Colors correspond to the height of the flow features in mm, as denoted by the colorbar.

In addition to only being observed on the $\beta = 90°$ patterned plate, bubble growth is only observed in certain flow conditions. No bubble growth is observed if the flow rate is too high or too low. At the higher flow rates, entrained bubbles may get swept downstream before they can grow big enough to be noticeable. That is, the inertial forces and pressure drag on the air bubbles are greater than the adhering force on hydrophobic band. At lower flow rates, perhaps the roller structures that appear to be responsible for air entrainment are not large enough or strong enough to entrain air (they do not have enough inertial energy).

FTP data can be used to estimate the bubble size and growth rate, as shown in figure 2.31. (Note that multiple bubbles may be observed to adhere to and grow on hydrophobic bands. However, only cases in which a single bubble was observed to grow were considered for the following analysis.) The bubble volume is found to decrease with decreasing bands size d and increasing flow rate Q. The plots also suggest that increasing the plate inclination angle α causes smaller bubbles. These observations imply that the interplay between pressure drag and adhesive forces on the bubble do indeed dictate bubble size.

Figure 2.31: Air entrainment on the $\beta = 90°$ patterned plate for varying band widths (d), flow rates (Q), and plate inclination angles (α). Data is plo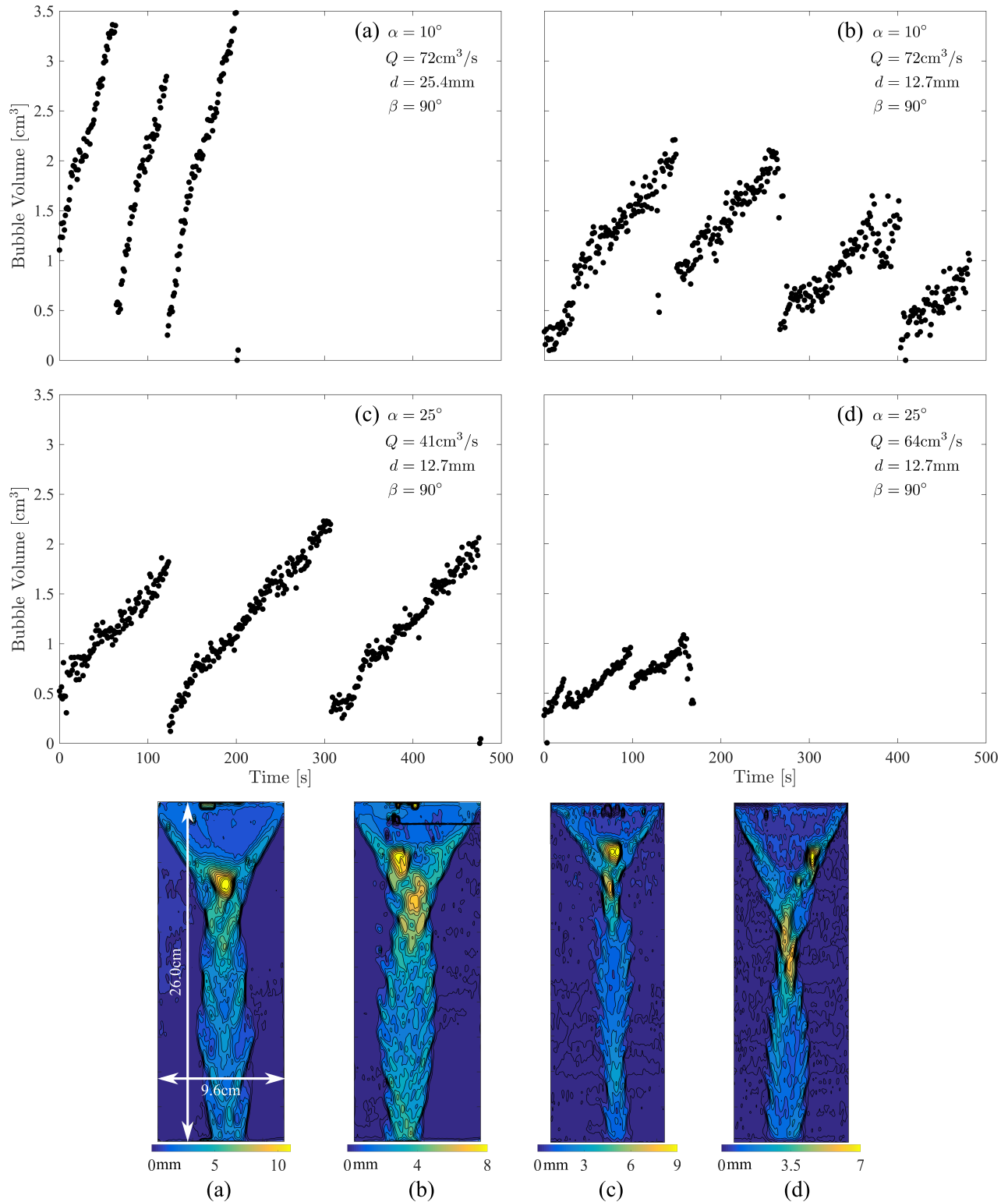tted on the same *x*- and *y*-axes for comparison, although FTP data may not extend through the full domain. Accompanying contour plots are also shown.

Interestingly, the plots show that the growth rate (as given by the slope) appears to be most strongly affected by d. This observation suggests that the small roller structures generated by the modulated contact line, whose size and strength is directly affected by d, affect the air entrainment process. This suggestion is also inline with observations made by Kim, Moon, and Kim (2013), who observed air entrainment at the unstable contact line created when liquid flows over a hydrophobic surface and then abruptly encounters a hydrophilic surface. The authors accredited the transition from Cassie-Baxter wetting on the hydrophobic region to Wenzel wetting on the hydrophilic region (as discussed in section 1.1) for the entrapment of bubbles. While these experiments were conducted for droplet impact, the unstable (or modulated) contact line may nonetheless be a mechanism for air entrainment in the current experiments. The combination of wetting regime transition, which occurs at the start and end of each small roller, and the rolling characteristic of the roller structures could thus explain the growth rate and air entrainment process's dependence on d.

Parallel bands ($\beta = 0°$)

The flow behavior observed over plates with alternating hydrophilic and hydrophobic bands parallel to the flow direction ($\beta = 0°$) is quite different from the $\beta = 90°$ case described above. The water preferentially follows the hydrophilic bands or tracks, as seen in figure 2.16. Thus, the contact line is only modulated in instances where the flow jumps over a hydrophobic track to rejoin a neighboring hydrophilic track, similarly to liquid bridges. As a result, the flow height is increased at these jumps, as seen in figure 2.32. These "digital jumps" are the equivalent of the small roller structures observed for the $\beta = 90°$ case.

The effect of band width for bands parallel to the flow direction ($\beta = 0°$) can also be investigated, as seen in figure 2.33. The opposite of the $\beta = 90°$ trend is observed in this case: as the band width becomes larger, the uniformly hydrophobic flow patterns are recovered. As the band width decreases, the uniformly hydrophilic flow behavior is recovered.
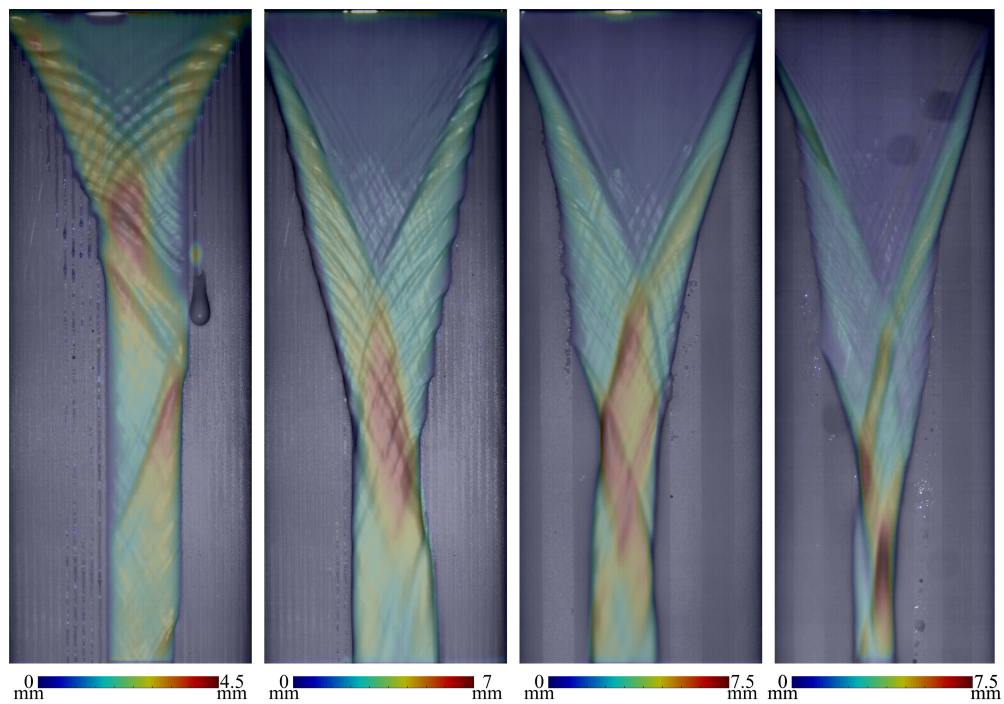
Figure 2.32: Flow over patterned plates with $\beta = 0°$ and, going left to right: ($d = 1.6$ mm, $\alpha = 10°$, $Q = 41$ cm^3/s), ($d = 1.6$ mm, $\alpha = 10°$, $Q = 108$ cm^3/s), ($d = 12.7$ mm, $\alpha = 10°$, $Q = 108$ cm^3/s), and ($d = 12.7$ mm, $\alpha = 25°$, $Q = 95$ cm^3/s). Flow is top to bottom. Darker bands are hydrophobic while lighter bands are hydrophilic. Colors represent the height of the flow at each location as obtained by Fourier transform profilometry.
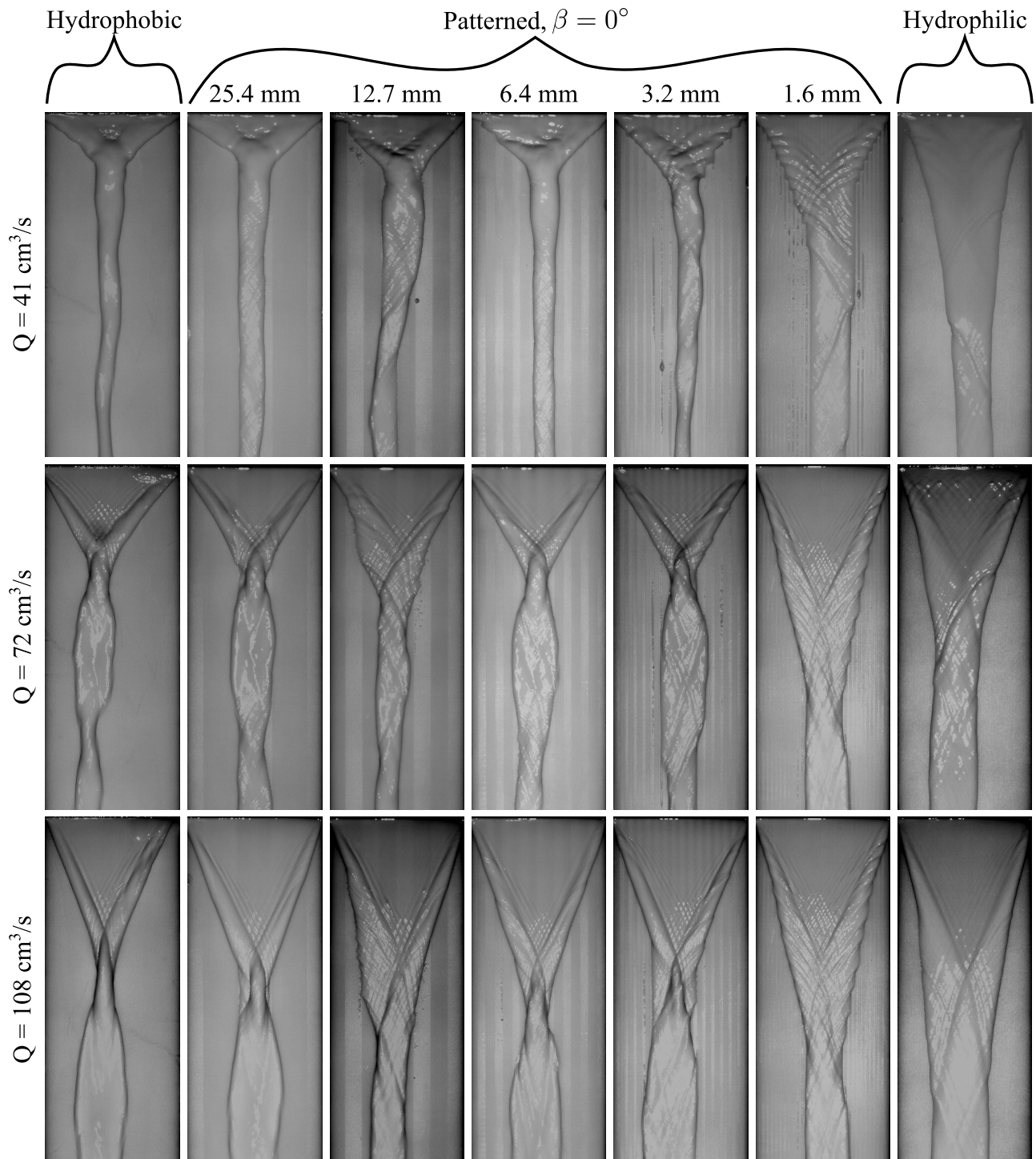
Figure 2.33: Flow over patterned plates inclined at $\alpha = 10°$ with respect to the horizontal for different flow rates (rows). The plates are patterned with alternating hydrophilic (light gray) and hydrophobic (dark gray) bands oriented parallel to the flow direction. Columns correspond to decreasing band width, with the first and last column corresponding to the uniformly hydrophobic and uniformly hydrophilic plates, respectively, for comparison. Flow is top to bottom.

2.3.5 Contact line unpinning

In order to investigate how gravitational and inertial forces affect the water's preference for flowing over hydrophilic tracks, further experiments were carried out for patterns oriented at angles between 0° and 90°. A 29.8 cm diameter disk was coated with alternating hydrophilic and hydrophobic stripes of width d. Two stripe widths were studied: $d = 3.2$ mm and $d = 12.7$ mm. The disk was butted against a hydrophilic block, whose straight edge was flush to the wall jet, as seen in figure 2.34. Two plate inclination angles were studied as well: $\alpha = 10°$ and $\alpha = 25°$. The critical pattern orientation angle β_c at which the flow no longer follows the hydrophilic tracks was recorded for flow rates (based on jet nozzle conditions) ranging from 4-95 cm^3/s.
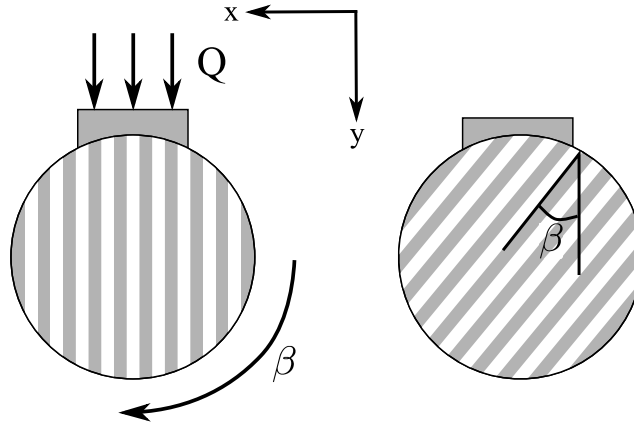
Figure 2.34: Schematic of the disk used in experiments. The bands represent the different wettability regions (white for hydrophilic, grey for hydrophobic).

When the water flows over the hydrophilic tracks, its contact line is pinned to the hydrophilic surface. Pinning forces are stabilizing forces that act normal to the contact line. They are a function of the contact angle hysteresis, with a maximum value set by the the advancing and receding contact angles of the surface. This can be expressed as

$$F_p \leq F_p^{max} = \gamma(\cos\theta_r - \cos\theta_a), \tag{2.11}$$

where F_p is the pinning force per unit length. As the hydrophilic surface has a large contact angle hysteresis (54°) compared to the hydrophobic surface (8°), its pinning force is much larger than on the hydrophobic bands ($F_p^{max} = 65$ mN per unit length versus 4 mN per unit length).

The inertial force per unit length can be approximated as $\rho U^2 h_{jet}/2$, where $\rho = 1000$ kg/m^3 is the density of water, $U = Q/(w_{jet} h_{jet})$ is the average flow velocity, and $h_{jet} = 1.6$ mm. The inertial force thus ranges from 0.5-275 mN per unit length based on the jet conditions in the current experiments. The gravitational force per unit length is estimated as $\rho A g \sin\alpha$, where g is the gravitational acceleration and $A = \pi h_{jet}^2$ is cross section of the flow (grossly approximated to be a half-circle). The gravitational acceleration is on the order of 7 mN per unit length for $\alpha = 10°$ and 16 mN per unit length for $\alpha = 25°$ in the current experiments.

When the inertial and gravitational forces overcome the pinning force, the contact line becomes unpinned and the water no longer flows down the hydrophilic track but rather flows along the y-axis in the direction of the applied gravity force. (Not that the viscous force acts as a decelerating term opposite the motion of the fluid. However, its values are on the order of 0.02-0.52 mN per unit length, as approximated by μU with $\mu = 8.9 \times 10^{-4}$ Pa s for water. This suggests that viscosity is not a major contributor to contact line unpinning in the current experiments.)

Interestingly, two critical band angles are found in experiments, as seen in figure 2.35: β_{c1} below which flow is always pinned and β_{c2} above which flow is always unpinned. When $\beta_{c1} < \beta < \beta_{c2}$, the flow is partially pinned. That is, the contact line may begin as unpinned and then may re-pin further downstream. Or, it may start off pinned and then become unpinned further downstream. These different pinning conditions are shown in figure 2.36.

Additionally, these experiments demonstrate that the critical pattern orientation for which the flow no longer follows the hydrophilic tracks is a strong function of the flow rate and inclination angle. As the flow rate increases, the pattern orientation angle β at which unpinning occurs decreases. At very high flow rates, where braiding occurs, the partial pinning state is non-existent. Furthermore, as the plate's inclination angle α increases, the critical band angle β_c for unpinning decreases. These observations are expected as the inertial force is increased with Q and the gravitational force is increased with α whereas the pinning force that allows the flow to follow the hydrophilic tracks remains unchanged (it is a property of the surface and the fluid only and thus independent of Q or α).

The experiments further show that the band size d does not appear to have a significant effect on contact line unpinning.
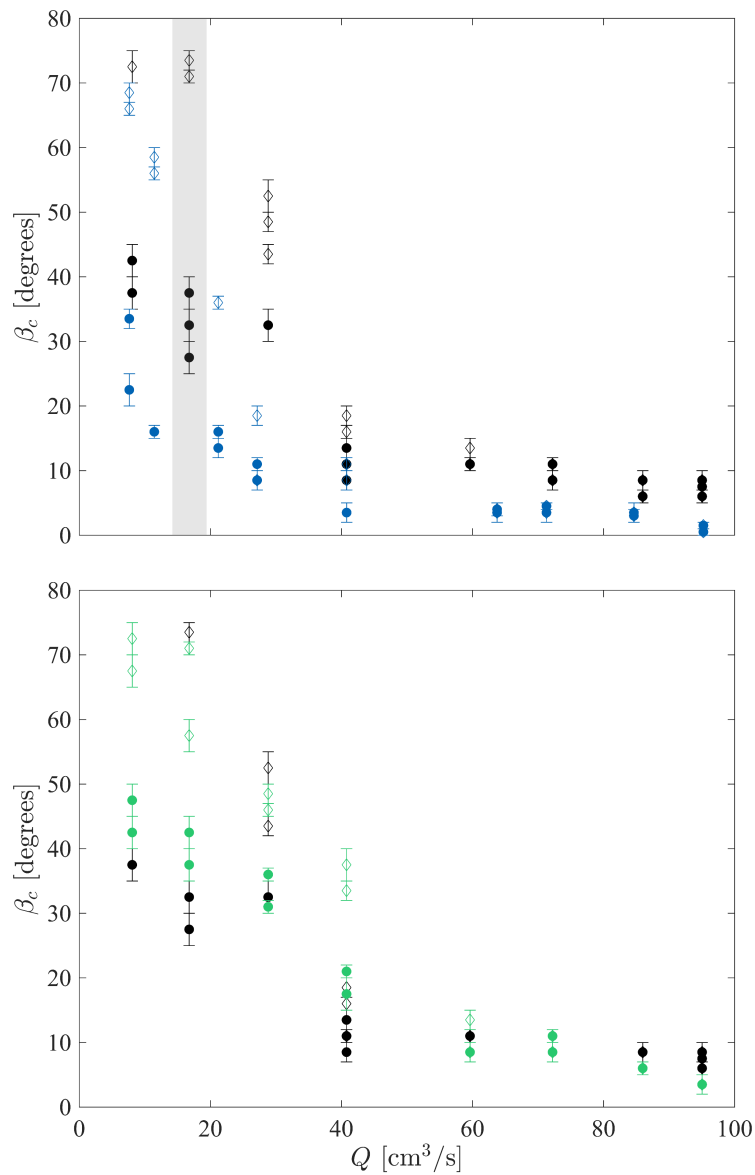
Figure 2.35: Contact line unpinning over non-uniform surfaces as a function of band orientation β and flow rate Q. Top: Effect of plate inclination angle α. Bottom: Effect of band width d. Closed symbols correspond to Q_{c1}, while open symbols correspond to Q_{c2}. Blue: $d = 12.7$ mm, $\alpha = 25°$. Black: $d = 12.7$ mm, $\alpha = 10°$. Green: $d = 3.2$ mm, $\alpha = 10°$. The grey shaded region corresponds to the flow in figure 2.36
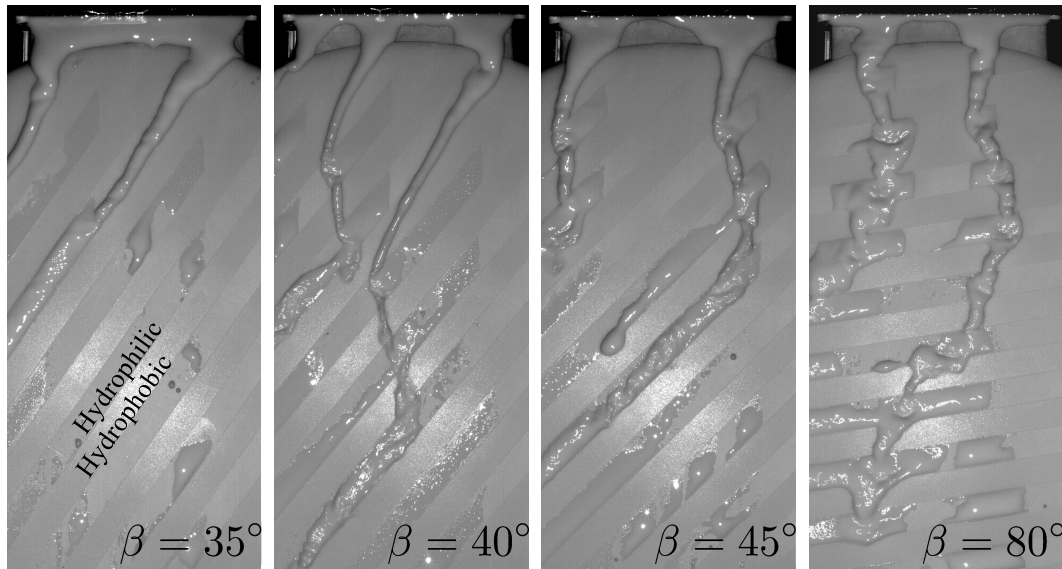
Figure 2.36: Pinning conditions for $\alpha = 10°$, $Q = 16$ cm^3/s, $d = 12.7$ mm: (a) fully pinned; (b-c) partially pinned; and, (d) fully unpinned.

2.3.6 Transitions between flow regimes

Having elucidated the various regimes that occur in the current experiments, the transition between regimes can now be considered. As the flow regimes are dependent on the flow conditions, some of the regimes may not be observed depending on experimental parameters such as liquid density, viscosity, surface tension, contact angle, plate inclination angle, and flow rate (Schmuki and Laso, 1990).

Previous work on rivulet flow regimes observed that as the plate inclination angle α increases, the transitional flow rate between regimes decreases (Schmuki and Laso, 1990; Marshall and Wang, 2005). Assuming that the regimes are only dependent on the gravity component tangential to the surface and the flow rate (since the liquid and surface properties between experimental cases is unchanged), Schmuki and Laso obtained

$$Q_{c1} \sin \alpha_1 = Q_{c2} \sin \alpha_2, \tag{2.12}$$

where Q_{c1} is the transitional flow rate between any two regimes for rivulets flowing down a plate inclined at angle α_1 with the horizontal and Q_{c2} is the transitional flow rate between the same two regimes for flow down a plate inclined at angle α_2.

This differs from Le Grand-Piteira, Daerr, and Limat (2006)'s derivation of the critical flow rate for transition from the straight rivulet regime to the meandering

regime, which states

$$Q_c \propto \left(\frac{\gamma}{\rho}\right)^{4/5} \left(\frac{\nu}{g \sin \alpha}\right)^{3/5}. \tag{2.13}$$

Le Grand-Piteira, Daerr, and Limat also observed experimentally that the meandering-to-pendulum regime transition followed the same relationship. In addition to having been developed for the straight rivulet-to-meandering and meandering-to-pendulum regime transitions, their expression is developed for round rivulets. However, this expression is expanded to all regimes in for comparison of the thin film experimental regimes.

The two theories can be compared to experiments, as presented in figure 2.37, where the uniformly hydrophobic results are used to define the transition curves. It should also be noted that when multiple rivulets form on a surface, they are capable of exhibiting different flow regimes. As the flow instabilities discussed are functions of flow rate (or $We \propto Q^2$ and $Ca \propto Q$), the rivulets' flow rates are expected to differ.

Unfortunately, the flow visualization data collected for the current experiments does not provide velocity data. The flow rate of the rivulets must therefore be approximated. This is done by assuming constant flux flow (that is, the velocity is the same in all rivulets) such that each rivulet's flow rate is given by

$$Q_i \approx Q \frac{A_i}{\sum_{j=1}^{N} A_j}, \tag{2.14}$$

where Q_i and A_i are the ith rivulet's flow rate and area, Q is the flow rate corresponding to the jet (as set by the pump's valve setting), and N is the total number of rivulets on the plate. The rivulet's area is further approximated as having a width L as measured in images and height h on the same order as h_{jet}. Thus, if there are two rivulets on the plate with one that is twice as large as the other, their flow rates are approximated as $2Q/3$ and $Q/3$, respectively.

Furthermore, note that the $\beta = 0°$ patterned plate is omitted from this analysis as its flow regimes are not always easily classified. Additionally, only the 12.7 mm wide bands are considered for the $\beta = 90°$ case.

The results presented in figure 2.37 show that the uniformly hydrophobic data has a better agreement with the expression derived by Le Grand-Piteira, Daerr, and Limat (solid line) than that of Schmuki and Laso. However, as the flow rates have been

estimated and not all flow rates are properly captured due to the fingering instability reducing the flow rate in individual rivulets, more experiments need to be conducted at the intermediate flow rates to determine if this statement holds true.
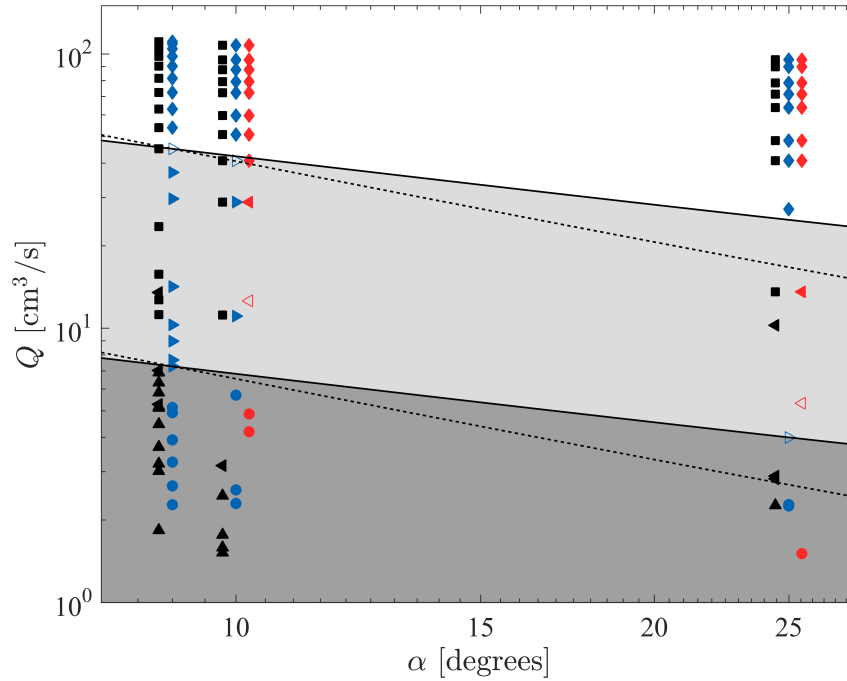
Figure 2.37: Flow regimes as a function of flow rate Q and plate inclination angle α. Markers denote experimental observations: drops ($\bullet$), linear rivulets($\blacktriangle$), meanders ($\blacktriangleleft$), pendulums ($\blacktriangleright$), films ($\blacksquare$), braids ($\blacklozenge$). Open symbols denote transitions between regimes. Colors correspond to different wetting conditions: uniformly hydrophilic (black), uniformly hydrophobic (blue), the $\beta = 90°$, $d = 12.7$ mm patterned plate (red). Shaded regions denote theoretical regime domains as described by equation 2.13. Dashed lines denote regimes transitions as described by equation 2.12.

Figure 2.37, also illustrates that the meandering regime replaces the pendulum regime for the $\beta = 90°$ patterned case as oscillations are damped by the hydrophilic bands. In addition, the droplet-like regime is expanded, as seen by the unfilled, red left-facing triangle signaling the transition between the meandering and droplet regime for the patterned plate falling squarely in the uniformly hydrophobic case's pendulum regime. It should be noted that this droplet-meandering transition causes the end of the meander to oscillate a bit whenever a volume of water is shed. As the top of the meander is stationary, the oscillations are associated with the droplet instability and not a pendulum instability. Therefore, this type of flow behavior is classified as the drop-to-meander transition rather than a pendulum.

The onset of the braiding regime also appears to start slightly earlier for the $\beta = 90°$ patterned case than the uniformly hydrophobic case. This is evidenced by the flow on the $\beta = 90°$ case already being fully braided (solid, red diamond) while the uniformly hydrophobic case is just transitioning (unfilled, right-facing triangle) for the $\alpha = 10°, Q = 41$ cm^3 condition in figure 2.37.

The theories do not adequately capture when film flow occur for the uniformly hydrophilic plate. The transitions on the hydrophilic plate occur at much lower flow rates than on the hydrophobic plate. This discrepancy is to be expected as neither expression for transition accounts for the contact angle, and the uniformly hydrophobic plate regimes have been used to define transitions. Furthermore, the meandering and linear rivulet regimes are interspersed with one another for the uniformly hydrophilic case, corroborating Couvreur and Daerr's observation that flow behavior is sensitive to initial conditions (such as local surface defects).

Mertens, Putkaradze, and Vorobieff further developed a model for braiding, deriving a coupled pair of ODEs describing the flow's downstream velocity and the braid pattern's width. The ODEs were obtained by approximating the height of the braid pattern as a fourth-order polynomial and applying the lubrication approximation to the equations of motion.

Their analysis results in a power-relationship between two dimensionless constants $\Pi_1 = 3\nu\rho^2 q(g\sin\alpha)\gamma^{-2}$ and $\Pi_2 = 3\nu\rho^7 q^5(g\sin\alpha)^4\gamma^{-7}$ (where q is the half-braid flow rate, i.e. $q = Q/2$), which can be used to determine when a rivulet will braid. The braiding law is dependent on solving an eigenvalue problem for the system once linearized about the stable equilibrium or critical point. Note that only stable points are considered as braiding is a stable flow phenomenon. Furthermore, the authors only studied hydrophilic surfaces, which are found to have a different stable point than hydrophobic surfaces.

Linearizing the system of ODEs near the stable critical point and solving the eigenvalue problem, results in solutions for the wavelength of the braid ($2\pi/Im[\lambda]$, where λ is the eigenvalue of the problem). As $\lambda \to \infty$, rivulet flow is recovered. Thus, the transition point, as a function of Π_1 and Π_2, can be found for a given system and is used to define the braiding (or bifurcation) law.

Using this model with the flow conditions for the current experiments gives the results presented in figure 2.38, where the black line delimits the braided and non-braided regimes as obtained from the bifurcation law. Note that the model does

not capture flow instabilities that cause droplet formation, meanders, or oscillating rivulets. The droplet, meandering, and pendulum regimes are thus lumped together with the linear rivulet regime and represented by open symbols.

From figure 2.38, it is clear that the model's bifurcation analysis is not a good indicator of the onset of braiding for the current experiments in either the uniformly hydrophobic case or the uniformly hydrophilic case (where film flow can be treated as an extremely long and wide braid). The $\beta = 90°$ patterned plate is also included in the figure for comparison to uniformly hydrophobic plate.

In order to obtain good agreement between the model and the experimental data, the model would have to underestimate the contact angle in both uniform cases. That is, the model predicts that the flow behavior observed occurs for more hydrophilic and less hydrophobic surfaces, respectively.

Note that the model does not account for pinning forces, which should affect the transition point between flow regimes. As shown in the contact line unpinning experiments of section 2.3.4 as well as by Couvreur and Daerr (2012) as well as Le Grand-Piteira, Daerr, and Limat (2006), the pinning force is a major contributor to flow behavior and thus transition between regimes. This force should thus be included in transition models.

Also note that the theory, while verified using round jet experiments in Mertens, Putkaradze, and Vorobieff (2005), is developed without considering the nozzle geometry from which the jet is issued. Thus, although the current experiments concern a rectangular jet, the theory should still be applicable for the uniformly coated cases. In any case, the upstream portion of the flow (before the first outer rim collision point) can be thought of as the bottom half of an exceptionally wide braid. Once the sheet has converged at the first peak, braiding resumes as if emitted from a round rivulet with a diameter equivalent to the width of the flow at the first peak. In the uniformly hydrophilic case, film flow can be thought of as an exceptionally long and wide braid of maximum width w_{jet}.
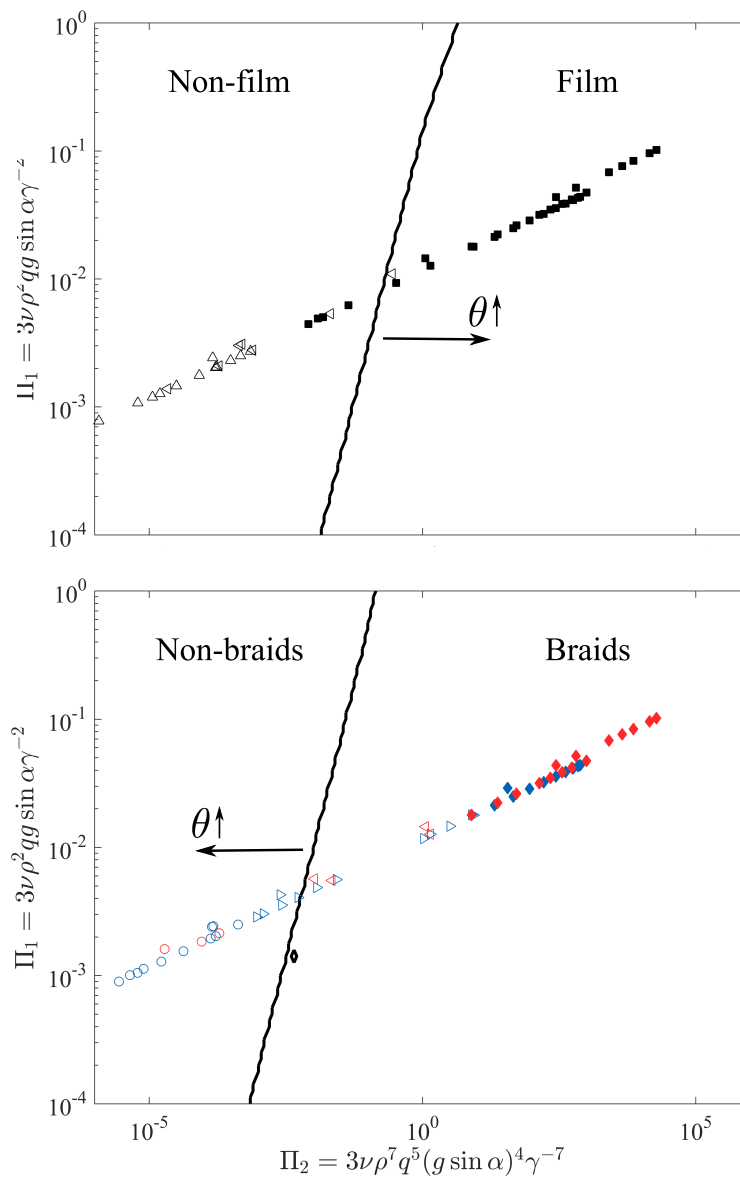
Figure 2.38: Comparison of experimental data to the theory developed by Mertens, Putkaradze, and Vorobieff (2005) for the hydrophilic plate (top) and the hydrophobic plate (bottom). The black line represents the bifurcation law delimiting the braided and non-braided regimes. Symbols correspond to experimentally observed regimes: drops (○), linear rivulets (△), meanders (◄), pendulums (▷), braids (◆), and films (■). The black, blue, and red symbols represent the uniformly hydrophilic, uniformly hydrophobic, and the ($\beta = 90°$, $d = 12.7$ mm) patterned plates, respectively.

More experiments need to be conducted to cover the full spectrum of flow rates in order to fully define transition points. In addition, more accurate flow rate (or velocity) measurements are needed. This can be accomplished either by using a new flow visualization technique which allows for velocity measurements of individual rivulets or by redoing the experiments with a round jet rather than a rectangular 2D jet to avoid the fingering instability that causes rivulets of different flow rates to form in the first place.

As a final note, plotting Π_2 versus Π_1 is equivalent to plotting Fr versus $We^{5/6}$. Recall that

$$\Pi_1 = 3\nu\rho^2 q(g\sin\alpha)\gamma^{-2} \tag{2.15a}$$

$$\Pi_2 = 3\nu\rho^7 q^5(g\sin\alpha)^4\gamma^{-7}, \tag{2.15b}$$

and the half-braid flow rate q equals $Q/2$. Thus,

$$\frac{\Pi_2}{\Pi_1} = \frac{1}{16}\frac{\rho^5 Q^4(g\sin\alpha)^3}{\gamma^5}. \tag{2.16}$$

Furthermore, recall that, using the average velocity $U = Q/A_{\text{jet}}$ where A_{jet} is the jet nozzle area,

$$We = \frac{\rho Q^2 L}{\gamma A_{\text{jet}}^2} \tag{2.17a}$$

$$Fr = \frac{Q}{A_{\text{jet}}\sqrt{g\sin\alpha h}}, \tag{2.17b}$$

where L is the relevant length scale for computing the Weber number and h is the height of the rivulet. Hence, the ρ^5/γ^5 term in equation 2.16 is proportional to We^5 and the $(g\sin\alpha)^3$ term is proportional to Fr^{-6}. Plugging the definitions for Fr and We into equation 2.16 yields

$$\frac{\Pi_2}{\Pi_1} = \frac{1}{16}\frac{A_{\text{jet}}^4}{h^3 L^5}\frac{We^5}{Fr^6}. \tag{2.18}$$

Therefore, $\Pi_2/\Pi_1 \propto We^5/Fr^6$ and plotting plotting Π_2 versus Π_1 amounts to plotting Fr versus $We^{5/6}$.

Likewise, expression 2.13 given by Le Grand-Piteira, Daerr, and Limat (2006) amounts to

$$\frac{A_{jet}^5}{h^3 L^7} Re^3 \propto We^{-4} Fr^6 \tag{2.19}$$

at transition points, where $Re = QL/(A_{jet}\nu)$.

Furthermore, Bush and Hasha (2004) also plotted a diagram for the regimes observed when two laminar round jets collide at an oblique angle in air, resulting in fluidic chains among other flow regimes. Their regime diagram results from plotting Re versus We.

Thus, from this breakdown, it is clear that three dimensionless numbers can be used to classify the regimes of these type of flows: Fr, We, and Re. Or, equivalently, the dominant forces are inertia, gravity, surface tension, and viscosity. Thus plotting Fr as a function of either We or Re, as shown in figure 2.39, should result in a phase diagram. As viscosity was estimated to be at least an order of magnitude less than the inertial, pinning, and gravitational forces in the contact line pinning estimates for the experiments in section 2.3.4, We is used here rather than Re.

Care must be taken when selecting the relevant length scale L in the Weber number as it is dependent on the flow regime: the drop width, which is on the same order as the jet nozzle height, should be used in the droplet regime; the rivulet width, which is set by the nozzle height via the fingering instability, should be used in the rivulet regimes; and, the width of the braid, as set by the jet nozzle width, should be used in the braiding regime. The height of the flow features h is assumed to be on the order of the jet nozzle height h_{jet} while the width of the braid is approximated by w_{jet}. (Note that the Weber numbers reported in table 2.1 are solely based on the jet conditions independent of the resulting flow regimes such that the relevant length scale is h_{jet} for all Q.)

From figure 2.39, it is evident that only a very limited portion of the phase diagram has been investigated in the current experiments. In addition, some of the transition points (open symbols) seem to fall in the middle of a flow regime rather than the edges as would be expected. This may be due to the fact that the flow rate is estimated and the relevant length scales for the Froude and Weber numbers are approximated by the jet nozzle dimensions.

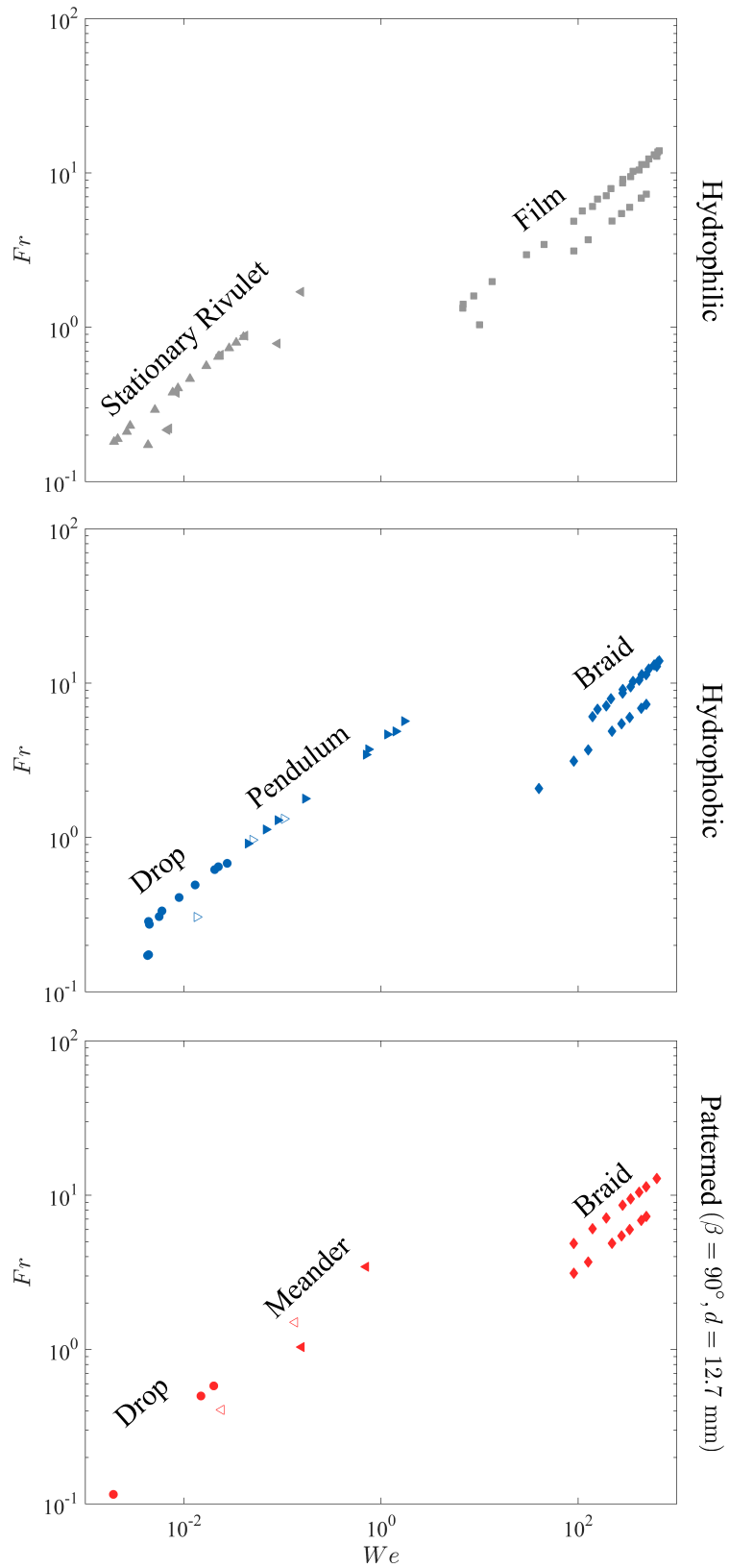**Figure 2.39:** *Fr* vs *We* (based on flow dimensions) phase diagram. Symbols represent flow regimes: drops (●), linear rivulets (▲), meanders (◄), pendulums (►), braids (♦), and films (■). Open symbols correspond to transition points between regimes as observed in experiments.

Furthermore, as has been shown previously, the hydrophilic plate's meandering and linear rivulet regimes are not separated from one another. Nevertheless, the linear rivulet and meander regimes are stationary; therefore, perhaps "stationary" rivulet is a better name for this general flow behavior.

2.4 Concluding Remarks

In summary, distinct, large-scale wettability heterogeneities on a surface greatly affect the contact line and flow behavior of thin films. Two patterns are considered: alternating hydrophilic and hydrophobic bands parallel to the flow direction ($\beta = 0°$) or perpendicular to the flow direction ($\beta = 90°$). The effect of these two patterns are observed in a range of flow regimes.

At low flow rates, patterned wetting properties are capable of tuning the wavelength of the fingering instability ($\beta = 0°$) and modifying the finger's morphology ($\beta = 90°$). When fingers enter the droplet regime, which is driven by similar mechanisms as the Rayleigh-Plateau instability in liquid columns falling in air, bands perpendicular to the flow direction were shown to inhibit the formation of distinct drops while bands parallel to the flow direction suppress drop formation altogether. The perpendicular bands were further shown to dampen the pendulum regime exhibited on uniformly hydrophobic surfaces at higher flow rates.

The majority of this chapter concerns the braiding regime which occurs at higher flow rates, as the objective of this work was to demonstrate whether large-scale heterogeneous wettability can have an effect at larger Reynolds numbers for later naval applications. Although the Reynolds numbers considered here ($Re \sim O(10 - 10^3)$, based on the jet nozzle height) are considerably lower than the Reynolds number in naval contexts ($Re \sim O(10^9)$, based on ship length), the current experiments have successfully demonstrated that large scale wettability heterogeneities do modify the contact line and flow behavior at the higher Reynolds numbers considered.

The $\beta = 90°$ pattern is observed to not only modulate the contact line but to additionally generate small roller structures. The resulting braid patterns are also elongated in comparison to the uniformly hydrophobic case, although the effect on braid size diminishes with increasing flow rate. Furthermore, the braiding pattern is observed to approach the uniformly hydrophobic case as the size of the bands decreases. Air entrainment is also observed on these patterned surfaces with the bands acting as a trapping mechanism, allowing the bubbles to grow to appreciable sizes. Furthermore, the air entrainment process is affected by the modulated contact

line and smaller roller structures, as evidenced by the bubble growth rate's significant dependence on the pattern size.

More experiments are necessary to quantify the air entrainment process and determine to what degree air entrainment is affected by the smaller roller structures. New measurement techniques should be employed in order to also quantify air entrainment on uniform surfaces where very fine bubbles get swept downstream immediately and thus are not captured by FTP visualization. Towards this end, techniques that can measure the chemical composition of the flow would be ideal for determining how much air has been ingested.

Flow over the $\beta = 0°$ bands is observed to follow the hydrophilic bands. This preferential flow over hydrophilic tracks is also observed for $\beta > 0°$ when the inertial and gravitational forces in the system are smaller than the contact line pinning force. The $\beta = 0°$ pattern is also observed to generate digital jumps, reminiscent of liquid bridges, as water briefly crosses over hydrophobic bands to travel from one hydrophilic track to another.

In addition, as the band size decreases, the flow behavior on the $\beta = 0°$ plate approaches that of the uniformly hydrophilic case. Conversely, as the band size increases, flow begins to resemble the uniformly hydrophobic case. Further experiments need to be conducted to investigate what happens to the flow behavior as the band size is further increased as it is expected that the flow will recover the uniformly hydrophilic (hydrophobic) behavior if bands are so large that water flows mainly on a single hydrophilic (hydrophobic) band.

With regards to transitions between flow regimes, the $\beta = 90°$ case is shown to replace the pendulum regime with a meandering regime. Experiments also suggest the droplet regime is expanded for this case compared to the uniformly hydrophobic case. However, more experiments are needed to sample intermediate flow rates and determine transition more clearly. Furthermore, a new flow visualization technique is needed in order to obtain velocity data. The flow visualization technique employed in this chapter (Fourier transform profilometry) measures surface deformations only. As the thin sheet undergoes a fingering instability, the flow rate of individual fingers in unknown, and the FTP data is incapable of giving the required information. Thus, the flow rate was rather crudely estimated for analysis.

As the flows are highly three-dimensional in addition to being only a few millimeters deep, traditional methods for velocity measurements (such as particle imaging ve-

locimetry) may not be practical. Using a round jet rather than a rectangular jet, may prove a more practical solution as the round jet is not expected to undergo fingering instabilities. Therefore, the flow rate of the rivulet will be equal to that of the jet. In addition, the literature available on the droplet, rivulet, meander, pendulum, and braiding regimes concern solely round jets, allowing for more direct comparison to theories and models.

As a wide range of flow regimes were observed for this exploratory work, more systematic studies of each individual regime could also stand to be conducted. It would also be interesting to study the effect of varying band sizes ($d_{pho} \neq d_{phil}$) on the flow regimes and transitions observed.

C h a p t e r   3

APPLICATION TO NAVAL CONTEXTS: HYDROFOIL EXPERIMENTS

3.1   Background and Objectives

In naval contexts, the contact line, or triple-phase line, is the intersection between air, water, and the hull of the ship. The contact line forms along the entire perimeter of the ship. As such, its dynamics are an important aspect of the flow around the vessel, influencing forces and flow features such as spray generation, surface waves, and air entrainment.

The aim of this work is to investigate how modifying the contact line can affect the forces and flow features around surface-piercing bodies. Specifically, the interest is in generating transverse (or side) forces as they are critical to maneuvering. Vessels traveling in oblique seas or in close proximity to other vessels need to generate a transverse force in order to maintain heading and track. On most ships, transverse forces cannot be directly generated, as directional control comes from rudders or differential propeller thrust (Bertram, 2012, Chap. 6). Some ships may be able to generate side forces with bow or stern thrusters, which are either composed of sideways-facing propellers or pipes running through the hull from which water is pumped to either side of the ship. However, these thrusters are only effective at low speeds and are mainly used when ships are docking at ports. Certain ships also have multiple pod thrusters, which generate transverse forces for station keepers such as ocean drilling vessels, but in general these are not used while the vessel is in motion. In the absence of direct transverse force generation, ships must use a zig-zag motion while at sea, which results in a significant loss of speed and an increased effective resistance (drag) (Chuang and Steen, 2012).

The objective is thus to directly generate transverse forces and alleviate the need to zig-zag by modifying contact line dynamics around a ship. As observed in the preceding chapters, one way to modify the contact line is to change a solid surface's wetting properties. If a hydrophilic plate were partially submerged in water, the free surface (the air-water interface that is shown in figure 3.1a), would be pulled up, spreading over the plate and wetting it. On the other hand, if the plate were hydrophobic, the water would minimize its contact with the plate, introducing an
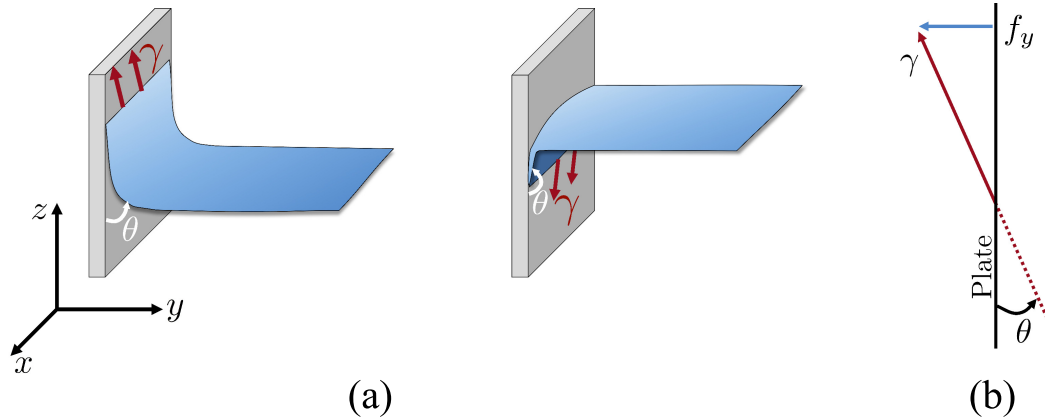
air layer between it and the repulsive surface.

Figure 3.1: (a) Schematic of the water free-surface behavior when in contact with a hydrophilic (left) or hydrophobic (right) partially-submerged plate. Red arrows show the surface tension point forces at the contact line. This point force γ is enlarged in (b)

If we were to look at a point force along the contact line in these scenarios (figure 3.1b), we would find that the surface tension point force γ results in both vertical (z-direction) and transverse (y-direction) forces on the plate. Here γ is the air-water surface tension. The magnitude and orientation of the point force depends on the angle θ, which is the contact angle the water's free surface makes with the solid. Hydrophilic surfaces have contact angles less than 90° while hydrophobic surfaces have contact angles greater than 90°. From the schematic, we find that the transverse force generated by surface tension effects is proportional to $\sin \theta$.

If a ship that is symmetric about the x-axis, as shown in figure 3.2, is uniformly hydrophilic, the y-components of the surface tension point forces acting along the perimeter of the body will cancel each other out. Therefore, no net transverse force is generated from surface tension effects. However, if we change the contact angle on one side of the body, creating asymmetric wetting conditions, we expect that the y-components of the transverse forces on either side of the ship will no longer cancel each other out. Thus, a net transverse force will result. (Transverse force estimates based on this hypothesis are presented in section 3.3.)

There are various ways asymmetric wetting conditions can be achieved. With technological advances being made in microfluidics and material sciences, we can envision modifying the wetting properties of a ship by using techniques such as electrowetting, which can tune the contact angle water makes with the surface. Electrowetting requires the solid be an electrode (like the metallic hull of ships)

and that the liquid be an electrolyte (like salty seawater). Applying a voltage to the electrode causes large (tens of degrees) and reversible variations in the contact angle (Mugele and Baret, 2005). If the hull of a ship were outfitted with additional arrays of electrodes, the surface could be programmed to decide when, where, and how the contact angle is affected based on current maneuvering needs.
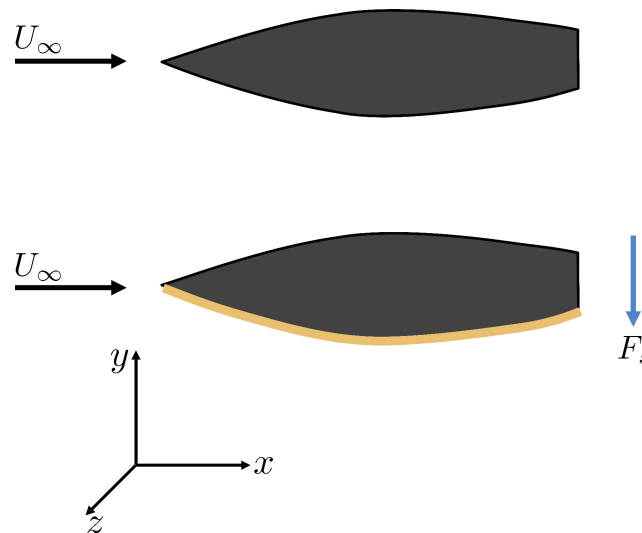
Figure 3.2: An illustration of the hypothesis: a symmetric ship that has uniform wetting conditions (top) will experience no surface-tension driven transverse force while a ship with asymmetric wetting conditions (as illustrated by the orange surface in the bottom image) will.

A much simpler solution is used to create asymmetric wetting conditions in the current experiments: a hydrophobic coating is applied to one side of a naturally hydrophilic surface-piercing body. Care must be taken in selecting a hydrophobic coating as its contact angle θ_2 should not equal $180° - \theta_1$, where θ_1 is the contact angle of the hydrophilic surface. The sine of θ_1 equals the sine of $180° - \theta_1$, as shown in figure 3.3. Hence the hypothetical transverse forces produced by surfaces with these contact angles would be equal. A body with asymmetric wetting conditions composed of these two surfaces would thus hypothetically experience no net transverse force. (Not that this statement neglects to account for changes in flow structures which could also affect the forces on the body.) In the current experiments, $\theta_1 \approx 68°$ and $\theta_2 \approx 157°$, which satisfies the hypothetical criteria set out above.

In addition to asymmetric wetting conditions for the generation of transverse forces, non-uniform wetting properties can be introduced on the coated side. Specif-

ically, alternating hydrophilic and hydrophobic bands can be used instead of a uniformly hydrophobic surface on one side of the hydrofoil (the other side remains hydrophilic). Based on the thin film experiments discussed in the previous chapter, introducing these bands of alternating wetting properties should modify flow features, particularly by modulating the contact line and generating rollers at the hydrophilic-hydrophobic interfaces.
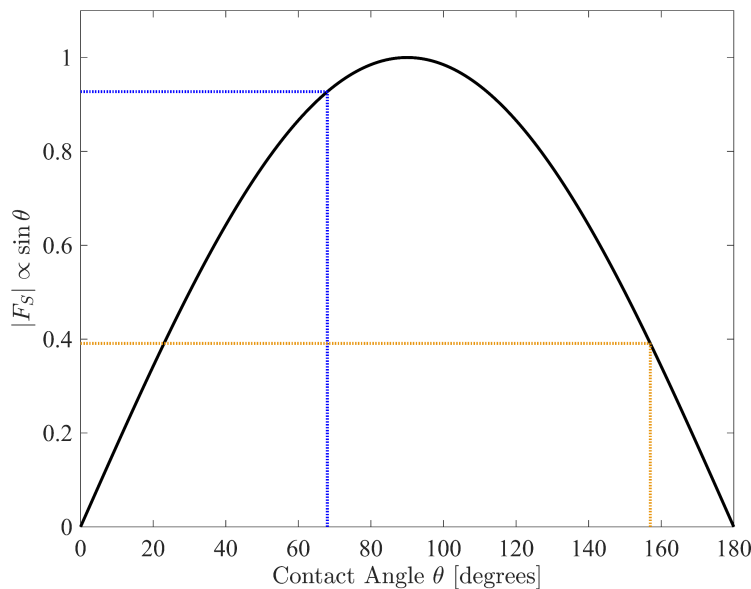
Figure 3.3: Contact angle effect on the magnitude of the hypothesized transverse force generated by surface tension effects. The blue dotted line represents the hydrophilic wetting properties of the hydrofoil used in experiments while the orange dotted line represents the hydrophobic wetting properties of the coating.

It is thus hypothesized that introducing asymmetric wetting conditions on a surface-piercing body will lead to side force generation and that combining this asymmetric condition with non-uniform wetting conditions will additionally modify flow features around the body. In order to test this hypothesis, experiments were conducted on a partially-submerged hydrofoil.

3.2   Experimental Methods

Experiments are conducted with a solid aluminum NACA0012 hydrofoil with a 30.5 cm chord c and a 30.5 cm span b which is partially submerged in a 2m x 1m water tunnel test section, as shown in figures 3.4 and 3.5. The total water depth H in the tunnel test section is 40.6 ± 0.1 cm. The hydrofoil's submerged depth h (when the water is still) equals 7.6 ± 0.1 cm, resulting in an aspect ratio h/c of 0.25. Naval

ships have aspect ratios that are typically three to six times less (see appendix D). The width-to-length ratio d/c, where the hydrofoil thickness d is 12% of the chord length for a NACA0012 cross section, is similar to naval ships however.

For ease of manufacturing, an existing hydrofoil was used. As can be seen in figure 3.4, the hydrofoil is run in reverse of how hydrofoils and airfoils are typically used: the thin, tapered end is the leading edge and the blunt, rounded end is the trailing edge in these experiments. This configuration was chosen to better model the typical hull designs of naval ships, as discussed in appendix D.
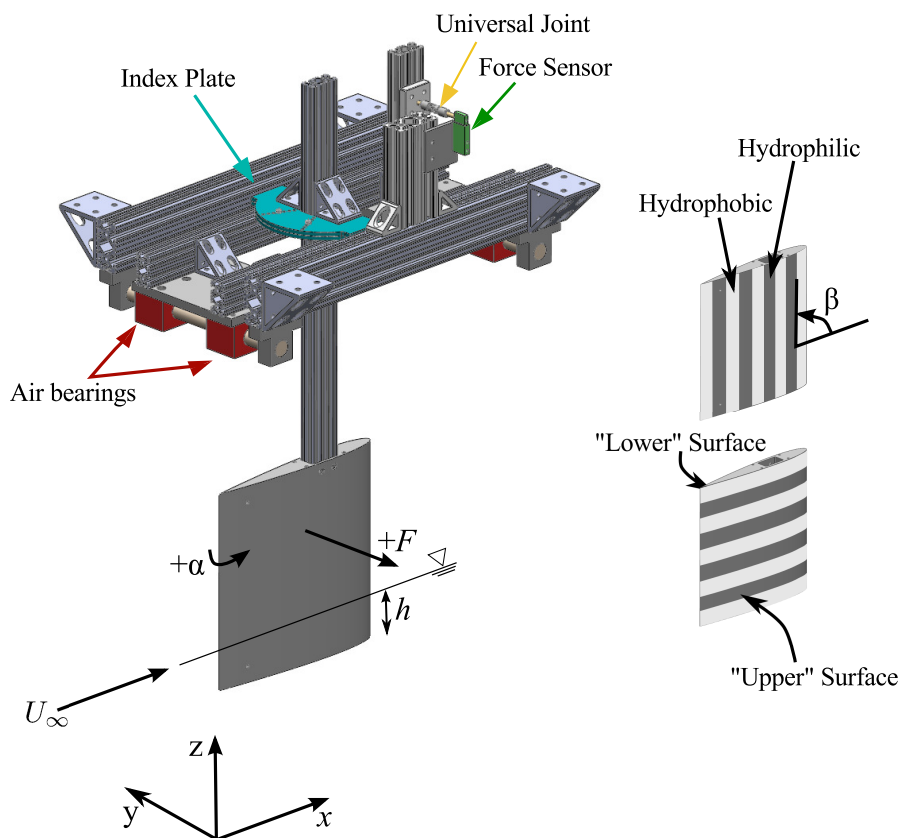
Figure 3.4: Schematic of the support structure as well as the force and angle of attack conventions. The "upper" surface of the hydrofoil is the manipulated side, as seen to the right. It can be uniformly hydrophilic, uniformly hydrophobic, or have alternating hydrophilic and hydrophobic bands at an inclination angle β equal to 90° (top) or 0° (bottom) with the x-axis, as shown. The "lower" surface (not shown) is always uniformly hydrophilic.
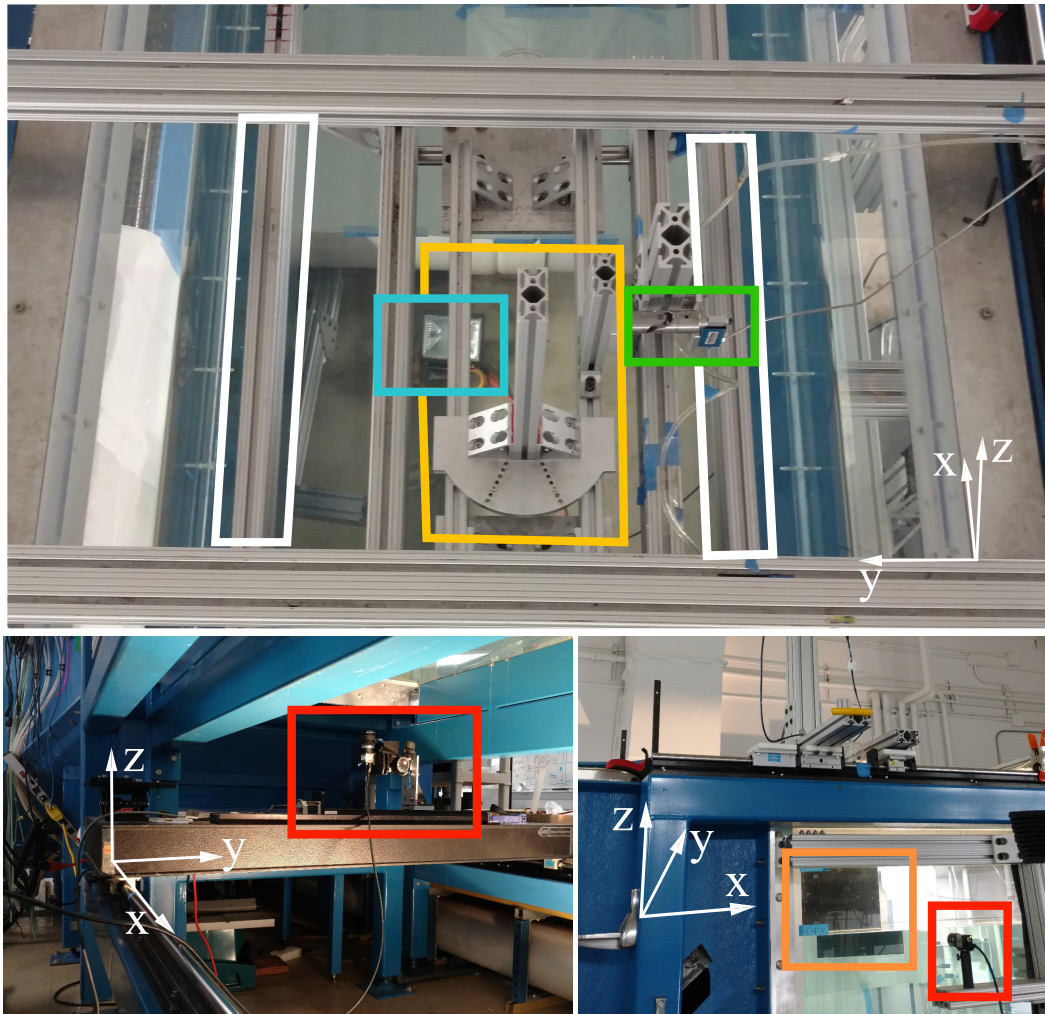
Figure 3.5: Photos of the experimental setup in the water tunnel. Top: Aerial view of the carriage with the index plate mechanism (yellow) and the universal joint and load cell (green). The two long beams aligned to the x-axis (white) are used to support a white screen for shadowgraph imaging. The work light seen in the background on the room floor (blue) is used for lighting in the shadowgraph technique. Bottom left: View from beneath the water tunnel test section. A camera rests on a traversing rig (red) that allows movement in the y-direction. The camera setup sits on an optical table that can move along rails in the x-direction. Bottom right: Side view showing the side-view camera (red) and hydrofoil (orange).

An aluminum beam passes through the center of mass of the hydrofoil and connects to an index plate mechanism at the top (highlighted in blue in figure 3.4). The index plate mechanism is used to set the hydrofoil's angle of attack with respect to the incoming flow direction (the x-axis). It is made up of two plates: the bottom plate is fixed to a carriage, made up of two horizontal beams resting on top of

four air bearings (shown in red), while the top plate is connected to the hydrofoil's center beam and can be rotated to change the hydrofoil's angle of attack α. The index plates have aligned holes that allow for repeatable selection of the angle of attack (α). The carriage and its air bearing structure allow the hydrofoil to freely move in the y-direction without friction and isolates the transverse force during measurements.

An Interface MB-5 miniature beam load cell (in green) is then mounted onto the water tunnel and connected to the carriage via a universal joint (in yellow). The load cell outputs its signal to a Futek amplifier (model IAA100), which connects to a National Instruments (NI) USB-6211 DAQ board run by a LabView program. This force sensor system is used to measure the y-direction transverse force acting on the partially submerged hydrofoil.

Force data is collected at $\alpha = 0°$, $3°$ and $6°$, for ten free stream velocities (ranging from 0 to 0.9 m/s in approximately 0.1m/s increments). Figure 3.4 shows the angle of attack as well as coordinate system conventions. Positive angles of attack correspond to rotating the hydrofoil clockwise, resulting in positive force readings. Note that the true $0°$ angle of attack lies somewhere between the nominal $-1°$ and $0°$ angles of attack set by the index plate.

The range of test conditions and corresponding non-dimensional numbers are presented in table 3.1.

Definition	Relation	Values
U_∞	m/s	0.1 - 0.9
$Ca = \mu U_\infty / \gamma$	Viscosity/surface tension	1×10^{-3} - 11×10^{-3}
$Fr = U_\infty / \sqrt{gc}$	Inertia/gravity	0.06 - 0.52
$Fr_h = U_\infty / \sqrt{gh}$	Inertia/gravity	$0.12 - 1.05$
$Re = \rho U_\infty c / \mu$	Inertia/ viscosity	$4 \times 10^4 - 3.1 \times 10^5$
$We = \rho U_\infty^2 c / \gamma$	Inertia/ surface tension	$40 - 3470$

Table 3.1: Experimental parameters for hydrofoil experiments with $\rho = 1000$ kg/m^3, $\mu = 8.94 \times 10^{-4}$ Pa s, and $\gamma = 72$ mN/m for water, $g = 9.81$ m/s^2, and $c = 30.5$ cm and $h = 7.6$ cm for the hydrofoil.

From these non-dimensional numbers, it can be concluded that the gravitational (body) forces are greater than or equal to inertial forces in the experiments and that surface tension forces are much weaker than both. Viscous forces are much smaller than all other forces present in the experiments.

The Froude numbers the experiments are run at for higher Reynolds numbers are similar to those of naval ships. However, the Reynolds numbers are four orders of magnitude smaller than those of naval ships. Likewise, the capillary numbers are two orders of magnitude smaller and the Weber numbers are six orders of magnitude smaller. This is expected as the Reynolds number scales like $U_\infty c$, capillary number scales like U_∞ and Weber number scales like $U_\infty^2 c$ while Froude number scales like $U_\infty/\sqrt{c}$. Therefore only one of the four non-dimensional numbers can be matched between experiments and full scale ships. The Froude number was chosen as it is the most practical and also the most widely used for ship modeling since matching *Fr* for geometrically similar models ensures that the wave patterns observed in experiments are similar to those in naval contexts.

3.2.1 Facility

The free surface water tunnel facility in the Graduate Aerospace Laboratories at the California Institute of Technology was used for these experiments. This tunnel, shown in figure 3.6, was originally designed as a recirculating shear layer facility and thus has two streams which can be independently controlled. Each stream is driven by a 20hp end suction centrifugal pump. Both pumps are run at the same frequency for this work to ensure that the two streams are identical.
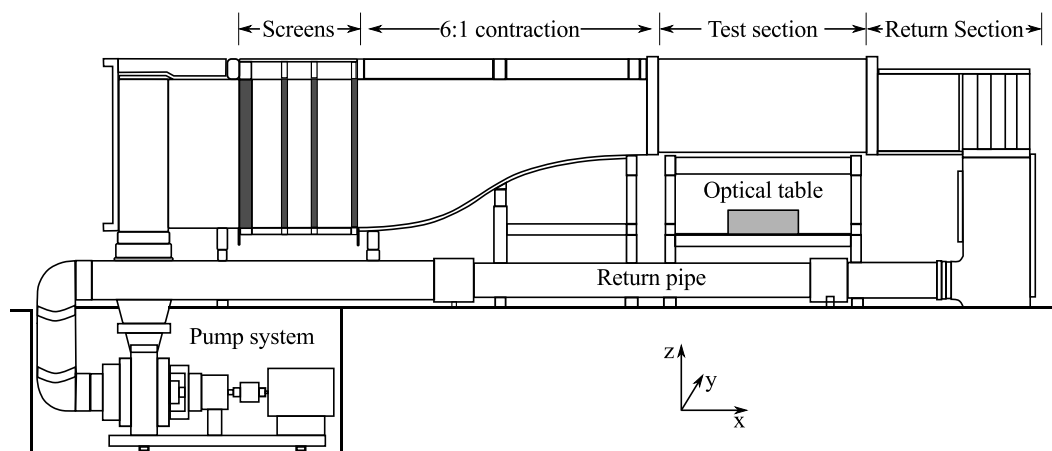

Figure 3.6: Water tunnel schematic. Adapted from Bobba (2004).

The flow is conditioned by passing through a perforated plate, a honeycomb, three turbulence reducing screens, and a 6:1 contraction before entering the test section. Conditioning the flow in this way results in a reported free-stream turbulence intensity of less than 0.1% of the free-stream velocity (LeHew, 2012).

The tunnel was calibrated in 2014 using a MiniLDV-G5L laser doppler velocimeter (LLDV) from Measurement Science Enterprise. The MSE 1D Acquisition Manager (3.1.5093.24093) software was used to run the LDV and record data. Data was collected at twelve water depths, ranging from 25.4 cm to 53.3 cm in 2.5 cm increments. Each water depth was tested at tunnel motor frequencies f_m ranging from 10Hz to 50Hz in 5Hz increments. The results of the tunnel calibration are presented in figure 3.7.
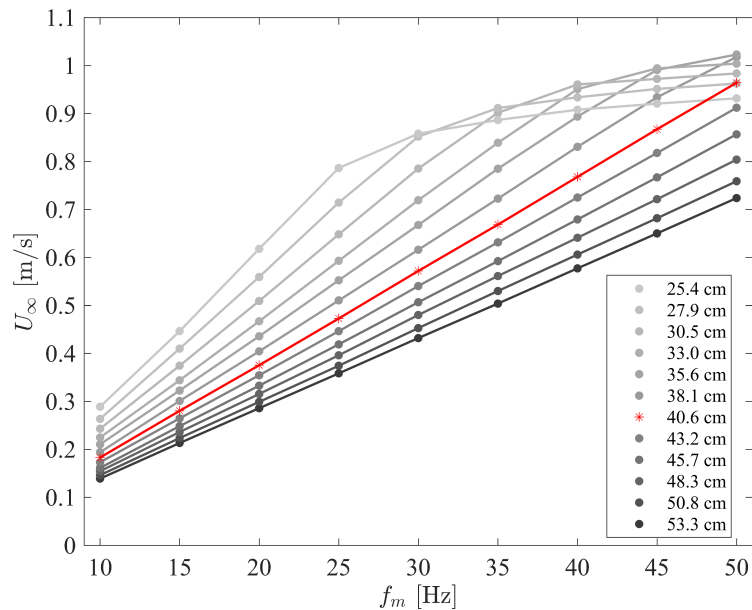
Figure 3.7: Water tunnel free stream velocity as a function of the tunnel motor frequency. The red line with star markers represents the tunnel settings used during experiments.

The free stream velocity is linearly related to the motor frequency for water depths at or above 38.1 cm. In addition, the maximum tunnel velocity decreases as the water depth increases. Therefore, the 40.6 cm water depth was selected for the hydrofoil experiments in order to ensure a linear velocity fit and a maximum tunnel velocity of around 1m/s. The least-squares line of best fit for the 40.6 cm water depth setting is

$$U_\infty = 0.0196 f_m - 0.01. \tag{3.1}$$

This equation is used to find the tunnel settings at which experiments are run, corresponding to roughly 0.1-0.9 m/s flow speeds in 0.1 m/s increments.

3.2.2 Wetting Conditions

The hydrofoil is anodized and has a contact angle (with deionized water) of $68° \pm 4°$, as shown in figure 3.8. (Note that the advancing and receding contact angles were not measured for the hydrofoil's bare surface.) As the hydrofoil is naturally hydrophilic, Rust-Oleum's hydrophobic NeverWet Multi-Surface coating (contact angle of $157° \pm 2°$) is used to introduce hydrophobicity as desired.

Figure 3.8: Contact angle of a 10 μL drop of deionized water on (left) the bare hydrofoil surface ($68° \pm 4°$) and (right) the hydrophobically coated surface ($157° \pm 2°$). Blue dotted curves are outlines of the drop used to compute the contact angle in ImageJ's DropSnake plugin (developed by the Biomedical Imaging Group at EPFL. See Stalder, Kulik, Sage, Barbieri, and Hoffmann (2006)).
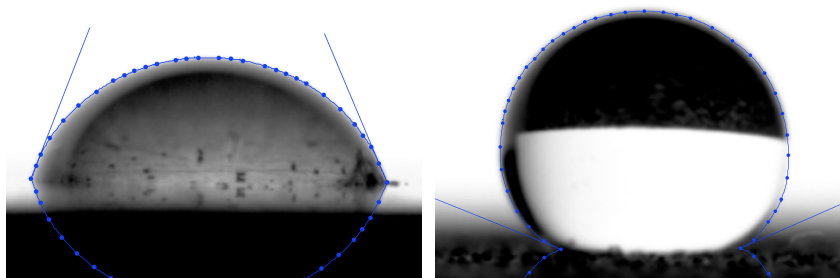
To create the non-uniform wetting properties, masks of the desired stripe pattern are first drawn in SolidWorks and saved as .dxf files. The masks are then imported into the Cricut Design Space program, which runs a Cricut Explore One cutting machine. The machine cuts the masks into adhesive vinyl sheets, which are then applied to one side of the hydrofoil. That half of the hydrofoil is then coated with the hydrophobic coating. Once the hydrophobic coating has cured, the vinyl mask is peeled off. The result is a hydrofoil with alternating hydrophobic and hydrophilic bands on one side and a uniformly hydrophilic surface on the untouched side.

Three different wetting conditions are tested: one uniformly hydrophilic hydrofoil (symmetric wetting conditions plus uniform wetting properties), one hydrofoil with one side that is uniformly hydrophilic and one side that is uniformly hydrophobic (asymmetric wetting conditions plus uniform wetting properties), and four hydrofoils with one side that is uniformly hydrophilic and the other side that is patterned in alternating hydrophilic and hydrophobic bands (asymmetric wetting conditions plus non-uniform wetting properties, i.e., large-scale wettability heterogeneities). Two band inclination angles, defined with respect to the x-axis, are considered: $\beta = 0°$ (bands parallel to the flow direction) and $\beta = 90°$ (bands perpendicular to the flow

direction). In addition, three band wavelengths λ are tested: 5.4 mm, 11 mm, and 22 mm. The band wavelength is the sum of the hydrophilic and hydrophobic band widths, which are equal to each other for all tests conducted in the present work. Thus, a 5.4 mm band wavelength is the result of 2.7 mm wide hydrophilic and hydrophobic bands.

The band wavelengths studied correspond to approximately two, four, and eight times the capillary wavelength of water (respectively), where the capillary wavelength is defined as

$$\lambda_c = \sqrt{\frac{\gamma}{\rho g}}. \tag{3.2}$$

The combination of band wavelength and stripe inclination angle for each patterned hydrofoil is presented in table 3.2.
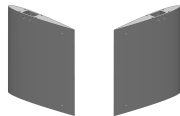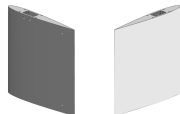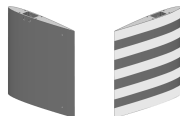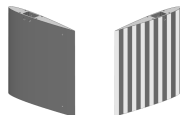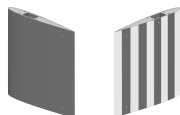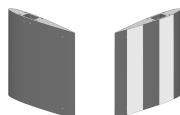
Case	Name	Wetting Condition	β	λ [mm]	Schematic
1	Hydrophilic	SC + UP	-	-	
2	Half-hydrophobic	AC + UP	-	-	
3	Half-patterned	AC + NUP	0°	11	
4	Half-patterned	AC + NUP	90°	5.4	
5	Half-patterned	AC + NUP	90°	11	
6	Half-patterned	AC + NUP	90°	22	

Table 3.2: Cases and corresponding wetting conditions tested in hydrofoil experiments. UP: uniform wetting properties; NUP: Non-uniform wetting properties; SC: Symmetric wetting conditions; AC: Asymmetric wetting conditions. Schematics show the "lower" (left) and "upper" (right) surfaces.

Note that the upper surface of the hydrofoil is the manipulated side while the lower surface remains hydrophilic. The decision to coat the upper surface is based on the need for transverse force generation (as estimated in section 3.3) to load the sensor in compression as the sensor is only rated in that direction.

3.2.3 Experimental Procedures

Experiments are run by selecting the hydrofoil angle of attack via the index plate mechanism (detailed on page 80) and then collecting 60 seconds worth of data sampled at 1000 Hz at each sequential free stream velocity (or, equivalently, Reynolds number) of interest. Once data is collected at all velocities, the tunnel is turned off. The water is allowed to settle (approximately 5 minutes) before a new test is begun at the same angle of attack. A maximum of four tests are conducted at a given α before moving to a different angle of attack. This maximum of four tests constitutes one data set.

The hydrofoil is removed from the test section and the tunnel is filtered for at least thirty minutes between sets. The free surface is vacuumed and clean, filtered water is added back to the tunnel as needed to ensure a 40.6 cm water depth in the test section. The hydrofoil is then put back in the test section, and a level is used to check that the hydrofoil is aligned to the z-axis and that the universal joint is aligned to the y-axis (in order to measure force in the y-direction only) before new tests are conducted.

A maximum of three data sets are collected for each hydrofoil coating to avoid running tests with worn out coatings. Once these sets have been collected, the hydrofoil is removed from the tunnel. If the hydrofoil is patterned or half-hydrophobic, the coating is taken off using paint thinner and the hydrofoil is then washed clean with acetone. The hydrofoil is then re-patterned with a fresh hydrophobic coating before continuing experiments. (It should be noted that these precautions are based on the tests conducted in section 2.2.3, which showed that the hydrophobic coated is degraded after lengthy contact with water and particle deposits. No degradation of the hydrofoil coating was observed during the current experiments when implementing these procedures.)

In order to ensure the free surface conditions are similar for all tests, the tunnel is also throughly cleaned each morning. This entails running the tunnel at 0.9 m/s for 15 minutes to stir up the water and any particles accumulating on the screens or on the tunnel floor. The speed is then reduced to approximately 0.5 m/s and a squeegee

is run over each screen in the divergent section of the tunnel. This process removes particles that remain stuck to the screens. The tunnel is then turned off and the filter turned on. Approximately one hour is needed to filter the particles from the water and recover clarity. During the hour, the tunnel floor is vacuumed in the divergent section and scrubbed in the test section. The test section and tunnel walls are also scrubbed near the free surface to release particles that have dried up or accumulated there. When the water is clear, the free surface is vacuumed in order to aspirate floating particles and dust. The filter is then turned off and clean, filtered water is added back to the tunnel until a 40.6 cm depth is reached in the test section.

3.2.4 Force Sensor Characterization

An Interface Miniature Beam load cell (model MB-5) was used to measure the transverse force acting on the hydrofoil. This force sensor is rated to 22.2 N (5 lbf). The load cell is connected to a Futek IAA100 analog amplifier which conditions the signal before passing it through a National Instrument data acquisition board (NI USB-6211) which is run via LabView. The DAQ board has a 16 bit resolution, resulting in an (ideal) resolution of 3.4×10^{-4} N per count.

The hysteresis, non-linearity, and non-repeatability of the load cell are reported to be at most ±0.02% of the sensor's full scale capacity (FS), ±0.03%FS and ±0.01%of the sensor's rated output, respectively as specified by the manufacturer. This amounts to errors of $±6.6 \times 10^{-3}$N, $±4.4 \times 10^{-3}$N, and $±2.2 \times 10^{-3}$N respectively.

Calibration

The force sensor is calibrated by attaching it to a traverse and positioning it over an Ohaus CL5000 scale with a capacity of 5000 g and a readability of 1 g. The sensor is slowly brought down to touch the scale. The mass measurement read by the scale corresponds to the equal and opposite force felt by the sensor ($F = mg$, where g is gravitational acceleration and m is the mass reading from the scale). The voltage obtained from the sensor, which samples at 1000 Hz for 10 seconds, is recorded for mass readings of 0 to 1600 g in increments of 200 g. The results of the sensor calibration are presented in figure 3.9. Note that a low pass 60 Hz finite impulse response (FIR) filter has been applied to the data to eliminate higher frequency noise.
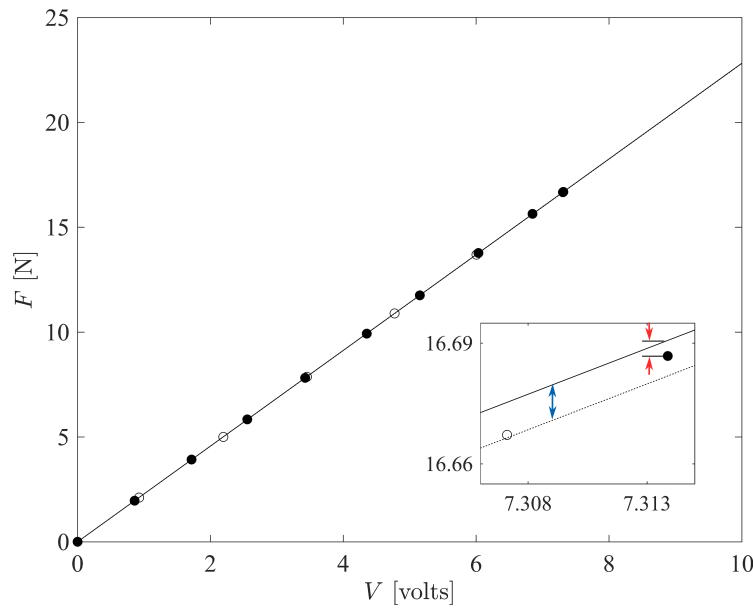
Figure 3.9: Force sensor calibration. Closed circles are the average output voltage of the 10,000 samples taken when loading the scale at each force reading. Open circles correspond to the average voltage measured when unloading the scale. The solid and dashed lines are linear fits to the loading and unloading data, respectively. Error bars (representing plus or minus one standard deviation for voltage readings and uncertainty for the force measurements) are too small to see. The red and blue arrows in the inset illustrate the non-linearity and hysteresis calculations, respectively.

A linear least-squares regression line is fit to the data, forcing the intercept to zero so that zero voltage gives zero force. The line of best fit is given by

$$F = 2.282V, \tag{3.3}$$

where V is the voltage measured. The slope of the line is expected to be around 2.22, as found, since the maximum output of 10V should correspond to a maximum sensor capacity of 22.2 N.

The non-linearity of the sensor is calculated as the maximum difference between the data and the line of best fit divided by the full scale value (i.e., F at $V = 10$ volts). The non-linearity calculation is illustrated in red in the inset of figure 3.9. The nonlinearity of the sensor is found to be 0.038 % of the full scale, which is slightly larger than the 0.03% reported by the manufacturer. The difference may be attributed to the addition of the amplifier and DAQ board noise to the sensor noise. Furthermore, the traverse used to lower the sensor onto the scale is spring loaded, as

is the scale. Hence, there is a slight rebound in the sensor position which can alter the scale reading by ±1 g during data collection and may contribute to the larger non-linearity measured.

In order to determine the sensor hysteresis, data is also collected as the sensor is raised off the scale (by increments of 200 g). The hysteresis of the system is found by first calculating a line of best fit for the data collected in this manner. This line of best fit corresponds to the dashed line in the inset of figure 3.9. In this case, the line is not forced to have zero-intercept as the zero voltage measurement does not necessarily correspond to zero force if there is hysteresis in the system. The line of best fit is given by

$$F = 2.281V - 4.1 \times 10^{-3}. \tag{3.4}$$

Once the line of best fit is found, the maximum error between it and the line of best fit given by equation 3.3 is computed (indicated by the blue arrow in figure 3.9) and divided by the full scale output. This gives the maximum hysteresis of the sensor, which is 0.046% FS. This is more than double the 0.02% specified by the manufacturer. Some of this may again be attributed to the amplifier and DAQ board noise as well as to the springs in the scale and traverse adjusting to new load settings while data is being recorded. Some of it may also be attributed to non-repeatability of the sensor (which the manufacturer specifies as 0.01% RO).

The error and non-linearity of the sensor are presented in table 3.3.

Standard Deviation	Force Uncertainty	Nonlinearity	Hysteresis
6.4 ×10^{-2} V	±9.8 × 10^{-3} N	± 0.038% FS	± 0.046% FS

Table 3.3: Interface MB-5 load cell error analysis from calibration data. FS stands for the full scale output from the sensor (sensor is rated to 22.2 N).

Noise Characterization

Two tests were run to characterize the noise in the experimental setup: first, with the hydrofoil taken out of the setup and, second, with the hydrofoil attached to the setup but completely removed from the water. In both cases, the load cell is attached to the air bearing structure via the universal joint, as shown in figures 3.4 and 3.5. Force data is recorded for 60 seconds at a 1000 Hz sample rate for the ten Reynolds numbers of interest.

The probability density function (PDF) and frequency response of the data at each Reynolds number are presented in figures 3.10 and 3.11, respectively. Whereas a roughly normal distribution associated with random, stochastic noise is ideally desired for the force data collected, bimodal distributions are obtained for both tests at $Re = 1.4 \times 10^5$ (inset e) and for the first test at $Re = 1.7 \times 10^5$ (black curve in inset f). The first test also results in distributions with a flattened peak at Reynolds numbers of 2.0×10^5 and 2.4×10^5 (black curves in insets g and h). In addition, the second test has a slightly skewed distribution at $Re = 2.8 \times 10^5$ (grey curve in inset i).
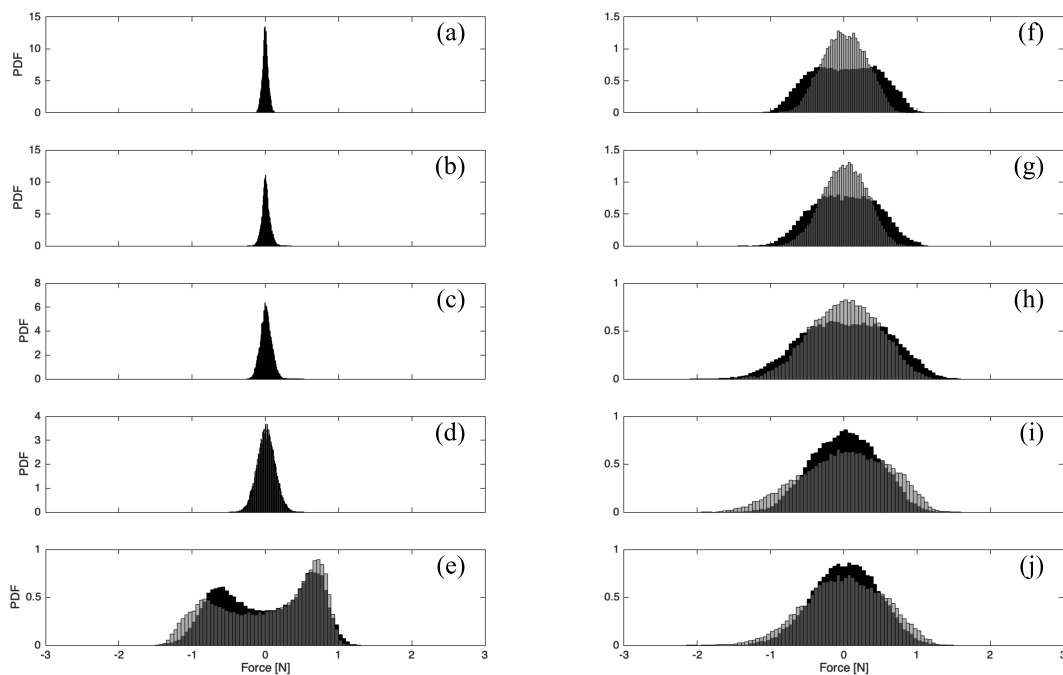
Figure 3.10: Probability density function (PDF) of the force sensor data as a function of force [N]. Black curves: hydrofoil removed from the setup. Grey curves: hydrofoil attached to setup but out of the water. Insets (a) to (j) correspond to increasing Reynolds number (from $Re = 0$ to 3.1×10^5 in increments of approximately 0.3×10^5).

These non-normal distributions are associated with singular sharp peaks in the frequency response, as observed in figure 3.11. Because the hydrofoil is out of the tunnel during these tests, the sharp peaks cannot be caused by vortex shedding, vortex induced vibrations, or other fluid-structure interaction flow phenomena. In addition, the frequency of these sharp peaks changes with the tunnel motor driving frequency (or, equivalently, with Reynolds number), suggesting that the peaks are not associated with resonance effects of the system.
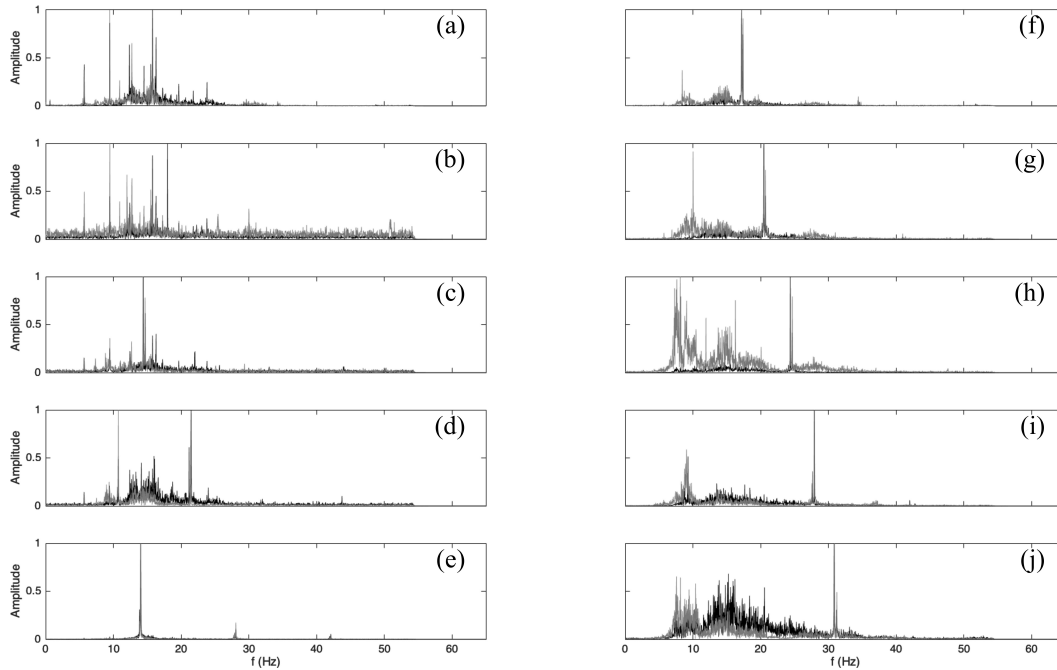
Figure 3.11: The force sensor data's normalized single-sided amplitude spectrum from FFT as a function of the tunnel motor frequency. Black curves: hydrofoil removed from the setup. Grey curves: hydrofoil attached to setup but out of the water. Insets (a) to (j) correspond to increasing Reynolds number (from $Re = 0$ to 3.1×10^5 in increments of approximately 0.3×10^5).

Plotting the frequency of the sharp peak (f_N) versus the tunnel motor driving frequency (f_m) in figure 3.12 reveals that there is a linear relationship between the two. This relationship is given by

$$f_N = 0.65 f_m + 0.25. \tag{3.5}$$

Upon investigation, the factor of two-thirds corresponds to the ratio between the tunnel's motor and pump pulleys. The motor's driving frequency, which is set by the controller, rotates a shaft connected to a 17.8 cm diameter pulley. This pulley drives a belt connected to a second pulley, which rotates the shaft driving the tunnel pump. The pump pulley has a 26.7 cm diameter. As the pulleys are connected, they must have the same number of revolutions per unit time, or equivalently $f_m r_m = f_p r_p$, where r_m and r_p are the radii for the motor and pump pulleys, respectively. The resulting pump frequency is $f_p = \frac{r_m}{r_p} f_m = 0.67 f_m$, similar to the tunnel noise f_N found. Thus, the noise in the system appears to be caused by vibrations from the pump driving the flow.
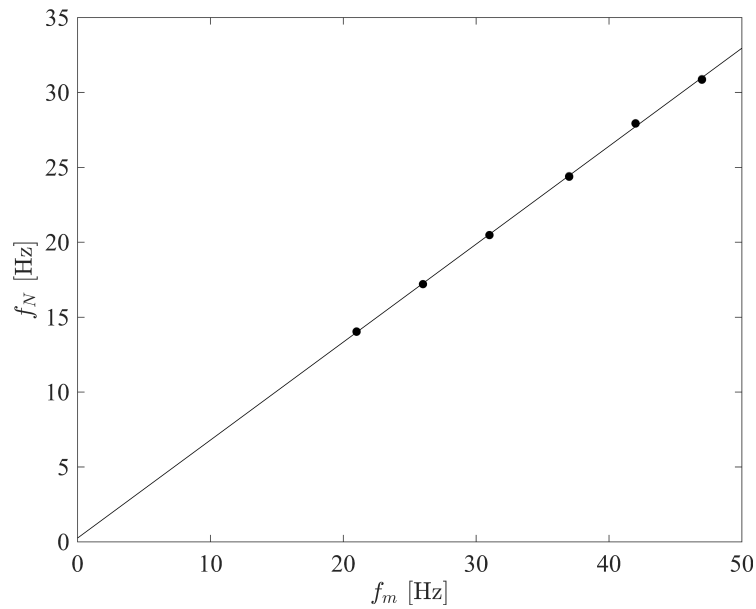
Figure 3.12: Frequency of the sharp peaks in the force data's FFT as a function of the tunnel motor frequency. The solid line is the fit given by equation 3.5.
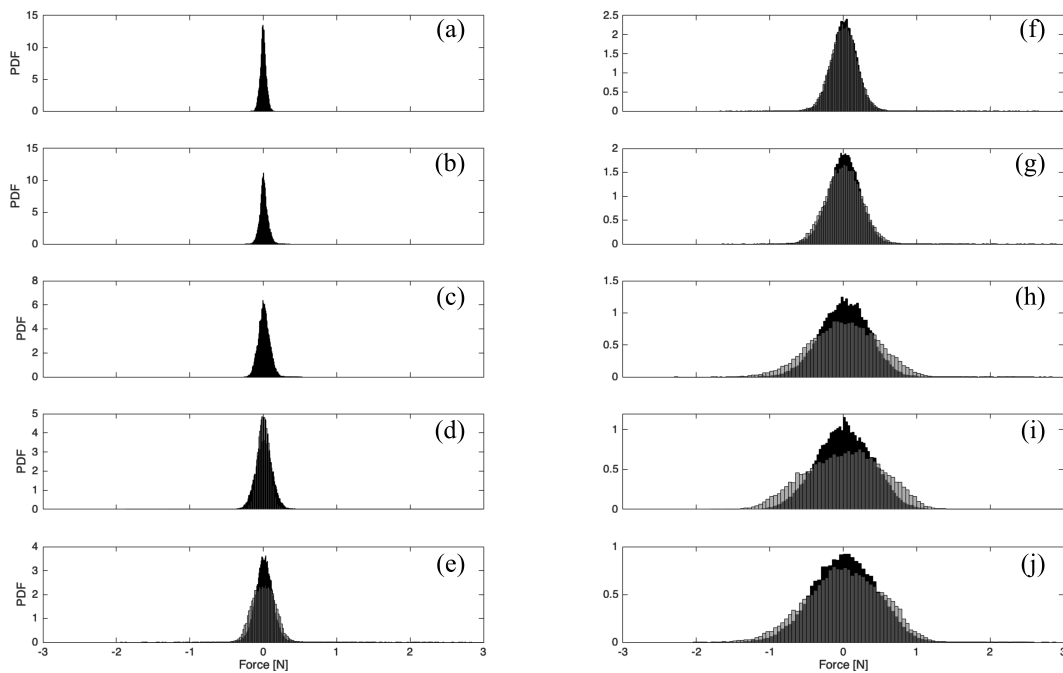
Figure 3.13: Probability density function (PDF) of the filtered force sensor data as a function of force [N]. Filtering the data results in normal distributions. Black curves: hydrofoil removed from the setup. Grey curves: hydrofoil attached to setup but out of the water. Insets (a) to (j) correspond to increasing Reynolds number (from $Re = 0$ to 3.1×10^5 in increments of approximately 0.3×10^5).

Because the peak noise frequency seems to be caused by mechanical vibrations, it is filtered out using a bandstop FIR filter over $f_N \pm 1$Hz. This filter is applied to all force data collected. The result of filtering on the PDF distributions is presented in figure 3.13. Normal distributions are now obtained, as expected.

3.2.5 Flow Visualization Methods

Videos of the flow field are taken using an IDS UI-3360CP-M monochromatic camera with 12.5 mm 1:1.4 Cosmicar Television lens run via the uEye Cockpit software in order to qualitatively observe the effect of wetting conditions on free-surface flow features. Videos are taken at around 65 frames per second for over 30 seconds. The camera is placed below the water tunnel's test section and looks up at the hydrofoil (see figure 3.5). The camera sits on a Velmex traverse (run by a Vexta 2phase motor, which is controlled by a Velmex VXM stepping motor control) so that its y-location can be adjusted. This allows us to align camera's horizontal centerline to the hydrofoil's chord. The traverse system also sits on a carriage supported by rails, so that the camera's x-location can be further adjusted.

A white screen is placed above the test section while a 500 watt halogen work light illuminates the flow from below. The result is a shadowgraph which can be used to capture vortex shedding, free surface waves, and free surface separation phenomena.

The control and $\beta = 0°$ test cases are also imaged from the side in order to see if any differences in free surface elevation and bow wave amplitude occur. Side videos are taken at 60 frames per second for 30 seconds using a IDS UI-3660CP-C color camera with a 12mm 1:1.4 Computar lens.

Flow field and side videos are taken at the ten water tunnel flow speeds of interest for the nominal $\alpha = 0°$ angle of attack only.

3.3 Force Estimates

The total transverse force F_y acting on the surface-piercing body is the sum of the lifting force F_L due to inertial effects (dependent on the angle of attack α) and the transverse force F_S due to surface tension effects. That is, $F_y = F_L + F_S$.

The expected lift force generated is:

$$F_L = \frac{1}{2}\rho U_\infty^2 S C_L, \tag{3.6}$$

where $\rho = 1000$ kg/m^3 is the density of water, U is the free stream velocity, $S = ch$ is the wetted planform area of the hydrofoil, and C_L is the lift coefficient of the

hydrofoil at a given angle of attack and Reynolds number.

As the hydrofoil has a very low aspect ratio (0.25), thin airfoil theory developed by Prandtl for thin, two-dimensional airfoils of infinite span is not applicable. Thus, the traditional $C_l = 2\pi \sin \alpha$ relationship cannot be used to estimate the lift coefficient.

Torres and Mueller (2004) conducted experiments in a wind tunnel with thin (thickness of $1.96 - 2.60\%$ of the chord), low aspect ratio (0.5 to 2), flat (0% camber), unswept wings at Reynolds number of $O(10^5)$. They studied four planforms, of which the inverse Zimmerman planform had a more tapered leading edge than trailing edge.

They compared their experimental data to Polhamus's adaptation of the leading-edge-suction analogy (Polhamus, 1966), which results in the following equation for the lift coefficient:

$$C_L = K_p \sin \alpha \cos^2 \alpha + K_v \cos \alpha \sin^2 \alpha. \tag{3.7}$$

K_p is a factor that depends on the wing's aspect ratio, sweep angle, and shape, and K_v is a factor that is mostly constant with a value of around π. Torres and Mueller used this equation to model their data, using the factor K_p as a fitting parameter. The value of K_p changes with aspect ratio and planform type, as shown in their paper and reproduced in figure 3.14.

A second order polynomial is fit to Torres and Mueller's K_p values for the inverse Zimmerman wing (which most closely resembles the reversed hydrofoil). This fit is used to extrapolate the approximate value of K_p for the current experiment's aspect ratio of 0.25. Using this K_p value in equation 3.7, results in good agreement with the preliminary data collected, as observed in figure 3.15. Note that there is still a small discrepancy between the theory and experimental data; however, this may be attributed to the K_p value corresponding to a different planform than that actually used in experiments in addition to the fact that free surface flows are associated with bow waves and other phenomena that would not occur in a wind tunnel experiment.

The largest lift coefficient obtained in experiments is about 0.2, resulting in a lift force of about 2N which is well below the Interface load cell capacity.

The transverse force generated due to asymmetric wetting conditions can also be estimated. This component of the transverse force is given by
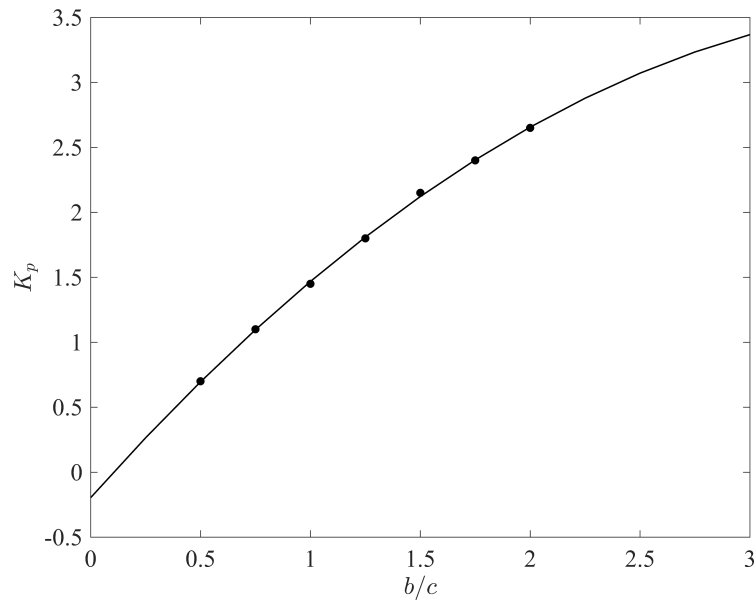
Figure 3.14: K_p values for determining the lift coefficient of thin, low aspect ratio, non-cambered, unswept wings in low Reynolds number flows. The markers represent data reproduced from Torres and Mueller's 2004 wind tunnel experiments using an inverse Zimmerman planform wing. The curve is a least-squares second order polynomial fit of the data used to extrapolate to lower aspect ratios.
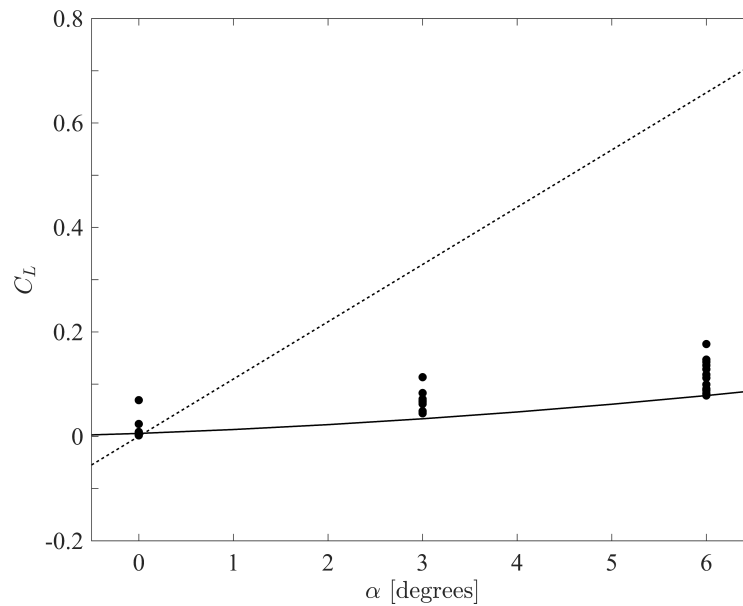
Figure 3.15: Comparison of Prandtl's lifting line theory (dashed line) and Torres and Mueller's lift coefficient equation (solid line) to the experimental data for the uniformly hydrophilic case (dots). The force coefficient in this case corresponds to the lift coefficient, as no transverse force generation from asymmetric wetting conditions occurs.

$$F_S = \gamma \frac{L}{2} \left(\sin \theta_L - \sin \theta_U \right), \tag{3.8}$$

where $\gamma = 72 \times 10^{-3}$ N/m is the surface tension of the air-water interface, L is the circumference of the hydrofoil (62.2 cm), and θ_L, θ_U are the contact angles the water makes with the lower and uppers surfaces of the hydrofoil, respectively.

For the uniformly hydrophilic case, $\theta_L = \theta_U = 68°$ and $F_S = 0$N. For the half-hydrophobic case, $\theta_L = 68°$ and $\theta_U = 157°$, giving $F_S = 1.2 \times 10^{-2}$N.

For the half-patterned case with $\beta = 0°$, if the contact line on the patterned side falls on a hydrophilic band, the uniformly hydrophilic case should be recovered. If the contact line falls on a hydrophobic band, the half-hydrophobic case should be recovered. Should the contact line cross over several bands of different wetting properties, an intermediate force (i.e., $0 < F_s < 1.2 \times 10^{-2}$N) is expected.

For the half-patterned case with $\beta = 90°$, the contact line on the patterned side of the hydrofoil will be half in contact with hydrophilic bands and half in contact with hydrophobic bands due to the alternating hydrophilic and hydrophobic bands having the same width. Therefore,

$$F_S = \gamma \left[\frac{L}{2} \sin \theta_1 - \frac{L}{4} \left(\sin \theta_1 + \sin \theta_2 \right) \right], \tag{3.9}$$

where $\theta_1 = 68°$ (hydrophilic regions) and $\theta_2 = 157°$ (hydrophobic regions). The transverse force generated by surface tension effects on the patterned hydrofoil with $\beta = 90°$ is thus 6×10^{-3}N.

The surface-tension-induced transverse forces calculated here are only rough estimates. They do not account for changes in the bow wave, free surface waves, free-surface elevation, or contact line dynamics that could arise from the introduction of asymmetric and non-uniform wetting conditions. The force estimates can, however, serve as a basis for checking if the force acquisition system being used is adequate.

The smallest estimated F_S is 6×10^{-3}N. Therefore the sensor must have a resolution smaller than this in order to resolve changes in F_y. The data acquisition system has an ideal resolution of 3.4×10^{-4}N, which is an order of magnitude smaller than the expected change in transverse force. However, the non-linearity, hysteresis and reported non-repeatability are of the same order of magnitude as the expected

surface-tension-induced transverse force for the patterned case. The limiting factor is thus not the resolution but system noise.

Additionally, note that the horizontal component of force is reduced on the coated surfaces compared to the uniformly hydrophilic surface. Thus, the net side force generated by surface tension effects points from the hydrophilic side to the coated side of the hydrofoil. Because the force sensor is rated in compression only (corresponding to the positive force direction), the upper surface of the hydrofoil is coated in order to get a net transverse force change in the positive force direction.

3.4 Force Data Results

As described in section 3.2.3, several data sets are collected for every angle of attack and wetting condition combination. Each set consists of one to four tests, each of which contains 60,000 measurements at every Reynolds number of study. The data is filtered using a 60 Hz lowpass FIR filter to reduce high frequency noise as well as a bandstop FIR filter around $f_N \pm 1$Hz to filter out the vibrational noise discussed in section 3.2.4. Table 3.4 lists the number of tests run in each data set collected for the different angle of attack and wetting conditions.

Case	$\alpha = 0°$	$\alpha = 3°$	$\alpha = 6°$
1	**3 2 2 1** 3 1 1 1 1 2 1 **3 2**	**3 3 2**	**3 1** 2 1 **3 2**
2	4 2 1 **2** 3 1 1 **2 1**	**3** 3	**3 3 2** 3
3	**3** 2	**2 2**	**2 2**
4	**3 3** 3 2	**3 3** 3	**3 3** 2
5	**3 2 3 2 2** 3 2 **2**	**3** 3	**3 2 3** 2
6	**4** 3	**3** 3	3 2

Table 3.4: Each entry represents a different set of data collected. The value corresponds to the number of tests composing that set. Sets that are bold were selected for the final force analysis. The remaining sets were neglected as their frequency response and PDFs do not conform to the general trends.

The probability density function and frequency response of the signals collected in each set are used to sort the data. The measurements from all tests in a set are lumped together for this analysis. (For example, the first set run for the uniformly hydrophilic case consists of three tests. The data of all three tests are pooled together such that 180,000 data points are used to compute the probability density function and frequency response.) Sets that have non-normal distributions for their PDFs or a sharp, singular peak in their frequency responses (despite filtering out the vibrational noise) are neglected in future analysis as the cause of these discrepancies

in data trends is unclear. The discrepancies could potentially be due to different free surface conditions. While the water tunnel and free surface are thoroughly cleaned before testing, there remain particles in the water which could accumulate over time and therefore alter how the free surface responds during testing. Changes in the free surface response could lead to a change in the force response picked up by the load cell.

The results of the sorted force data analysis are plotted in figure 3.16. Rows correspond to different angles of attack. The lefthand column contains plots of ΔF_y versus free stream velocity, where

$$\Delta F_y = \left(F_y\right)_t - \left(F_y\right)_1 \tag{3.10}$$

with the subscript 1 denoting the control case (case 1) and the subscript t denoting a test case (cases 2 to 6). As such, ΔF_y represents the side force generated from surface tension effects as it is expected that $(F_S)_1 = 0$ for the uniformly hydrophilic case. Therefore,

$$\left(F_y\right)_1 = (F_L)_1 \tag{3.11}$$

for the control case. As the lift force is an inertial effect, it should be unchanged between cases. Thus, $(F_L)_1 = (F_L)_t = F_L$, and subtracting the side force measured for the control case from that measured for an asymmetrically coated case will yield

$$\Delta F_y = \left(F_y\right)_t - \left(F_y\right)_1 \tag{3.12a}$$
$$= (F_S)_t + (F_L)_t - (F_L)_1 \tag{3.12b}$$
$$= (F_S)_t + F_L - F_L \tag{3.12c}$$
$$= (F_S)_t . \tag{3.12d}$$

The righthand column of figure 3.16 contains plots of ΔC_y versus Reynolds number, where ΔC_y is the non-dimensionalized ΔF_y given by

$$\Delta C_y = \frac{\Delta F_y}{\frac{1}{2}\rho U_\infty^2 S}. \tag{3.13}$$

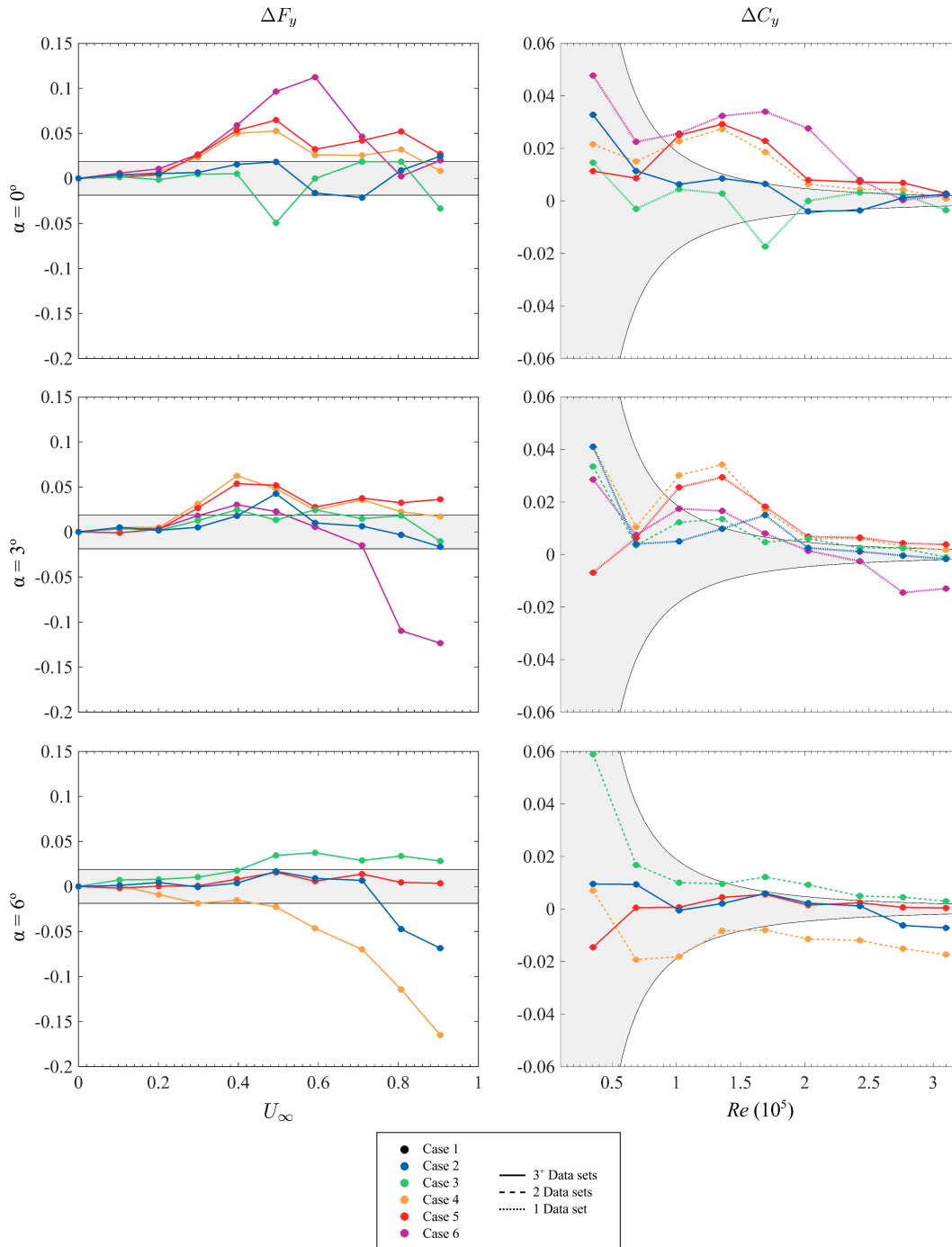**Figure 3.16:** Force analysis results for the hydrofoil experiments conducted at $\alpha = 0°$, $3°$, and $6°$. The lefthand column contains plots of ΔF_y versus U_∞. The righthand column contains plots of ΔC_y versus Re. The shaded regions correspond to the force sensor's maximum noise level. Refer to table 3.2 for information about each case.

The shaded region in all plots corresponds to the maximum anticipated noise level of the force sensor. The noise is given by the sum of the non-linearity and hysteresis plus non-repeatability of the system as reported in table 3.3. The sensor noise is non-dimensionalized by the same factor $q = 1/2\rho U_\infty^2 S$ used in computing ΔC_y for the ΔC_y plots.

(Note that non-dimensionalization by the factor q is the convention for lift, drag, and skin friction forces in airfoil and hydrofoil studies. On the other hand, since the force of interest is due to wetting conditions (and thus surface tension), the force could have been non-dimensionalized by γc. However, as γc is a constant, the results of this non-dimensionalization would simply yield the same plots found in the lefthand column of figure 3.16 but with different axis scales.)

The colors of the curves in all plots of figure 3.16 correspond to the different cases studied (see table 3.2). In addition, the line style of the curve gives a measure of the repeatability of the experiments. After sorting the data, certain experimental cases are left with only one or two useable data sets (see table 3.4). These are plotted with dotted and dashed lines, respectively, to signal that the repeatability of the results is not guaranteed. Solid lines are used for experiments with three or more data sets.

From the plots, it is observed that asymmetrically coating the hydrofoil does indeed result in a generally positive change in the transverse force as predicted in section 3.3. The half-patterned hydrofoil with ($\beta = 90°$, $\lambda = 5.4$ mm) bands (i.e., case 4) at $\alpha = 6°$ and the half-patterned hydrofoil with ($\beta = 90°$, $\lambda = 22$ mm) band (i.e., case 6) at $\alpha = 3°$ are the only major exceptions to this observation. Furthermore, while the side force generated by asymmetric wetting conditions typically decreases with increasing angle of attack, the side force generated for the half-hydrophobic case is generally around 1 to 2 $\times 10^{-2}$ N over the entire range of Reynolds numbers considered, as estimated. This unfortunately falls within the sensor noise range, albeit a conservative noise range.

The half-perpendicular band cases ($\beta = 90°$, $\lambda = 5.4, 11, 22$ mm, corresponding to cases 4-6) generate a transverse force that is around 0.06 N to 0.1 N for $\alpha = 0°$ for mid-range Reynolds numbers, which is an order of magnitude or more greater than the estimated 6×10^{-3} N. In fact, the half-patterned hydrofoils with bands oriented at angle $\beta = 90°$ with the flow direction have the greatest impact on C_y at all but the highest angle of attack, contrary to the force estimates. This is particularly evident for Reynolds numbers between 1.0 and 2.0$\times 10^5$.

The half-parallel bands case ($\beta = 0°$, $\lambda = 11$ mm, corresponding to case 3) has negligible effect on side force generation for most Reynolds numbers at $\alpha = 0°$. Its ΔC_y falls within the sensor noise band for all but two Reynolds numbers, of which one is still close to the noise limit. However, as the angle of attack is increased, its ΔC_y increases (although it remains close to the sensor noise limit). This trend is opposite what happens for the other asymmetrically coated cases. More experiments are needed to confirm the trend as only one to two sets of data are currently available for this case.

Turning to the effect of band wavelength for the $\beta = 90°$ cases, it seems that increasing λ increases ΔC_y for $\alpha = 0°$, while the opposite holds for the $\alpha = 3°$ experiments. The data trend observed for the $\alpha = 0°$ case is counterintuitive: it is expected that as λ increases, its ΔC_y approaches that of the half hydrophobic case (corresponding to $\lambda = 2c$), which is the trend observed for the $\alpha = 3°$ cases. More experiments need to be conducted, however, to confirm these observations as the $\lambda = 5.4$ mm and 22 mm cases contain only one or two data sets each. In addition, the $\lambda = 22$ mm case shows negative side force generation at high Reynolds numbers for $\alpha = 3°$ and the $\lambda = 5.4$ mm case shows negative side force generation for most Reynolds numbers at $\alpha = 6°$, which begs further investigation.

Despite the need for more data to elucidate trends, it can be concluded that asymmetric wetting conditions lead to transverse force generation as hypothesized. In addition, coupling non-uniform wetting conditions with asymmetric wetting conditions (the half-patterned cases, which effectively is like coupling an $L/2$-scaled heterogeneity with a d-scaled heterogeneity, where L is the perimeter of the hydrofoil and d is the pattern band size) results in greater side force generation than asymmetric wetting conditions alone (the half-hydrophobic case with an $L/2$-scaled heterogeneity only), contrary to prediction.

3.5 Flow Visualization Results

Videos of the free surface are taken for cases 1, 2, 3, and 5 when the hydrofoil is at zero angle of attack. The videos use a shadowgraph technique as described in section 3.2.5. Still frames of these videos are presented in figure 3.17 for three of the Reynolds numbers studied. Note that these images are mirrored so that the top side of the hydrofoil in each image corresponds to the upper surface of the hydrofoil. This side is uniformly hydrophilic for case 1, uniformly hydrophobic for case 2, and patterned with alternating hydrophilic bands of wavelength $\lambda = 11$mm and

inclination angle $\beta = 0°$ and 90° for cases 3 and 5, respectively. The bottom side in the images is then the lower surface of the hydrofoil which is always uniformly hydrophilic.
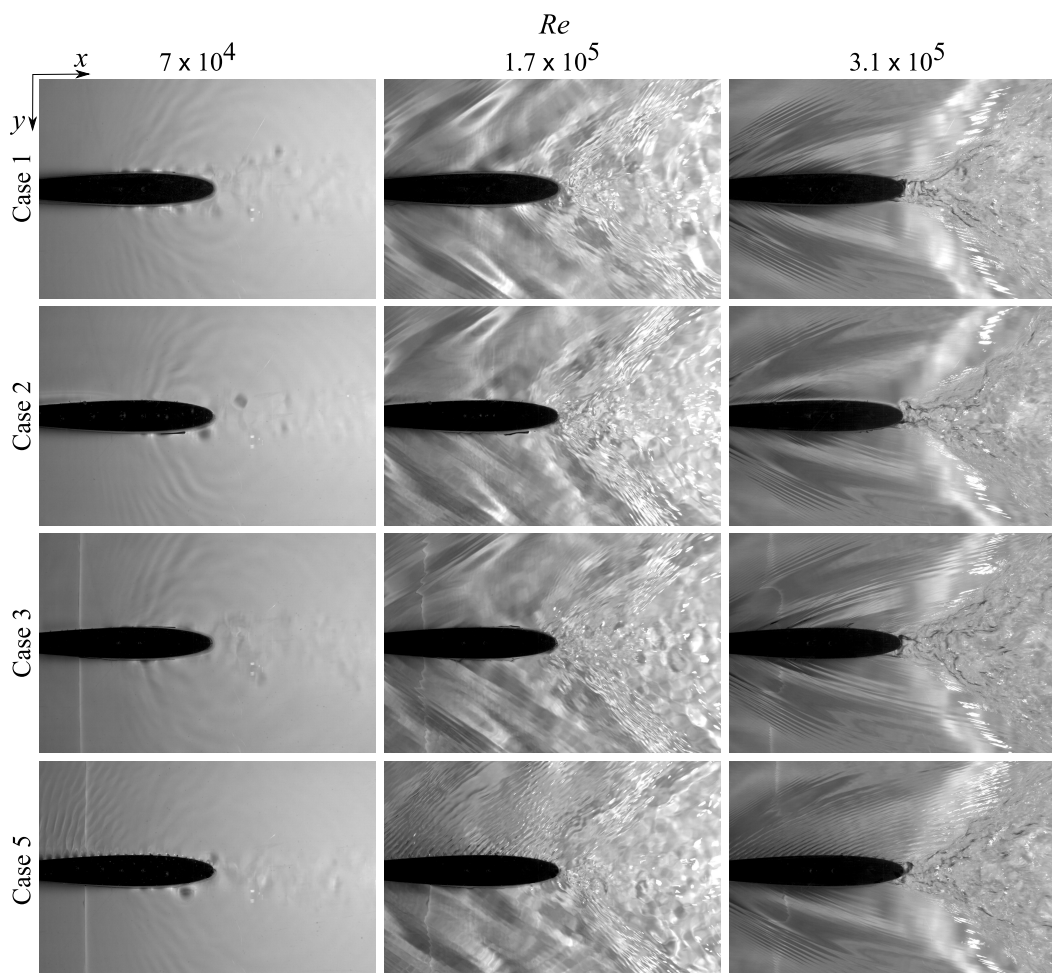
Figure 3.17: Instantaneous shadowgraph images of the hydrofoil experiments as seen from below. The hydrofoil is at $\alpha = 0°$. The top surface of the hydrofoil in the images corresponds to the hydrofoil's upper surface. This is the manipulated side. The bottom surface in the image is the hydrofoil's lower surface, which is uniformly hydrophilic for all cases. Flow is left to right.

Vortices are observed being shed at low Reynolds number in these images. The vortices are the dark circles along the body and in the wake. Vortex shedding is analyzed in section 3.5.2 for $Re = 4, 7$, and 10×10^4.

Surface waves are also observed on the upper surface of the patterned hydrofoils. These surface waves are persistent at even the highest Reynolds numbers studied, though not in regions of free surface turbulence or flow separation. These surface waves are characterized in greater detail in section 3.5.1.
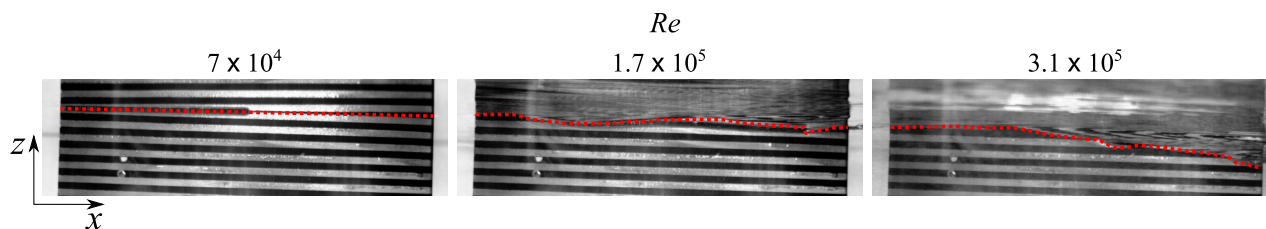
Figure 3.18: Instantaneous snapshots of the half-patterned hydrofoil experiments with ($\beta = 0°$, $\lambda = 11$mm) as seen from the side for $\alpha = 0°$. Each column corresponds to a different Reynolds number, as indicated.
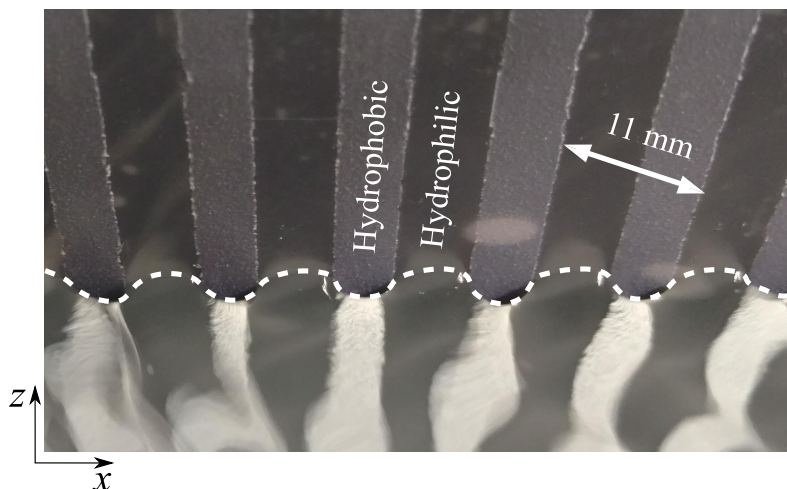
Figure 3.19: The modulated contact line for case 5.

Asymmetric wetting conditions are additionally found to cause asymmetric flow separation at the free surface at the higher Reynolds number studied. That is, separation occurs earlier along the hydrofoil on one side than the other. Free surface separation is discussed in greater detail in section 3.5.3.

3.5.1 Free Surface Wave Characterization

For the $\beta = 90°$ case, the surface waves are the caused by a modulated contact line. As evidenced in figure 3.19, the modulated contact line results from the change from a convex meniscus on the hydrophilic bands (wave crests) to a concave meniscus on the hydrophobic bands (wave troughs). This modulated contact line is analogous to the roller structures observed in the thin film experiments (see chapter 2).

Since the waves originate on the bands, the wavelength is fixed to that of the band wavelength (which equals 5.4, 11, or 22 mm for the $\beta = 90°$ patterns). Since the water depth in the tunnel test section is 40.6 cm, the ratio H/λ ranges from roughly 19 to 75. As $H/\lambda \gg 1$, the waves can be characterized as deep water waves.

The general dispersion equation is given by

$$\omega = \sqrt{\left(gk + \frac{\gamma}{\rho}k^3\right)\tanh kH}, \tag{3.14}$$

where $k = 2\pi/\lambda$ is the wavenumber and ω is the angular frequency of the waves (Vanden-Broeck, 2010). For $H/\lambda \gg 1$, as in the current experiments, the term $\tanh kH \rightarrow 1$. Thus, equation 3.14 becomes

$$\omega = \sqrt{gk + \frac{\gamma}{\rho}k^3}. \tag{3.15}$$

The phase speed of deep water waves, defined as $c_p \equiv \omega/k$, is thus

$$c_p = \sqrt{\left(\frac{g}{k} + \frac{\gamma}{\rho}k\right)}. \tag{3.16}$$

The group velocity is defined as $c_g \equiv \partial\omega/\partial k$, yielding

$$c_g = \frac{1}{2}\left(\frac{g}{k} + \frac{3\gamma k}{\rho}\right)c_p^{-1}. \tag{3.17}$$

Waves with $g \neq 0, \gamma = 0$ are referred to as pure gravity waves. In deep water, they are characterized by the dispersion relation

$$\omega = \sqrt{gk}, \tag{3.18}$$

which results in $c_p = \sqrt{g/k}, c_g = 0.5c_p$.

Waves with $g = 0, \gamma \neq 0$ are referred to as pure capillary waves. In deep water, they are characterized by the dispersion relation

$$\omega = \sqrt{\frac{\gamma}{\rho}k^3}, \tag{3.19}$$

which results in $c_p = \sqrt{\gamma k/\rho}, c_g = 1.5c_p$.

The non-dimensionalized phase and group velocities versus the non-dimensionalized wavenumber which result from equations 3.16 and 3.17 are presented in figure 3.20. Velocities are non-dimensionalized by $\sqrt[4]{g\gamma/\rho}$ and wavenumbers are non-dimensionalized by the capillary length $\lambda_c = \sqrt{\gamma/(\rho g)}$.

The non-dimensionalized phase (blue) and group (red) velocities for the general dispersion relation (equation 3.14) are plotted as solid lines. The deep water gravity wave simplifications are plotted as dotted lines, while the deep water capillary approximations are plotted as dashed lines. Solid, black lines correspond to the experimental wavelengths observed.
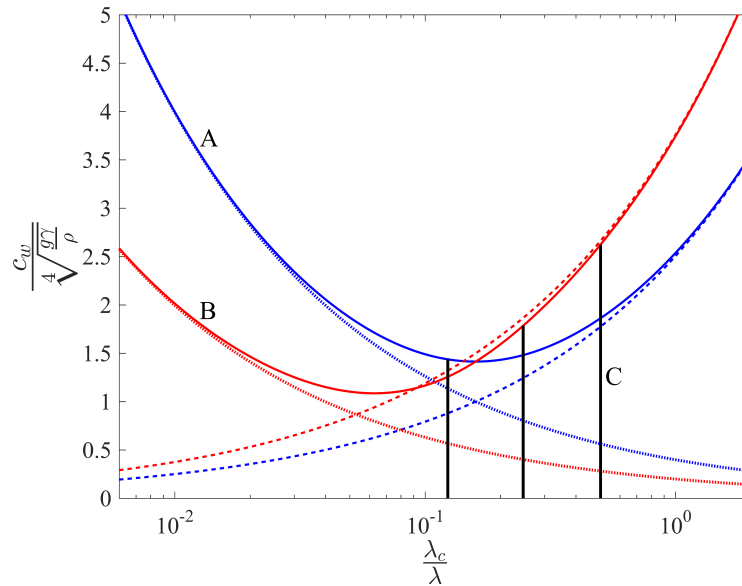
Figure 3.20: Dispersion of gravity-capillary waves on the surface of deep water ($H = 40.6$ cm $>> \lambda$). Non-dimensionalized group and phase velocities are plotted as functions of non-dimensionalized inverse relative wavelength. Blue lines (A): phase velocity. Red lines (B): group velocity. Solid lines: general dispersion relation for gravity-capillary waves. Dashed line: dispersion relation for deep water capillary waves. Dotted line: dispersion relation for deep water gravity waves. Black lines: experimental data's non-dimensionalized inverse relative wavelength.

From where the experimental data falls on the general dispersion relation, it is found that the group velocity is well modeled by pure deep water capillary waves for all experimental λ. The same is not true of the phase velocity, however. As λ increases in experiments, the phase velocities go from being well modeled by deep water capillary waves to being poorly modeled by either pure deep water capillary or pure deep water gravity waves. Therefore, while the waves are deep water capillary waves at smaller λ, they are general deep water gravity-capillary waves at the largest $\lambda = 22$mm.

Using geometric considerations, the angle η the waves should make with the body can be estimated and compared to experiments. From schematic 3.21, it is found that $\eta = \sin^{-1}(c_g/U_\infty)$, where c_g is found by using equation 3.17 for the prescribed

λ. For the Reynolds numbers presented in figure 3.17, the predicted η are $90°, 36°$, and $19°$ as Re increases. The values obtained from the experimental data are $\eta = 82 - 88°, 36 - 44°$, and $16 - 23°$, which are in good accord with the values predicted. (Note that, because the body is curved, the waves also curve in the flow field. The η values reported represent angles measured with respect to the tangent to the body if evaluated close to the body or with respect to the flow direction if evaluated in the far field.) This analysis confirms that the waves generated for the non-uniform wetting conditions with $\beta = 90°$ are indeed locked to the band pattern.
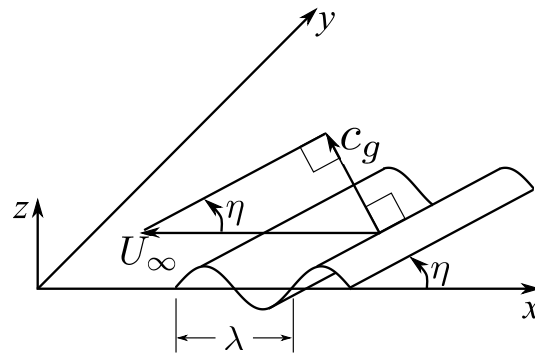
Figure 3.21: Schematic of the free surface waves generated by the non-uniform wetting conditions, as observed in the lab frame. The waves travel with the hydrofoil at speed U_∞ in the negative x-direction. They form an angle η with respect to the x-axis and have a group velocity c_g, as determined by the gravity-capillary dispersion relation, perpendicular to this angle.

The surface waves generated by the $(\beta = 0°, \lambda = 11\text{mm})$ patterned hydrofoil are also the result of the free surface crossing a hydrophobic band, as seen in figure 3.18, however they have a qualitatively different morphology. These are analogous to the digital jumps observed in the thin film experiments.

As a final note, because the waves generated on patterned surfaces originate from surface tension effects, increasing the inertial forces they interact with by increasing Re diminishes their presence or destroys them. Thus, the waves are not observed in regions of free surface turbulence or separation which occur at higher Reynolds numbers, nor are they expected to exist at higher angles of attack in which free surface turbulence and flow separation occur more readily at lower Reynolds. This may explain why the force data show generally decreasing transverse force generation with increasing angle of attack.

3.5.2 Fourier Transform Analysis

As mentioned earlier, vortices can be observed shedding from the body in the shadowgraph videos of the free surface. Vortex shedding is analyzed at three of the lowest Reynolds numbers: $Re = 4, 7, 10 \times 10^4$. Vortex shedding at higher Reynolds numbers is muddled by free surface waves, turbulence, and flow separation. Therefore, it cannot be studied via shadowgraph data.

Each video is split into three interrogation windows, as seen in figure 3.22: the manipulated section on the upper surface of the hydrofoil (region 1), which can be uniformly hydrophilic or coated depending on the experimental case; the hydrophilic section, which corresponds to the lower surface of the hydrofoil (region 2); and the wake (region 3).
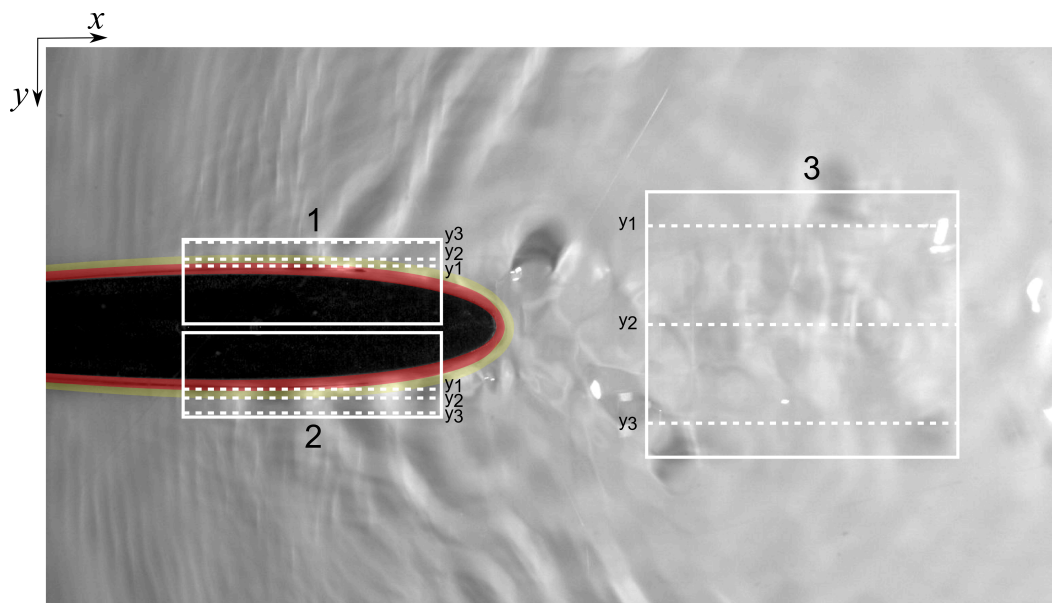
Figure 3.22: Regions of interest used for 2D FFT analysis at lower Reynolds numbers. White boxes are windows used: 1 is the upper surface, which is the manipulated half of the hydrofoil and may thus be hydrophilic, hydrophobic, or patterned depending on the case studied; 2 is the lower surface, which is always uniformly hydrophilic; 3 is the wake. White dashed lines are the y-locations at which xt diagrams are constructed to be used in the 2D FFT analysis. Red and yellow regions around the hydrofoil indicate the δ_{99} boundary layer thickness for the highest and lowest Re considered in FFT analysis, respectively.

The reason for splitting each frame into the top and bottom windows is to investigate vortex shedding on the coated and uncoated sides of the hydrofoil before vortices interact with one another. Comparing the dominant shedding frequency in these two windows allows for understanding whether asymmetric and non-uniform wetting

conditions have an effect on vortex shedding. These windows can also be compared to the uniformly hydrophilic case, which serves as the experimental control. The wake window then allows us to see how the vortices interact with one another.

Three y-locations are selected in each interrogation window to construct xt-diagrams for 2D FFT analysis, as shown by the white dashed lines in figure 3.22. An example of an xt-diagram is shown in figure 3.23, alongside the axis convention for the images.
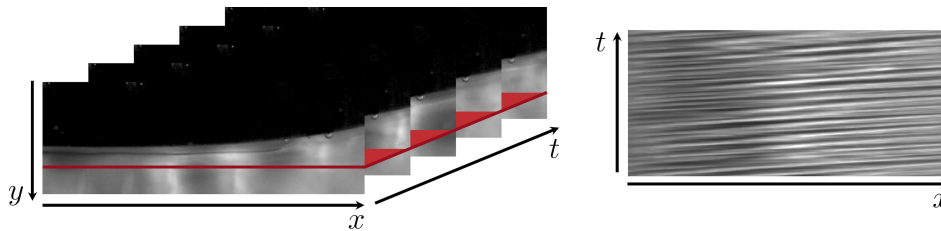
Figure 3.23: Example of a video stack and the resulting xt plot on which 2D FFT is performed. The xt plot is taken at the y-location shown in red in the stack. Each line in the xt plot corresponds to a vortex being shed. The slope of the line is an indication of the vortex convection speed.

The maximum theoretically estimated boundary layer thickness (see appendix B) is indicated by the red and yellow regions in the figure. The maximum boundary layer thickness is given by the δ_{99} formulation, corresponding to the y-location at which the velocity in the boundary layer is $0.99U_\infty$ in the case of no-slip at the surface (i.e. a hydrophilic surface). As the boundary layer is inversely proportional to the square of the Reynolds number, the red region indicates δ_{99} for the greatest Re studied in FFT analysis ($Re = 1.0 \times 10^5$), while the outer limit of yellow region indicates δ_{99} for the lowest Reynolds number studied ($Re = 4 \times 10^4$). Intermediate Reynolds number flows will have a boundary layer thickness which falls somewhere inside this yellow region. Some of the y-locations chosen fall within the maximum boundary layer estimated by theory. This observation will be important later on.

A total of 5000 frames are analyzed per video, except for the wake interrogation window for which only 2000 frames are analyzed due to the large size of the window increasing processing time. The average background of all the frames in a window is subtracted from each frame in order to make flow perturbations stand out more and thus facilitate analysis.

After obtaining the xt-diagram at each y-location of the interrogation windows, the 2D fast Fourier transform (FFT) is computed. The FFT is then normalized so its

values fall between 0 and 1, making comparison between cases easier. The normalized 2D FFT results are presented in subsequent figures. The x-axis represents the non-dimensionalized wavenumber $k/k_c = \lambda_c/\lambda$. The y-axis represents the Strouhal number $St = fd/U_\infty$, where d is the maximum hydrofoil thickness of 3.7 cm. The colors represent the normalized single-sided amplitude of the FFT, as indicated by the colorbars.

For the uniformly hydrophilic (control) case, the flow dynamics on either side of the body should be identical in this case. Thus, the FFTs of these two interrogation windows should also be identical. Comparing rows in at figures 3.24, 3.25, and 3.26, the upper and lower surfaces of the control hydrofoil do indeed have similar FFTs at any given Reynolds number and y-location.

These plots are characterized by non-zero FFT values that are arranged in a diagonal line, representing the dispersion relation for vortex shedding. The sharpness of the peak FFT values in the line reflect how sinusoidal vortex shedding is: the more sinusoidal the shedding is, the stronger the peaks are and the fainter the rest of the line becomes.
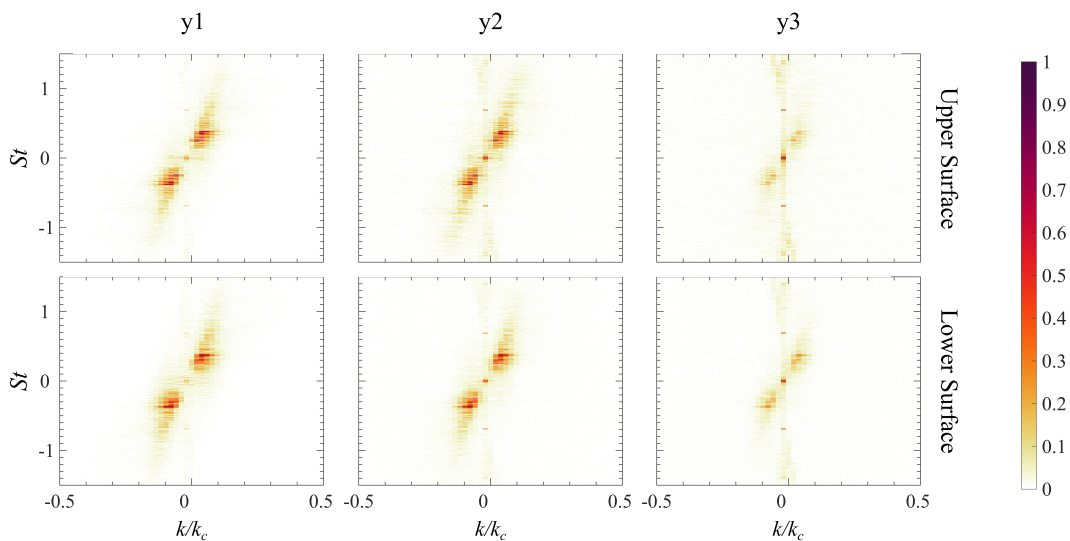
Figure 3.24: 2D FFT of xt plots for the control case (case 1) at $\alpha = 0°$ and $Re = 4 \times 10^4$. The results on the upper and lower surfaces are plotted in the first and second rows, respectively. Columns correspond to different the y-locations at which the xt plots are taken. Distance from the body increases when moving from left to right.
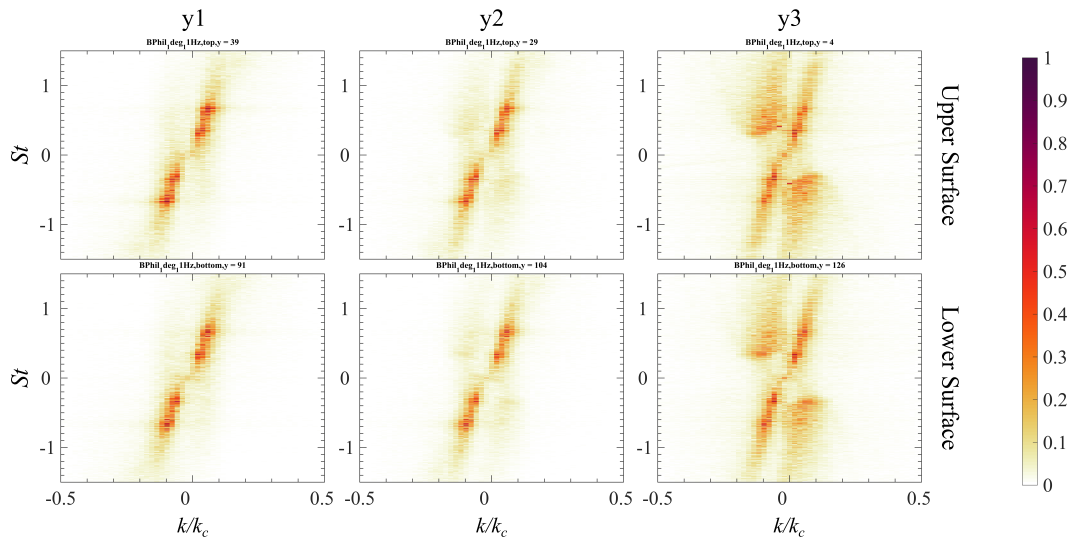
Figure 3.25: 2D FFT of *xt* plots for the control case (case 1) at $\alpha = 0°$ and $Re = 7 \times 10^4$. The results on the upper and lower surfaces are plotted in the first and second rows, respectively. Columns correspond to different the *y*-locations at which the *xt* plots are taken. Distance from the body increases when moving from left to right.
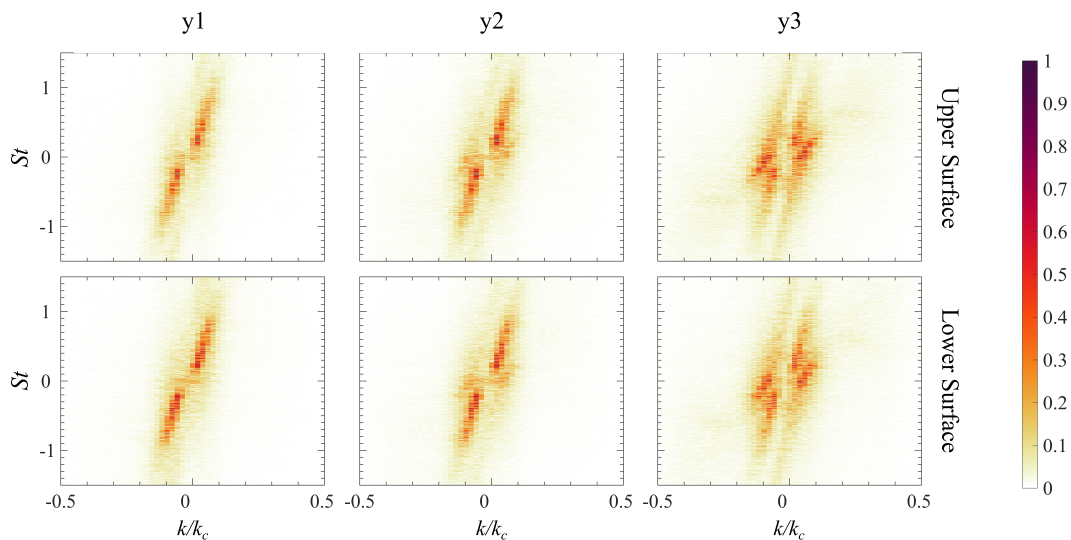
Figure 3.26: 2D FFT of *xt* plots for the control case (case 1) at $\alpha = 0°$ and $Re = 1.0 \times 10^5$. The results on the upper and lower surfaces are plotted in the first and second rows, respectively. Columns correspond to different the *y*-locations at which the *xt* plots are taken. Distance from the body increases when moving from left to right.

As the Reynolds number increases, broader peaks appear in the FFT along with the vortex shedding line. These broader peaks become more apparent when moving away from the body, suggesting that there are surface waves generated at higher

Reynolds numbers that are located away from the body. These broader peaks are indeed associated with the generation of surface waves, as evidenced in the original shadowgraph images of figure 3.27. These waves, which originate on the body near locations where vortices form, are radial and propagate outwards, explaining why they are picked up more strongly when moving away from the body in the FFT windows. As a result of these radial waves, detecting and singling out the vortex shedding process becomes harder, as evidenced by the main diagonal line (corresponding to vortex shedding) not standing out as much and not being as sharp in the FFTs.

For the coated cases (half hydrophobic as well as patterned), the flow dynamics and vortex shedding on the lower surface, which is hydrophilic across all cases, should be identical to those of the control case. Thus, the 2D FFTs of the bottom interrogation window should be identical for all test cases at a given Reynolds number and y-location. Comparing rows in figures 3.28, 3.29, and 3.30 shows that that is indeed the case.
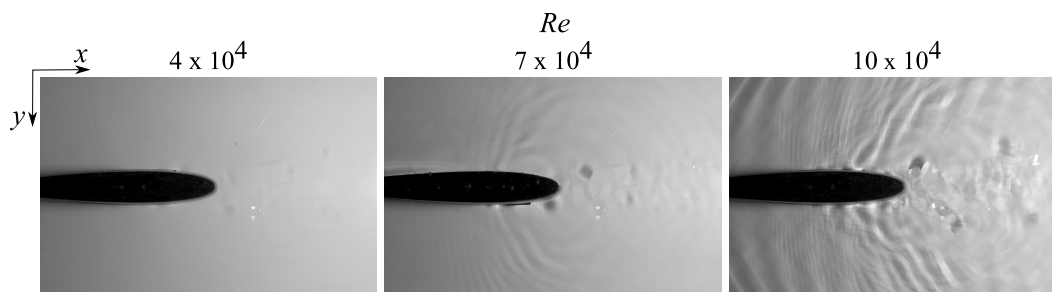
Figure 3.27: Shadowgraph images of radial waves in flow for the control case (case 1) at Reynolds numbers of (a) 4×10^4 , (b) 7×10^4, and (c) 1.0×10^5
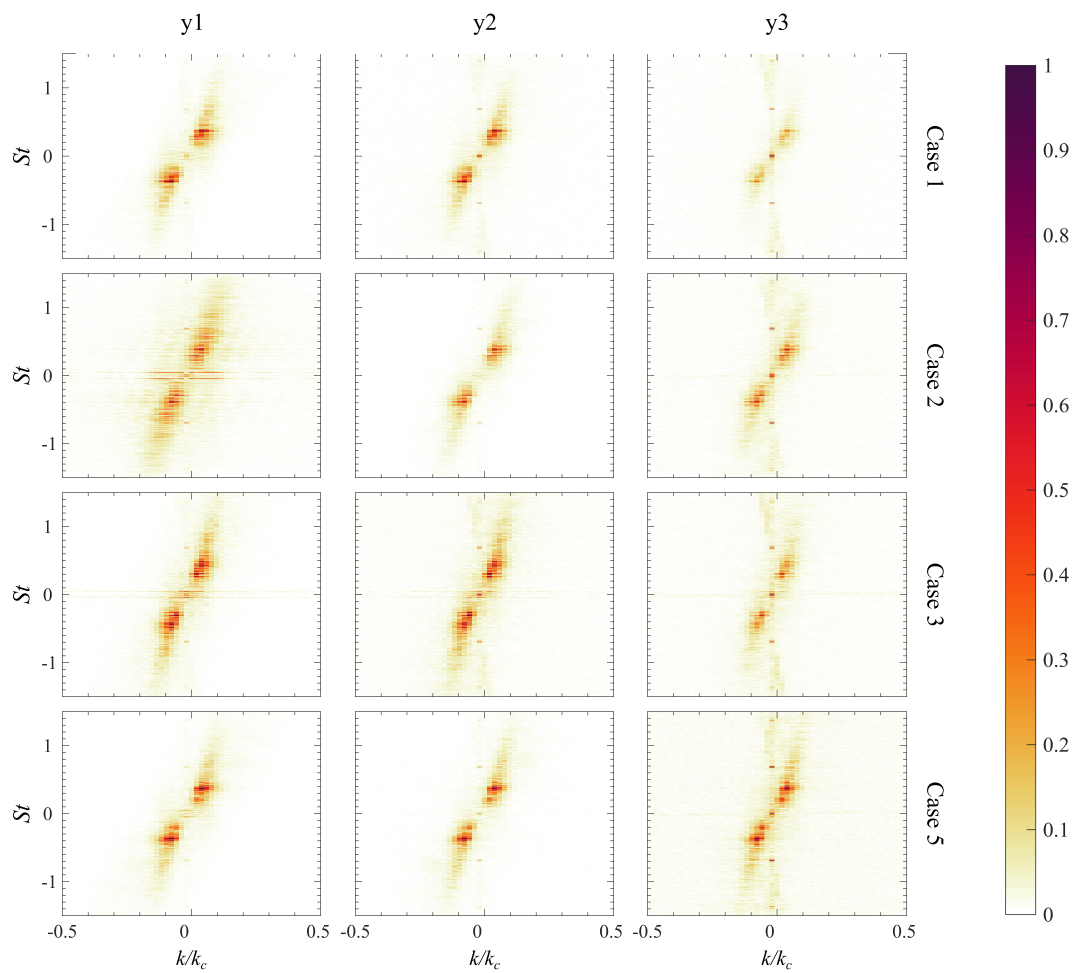
Figure 3.28: 2D FFT of *xt* plots of the lower surface of the hydrofoil at $\alpha = 0°$ and $Re = 4 \times 10^4$. Rows correspond to different cases and columns correspond to different *y*-locations (moving away from the body left to right).
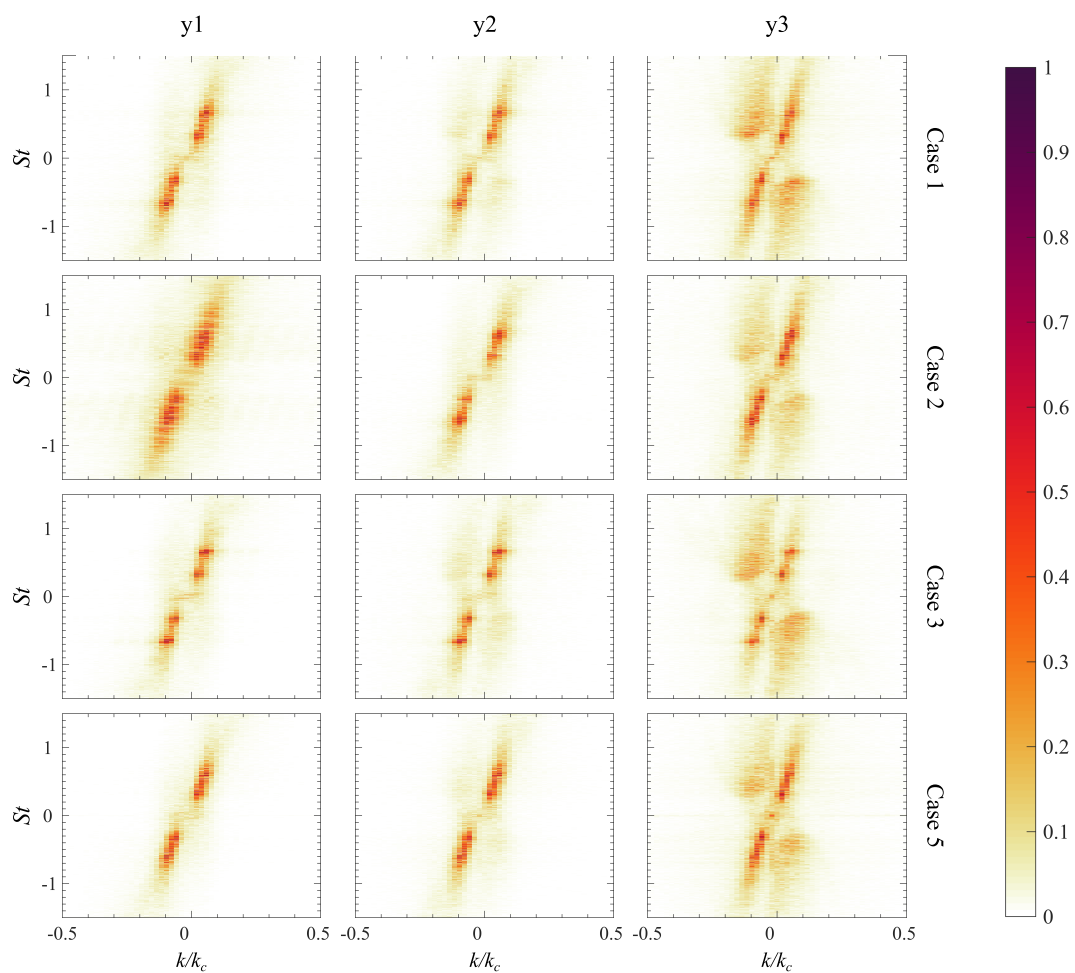
Figure 3.29: 2D FFT of *xt* plots of the lower surface of the hydrofoil at $\alpha = 0°$ and $Re = 7 \times 10^4$. Rows correspond to different cases and columns correspond to different *y*-locations (moving away from the body left to right).
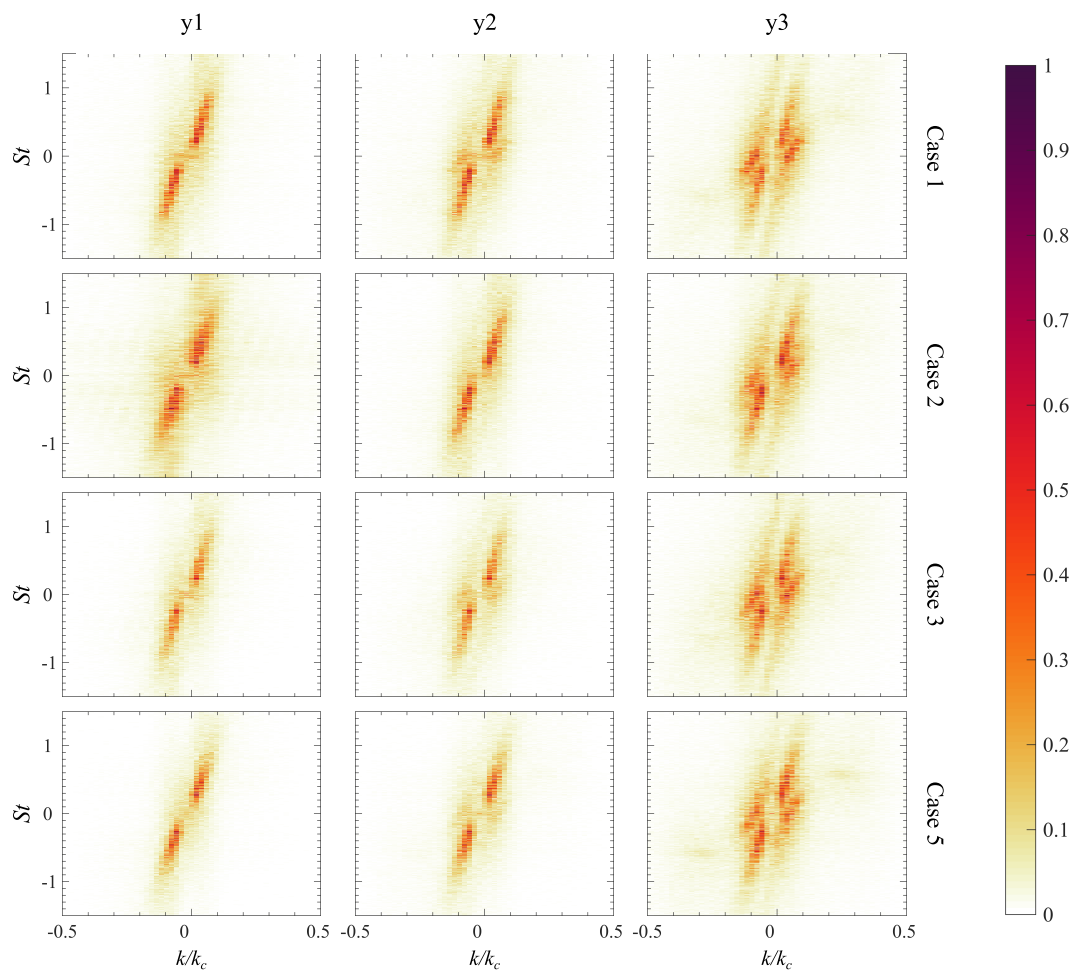
Figure 3.30: 2D FFT of *xt* plots of the lower surface of the hydrofoil at $\alpha = 0°$ and $Re = 1.0 \times 10^5$. Rows correspond to different cases and columns correspond to different *y*-locations (moving away from the body left to right).

On the other hand, it was hypothesized that the patterned cases would modify the contact line and cause free surface waves to appear, which may also effect vortex shedding. Thus a difference is expected in the FFTs of the upper surface, which is the coated side of the hydrofoil. From figures 3.31, 3.32, and 3.33, case 5 (half-patterned with $\beta = 90°$ and $\lambda = 11$mm) is found to result in the greatest change in the FFTs, particularly at the two higher Reynolds numbers. Many additional diagonal lines appear in these FFTs.
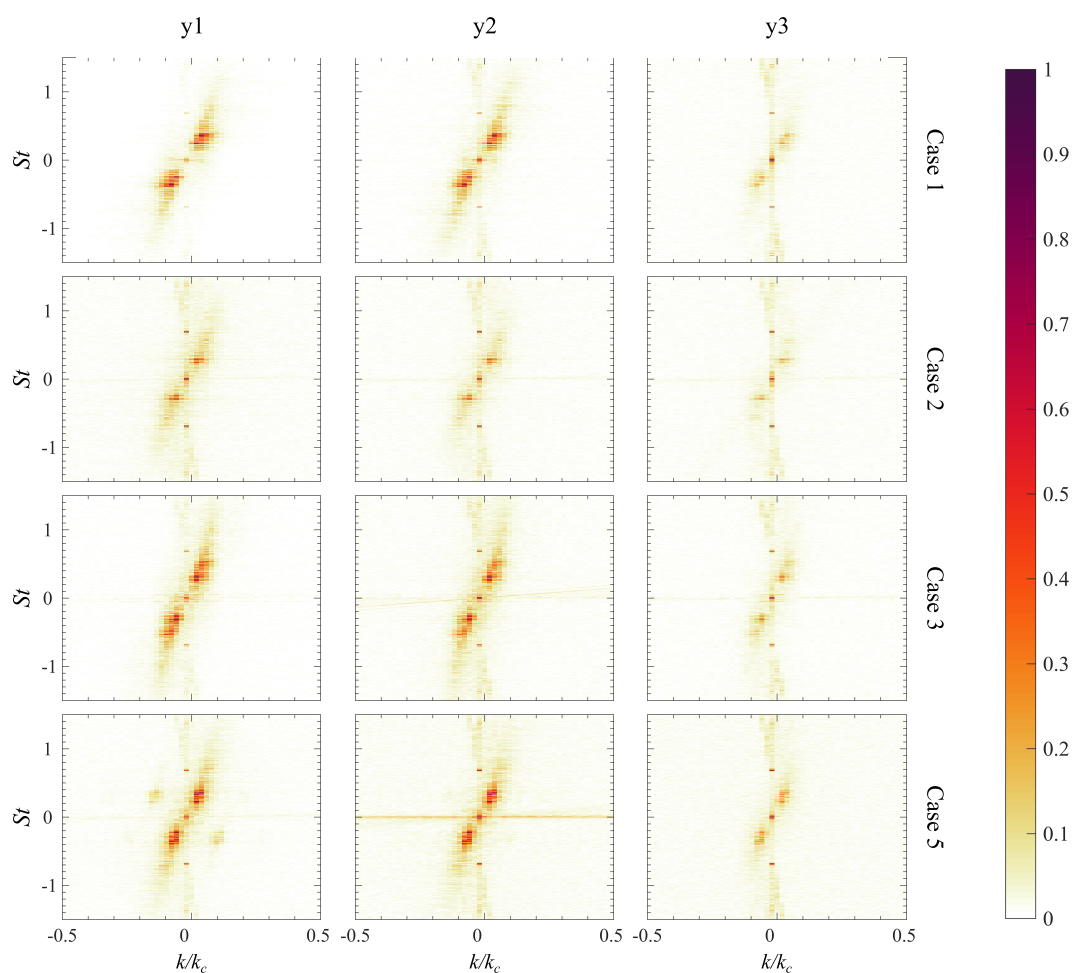
Figure 3.31: 2D FFT of *xt* plots of the upper surface of the hydrofoil at $\alpha = 0°$ and $Re = 4 \times 10^4$. Rows correspond to different cases and columns correspond to different *y*-locations (moving away from the body left to right).
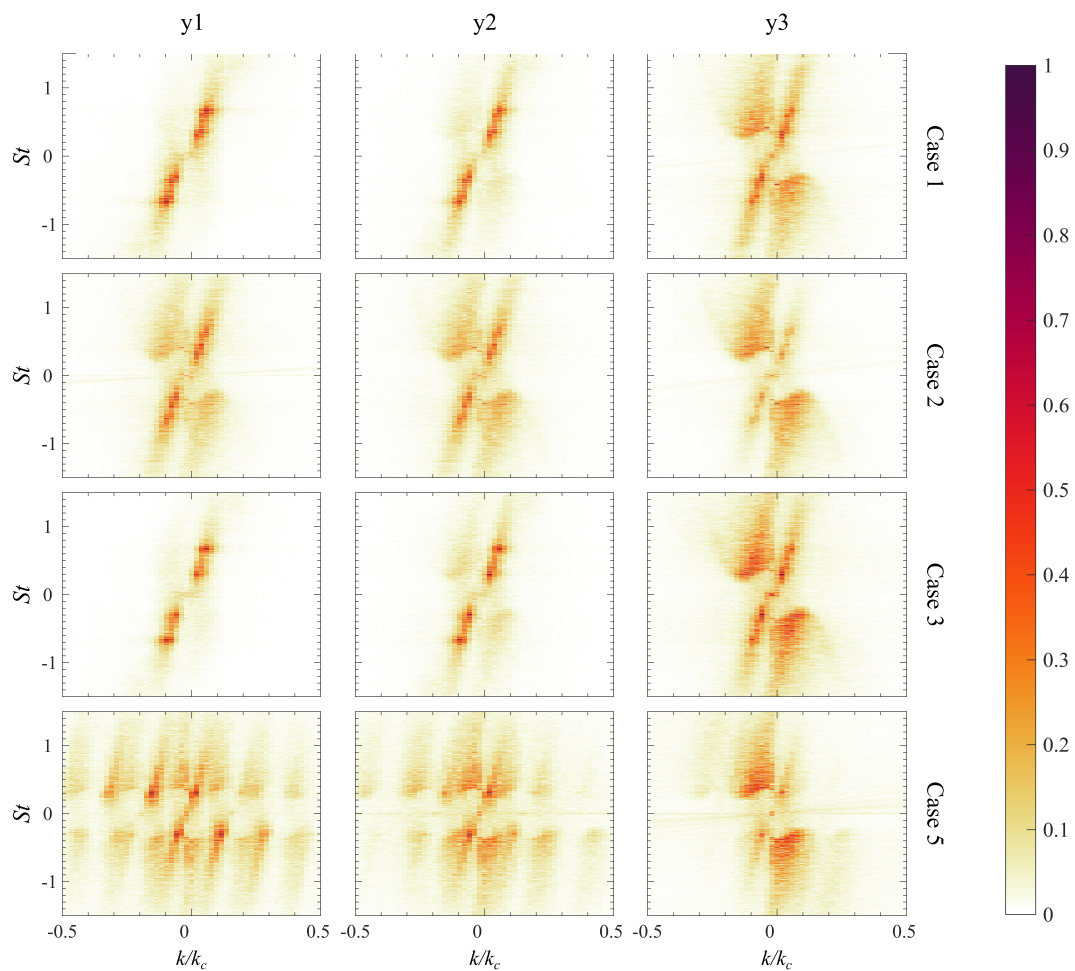
Figure 3.32: 2D FFT of *xt* plots of the upper surface of the hydrofoil at $\alpha = 0°$ and $Re = 7 \times 10^4$. Rows correspond to different cases and columns correspond to different *y*-locations (moving away from the body left to right).
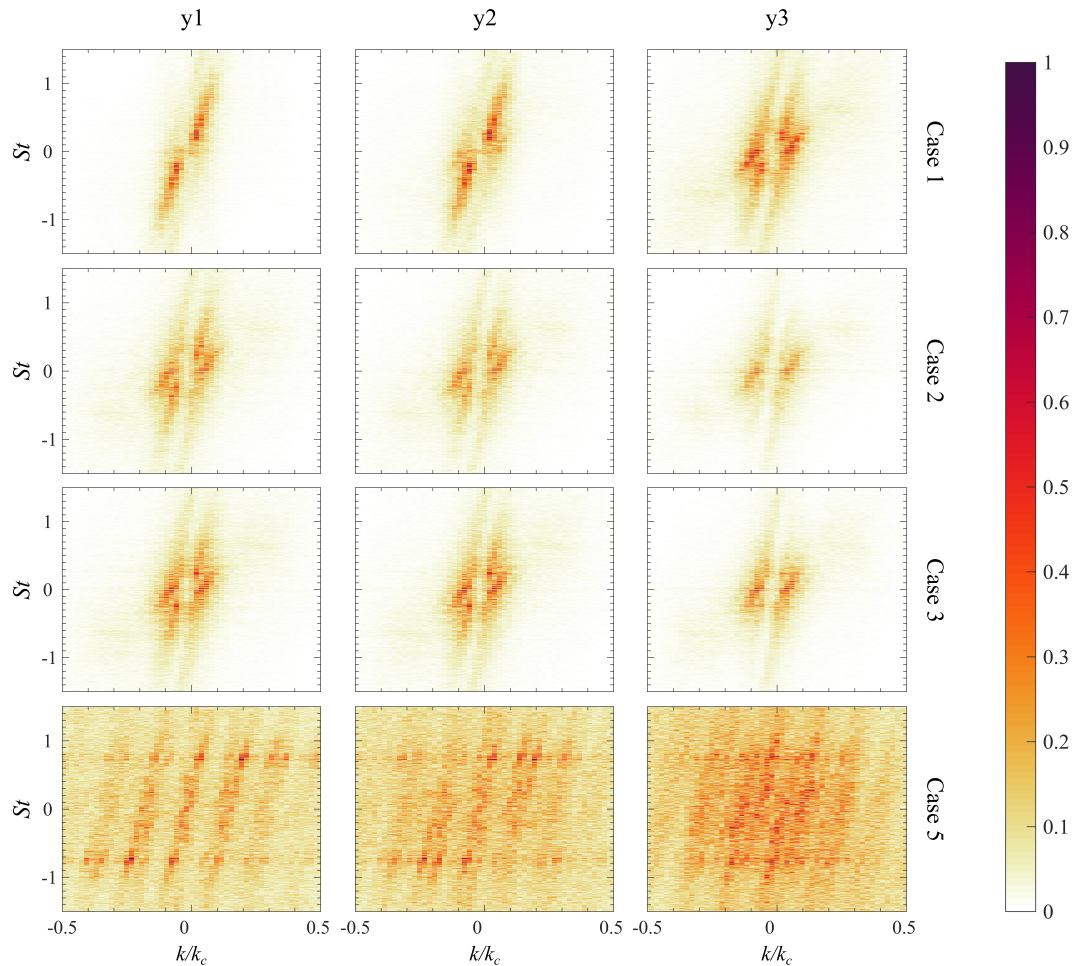
Figure 3.33: 2D FFT of *xt* plots of the upper surface of the hydrofoil at $\alpha = 0°$ and $Re = 1.0 \times 10^5$. Rows correspond to different cases and columns correspond to different *y*-locations (moving away from the body left to right).

To understand the origin of these additional diagonal lines, the flow is modeled by decomposing it into the free surface waves caused by the modulated contact line and the shedding vortices, as shown in figure 3.34. The free surface waves are still in the hydrofoil frame of reference, and hence their convection speed is zero. Thus the same wave profile is obtained at each *x*-location for all time in the shadowgraph visualization. The resulting *xt* plot would be characterized by vertical lines (slope of 1/0) as shown, with a spatial frequency $k_1 = 1/\lambda$ (where *k* represents a spatial frequency rather than the wavenumber here) set by the non-uniform wetting conditions. These waves can be expressed as time-independent waves of the form $A_1 \cos(2\pi k_1 x)$ in the *xt* frame. A two-dimensional FFT of the *xt* plot would only have two peaks located at $(\pm k_1, 0)$.

The vortices being shed move relative to the hydrofoil frame of reference at a

convection speed U_c. They are thus associated with not only a spatial frequency k_2 in the x-direction but a temporal frequency f_2 corresponding to the shedding frequency. The relationship between these two frequencies is set by the vortex convection speed, which is $U_c = f_2/k_2$. An xt plot of the vortices would show diagonal lines with slope $1/U_c$, corresponding to waves of the form $A_2 \cos(2\pi[f_2 t + k_2 x])$. A two-dimensional FFT of the xt plot would again result in only two peaks, now located at (k_2, f_2) and $(-k_2, -f_2)$.

If the effects of these two waves are simply added together, the xt plot shown at the top of figure 3.34 would be obtained, with the resulting FFT shown below. However, that is not what seen in the FFTs. In fact, the xt diagrams are characterized by wavy diagonal line (bottom of figure 3.34), suggesting that the standing waves modulate the amplitude of the vortex waves. The resulting waves would have the form $A_1 \cos(2\pi k_1 x) \cdot A_2 \cos(2\pi[f_2 t + k_2 x])$. The 2D FFT of such a modulated wave contains four peaks forming a quadrilateral of width $2k_1$ and height $2f_2$ The two peaks in the second and third quadrants are $2k_2$ apart, as are the two peaks in the first and fourth quadrant. These peak-pairs describe the dispersion relation corresponding to vortex shedding. Thus, the FFT shows two manifestations of the vortex dispersion relation located $2k_1$ from each other.

Figure 3.34 shows the xt plot for the upper surface of the ($\beta = 90°$, $\lambda = 11$mm) hydrofoil at the middle y_2-location for $Re = 7 \times 10^4$. As can be observed in the xt plot, the standing waves do not affect the entire window. Changing the model to account for this results in an FFT with three manifestations of the vortex shedding frequency, one of which is now centered about the origin. These are much like what is observed in the experimental FFTs.

As the free surface waves in experiments fluctuate in the hydrofoil frame of reference, the peaks observed in the experimental FFTs are not as clear as in the model presented. In addition, the finest spatial and temporal frequencies that can be resolved in the experimental FFTs are 0.33 m^{-1} (top and bottom windows) to 2.60 m^{-1} (wake) and 0.008-0.064 Hz, respectively. They are 0.15 m^{-1} and 0.099 Hz in the model. The coarser the resolution, the broader the peaks.

Thus, it would seem that the standing waves modulate the vortices being shed off the hydrofoil. The frequency of vortex shedding does not appear to have been affected, however. Furthermore, the effects this modulation has on the vortex strength cannot be reported as the shadowgraph data do not provide that information.
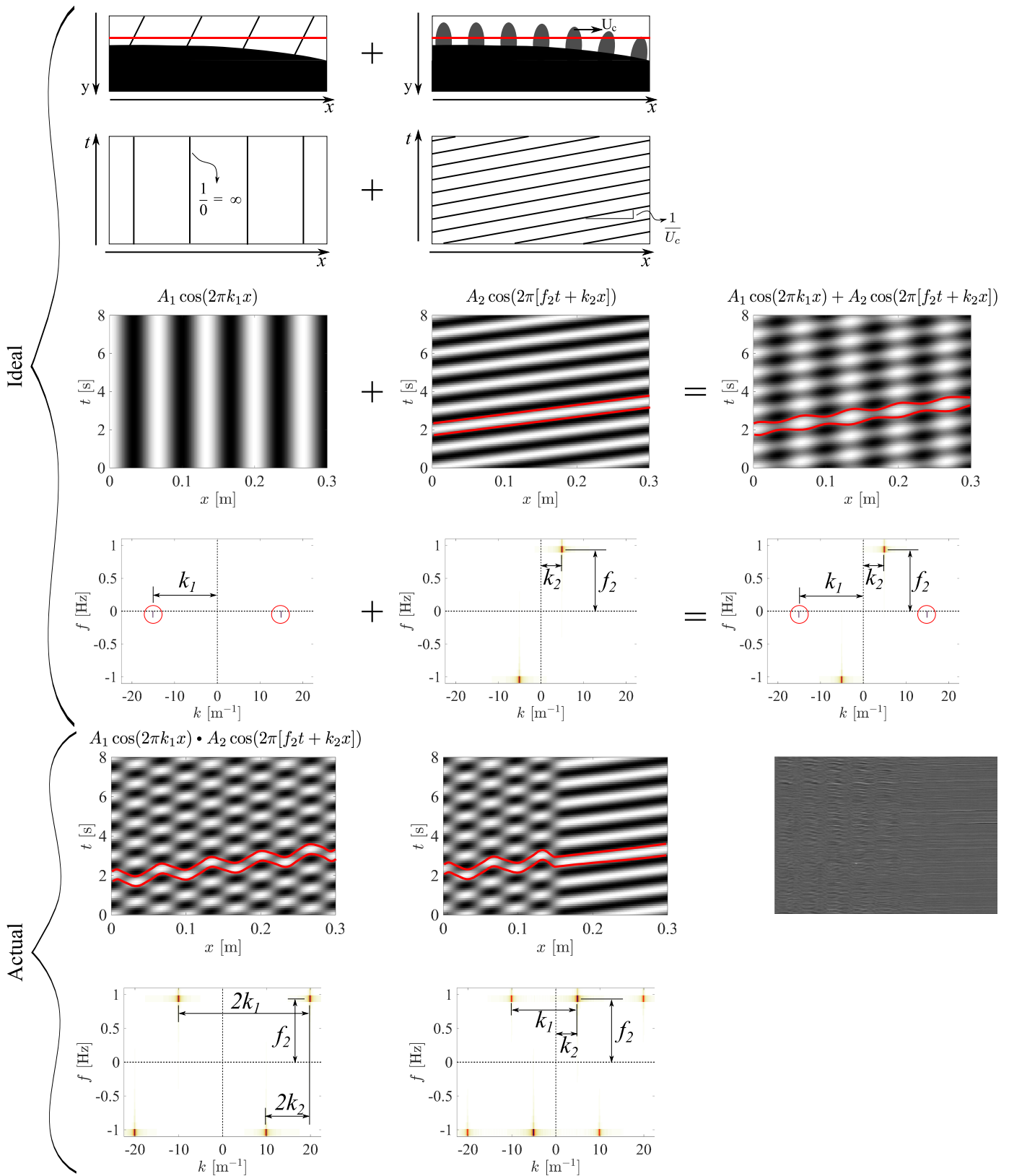
Figure 3.34: Modeling the interaction between vortex shedding and standing waves generated on surfaces with non-uniform wetting properties.

Nonetheless, conclusions can be drawn about the surface waves: additional manifestations of the vortex shedding dispersion relation (the additional diagonal lines in the FFTs) become more pronounced as Reynolds number increases, as evidenced by the increased FFT values for $Re = 1.0 \times 10^5$. In addition, the lines becomes less sharp when moving away from the body. That is, the surface waves are more apparent closer to the body where they originate and become more pronounced with increasing Reynolds number.

Broader peaks are also found in the upper surface's FFT for the half-hydrophobic hydrofoil (case 2) at all y-locations for the two higher Reynolds numbers. These peaks are similar to the FFT signatures of the radial waves discussed previously. However, the half patterned case with $\beta = 0°$ and $\lambda = 11$mm does not show these signatures as strongly for $Re = 7 \times 10^4$, suggesting that the parallel bands affect the generation of these radial waves. As the radial waves seem to be generated at the same location as vortices, the parallel bands may affect vortex shedding as well. In addition, the shadowgraph images of the bow wave illustrate that free surface waves are generated for this case wherever the free surface crosses a hydrophobic band (see figures 3.17 and 3.18), particularly at high Reynolds numbers. These surface waves may either not be apparent at these lower Reynolds numbers under study for FFT analysis or, as they are not periodic in nature, may appear as noise rather than distinct features in the FFTs.

Because the flow behavior on the upper surface is modified by asymmetric wetting conditions for the half-hydrophobic and half-patterned cases, the wake should also be modified, specifically at the y_1 location which is closest to the hydrofoil's coated upper surface. From the FFTs for the wake, presented in figures 3.35, 3.36, and 3.37, it is clear that the lowest Reynolds number show no appreciable difference between cases, similar to what was found for the upper surface FFTs. However, as Reynolds number increases, the appearance of secondary diagonal lines are observed in the FFTs for case 5. These secondary lines are more obvious at the y_1 location, which is closest to hydrofoil's coated upper surface, and are faint at the y_3 location which is closest to the hydrofoil's unmodified hydrophilic surface. They become more apparent at all y-locations as Re increases. This last observation suggests that the free surface waves created by the modulated contact line in case 5 are widespread downstream of the hydrofoil and begin to affect the flow field below the centerline as the Reynolds number increases. Unfortunately, the strong frequency response of these surface waves makes isolating vortex shedding phenomena difficult.
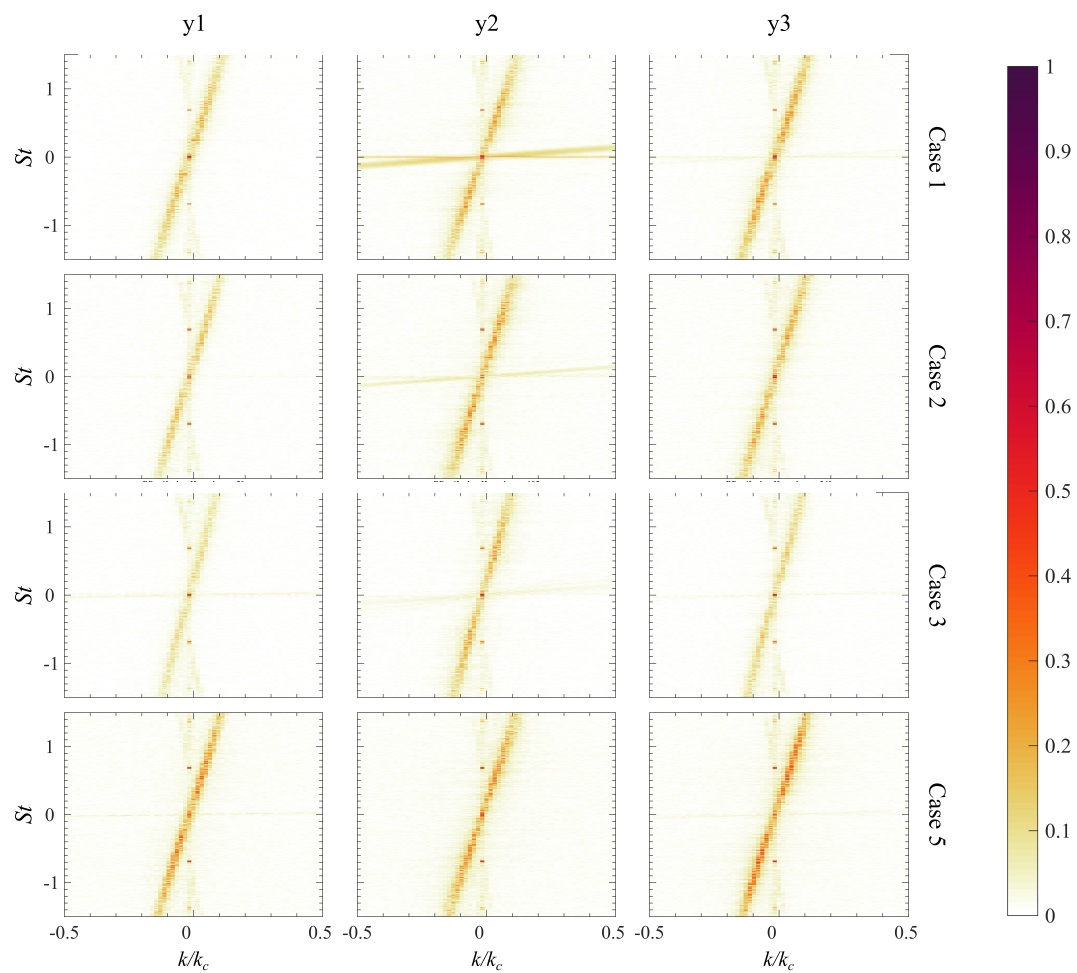
Figure 3.35: 2D FFT of *xt* plots of the wake of the hydrofoil at $\alpha = 0°$ and $Re = 4 \times 10^4$. Rows correspond to different cases and columns correspond to different *y*-locations: y_1 is closer to the upper surface of the hydrofoil, y_2 is the middle of the flow field, and y_3 is closer to the lower surface of the hydrofoil.
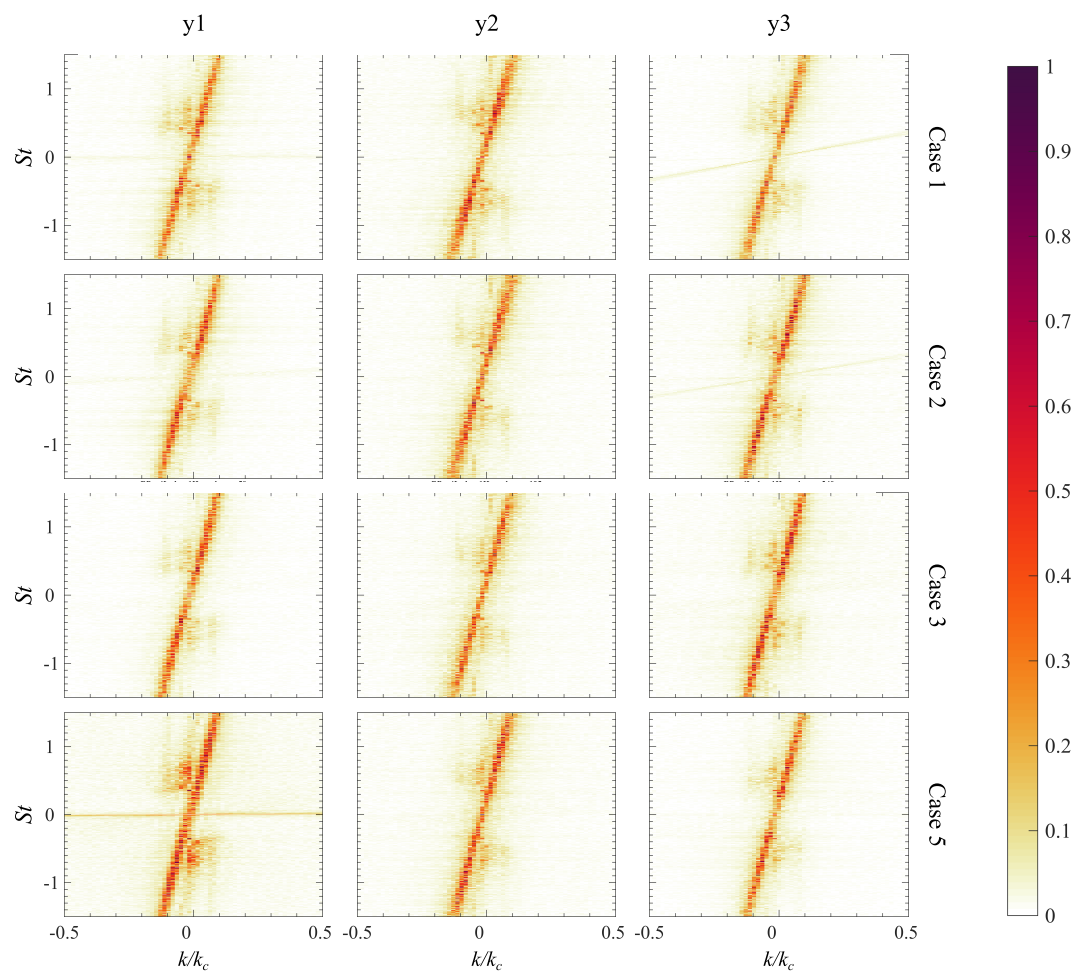
Figure 3.36: 2D FFT of *xt* plots of the wake of the hydrofoil at $\alpha = 0°$ and $Re = 7 \times 10^4$. Rows correspond to different cases and columns correspond to different *y*-locations: y_1 is closer to the upper surface of the hydrofoil, y_2 is the middle of the flow field, and y_3 is closer to the lower surface of the hydrofoil.
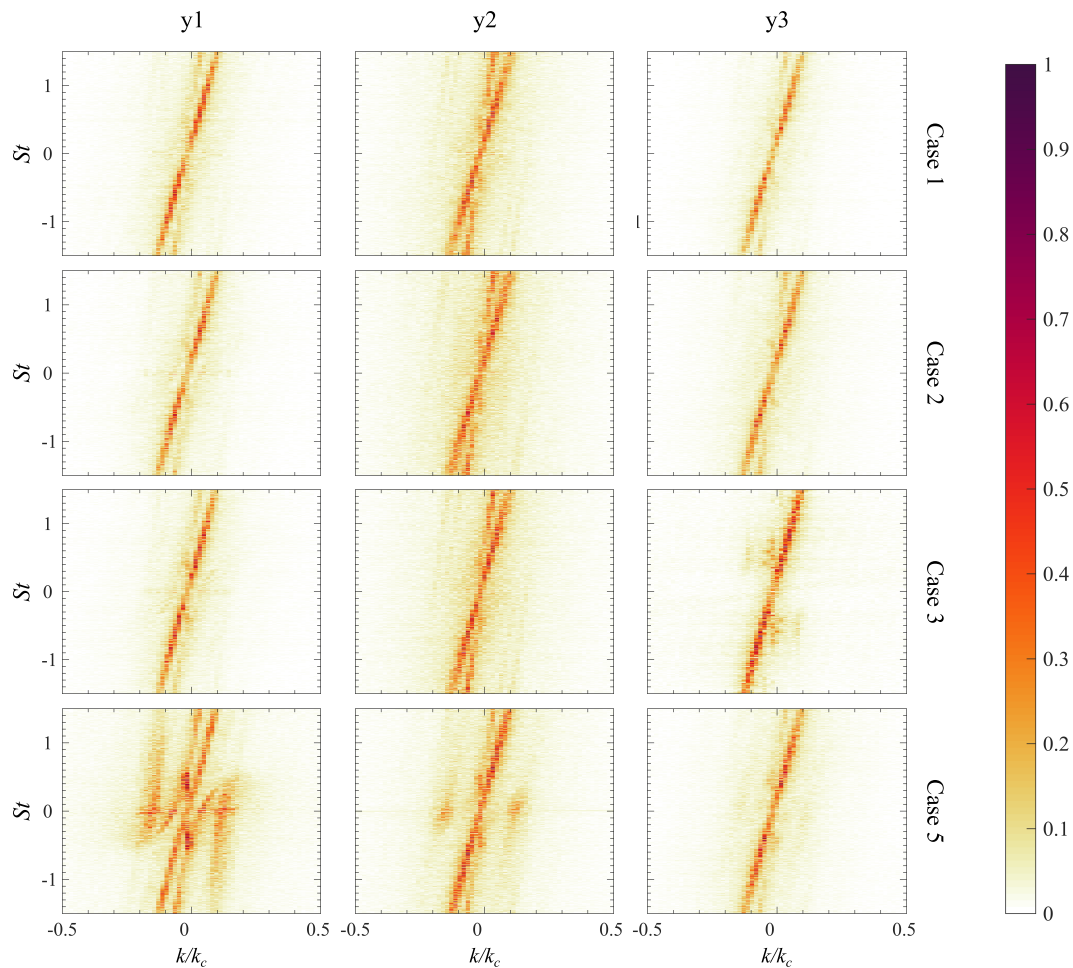
Figure 3.37: 2D FFT of *xt* plots of the wake of the hydrofoil at $\alpha = 0°$ and $Re = 1.0 \times 10^5$. Rows correspond to different cases and columns correspond to different *y*-locations: y_1 is closer to the upper surface of the hydrofoil, y_2 is the middle of the flow field, and y_3 is closer to the lower surface of the hydrofoil.

It can be concluded that asymmetric wetting conditions alone have limited effect on free surface flow behavior and apparent vortex shedding at these three lowest Reynolds numbers studied. However, coupling asymmetric wetting conditions with non-uniform wetting properties (i.e., large-scale wettability heterogeneities) results in large modification of the free surface if alternating hydrophilic and hydrophobic bands oriented perpendicular to the flow ($\beta = 90°$) are used. These modifications are widespread in the flow field, affecting not only flow near the non-uniform surface but also flow in the wake. These modifications become more widespread and pronounced as Reynolds number increases. The strong presence of these free surface modifications, which are due to free surface waves originating from a modulated contact line, make isolating vortex shedding phenomena difficult. Coupling this

with the lack of velocity information from the shadowgraph technique, the effect these free surface modification have on vortex strength remains unclear.

Vortex Convection Speed

The approximate convection speed of the vortices being shed off the hydrofoil can be calculated in order to determine if asymmetric wetting conditions and non-uniform wetting properties affect this measure. In order to do this, recall that the main diagonal line characterizing the 2D FFT plots corresponds to the dispersion relation of the vortex shedding phenomenon. The slope of this line thus corresponds to the group velocity $c_g = \partial f / \partial k$, while the (f, k) value of the dominant peak gives the characteristic phase velocity $c_p = f/k$ of the vortices. As the dispersion relation is given by a linear line in the current experiment, the group and phase velocities of the vortices should be the same. Therefore only one of the two needs to be computed.

The phase velocity for each case is obtained at all three y-locations in every window of interrogation by selecting the most dominant peak in the 2D FFT plot and computing f/k for that point. These speeds are then averaged together for each window. The average non-dimensionalized convection speed U_c/U_∞ for each window plus the associated uncertainty (given by $\Delta U_c = \sqrt{(U_c \Delta f / f)^2 + (U_c \Delta k / k)^2}$) are presented in figure 3.38.

The vortex convection speeds in the windows of interrogation near the upper (circles) and lower (triangles) hydrofoil surfaces are around half the free stream velocity for all cases. However, the convection speed in the wake (diamonds) is close to the free-stream velocity. This may be due to the boundary layer affecting the vortex convection speed along the lower and upper surfaces. As shown in figure 3.22, the boundary layer thickness (as estimated in appendix B) extends to the y-locations currently being studied. The boundary layer will on average have a flow speed of $U_\infty/2$ as its flow speed varies from 0 m/s near the surface (no slip boundary condition) to U_∞ at a distance δ_{99} from the surface, where δ_{99} is the boundary layer thickness.

As far as the effect of asymmetric wetting conditions on convection speed, there are no clear trends in the data. Also note that any difference between the asymmetrically coated cases and the control case fall within measurement uncertainty. Thus, it does not appear that asymmetric wetting conditions nor non-uniform wetting properties affect the convection speed of the shed vortices.
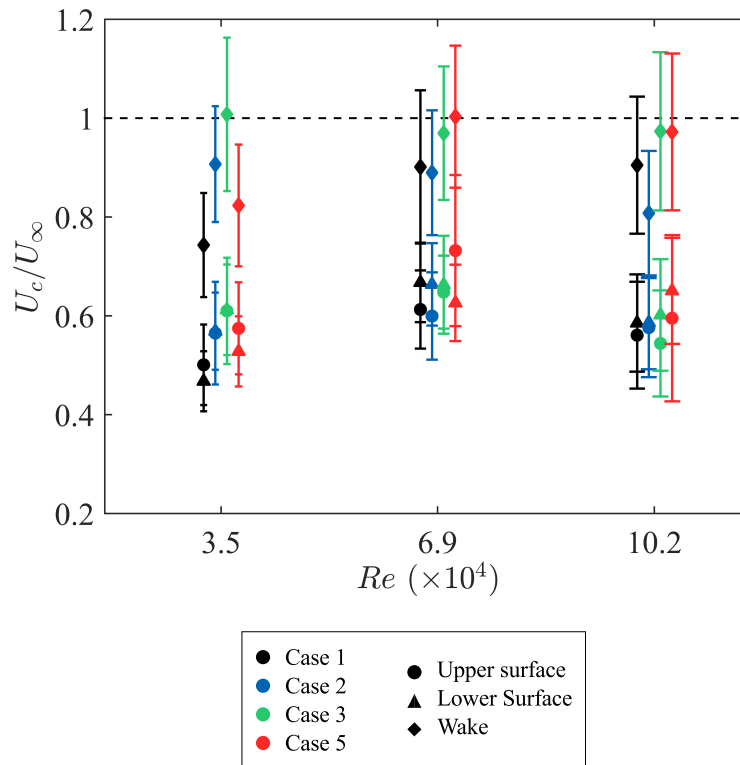
Figure 3.38: Convection speed of free surface flow features observed in the 2D FFT plots. Colors represent the different experimental cases. Symbols represent the FFT window the slope corresponds to. Error lines represent the uncertainty in the velocity calculation.

3.5.3 Free Surface Separation Analysis

As mentioned earlier, shadowgraph videos reveal that asymmetric wetting conditions cause free surface separation to occur, on average, earlier on one side than the other. This asymmetric flow separation differs from von Karman shedding, which is asymmetrical at any moment in time but symmetrical on average.

In order to study this asymmetric separation, 250 sequential frames are analyzed from video captured for each experimental case. Only the three highest Reynolds numbers ($Re = 2.4, 2.8, 3.1 \times 10^5$) are studied in this analysis, as flow separation is either not evident or hard to define consistently at lower Reynolds numbers. The separation point on the upper and lower surfaces of the hydrofoil are picked out manually for every other frame, as shown in figure 3.39.

The distance along the hydrofoil from the trailing edge to the point of separation is found by first projecting the cluster of 125 points onto the hydrofoil as some of the points are located slightly off the body. These points are projected onto the body by finding the (x, y) coordinate of the hydrofoil that is closest to the point in question.
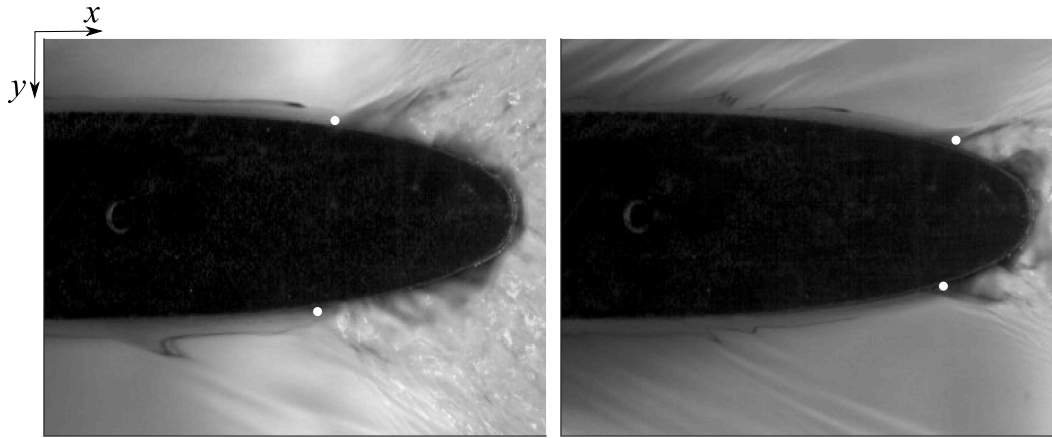
Figure 3.39: Selecting flow separation points (in white) on the uniformly hydrophilic hydrofoil (case 1) at $\alpha = 0°$ for $Re = 2.4 \times 10^5$ (left) and $Re = 3.1 \times 10^5$ (right). Flow is left to right.

The hydrofoil curve is given by

$$y(x) = 0.6c \left[0.2969 \sqrt{\frac{x}{c}} - 0.1260\frac{x}{c} - 0.3516 \left(\frac{x}{c}\right)^2 + 0.2843 \left(\frac{x}{c}\right)^3 - 0.1015 \left(\frac{x}{c}\right)^4 \right]$$

with x ranging from 0 to the chord length c (Abbott and Doenhoff, 1959).

The distance from the trailing edge is given by

$$s = \int_{x_1}^{x_2} \sqrt{1 + \left(\frac{dy}{dx}\right)^2} \, dx, \tag{3.20}$$

where x_1 is the x-location of the trailing edge (c) and x_2 is the x-location of the projected point. The separation point distance s for each experimental case is presented in figure 3.40.

Looking at the control case (in black) first, since both sides of the hydrofoil are uniformly hydrophilic in this case, the flow is expected to behave similarly on either side. Therefore, free surface flow separation should occur at approximately the same location on the upper and lower surfaces. That is indeed what is observed. In addition, the free surface flow separation is delayed as Reynolds number is increased. That is, s decreases and the location of separation approaches the trailing edge with increasing Reynolds number. The stability of the free surface flow separation point also increases as Re increases (i.e., the boxplots and whiskers become smaller).
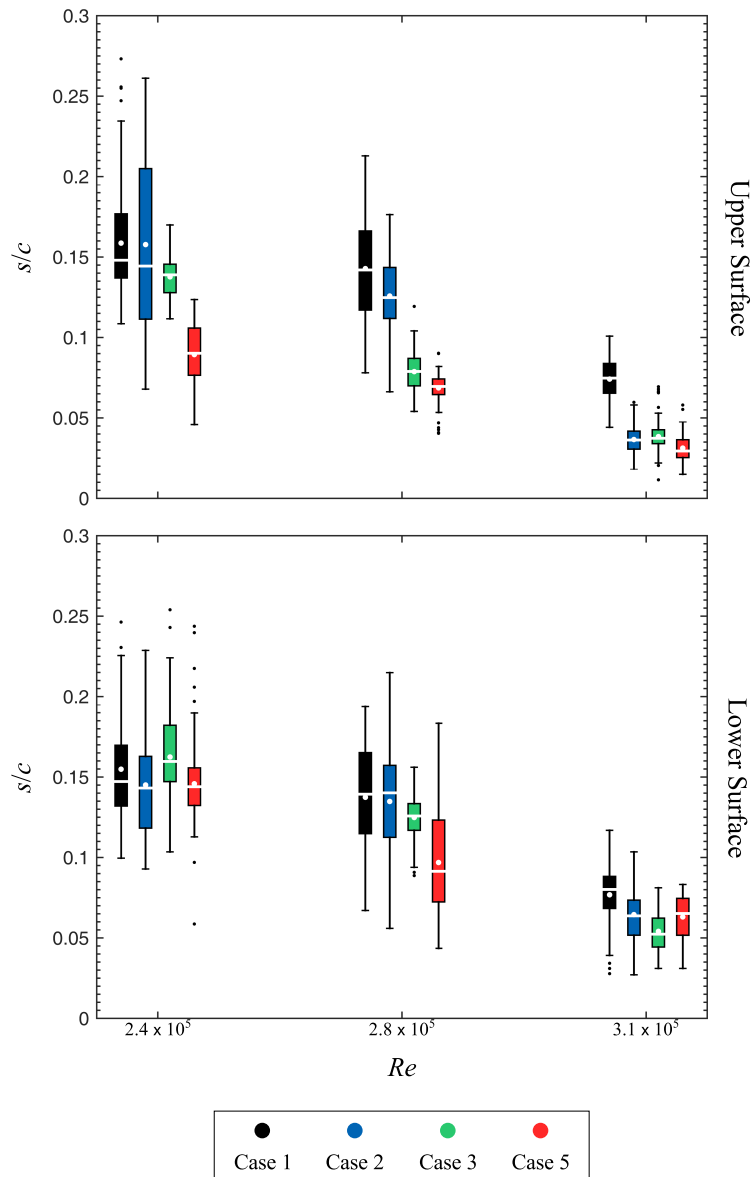
Figure 3.40: Boxplots of non-dimensionalized separation point location s/c on the upper surface (top) and lower surface (bottom) of the hydrofoil as a function of Reynolds number for $\alpha = 0°$. White lines give the data's median. White dots give the average. Box limits represent the first and third quartiles (25th and 75th percentiles) of the data. Whiskers represent approximately 99.3 % data coverage. Black dots are outliers. Colors correspond to different experimental cases.

The asymmetrically coated cases can now be compared to the control case. Free surface flow separation on the lower surface is found to occur around the same location for all cases. This is expected as the lower surface of the hydrofoil is hydrophilic for all cases studied. There is a slight delay (smaller *s*) in free surface

flow separation at higher *Re* on the lower surface for hydrofoils that have asymmetric wetting conditions. However, the overall range of the data is comparable as is the stability (size of the box and whiskers) for the free surface separation point.

A greater difference in the free surface flow separation location between the control case and the asymmetrically coated cases is found for the upper surface (the manipulated side). In general, free surface flow separation is delayed on the asymmetrically coated cases, with the half patterned ($\beta = 90°$, $\lambda = 11$mm) case showing the greatest delay and the half hydrophobic case (in blue) showing the least amount of change (particularly at $Re = 2.4 \times 10^5$). Likewise, the half patterned cases show increased separation point stability. The half hydrophobic case does not change the stability much at the highest Reynolds numbers and actually appears to decrease stability at the lower Reynolds number.

Thus, it can be concluded that introducing asymmetric wetting conditions on a surface-piercing body changes the free-surface flow separation point location and behavior. Coupling asymmetric wetting conditions with non-uniform wetting properties (i.e., large-scale wettability heterogeneities) amplifies the effect and leads to delayed free-surface flow separation and increased stability of the flow separation point, particularly if the non-uniform wetting conditions are in the form of alternating hydrophilic and hydrophobic bands oriented perpendicular to the flow direction ($\beta = 90°$). Note that while free-surface separation is affected, no conclusions can be drawn on whether the bulk flow's separation is affected as the shadowgraph data only measures free surface behavior. Different experimental techniques need to be employed to investigate how free surface effects modify bulk flow properties.

3.6 Comparison to Naval Ships

The side force due to asymmetric wetting conditions can be compared to typical forces on ships. The Arleigh Burke class of destroyers is outfitted with four General Electric gas turbines, providing around 78,000 kW of power in total (*America's Navy: U.S. Navy Ships*). As power is given by

$$P = FU_\infty, \tag{3.21}$$

and the maximum speed of this class of destroyers is about 15.5 m/s (*America's Navy: U.S. Navy Ships*), the force generated by the turbines is on the order of 10^6 N. The largest side force generated by asymmetric wetting conditions is around 0.1 N for the $\beta = 90°$, $\alpha = 0°$, $\lambda = 22$ mm, and $U \approx 0.6$ m/s. Scaling this up to ship

dimensions, based on ship length, gives a force of around 50 N. This is around five orders of magnitude smaller than the thrust generated by the Arleigh Burke's turbines. It should be noted, however, that the power and force reported for the turbines represents thrust and not side force. The amount of side force the turbines could generate is dependent on the rudder used to turn the ship and the resulting yaw moment. It will therefore be less than the maximum reported value. In addition, the current experiments are run at much lower Reynolds numbers than ships, affecting the frictional resistance (or drag) and the form resistance.

Furthermore, if the Froude number between experiments and full-scale conditions is around the same, the wave-making resistance should be approximately the same for both as long as the model is geometrically similar (Carlton, 2007). As the current model has a draft size (h) that is about four times greater than a comparable Arleigh Burke destroyer model, this statement no longer holds, making scaling up the forces difficult.

The force coefficient $C_F = F/(1/2\rho U_\infty^2 S)$ can nonetheless be computed and compared. This type of non-dimensionalization of the force accounts for some of the Reynolds number effects as well as model scale effects. For the current experiments S is about 0.02 m^2 and $U_\infty = 0.6$ m/s during maximum side force generation. For the Arleigh Burke destroyers, S is about 1300 m^2 and $U_\infty \leq 15.5$ m/s (see appendix D). The result is force coefficients on the order of 10^{-2} for both cases. While the force coefficients are comparable using this type of force non-dimensionalization, the fact that the models are not geometrically similar means direct comparisons such as this may be misleading.

In addition, as was previously mentioned, the side force in experiments is due to wetting conditions (and hence surface tension effects). Thus, the force could also be non-dimensionalized by γL where $L = c = 30$ cm for the hydrofoil used in experiments and L is about 142 m for the Arleigh Burke destroyers. The resulting force coefficients are on the order of 10^5 for the destroyer and 10^1 for the hydrofoil experiment. This type of non-dimensionalization neglects inertial effects due to the vastly different Reynolds number regimes the two cases are run at, however.

Which measure or non-dimensionalization is most appropriate depends on how much asymmetric wetting conditions affect the bulk flow. As no data has been collected with regards to the bulk flow, the effect remains unknown.

The side force due to asymmetric wetting conditions can also be compared to bow

thrusters, which are used at low speeds to help ships maneuver at port. Bow thrusters generate side forces, but as the side force is located at the bow of the ship, the result is a turning moment about the ship's center of mass rather than a direct transverse force (i.e. the ship turns rather than shifting laterally). These thrusters, which become less efficient with increased speed, are used at berthing speeds that are typically around 5 cm/s (Roubos, Groenewegen, and Peters, 2017), resulting in $Re \approx 8 \times 10^6$ and $Fr \approx 10^{-3}$ for Arleigh Burke destroyers.

Bertram (2012) reports that under these conditions bow thrusters are capable of generating 80-120 N/m^2 of force per underwater area. This is only one order of magnitude greater than the 5 N/m^2 asymmetrically coated surfaces are capable of generating for $Fr = 0.35$ and $Re = 2.0 \times 10^5$. The force per unit contact line, however, is three orders of magnitude greater for bow thrusters than asymmetrically coated surfaces. Note, however, that the Froude numbers and Reynolds numbers are not matched between the berthing conditions bow thrusters operate at and the conditions experiments were run at.

The above comparison highlights the fact that without a geometrically similar model, scaling up the forces from experiments to full-scale conditions is difficult. Nonetheless, it would seem that the current technique is not appropriate for the much higher Reynolds number flows that naval ships operate at. It may, however, function in berthing conditions when ships operate at much lower flow speeds. Experiments with larger models, which would simultaneously allow for testing of higher Reynolds numbers and lower Froude numbers that are closer to actual ship conditions, need to be conducted in order to clarify the feasibility of this application.

3.7 Concluding Remarks

In summary, asymmetric wetting conditions on a surface-piercing body are capable of direct transverse-force generation, as hypothesized. In addition, coupling asymmetric wetting conditions with non-uniform wetting properties leads to greater transverse-force generation. These surfaces are capable of generating around 5 N/m^2 of transverse force per underwater area for $Fr = 0.35$ and $Re = 2.0 \times 10^5$. This is only 16 to 24 times less than values reported for bow thrusters (0.08- 0.12 kN/m^2) by Bertram (2012).

However, as was mentioned previously, bow thrusters, which are mainly used when the vessel is maneuvering at port, operate at Reynolds numbers that are one to two orders of magnitude greater than in the current experiment and Froude numbers that

are two orders of magnitude smaller. As the hydrofoil model used in this work is not geometrically similar to naval ships due to the submerged depth being much larger than most ship drafts, it is not certain how the direct transverse-force generation observed in experiments will scale to full-scale ship models. However, because the transverse-force generation is caused not by inertial or gravitational effects, which the draft affects, but by surface tension effects occurring at the free surface, it is possible that the current results are independent of the hydrofoil submerged depth as long as the Froude number, ship wetted length and beam (which determine the length of the contact line) are matched between models.

We must also be wary of the higher (four orders of magnitude greater) Reynolds number ships operate at in open sea as the greater the Reynolds number the lower the direct- transverse force generation is in the current experiments. Thus, it appears the current technique is more suitable for berthing applications than open sea applications.

More experiments must be conducted to further elucidate trends in the force analysis, particularly with regards to the effect of the pattern wavelength. A more sensitive force sensor with smaller noise should also be used in order to observe more clearly what happens at the lower Froude and Reynolds numbers. More band widths should also be tested, including in the $\beta = 0°$ case where no such testing has been conducted thus far.

Another avenue to explore is the use of a torque sensor to measure any yaw-moments created by the asymmetric wetting conditions, as generating yaw-moments would also help ease turning maneuvers ships make. It would additionally be interesting to know if the resistance or drag on the hydrofoil is modified by the changes in free surface phenomena as there is great interest in the naval community to reduce the drag on vessels and improve their efficiency (see Mäkiharju, Perlin, and Ceccio, 2012; Ceccio, 2010).

In addition to direct-transverse force generation, non-uniform wetting properties were also found to cause an appreciable change in the flow field around surface-piercing bodies, particularly when the non-uniform wetting properties take the form of alternating hydrophilic and hydrophobic bands that are oriented perpendicular to the flow direction ($\beta = 90°$). This type of non-uniform wetting condition generates far reaching surface capillary-gravity waves with wavelengths set by the pattern's band width. In addition, this non-uniform wetting condition delays free surface flow separation and stabilizes the separation point. Non-uniform wetting conditions with

bands aligned to the flow direction ($\beta = 0°$) also delay free surface flow separation and stabilize the separation point, however they do not generate such wide-spread free surface waves. Additionally, neither non-uniform wetting condition leads to an apparent change in vortex shedding behavior (neither in the shedding frequency nor the convection speed) at the lower Reynolds numbers analyzed, though these results are muddled by the generation of free surface waves and would require further experiments (using different measurement techniques) to be confirmed. The effects on vortex strength also remain open to investigation.

Different flow visualization techniques are required to understand what happens in the middle range of Reynolds numbers studied as neither the flow separation or frequency analyses deployed are easily adaptable to the shadowgraph images captured in the current experiments over this Reynolds number range. One such technique is the free surface gradient detector method, as described by Zhang, Dabiri, and Gharib (1996). This technique is like a color Schlieren, creating a one-to-one correspondence between color and slope of the free surface deformation. The slopes can then be integrated to recover the free surface elevation profile and study how the bow waves and other free surface phenomena are affected by asymmetric wetting conditions. This technique, like the ones used in the current experiments, however, is limited to capturing free surface phenomena. Another technique, such as particle imaging velocimetry (PIV), should be used to observe flow dynamics underneath the free surface. If using PIV, care must be taken to seed the flow with particles that do not damage the hydrophobic coating or change the free surface properties. (It is for this reason that PIV was not employed in the current experiments). Suggestions have been made to use hydrogen bubbles as the seeding particle.

As a final note, these non-uniform surfaces may work more effectively in bubbly flows, such as those ships encounter. The hydrophobic bands should trap air bubbles, allowing the water to minimize its contact with the repulsive surface. Thus, riblet-like structures could form in the flow, which would affect the forces acting on the body. These riblet-like structures would likely affect the drag of the ship more than the transverse force. However, by creating an imbalance in the drag on either side of the body, a moment could be generated. This moment could also help ships maintain heading and track when in oblique seas or maneuver when passing other vessels, just as the transverse-force-generation idea investigated in this chapter could.

C h a p t e r   4

SUMMARY AND FUTURE WORK

To summarize, the effects of large-scale (ranging from 2-25 mm wide by and tens of centimeters long) wettability heterogeneities have been shown to largely impact contact line dynamics. These wettability heterogeneities are introduced as alternating hydrophilic and hydrophobic bands oriented at an angle β with the flow direction. Their effect has been studied on thin film flows, in which the contact line appears at the edges of the film, as well as in naval-like contexts, in which the contact line appears along the entire perimeter of a surface-piercing hydrofoil.

4.1   Conclusions

With regards to thin films (for *Re* of 50 -1200) flowing over inclined plates,

- alternating hydrophilic and hydrophobic bands parallel ($\beta = 0°$) to the flow direction
  - Tune the wavelength of the film's fingering instability, occurring at low Reynolds numbers, to the pattern size;
  - Force the flow to follow hydrophilic tracks. The creation of preferential tracks is also found for intermediate band orientation angles when below a critical value. This critical band angle is a function of the flow rate Q and the plate's inclination angle α as well as the pinning forces at the contact line, which are functions of the advancing and receding contact angles;
  - Induce "digital jumps," reminiscent of liquid bridges, from one hydrophilic track to another for small band sizes.

- alternating hydrophilic and hydrophobic bands perpendicular ($\beta = 90°$) to the flow direction
  - inhibit the Rayleigh-Plateau-like instability, which occurs at low Reynolds numbers and leads to the rivulet breaking-up into droplets;
  - dampen finger oscillations (leading to the so-called pendulum regime) that occur at larger Reynolds numbers by stabilizing the contact line;
  - elongate braids occurring at higher Reynolds numbers;

– modulate the contact line, leading to the development of small-scale roller structures (a few mm in height) at every hydrophilic-hydrophobic interface at higher Reynolds numbers;

– affect the air entrainment process caused by the large rollers formed when the fluid sheet first converges on the inclined plate;

– promote air bubble capture on hydrophobic bands, allowing for coalescence of entrained bubbles at larger Reynolds numbers.

With regards to flow around a surface-piercing, symmetric hydrofoil (for Re of 4×10^4 to 3.1×10^5), large-scale wettability heterogeneities

- generate direct-transverse forces, as hypothesized. Furthermore, coupling asymmetric wetting conditions with non-uniform wetting properties leads to larger transverse force generation than asymmetric wetting conditions alone. These wetting conditions can be thought of as two different scales of heterogeneities: one of scale $L/2$, where L is the perimeter of the body, and one of scale d, which is the width of the alternating hydrophilic and hydrophobic bands;

- modulate the contact line, creating widespread free-surface waves, which persist at higher Reynolds numbers;

- delay and stabilize the free-surface separation point.

4.2 Contributions

This thesis has contributed to the scientific community by

- studying pendulums and braids arising from a water sheet (i.e., a rectangular jet). Previous studies found in the literature have looked exclusively at round jets;

- studying large-scale changes in wettability (several mm to cm) in dynamic contexts at higher Reynolds numbers ($Re \sim 10^1$ to 10^5) than hereto considered. Previous studies in the literature concern microfluidic ($Re < 1$) or static applications with wettability heterogeneities that are microscopic or on the order of one millimeter;

- studying direct-transverse force generation via changes in wetting properties. No literature currently exists on this topic.

4.3 Future Work

Although this thesis has demonstrated that large-scale heterogeneities in wetting properties can modify thin film flows as well as flow around surface-piercing bodies,

- the applicability to the higher Reynolds numbers obtained in actual naval flows remains unclear. Whereas the Froude number in the hydrofoil experiments is on the same order as naval ships, facility limitations and practical concerns have limited the current study to Reynolds numbers of $O(10^4 - 10^5)$, which are several orders of magnitude smaller than the $Re \sim O(10^9)$ naval ships operate at in open sea and one order of magnitude smaller than the Reynolds number ships operate at in berthing conditions at port. Therefore, higher Reynolds number experiments should be conducted to elucidate the feasibility of contact line modification via this method for naval applications, particularly in berthing conditions which appear more promising than open sea applications;

- the behavior of the bulk flow (below the free surface) remains unknown. New measurement techniques must be used to understand how vortex shedding, flow separation, and other flow behavior are impacted in the bulk flow and to clarify whether the observed effects are responsible for direct side-force generation, as free-surface effects alone do not seem to account for these changes;

- the effect of bubbly flows (such as those encountered at sea) or active air injection in the bulk flow should be examined. The observation of bubble entrapment in the thin film experiments naturally raises questions regarding the promotion of bubble entrapment for the creation of underwater riblet-like structures in naval contexts. These structures could be used to support air films for drag reduction as well as to generate yaw moments if asymmetrically applied;

- the study of alternate wettability patterns (such as patches or bands of varying sizes) should be explored in order to determine if optimal designs exist for different scenarios.

BIBLIOGRAPHY

Abbott, I. H. and A. E. von Doenhoff (1959). *Theory of wing sections: Including a summary of airfoil data*. Dover Publications.

America's Navy: Momsen (DDG 92). `http://www.navy.mil/view_image.asp?id=17183`. Accessed: 2017-04-13.

America's Navy: U.S. Navy Ships. `http://www.navy.mil/navydata/our_ships.asp`. Accessed: 2017-04-13.

America's Navy: USS Enterprise (CVN 65). `http://www.navy.mil/view_image.asp?id=29548`. Accessed: 2017-04-13.

America's Navy: USS Freedom (LCS 1). `http://www.navy.mil/view_image.asp?id=66466`. Accessed: 2017-04-13.

America's Navy: USS Nimitz (CVN 68). `http://www.navy.mil/view_image.asp?id=44626`. Accessed: 2017-04-13.

Bertram, V. (2012). *Practical Ship Hydrodynamics*. Second Edition. Oxford: Butterworth-Heinemann. Chap. 6, pp. 241–298.

Bico, J., C. Marzolin, and D. Quéré (1999). "Pearl Drops". In: *Europhysics Letters* 47.2, pp. 220–226.

Bico, J., C. Tordeux, and D. Quéré (2001). "Rough Wetting". In: *Europhysics Letters* 55.2, pp. 214–220.

Birnir, B., K. Mertens, V. Putkaradze, and P. Vorobieff (2008). "Meandering Fluid Streams in the Presence of Flow-Rate Fluctuations". In: *Physical Review Letters* 101.11, pp. 114501–114504.

Bobba, K. M. (2004). "Robust Flow Stability: Theory, Computations and Experiments in Near Wall Turbulence". PhD thesis. California Institute of Technology.

Brinkmann, M. and R. Lipowsky (2002). "Wetting Morphologies on Substrates with Striped Surface Domains". In: *Journal of Applied Physics* 92.8, pp. 4296–4306.

Bush, J. W. M. and A. E. Hasha (2004). "On the Collision of Laminar Jets: Fluidic Chains and Fishbones". In: *Journal of Fluid Mechanics* 511, pp. 285–310.

Carlès, P., Z. Huang, G. Carbone, and C. Rosenblatt (2006). "Rayleigh-Taylor Instability for Immiscible Fluids of Arbitrary Viscosities: A Magnetic Levitation Investigation and Theoretical Model". In: *Physical Review Letters* 96.10, p. 104501.

Carlton, J. S. (2007). *Marine Propellers and Propulsion*. Second Edition. Oxford: Butterworth-Heinemann. Chap. 6, pp. 285–318.

Cassie, A. B. D. and S. Baxter (1944). "Wettability of Porous Surfaces". In: *Transactions of the Faraday Society* 40, pp. 546–551.

Ceccio, S. L. (2010). "Friction Drag Reduction of External Flows with Bubble and Gas Injection". In: *Annual Review of Fluid Mechanics* 42, pp. 183–203.

Chuang, Z. and S. Steen (2012). "Speed Loss Due to Seakeeping and Maneuvering in Zigzag Motion". In: *Ocean Engineering* 48, pp. 38–46.

Clanet, C. and J. C. Lasheras (1999). "Transition from Dripping to Jetting". In: *Journal of Fluid Mechanics* 383, pp. 307–326.

Cobelli, P. J., A. Maurel, V. Pagneux, and P. Petitjeans (2009). "Global Measurement of Water Waves by Fourier Transform Profilometry". In: *Experiments in Fluids* 46, pp. 1037–1047.

Couvreur, S. and A. Daerr (2012). "The Role of Wetting Heterogeneities in the Meandering Instability of a Partial Wetting Rivulet". In: *Europhysics Letters* 99, p. 24004.

Cubaud, T. and M. Fermigier (2004). "Advancing Contact Lines on Chemically Patterned Surfaces". In: *Journal of Colloid and Interface Science* 269, pp. 171–177.

Dettre, R. H. and R. E. J. Johnson (1965). "Contact Angle Hysteresis. IV. Contact Angle Measurements on Heterogeneous Surfaces". In: *Journal of Physical Chemistry* 69.5, pp. 1507–1515.

Diez, J. A. and L. Kondic (2001). "Contact Line Instabilities of Thin Liquid Films". In: *Physical Review Letters* 86.4, pp. 632–635.

Drelich, J., J. D. Miller, and R. J. Good (1996). "The Effect of Drop (Bubble) Size on Advancing and Receding Contact Angles for Heterogeneous and Rough Solid Surfaces as Observed with Sessile-Drop and Captive-Bubble Techniques". In: *Journal of Colloid and Interface Science* 179, pp. 37–50.

Eral, H. B., D. J. C. M. 't Mannetje, and J. M. Oh (2013). "Contact Angle Hysteresis: a Review of Fundamentals and Applications". In: *Colloid and Polymer Science* 291.2, pp. 247–260.

Fernandez, J., P. Kurowski, L. Limat, and P. Petitjeans (2001). "Wavelength Selection of Fingering Instability Inside Hele-Shaw Cells". In: *Physics of Fluids* 13.11, pp. 3120–3125.

Gao, L. and T. J. McCarthy (2007). "How Wenzel and Cassie Were Wrong". In: *Langmuir* 23, pp. 3762–3765.

Garrod, R. P., L. G. Harris, W. C. E. Schofield, J. McGettrick, L. J. Ward, D. O. H. Teare, and J. P. S. Badyal (2007). "Mimicking a Stenocara Beetle's Back for Microcondensation Using Plasmachemical Patterned Superhydrophobic-Superhydrophilic Surfaces". In: *Langmuir* 23.2, pp. 689–693.

Gennes, P. G. de, F. Brochard Wyart, and D. Quéré (2004). *Capillarity and Wetting Phenomena: Drops, Bubbles, Pearls, Waves*. Springer.

Ghosh, A., R. Ganguly, T. M. Schutziusac, and C. M. Megaridis (2014). "Wettability Patterning for High-Rate, Pumpless Fluid Transport on Open, Non-Planar Microfluidic Platforms". In: *Lab on a Chip* 14, pp. 1538–1550.

Huppert, H. (1982). "Flow and Instability of a Viscous Current down a Slope". In: *Nature* 300, pp. 427–429.

Jiménez, J. (2004). "Turbulent Flows over Rough Walls". In: *Annual Review of Fluid Mechanics* 36, pp. 173–196.

Johnson, M. F. G., R. A. Schulter, M. J. Miksis, and S. G. Bankoff (1999). "Experimental Study of Rivulet Formation on an Inclined Plate by Fluorescent Imaging". In: *Journal of Fluid Mechanics* 394, pp. 339–354.

Jokinen, V., L. Sainiemi, and S. Franssila (2008). "Complex Droplets on Chemically Modified Silicon Nanograss". In: *Advanced Materials* 20, pp. 3453–3456.

Karakare, S., A. Kar, A. Kumar, and S. Chakraborty (2010). "Patterning Nanoscale Flow Vortices in Nanochannels with Patterned Substrates". In: *Physical Review Letters* 81.1, p. 016324.

Kataoka, D. E. and S. M. Troian (1999). "Patterning Liquid Flow on the Microscopic Scale". In: *Nature* 402, pp. 794–797.

Kibar, A., H. Karabay, K. S. Yigit, I. O. Ucar, and H. Y. Erbil (2010). "Experimental Investigation of Inclined Liquid Water Jet Flow onto Vertically Located Superhydrophobic Surfaces". In: *Experiments in Fluids* 49, pp. 1135–1145.

Kim, S., M.-W. Moon, and H.-Y. Kim (2013). "Drop Impact on Super-Wettability-Contrast Annular Patterns". In: *Journal of Fluid Mechanics* 730, pp. 328–342.

Le Grand-Piteira, N., A. Daerr, and L. Limat (2006). "Meandering Rivulets on a Plane: A Simple Balance Between Inertia and Capillarity?" In: *Physical Review Letters* 96.25, p. 254503.

Ledesma-Aguilar, R., A. Hernández-Machado, and I. Pagonabarraga (2010). "Dynamics of Gravity Driven Three-Dimensional Thin Films on Hydrophilic-Hydrophobic Patterned Substrates". In: *Langmuir* 26.5, pp. 3292–3301.

LeHew, J. A. (2012). "Spatio-Temporal Analysis of the Turbulent Boundary Layer and an Investigation of the Effects of Periodic Disturbances". PhD thesis. California Institute of Technology.

Lipowsky, R. (2001). "Morphological Wetting Transitions at Chemically Structured Surfaces". In: *Current Opinon in Colloid and Interface Science* 6, pp. 40–48.

Lopez, P. G., M. J. Miksis, and S. G. Bankoff (1997). "Inertial Effects on Contact Line Instability in the Coating of a Dry Inclined Plane". In: *Physics of Fluids* 9.8, pp. 2177–2183.

Mäkiharju Simo A.kiharju, S. A., M. Perlin, and S. L. Ceccio (2012). "On the Energy Economics of Air Lubrication Drag Reduction". In: *International Journal of Naval Architecture and Ocean Engineering* 4, pp. 412–422.

Marshall, J. S. and S. Wang (2005). "Contact-Line Fingering and Rivulet Formation in the Presence of Surface Contamination". In: *Computers and Fluids* 34, pp. 664–683.

Maurel, A., P. J. Cobelli, V. Pagneux, and P. Petitjeans (2009). "Experimental and Theoretical Inspection of the Phase-to-Height Relation in Fourier Transform Profilometry". In: *Applied Optics* 48.2, pp. 380–392.

Mertens, K., V. Putkaradze, and P. Vorobieff (2005). "Morphology of a Stream Flowing down an Inclined Plane. Part 1. Braiding". In: *Journal of Fluid Mechanics* 531, pp. 49–58.

Mugele, F. and J.-C. Baret (2005). "Electrowetting: from Basics to Applications". In: *Journal of Physics: Condensed Matter* 17, R705–R774.

Nakagawa, T. (1992). "Rivulet Meanders on a Smooth Hydrophobic Surface". In: *International Journal of Multiphase Flow* 18.3, pp. 455–463.

Nakagawa, T. and R. Nakagawa (1992). "A Novel Oscillation Phenomenon of the Water Rivulet on a Smooth Hydrophobic Surface". In: *Eleventh Australasian Fluid Mechanics Conference*. Ed. by M. R. Davis and G. J. Walker. Australasian Fluid Mechanics Society, pp. 1041–1044.

Nakagawa, T. and J. Scott (1982). "Stream Meanders on a Smooth Hydrophobic Surface". In: *Journal of Fluid Mechanics* 149, pp. 89–99.

Naval Vessel Register. `http://www.nvr.navy.mil`. Acessed: 2017-04-13.

NavSource Naval History: USS Bunker Hill (CG 52). `http://www.navsource.org/archives/04/1152/04015205.jpg`. Acessed: 2017-04-13.

NavSource Naval History: USS Ticonderoga (CG 47). `http://www.navsource.org/archives/04/1147/04014722.jpg`. Acessed: 2017-04-13.

Parker, A. K. and C. R. Lawrence (2001). "Water Capture by a Desert Beetle". In: *Nature* 414, pp. 33–34.

Paterson, A. and M. Fermigier (1997). "Wetting of Heterogeneous Surfaces: Influence of Defect Interactions". In: *Physics of Fluids* 9.8, pp. 2210–2216.

Polhamus, E. (1966). *A Concept of the Vortex Lift of Sharp-Edge Delta Wings Based on a Leading-Edge-Suction Analogy*. Tech. rep. NASA.

Priezjev, N. V., A. A. Darhuber, and S. M. Troian (2005). "Slip Behavior in Liquid Films on Surfaces of Patterned Wettability: Comparison Between Continuum and Molecular Dynamics Simulations". In: *Physical Review E* 71.4, p. 041608.

Przadka, A., B. Cabane, V. Pagneux, A. Maurel, and P. Petitjeans (2012). "Fourier Transform Profilometry for Water Waves: How to Achieve Clean Water Attenuation with Diffusive Reflection at the Water Surface?" In: *Experiments in Fluids* 52, pp. 519–527.

Quiroga, J. A. and E. Bernabeu (1994). "Phase-Unwrapping Algorithm for Noisy Phase-Map Processing". In: *Applied Optics* 33.29, pp. 6725–6731.

Rajoub, B. A., D. R. Burton, and M. J. Lalor (2005). "A New Phase-to-Height Model for Measuring Object Shape Using Collimated Projections of Structured Light". In: *Journal of Optics A: Pure and Applied Optics* 7, S368–S375.

Rajoub, B. A., M. J. Lalor, D. R. Burton, and S. A. Karout (2007). "A New Model for Measuring Object Shape Using Non-Collimated Fringe-Pattern Projections". In: *Journal of Optics A: Pure and Applied Optics* 9, S66–S75.

Roubos, A., L. Groenewegen, and D. J. Peters (2017). "Berthing Velocity of Large Seagoing Vessels in the Port of Rotterdam". In: *Marine Structures* 51, pp. 202–219.

Ruijter, M. J. de, M. Charlot, M. Voué, and J. De Coninck (2000). "Experimental Evidence of Several Time Scales in Drop Spreading". In: *Langmuir* 16, pp. 2363–2368.

Saffman, P. G. (1986). "Viscous Fingering in Hele-Shaw Cells". In: *Journal of Fluid Mechanics* 173, pp. 73–94.

Schmuki, P. and M. Laso (1990). "On the Stability of Rivulet Flow". In: *Journal of Fluid Mechanics* 215, pp. 125–143.

Schutzius, T. M., M. Elsharkawy, M. K. Tiwari, and C. M. Megaridis (2012). "Surface Tension Confined (STC) Tracks for Capillary-Driven Transport of Low Surface Tension Liquids". In: *Lab on a Chip* 12, pp. 5237–5242.

Seo, J., S. Lee, J. Lee, and T. Lee (2011). "Guided Transport of Water Droplets on Superhydrophobic-Hydrophilic Patterned Si Nanowires". In: *ACS Applied Materials and Interfaces* 3, pp. 4722–4729.

Silvi, N. and E. B. Dussan V (1985). "The Rewetting of an Inclined Solid Surface by a Liquid". In: *Physics of Fluids* 28.1, pp. 5–7.

Stalder, A., G. Kulik, D. Sage, L. Barbieri, and P. Hoffmann (2006). "A Snake-Based Approach to Accurate Determination of Both Contact Points and Contact Angles". In: *Colloids and Surfaces A: Physicochemical and Engineering Aspects* 286, pp. 92 –103.

Su and, X. and L. Xue (2001). "Phase Unwrapping Algorithm Based on Fringe Frequency Analysis in Fourier-Transform Profilometry". In: *Optical Engineering* 40.4, pp. 637–643.

Suk, J. W. and J.-H. Cho (2007). "Capillary Flow Control Using Hydrophobic Patterns". In: *Journal of Micromechanics and Microengineering* 17, N11–N15.

Takeda, M., H. Ina, and S. Kobayashi (1982). "Fourier-Transform Method of Fringe-Pattern Analysis for Computer-Based Topography and Interferometry". In: *Journal of the Optical Society of America* 72.1, pp. 156–160.

Takeda, M. and K. Mutoh (1983). "Fourier Transform Profilometry for the Automatic Measurement of 3-D Object Shapes". In: *Applied Optics* 22.24, pp. 3977–3982.

Takeda, M., Q. Gu, M. Kinoshita, H. Takai, and Y. Takahashi (1997). "Frequency-Multiplex Fourier-Transform Profilometry: A Single-Shot Three-Dimensional Shape Measurement of Objects with Large Height Discontintuities and/or Surface Isolations". In: *Applied Optics* 36.22, pp. 5347–5354.

Torres, G. E. and T. J. Mueller (2004). "Low-Aspect-Ratio Wing Aerodynamics at Low Reynolds Numbers". In: *AIAA Journal* 42.5, pp. 865–873.

Troian, S. M., E. Herbolzheimer, S. A. Safran, and J. F. Joanny (1989). "Fingering Instabilities of Driven Spreading Films". In: *Europhysics Letters* 10, pp. 25–30.

U.S. Department of Defense: USS Freedom (LCS 1). `http://archive.defense.gov/photos/newsphoto.aspx?newsphotoid=15962`. Acessed: 2017-04-13.

Vanden-Broeck, J.-M. (2010). *Gravity-Capillary Free Surface Flows*. Cambridge University Press.

Vanherzeele, J., P. Guillaume, and S. Vanlanduit (2005). "Fourier Fringe Processing Using a Regressive Fourier-Transform Technique". In: *Optics and Lasers in Engineering* 43.6, pp. 645–658.

Wenzel, R. N. (1936). "Resistance of Solid Surfaces to Wetting by Water". In: *Industrial and Engineering Chemistry* 28.8, pp. 988–994.

Zhai, L., M. C. Berg, F. k. Cebeci, Y. Kim, J. M. Milwid, M. F. Rubner, and R. E. Cohen (2006). "Patterned Superhydrophobic Surfaces: Toward a Synthetic Mimic of the Namib Desert Beetle". In: *Nano Letters* 6.6, pp. 1213–1217.

Zhang, X., D. Dabiri, and M. Gharib (1996). "Optical Mapping of Fluid Density Interfaces: Concepts and Implementations". In: *Review of Scientific Instruments* 67.5, pp. 1858–1868.

FOURIER TRANSFORM PROFILOMETRY

Fourier transform profilometry (FTP) is a non-intrusive technique that measures surface deformations by projecting fringe patterns onto a surface. The phase shift in the projected fringes is directly related to surface deformations. This technique can be used for solid surfaces as well as fluid surfaces, given that the surface is opaque.

Fourier Transform Profilometry was first introduced by Takeda, Ina, and Kobayashi in 1982. This technique had several benefits over the current three-dimensional object reconstruction techniques, such as moire topography or fringe scanning techniques. These benefits included the ability to distinguish between depressions and elevations in the object, increased sensitivity and accuracy, all without involving moving parts. In addition, Takeda, Ina, and Kobayashi (1982) were able to extract all necessary information from a single image (referred to as the deformed image throughout this section). This last statement, however, is true only for parallel optical axes configuration (since at h = 0, one gets $\varphi = 0$). Takeda and Mutoh (1983) later proposed using the phase difference (which involves obtaining a reference image) to generalize to crossed-optical axes configurations, where the phase for $h = 0$ will not be equal to zero, while stating that using the phase difference can also cancel errors by misalignments and distortions of the lenses for any and all configurations. The phase-to-height relation derived in this last paper has since been found to be incorrect (Maurel et al., 2009; Rajoub, Burton, and Lalor, 2005; Rajoub et al., 2007). The derivation provided in section A.2, which follows that of Maurel et al. (2009), gives a corrected and more generalized phase-to-height relation.

A.1   Signal Processing

In order to perform FTP, a camera and projector are needed. Traditionally, the projector is oriented such that it projects directly onto the surface of interest. However, the projector is too heavy to be mounted this in the current experiments. Thus, a mirror must be used to direct the projector's beam to the surface of interest.

The camera is placed at height L_c above the reference surface (the flat plates with no flow for the current experiments), while the mirror is located at height L_{p1} above the plate. The projector, located off to the side, projects a fringe pattern onto the

mirror, which then reflects the fringes down onto the camera's field of view (the plate's surface). The fringes are rotated θ degrees in the projector, such that they are aligned with the x-axis in the camera's field of view, as seen in figure A.2.

The projector's optical axis is a distance D from the camera's optical axis, and its optical opening is a total distance $L_p = L_{p1} + L_{p2}$ from the plate's surface, where L_{p2} is the distance between the mirror and the projector.

Three types of images are collected during experiments: a white image, a reference image and a deformed image. The white image is taken when white light is projected onto the dry surface. It is used to determine the additive background, which can be caused by inhomogeneous lighting, background variations, or flat-field errors in the camera lens and sensor. The reference image is taken when a sinusoidal fringe pattern is projected onto the dry surface. The higher the fringe frequency, the greater the height resolution during profilometry. However, care must be taken so that the phase shift in fringes is no more than a jump of $\pi/2$ radians. If the jump is more than this, phase unwrapping will fail (see A.3). The deformed image is taken when the fluid is flowing over the plate. The height variations in the flow cause the fringe pattern to deform and experience phase shifts. The goal is to recover the phase shifts from the image data in order to back-out the height profile of the flow features.

The intensities I_w, I_r, I_d of the white, reference, and deformed images (respectively) can be represented as follows (Cobelli et al., 2009):

$$I_w = b(x, y) \tag{A.1}$$

$$I_r = a(x, y)cos\left(\omega_o y + \varphi_r(x, y)\right) + b(x, y) \tag{A.2}$$

$$I_d = a(x, y)cos\left(\omega_o y + \varphi_d(x, y)\right) + b(x, y), \tag{A.3}$$

where $b(x, y)$ is the additive background, $a(x, y)$ is the local reflectivity of the plate's surface (which may cause modulation of the fringes' intensities), ω_o is the spatial frequency of the sinusoidal fringe pattern projected on the camera's field of view, and $\varphi_r(x, y), \varphi_d(x, y)$ are the phases of the reference and deformed images, respectively. The (x,y) coordinates belong to the camera's FOV, with the origin corresponding to the location of the camera's optical axis in the FOV (i.e., the center of the captured image).
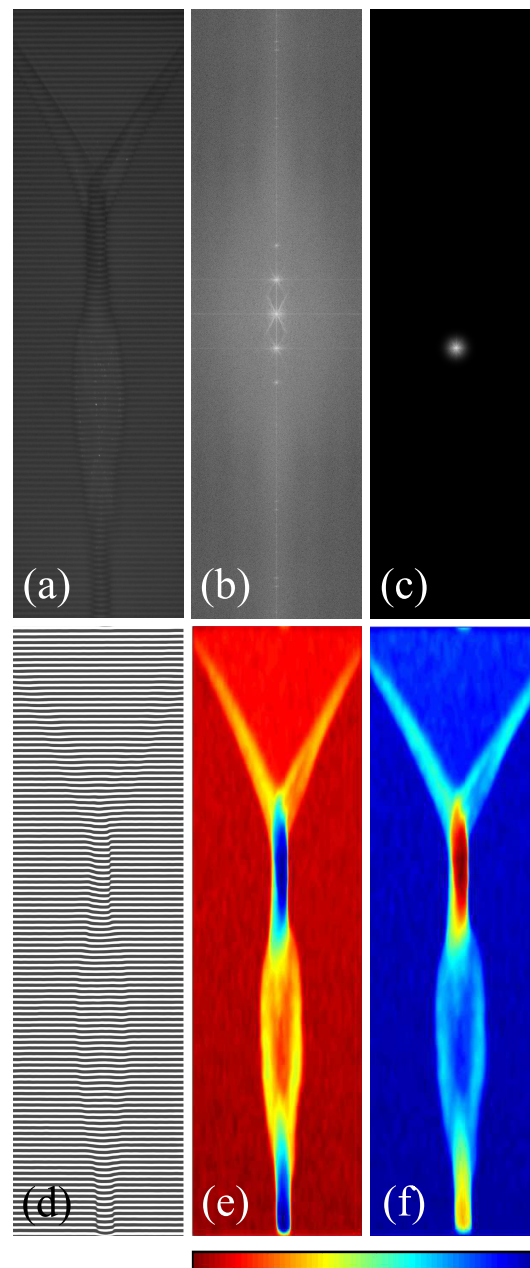
Figure A.1: Steps in FTP image processing (for 64 cm^3/s flow on a uniformly hydrophobic plate inclined at angle $\alpha = 25°$ with respect to the horizontal). (a) Fringes projected onto flow. (b) Shifted Fourier transform of reference image. White spots are the fundamental and harmonic frequencies. (c) Gaussian filter applied to select fundamental frequency of FFT. (d) Filter applied to image (a), leaving only deformed fringes. (e) Phase difference between image (d) and filtered reference image. Color bar goes from -3.0 to 0.2 radians. (f) Resulting height of flow features. Color bar goes from 0 to 11 mm.

The white image is used to remove the additive background from the reference and deformed images, yielding

$$I_{r2} \quad = \quad I_r - I_w = a(x, y)cos\left(\omega_o y + \varphi_r(x, y)\right) \tag{A.4}$$

$$I_{d2} \quad = \quad I_d - I_w = a(x, y)cos\left(\omega_o y + \varphi_d(x, y)\right). \tag{A.5}$$

These two intensities can be rewritten in terms of exponentials, as follows:

$$I_{r2} \quad = \quad c_r(x, y)e^{\omega_o iy} + c_r^*(x, y)e^{\omega_o iy} \tag{A.6}$$

$$I_{d2} \quad = \quad c_d(x, y)e^{\omega_o iy} + c_d^*(x, y)e^{\omega_o iy}, \tag{A.7}$$

where

$$c_r(x, y) \quad = \quad \frac{1}{2}a(x, y)e^{i\varphi_r(x,y)} \tag{A.8}$$

$$c_d(x, y) \quad = \quad \frac{1}{2}a(x, y)e^{i\varphi_d(x,y)} \tag{A.9}$$

and * denotes the complex conjugate. The phase information is contained in $c_r(x, y)$, $c_d(x, y)$ and their conjugates and must be extracted from them.

The Fourier transform of the reference and deformed images (I_{r2} and I_{d2}) is taken along the y-axis (the streamwise direction) to obtain:

$$\mathcal{I}_{r2} \quad = \quad C_r\left(x, \omega - \omega_o\right) + C_r^*\left(x, \omega + \omega_o\right) \tag{A.10}$$

$$\mathcal{I}_{d2} \quad = \quad C_d\left(x, \omega - \omega_o\right) + C_d^*\left(x, \omega + \omega_o\right). \tag{A.11}$$

A Gaussian filter is applied with a window centered about ω_o to extract the $C_r\left(x, \omega\right)$ and $C_d\left(x, \omega\right)$ spectra, which contain the height information. The inverse Fourier transform of the spectra is taken to recover $c_r(x, y)$ and $c_d(x, y)$, as given by equations A.9 and A.9. Taking the complex log of these two, as follows, and taking the imaginary part of the result yields the phase difference between the reference and deformed images, $\Delta\varphi(x, y) = \varphi_d(x, y) - \varphi_r(x, y)$.

$$\log\left[c_d(x, y)c_r^*(x, y)\right] \quad = \quad \log\left[\frac{1}{4}a(x, y)^2 e^{i\varphi_d(x,y)}e^{-i\varphi_r(x,y)}\right] \tag{A.12}$$

$$= \quad \log\left[\frac{1}{4}a(x, y)^2\right] + i\left[\varphi_d(x, y) - \varphi_r(x, y)\right]. \tag{A.13}$$

Another layer of complexity is added to the problem due to the multivalued nature of the complex logarithm. Recall that

$$\log z \;=\; \log |z| + i \arg z \tag{A.14}$$

$$\;=\; \log |z| + i \left(\text{Arg } z + 2\pi n\right), n = 0, 1, 2, ..., \tag{A.15}$$

where arg z is the argument of the complex number z and Arg z is the principal value of the argument, lying in the interval $(-\pi, \pi]$ or $(0, 2\pi]$, for example.

Unfortunately, when computing the complex logarithm, the principal value Arg z is returned. As such, the phase difference obtained in this step is actually modulo 2π, i.e. the phase difference is wrapped. It must be unwrapped in order to obtain the actual phase difference before continuing.

Once $\Delta\varphi(x, y)$ is unwrapped (as described in section A.3), a phase-to-height relation can be used to obtain the height of the flow at each (x, y) location. The phase-to-height relation is based on geometric considerations from the optical setup (Maurel et al., 2009). In the current experiments, because the fringes are aligned with the x-axis and the camera's optical axis is perpendicular to the plate's surface, the geometric relation for non-collimated projection in parallel-optical-axes geometry applies. The phase-to-height relation is thus

$$h(x', y') = \frac{L_c L_p \Delta\varphi(x, y)}{L_c \left[\Delta\varphi(x, y) - \omega_o \left(D + y\right)\right] + L_p \omega_o y}. \tag{A.16}$$

Note that the height is measured at (x', y'), not (x,y). These shifted coordinates are related to (x,y) as follows:

$$x' = x \left(1 - \frac{h}{L_c}\right)$$

$$y' = y \left(1 - \frac{h}{L_c}\right).$$

Upon obtaining h from A.16, the location of the height must be shifted to back to the camera's field of view coordinates (x,y).

A.2   Optical Principle

The phase-to-height relation used in FTP is derived by considering the optical configuration in figure A.2. The undeformed reference surface R defines the $xy-$ plane.

The camera's optical opening is a height L_c from this free surface, and its optical axis defines the z-axis (perpendicular to the $xy-$ plane). The projector's optical opening is located at a height L_p from the reference surface and a distance D from the camera's optical axis. The projector's optical opening is tilted θ degrees with respect to the z-axis and is assumed to produce non-collimated light. (Collimated light requires another derivation and can be found in Cobelli et al. (2009).)
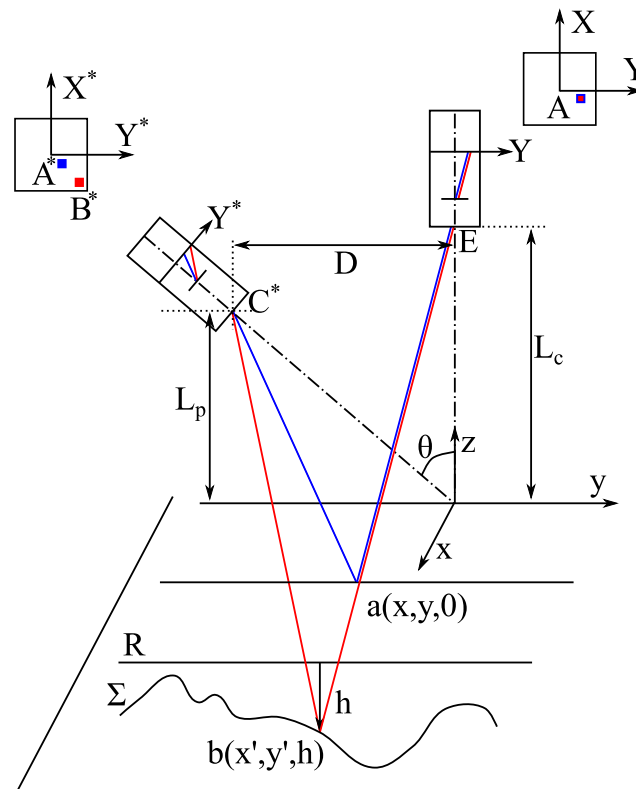
Figure A.2: Optical Principle. Reproduced from Maurel et al. (2009).

The (x, y, z) coordinate system corresponds to the physical coordinate system of the setup, with the xy-plane representing the camera's field of view. The $XY-$ plane is the camera's image plane (i.e. the camera sensor). Thus, defining the camera's magnification $M_c = f_c/L_c < 1$, where f_c is the camera's focal length, gives

$$X' = -M_c x \tag{A.17}$$
$$Y' = -M_c y \tag{A.18}$$

with a negative sign (and $M_c > 0$) because the image is inverted on the camera's sensor.

The projector's plane is defined by the (X^*, Y^*) coordinate system. The projector's magnification $M_p = L_p/(\cos\theta f_p)$ can also be defined, where f_p is the projector's focal length.

Consider a light ray originating from point $A^*(X_A^*, Y_A^*)$, shown as the blue point and blue ray in figure A.2. This light ray intersects the reference surface at point $a(x, y, 0)$ and is then reflected back to point $A(X_A, Y_A)$ in the camera's sensor. The image captured by the camera is represented by the intensity variation $I(X_A, Y_A)$. This intensity captured at point A in the XY-plane is due to the ray A^*aA, whose intensity is imposed by point A^* in the projector.

The intensity variation may be expressed as

$$I(X, Y) = 1 + \cos\varphi(X, Y), \tag{A.19}$$

where φ is the phase of the signal. Assuming a sinusoidal fringe pattern, with fringes aligned along the X^* axis, is projected onto the reference surface R, the phase φ_o for ray A^*aA may be written as

$$\varphi_o(X_A, Y_A) = \omega_p Y_A^*, \tag{A.20}$$

where $\omega_p \equiv \omega M_p$ is the fringe frequency in the projector, ω is the fringe frequency observed in the physical $xy-$ plane, and the subscript o refers to a ray reflecting off the reference surface R.

Now consider surface Σ with height $h(x, y)$ relative to the reference surface R. The point A in the camera now corresponds to ray B^*bA (shown in red in figure A.2), which originates from point B^* in the projector and reflects off point $b(x', y', h)$ on Σ. The intensity of this ray is imposed by the intensity of point B^*, yielding

$$\varphi(X_A, Y_A) = \omega_p Y_B^*. \tag{A.21}$$

The phase difference is defined as $\Delta\varphi(X_A, Y_A) = \varphi_o(X_A, Y_A) - \varphi(X_A, Y_A)$. Therefore,

$$\Delta\varphi(X_A, Y_A) = \omega_p(Y_A^* - Y_B^*). \tag{A.22}$$

The goal is thus to determine the relationship between (X_A, Y_A) in the camera's image plane and Y_A^*, Y_B^* in the projector. Doing so gives the desired relationship between $\Delta\varphi$ and $h(x, y)$. In order to do so, consider the schematic in figure A.3.
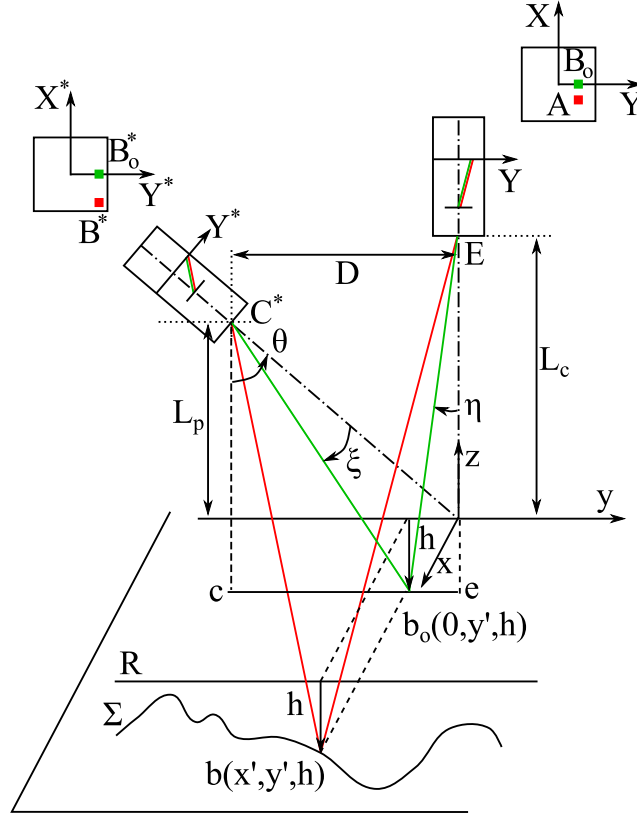
Figure A.3: Optical Principle. Schematic for deriving phase-to-height relation.

The point $b(x', y', h)$ has been projected onto the $x = 0$ $yz-$ plane, resulting in point $b_o(0, y', h)$. The light ray $B_o^* b_o B_o$ can then be drawn, shown in green in figure A.3. This ray originates from point B_o^* in the projector. Because the point $b_o(0, y', h)$ is at the same $yz-$ location as point $b(x', y', h)$, the corresponding points B_o^* and B^* in the projector have the same Y^*-location. That is, points B^* and B_o^* are both located at Y_B^* in the projector, although their X^*-locations are different. Likewise, the points of reflection onto the camera sensor (A and B_o) also share the same Y-location Y_A while having different X-locations.

Since the phase of the intensity variation is a function of Y or Y^*-location only (given that the sinusoidal fringes are aligned along the X^*- axis), the result is that φ for the rays $B^* bA$ and $B_o^* b_o B_o$ are the same:

$$\varphi(X_{B_o}, Y_{B_o}) = \varphi(X_A, Y_A) = \omega_p Y_B^* \qquad (A.23)$$

$b_o(0, y', h)$ can now be used to derive geometric relations in the $yz-$ plane (which

are two dimensional and therefore easier to manipulate than the three-dimensional relations necessary for using $b(x', y', h)$).

Note that the angle between the projected ray C^*b_o and the projector's optical axis OC^*, where C^* corresponds to the projector's optical opening, is given by $\widehat{OC^*b_o} = \xi$ (shown in greater detail in figure A.4a). Thus,

$$\tan(\theta + \xi) = \frac{D + y'}{L_p - h}.$$
(A.24)

It should be noted that as drawn in figures, $h < 0$, $y' < 0$, $\xi < 0$, and $\theta > 0$. Thus $(D + y') < D$, $\left(L_p - h\right) > L_p$, and $(\theta + \xi) < 0$.

Using the trigonometric identity

$$\tan(\theta + \xi) = \frac{\tan \theta + \tan \xi}{1 - \tan \theta \tan \xi}$$
(A.25)

yields

$$\tan \xi = \frac{D + y' - \left(L_p - h\right) \tan \theta}{(D + y') \tan \theta + L_p - h}.$$
(A.26)

Looking inside the projector (figure A.4b) gives

$$\tan \xi = -\frac{Y_B^*}{f_p}.$$
(A.27)

Combining equations A.26 and A.27, gives an expression for $Y_B^*(y')$.

$$Y_B^*(y') = -f_p \frac{D + y' - \left(L_p - h\right) \tan \theta}{(D + y') \tan \theta + L_p - h}.$$
(A.28)

The reflected ray can be used to obtain an expression for y' (Y_A). The angle between the reflected ray $b_o E$ and the camera's optical axis OE is given by $\widehat{OEb_o} = \eta$ (shown in greater detail in figure A.4c).
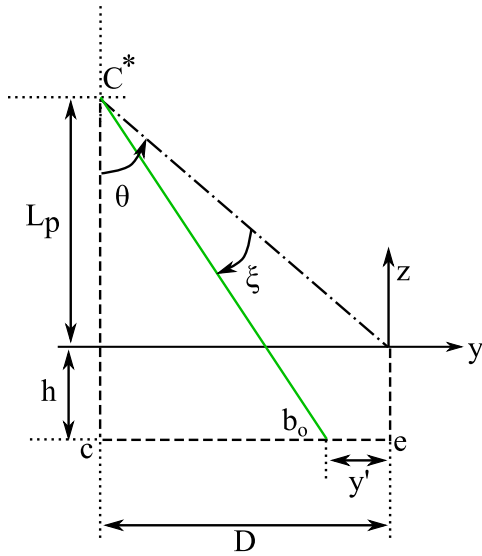
(a) Triangle made by the projector's optical axis and the light ray from point $b_o(0, y', h)$. The point C^* is located at $(0, -D, L_p)$
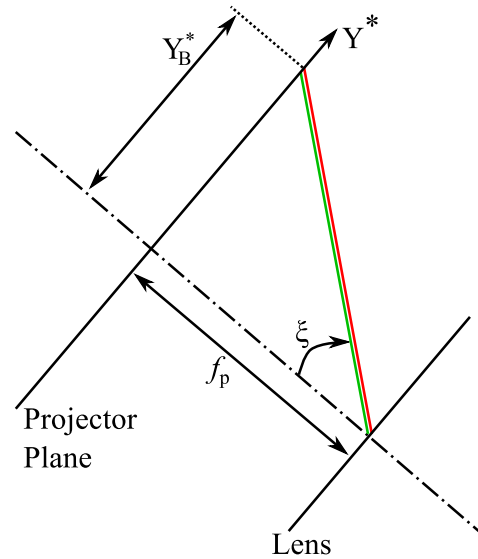
(b) Optics inside the projector. Note that $Y_B^* = Y_{B_o}^*$ but that $X_B^* \neq X_{B_o}^*$
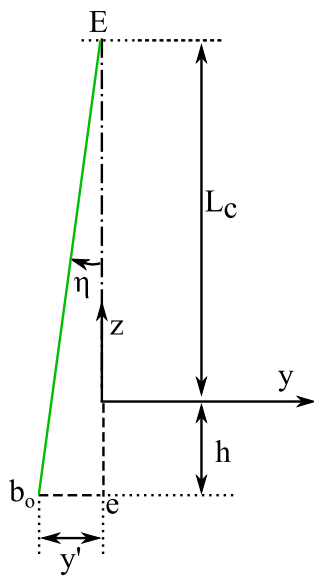
(c) Triangle made by the camera's optical axis and the light ray from point $b_o(0, y', h)$. The point E is located at $(0, 0, L_c)$
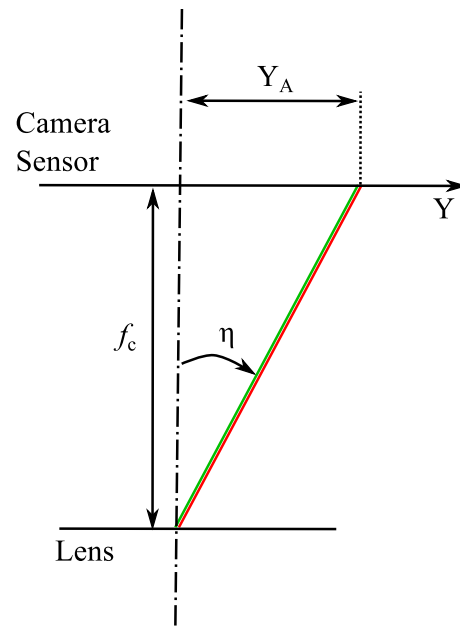
(d) Optics inside the camera. Note that $Y_B' = Y_{B_o}'$ but that $X_B' \neq X_{B_o}'$

Figure A.4: Optical Principle. Magnified views of projector and camera optical components.

Thus,

$$\tan \eta = \frac{y'}{L_c - h}. \tag{A.29}$$

Looking inside the camera (figure A.4c) shows that

$$\tan \eta = -\frac{Y_A}{f_c}. \tag{A.30}$$

Thus, combining equations A.29 and A.30 gives

$$y'(Y_A) = -\frac{L_c - h}{f_c} Y_A. \tag{A.31}$$

Combining the relations for $Y_B^*(y')$ and $y'(Y_A)$ results in

$$Y_B^*(Y_A) = -f_p \frac{D - (L_c - h) Y_A / f_c - \left(L_p - h\right) \tan \theta}{\left[D - (L_c - h) Y_A / f_c\right] \tan \theta + L_p - h}. \tag{A.32}$$

Substituting A.32 into A.23, gives

$$\varphi(X_A, Y_A) = \frac{\omega_c}{\cos \theta} \left\{ \frac{(1 - h/L_c) Y_A + M_c \left[\left(L_p - h\right) \tan \theta - D\right]}{\left(1 - h/L_p\right) + \tan \theta / L_p \left[D - (1 - h/L_c) Y_A / M_c\right]} \right\}, \tag{A.33}$$

where $\omega_c \equiv \omega / M_c = \omega_p / (M_p M_c) = \omega_p \cos \theta f_p / (M_c L_p)$ has been used.

To obtain a similar expression for $\varphi_o(X_A, Y_A)$, simply set $h = 0$ in A.33.

$$\varphi_o(X_A, Y_A) = \frac{\omega_c}{\cos \theta} \left\{ \frac{Y_A + M_c \left[L_p \tan \theta - D\right]}{1 + \tan \theta / L_p \left[D - Y_A / M_c\right]} \right\}. \tag{A.34}$$

With equations A.33 and A.34, an expression for $\Delta \varphi(X_A, Y_A)$ in terms of (X_A, Y_A, h) is obtained. Transformation to (x, y) coordinates is done by using equation A.18.

Note that in the present experiments, the projector-mirror module was aligned such that the sinusoidal fringes aligned to the x-axis in the camera's field of view. This configuration is equivalent to a parallel-optical axes configuration in which the angle $\theta = 0$ and the projector's image plane P coincides with the camera's object plane

R. (If $\theta \neq 0$, φ_o would not be periodic along y since planes P and R would not coincide.)Thus, the expression for $\Delta\varphi(x, y)$ becomes

$$\Delta\varphi(x, y) = -\omega_c M_c h \left[\frac{L_c(y + D) - L_p y}{L_p L_c - L_c h} \right], \tag{A.35}$$

where $\omega_c M_c = \omega$.

Also note that the height h is measured at the shifted location (x', y'), whereas $\Delta\varphi$ is measured at (x, y). Recall how $\Delta\varphi$ is obtained: the phase of the ray $A^* aA$ was first considered, where $a(x, y, 0)$ is in the reference plane R. This gave a phase $\varphi_o(X_A, Y_A)$ on the camera's sensor. Since the reference surface R is the camera's field of view plane, point a located at (x, y) on R is also located at point (x, y) in the camera's field of view. It therefore follows that the phase at point (X_A, Y_A) in the camera corresponds to the phase of point (x, y) in the camera's field of view. The point $b(x', y', h)$ was then considered. It was found that the phase of the corresponding ray $B^* bA$ equals the phase of point (X_A, Y_A) in the camera's image plane (i.e. the camera sensor). As such, the phase of ray $B^* bA$ corresponds to the phase measured at (x, y) in the camera's field of view. However, since b is located at (x', y', h), it follows that h is measured at (x', y') location. Thus, the height h is measured at the shifted location (x', y'), whereas $\Delta\varphi$ is measured at (x, y).

$h(x', y')$ can now be solved for as a function of $\Delta\varphi(x, y)$, yielding

$$h(x', y') = \frac{L_p L_c \Delta\varphi(x, y)}{L_c \left[\Delta\varphi(x, y) + \omega(y + D) \right] - \omega L_p y}. \tag{A.36}$$

The shifted coordinates (x', y') are related to (x, y) as follows:

$$x' = x + \delta_x \tag{A.37}$$

$$y' = y + \delta_y, \tag{A.38}$$

where δ_x and δ_y can be found by noting that the rays aE and bE, shown in blue and red respectively in figure A.2, are coincident. The cross product of the two rays must thus equal zero. The rays are given by the vectors $aE = -x\hat{i} + -y\hat{j} + L_c\hat{k}$ and $bE = -x'\hat{i} - y'\hat{j} + (L_c - h)\hat{k}$. The first term of $aE \times bE$ gives $y' = y(1 - h/L_c)$. The second term gives $x' = x(1 - h/L_c)$. Hence, $\delta_x = -h/L_c x$ and $\delta_y = -h/L_c y$.

A.3 Phase Unwrapping

Because the wrapped phase distribution ranges from $(-\pi, \pi]$ or $(0, 2\pi]$, any variation in the natural phase that is greater than 2π will result in a discontinuity in the wrapped phase. The discontinuities, for a simple one-dimensional phase distribution, can be easily corrected by adding or subtracting 2π: jumps from 2π to 0 necessitate adding 2π to the phase while jumps from 0 to 2π necessitate subtracting 2π.

Figure A.5 demonstrates the one-dimensional unwrapping process. Discontinuities in the wrapped phase (at the top) have been labeled 1 through 10. Discontinuities occur whenever the natural phase (at the bottom) passes through a 2π threshold (i.e., $2\pi, 4\pi, 6\pi,...$). The plot in the middle shows φ_a, which signals how many radians to add to the wrapped phase at each point in order to recover the unwrapped (natural) phase.
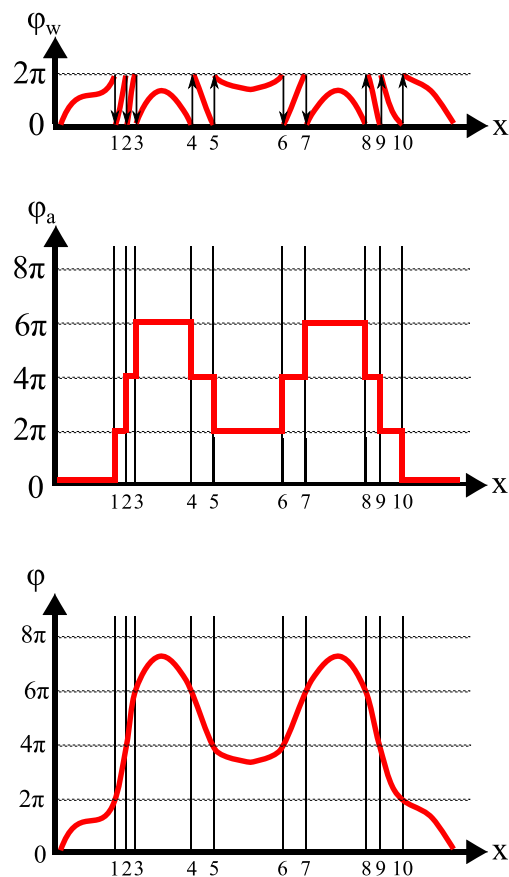

Figure A.5: Example of one dimensional unwrapping process. The wrapped phase is shown at the top and the original, unwrapped phase is seen at the bottom. The center figure is what must be added to the wrapped phase to recover the original phase.

Walking through it, let the unwrapping path start at $y' = 0$. No unwrapping needs to be done until the first discontinuity, labeled 1, is encountered. At this point, the wrapped phase jumps from 2π to 0. 2π must thus be added to the phase at point 1 and every point beyond it in the path in order to make the phase continuous. This is demonstrated by the 2π increase in φ_a at point 1 in the middle plot.

Continuing along the path, the next discontinuity is at point 2. Here, the wrapped phase once again jumps from 2π to 0 and another 2π must be added at point 2 and every point beyond it. The result is that φ_a increases to 4π at point 2 (2π carried over from the first discontinuity and 2π from the current discontinuity).

Another 2π needs to be added at the third discontinuity, causing φ_a to increase to 6π. When the fourth discontinuity occurs, however, the wrapped phase jumps from 0 to 2π. Thus 2π must be subtracted from point 4 and every point in the path beyond it. The result is that φ_a decreases to 4π at point 4. Likewise at point 5, φ_a must decrease another 2π, resulting in an unwrapped phase of 2π. The process continues until the end of the path is reached.

Extending to two dimensional phase data (represented by an *m*x*n* array), a simple unwrapping process can be tried consisted of first unwrapping rows one-by-one and then unwrapping columns one-by-one (or vice versa). While this unwrapping process is easy to implement, it only works for ideal phase data. When processing real images, which are subject to errors, this simple unwrapping scheme often fails to recover the original, unwrapped phase map.

The errors in real images include noise, local shadows and varying fringe visibility, discontinuities in the fringe pattern, excessive density or sparsity of fringe distribution (leading to under-sampling of the signal if the maximum phase change between neighboring points is more than π), all of which complicate obtaining a unique and correct phase (Su and and Xue, 2001; Quiroga and Bernabeu, 1994; Vanherzeele, Guillaume, and Vanlanduit, 2005; Takeda et al., 1997).

As a consequence, phase unwrapping, which should be path independent (i.e., one should always recover the same phase no matter where or how one starts the unwrapping process), may become path dependent. This path dependency poses a problem when coupled with the unwrapping process's cumulative nature: an error occurring at a given point can propagate along the path (Su and and Xue, 2001). Error propagation can be minimized if the unwrapping path is optimized.

Different algorithms have been proposed over the years, ranging from global algo-

rithms (that base the unwrapping algorithm on the minimization of a specific global function), region algorithms (that divide the phase map into regions and unwrap each region individually before unwrapping them with respect to one another), and path-following algorithms.

The simple unwrapping algorithm (unwrapping rows and then columns) was used for this body of work as it is easy to implement, does not take long to run, and does not result in abhorrent abnormalities or discontinuities in the resulting FTP images. Some discontinuities are present, but as the FTP is mostly used for qualitative purposes, this unwrapping process is adequate.

A p p e n d i x   B

BOUNDARY LAYER ESTIMATES

Consider water flowing over a flat plate. Near the wall, the x-velocity u is expected to be less than the free stream velocity U_∞ due to the boundary condition at the flat plate. That is, $u(x, y = 0) = u_s$, where u_s is the slip velocity. If $u_s = 0$, the traditional no-slip condition is recovered. This no-slip condition occurs when water molecules near the plate adhere to the surface and thus do not move relative to the surface. In order for this to happen, the plate's surface must have an affinity to water (i.e., it is hydrophilic). If the plate were hydrophobic, on the other hand, the water molecules would be repulsed by the surface, allowing them to effectively slip over the plate. The flow's velocity near the wall would thus be non-zero.

At a certain distance $y = \delta$ from the wall, the free stream velocity is recovered (i.e., $u(x, y > \delta) = U_\infty$). This distance δ is called the boundary layer thickness. It can be mathematically defined in numerous ways. For example, it can be defined as the y-location at which $u = 0.99 U_\infty$ (the 99% thickness δ_{99}), although the selection of 99% over another value such as 98% is rather arbitrary. A better definition is the displacement thickness δ^* by which the wall would have to be displaced in frictionless flow (with no boundary layer) in order to preserve the mass flux of the actual flow. Mathematically, δ^* is given by

$$\delta^* = \int_0^\infty \left(1 - \frac{u}{U_\infty}\right) dy. \tag{B.1}$$

The boundary layer thickness can also be thought of as the momentum thickness δ_m, where $\rho U_\infty^2 \delta_m$ is the momentum loss due to the presence of the boundary layer. Mathematically, δ_m is given by

$$\delta_m = \int_0^\infty \frac{u}{U_\infty} \left(1 - \frac{u}{U_\infty}\right) dy. \tag{B.2}$$

In order to find the boundary layer thickness, the velocity u in the boundary layer must first be determined. In order to do this, consider the general Navier-Stokes

equations for two-dimensional flow over a flat plate:

$$\frac{\partial \rho}{\partial t} + \frac{\partial \rho u}{\partial x} + \frac{\partial \rho v}{\partial y} = 0 \tag{B.3a}$$

$$\frac{\partial \rho u}{\partial t} + u\frac{\partial \rho u}{\partial x} + v\frac{\partial \rho u}{\partial y} = -\frac{\partial p}{\partial x} + \mu\left(\frac{\partial^2 u}{\partial x^2} + \frac{\partial^2 u}{\partial y^2}\right) \tag{B.3b}$$

$$\frac{\partial \rho v}{\partial t} + u\frac{\partial \rho v}{\partial x} + v\frac{\partial \rho v}{\partial y} = -\frac{\partial p}{\partial y} + \mu\left(\frac{\partial^2 v}{\partial x^2} + \frac{\partial^2 v}{\partial y^2}\right). \tag{B.3c}$$

For steady (i.e., $\partial()/\partial t \to 0$), incompressible flow, equations B.3a-c become

$$\frac{\partial u}{\partial x} + \frac{\partial v}{\partial y} = 0 \tag{B.4a}$$

$$u\frac{\partial u}{\partial x} + v\frac{\partial u}{\partial y} = -\frac{1}{\rho}\frac{\partial p}{\partial x} + \nu\left(\frac{\partial^2 u}{\partial x^2} + \frac{\partial^2 u}{\partial y^2}\right) \tag{B.4b}$$

$$u\frac{\partial v}{\partial x} + v\frac{\partial v}{\partial y} = -\frac{1}{\rho}\frac{\partial p}{\partial y} + \nu\left(\frac{\partial^2 v}{\partial x^2} + \frac{\partial^2 v}{\partial y^2}\right), \tag{B.4c}$$

where $\nu = \mu/\rho$.

Using scaling arguments, $u \sim U_\infty$, $x \sim L$ (where L is the characteristic length of the plate), and $y \sim \delta$ with $L >> \delta$. Plugging these into the continuity equation B.4a gives

$$\frac{U_\infty}{L} + \frac{v}{\delta} = 0,$$

from which the scaling for v is obtained: $v \sim \delta U_\infty/L$. This then gives

$$\frac{U_\infty^2}{L} + \frac{U_\infty^2}{L} = -\frac{1}{\rho}\frac{p}{L} + \nu\left(\frac{U_\infty}{L^2} + \frac{U_\infty}{\delta^2}\right),$$

for the x-momentum equation B.4b. Assuming that the pressure force is of the same order as the inertial forces gives pressure variations in the flow field on the order of $p - p_\infty \sim \rho U_\infty^2$. Defining $Re = U_\infty L/\nu$ then allows the following non-dimensional variables to be defined:

$$x' = \frac{x}{L} \qquad u' = \frac{u}{U_\infty} \qquad p' = \frac{p - p_\infty}{\rho U_\infty^2} \qquad \text{(B.5)}$$

$$y' = \frac{y}{L}\sqrt{Re} \qquad v' = \frac{v}{U_\infty}\sqrt{Re}.$$

Plugging these non-dimensional variables back into the system of equations and simplifying results in the new system of equations:

$$\frac{\partial u'}{\partial x'} + \frac{\partial v'}{\partial y'} = 0 \qquad \text{(B.6a)}$$

$$u'\frac{\partial u'}{\partial x'} + v'\frac{\partial u'}{\partial y'} = -\frac{\partial p'}{\partial x'} + \frac{1}{Re}\frac{\partial^2 u'}{\partial x'^2} + \frac{\partial^2 u'}{\partial y'^2} \qquad \text{(B.6b)}$$

$$\frac{1}{Re}\left(u'\frac{\partial v'}{\partial x'} + v'\frac{\partial v'}{\partial y'}\right) = -\frac{\partial p'}{\partial y'} + \frac{1}{Re^2}\frac{\partial^2 v'}{\partial x'^2} + \frac{1}{Re}\frac{\partial^2 v'}{\partial y'^2}. \qquad \text{(B.6c)}$$

Each term is of order one unless pre-multiplied by the Reynolds number. As $Re \to \infty$, the $\frac{1}{Re}$ and $\frac{1}{Re^2}$ terms go to zero, simplifying the system of equations. Going back to dimensional variables, gives

$$\frac{\partial u}{\partial x} + \frac{\partial v}{\partial y} = 0 \qquad \text{(B.7a)}$$

$$u\frac{\partial u}{\partial x} + v\frac{\partial u}{\partial y} = -\frac{\partial p}{\partial x} + \frac{\partial^2 u}{\partial y^2} \qquad \text{(B.7b)}$$

$$\frac{\partial p}{\partial y} = 0. \qquad \text{(B.7c)}$$

The y-momentum equation B.7c implies that the pressure at any x-location in the boundary layer is equal to the pressure in the free stream. Inviscid theory gives $p + \rho U_\infty^2/2 = $ constant outside the boundary layer for uniform flow over a flat plate. Thus, the pressure is independent of x and the dp/dx term in equation B.7b can drop out.

The boundary conditions for the system of equations B.7 are the slip condition at the wall ($u(x, y = 0) = u_s$), non-permeability of the wall ($v(x, y = 0) = 0$, i.e. no flow in or out of the wall), and the matching condition between the boundary layer and outer flow ($u(x, y \to \infty) = U_\infty$).

The problem also has an initial condition, which takes the form of an initial velocity profile. To simplify the system of equations, the initial velocity profile is assumed to be forgotten far enough downstream of the initial condition. Thus, a similarity solution can be found for the problem.

The stream function $\psi(x, y) = Ax^P f(\eta)$ can be defined, where $\eta = Bx^Q y$ is the self-similarity variable. Using $u = \partial\psi/\partial y$ and $v = -\partial\psi/\partial x$ and plugging into B.7, yields

$$(P + Q)f'^2 - Pff'' = \nu \frac{B}{A} x^{Q-P+1} f''',\tag{B.8}$$

where $()'$ denotes the η-derivative $\partial()/\partial\eta$. The boundary conditions are as follows:

$$\frac{\partial\psi}{\partial y}\Big|_{y=0} = ABx^{P+Q}f'(0) = u_s\tag{B.9a}$$

$$\frac{\partial\psi}{\partial y}\Big|_{y\to\infty} = ABx^{P+Q}f'(\infty) = U_\infty\tag{B.9b}$$

$$\frac{\partial\psi}{\partial x}\Big|_{y=0} = Ax^{P-1}Pf(0) = 0.\tag{B.9c}$$

As the desired solution should be independent of x, it follows that $Q - P + 1 = 0$ in equation B.8. By the same logic, $P + Q = 0$ in equation B.9a. Thus, $P = 1/2$ and $Q = -1/2$. Equation B.9a then yields $f'(0) = u_s/(AB)$.

Equation B.9c yields $f(0) = 0$ in order for the boundary condition to hold at all x, and equation B.9b gives $f'(\infty) = U_\infty/(AB)$. Let $AB = U_\infty$ so that $f'(\infty) = 1$. Also let $\nu B/A = 1$ to simplify the expression in equation B.8. Thus, $A = \sqrt{U_\infty \nu}$ and $B = \sqrt{U_\infty/\nu}$. As a result, $f'(0) = u_s/U_\infty$ from equation B.9a.

The result is a second-order ordinary differential equation of the form

$$f'''(\eta) + \frac{1}{2}f(\eta)f''(\eta) = 0\tag{B.10}$$

$$f(0) = 0 \qquad f'(0) = \frac{u_s}{U_\infty} \qquad f'(\infty) = 1,$$

where

$$\eta = \sqrt{\frac{U_\infty}{\nu x}}y$$

$$\psi(x, y) = \sqrt{U_\infty \nu x} f(\eta) \tag{B.11}$$

$$u(x, y) = U_\infty f'(\eta) \qquad v(x, y) = \frac{1}{2} U_\infty Re_x^{-1/2} [\eta f'(\eta) - f(\eta)].$$

This is Blausius' equation. It can be solved using the shooting method. The ODE must first be re-written as the system of equations given by

$$\begin{bmatrix} \frac{df}{d\eta} \\ \frac{df'}{d\eta} \\ \frac{df''}{d\eta} \end{bmatrix} = \begin{bmatrix} f' \\ f'' \\ -\frac{1}{2}ff'' \end{bmatrix} \tag{B.12}$$

with $f(0) = 0, f'(0) = u_s/U_\infty, f'(\infty) = 1$. To solve the problem, the $\eta = 0$ boundary conditions for f, f', and f'' must be used. As the boundary condition for $f''(0)$ is not given, an initial value t is guessed. The system of equations is then solved, checking to see if $f'(\infty; t)$ from the guessed initial value matches the actual $f'(\infty) = 1$ boundary condition. If not, the process is re-iterated with a new initial guess.

The new initial guess is updated via Newton's method. Let $m(t) = f'(\infty; t) - 1$, where the 1 comes from the actual boundary condition $f'(\infty) = 1$. The root for $m(t)$ gives t when the boundary condition matches. Using Newton's method, the root is given by

$$\begin{aligned} t_{n+1} &= t_n - \frac{m(t_n)}{\frac{\partial}{\partial t}m(t_n)} \tag{B.13} \\ &= t_n - \frac{f'(\infty; t_n) - 1}{\frac{\partial}{\partial t}f'(\infty; t_n)}. \end{aligned}$$

However, $\partial f'/\partial t$ is unknown. Letting $f'''(\eta) = g(\eta, f, f', f'')$,

$$\begin{aligned} \frac{\partial f'''}{\partial t} &= \frac{\partial g}{\partial f}\frac{\partial f}{\partial t} + \frac{\partial g}{\partial f'}\frac{\partial f'}{\partial t} + \frac{\partial g}{\partial f''}\frac{\partial f''}{\partial t} \tag{B.14} \\ &= -\frac{1}{2}f''\frac{\partial f}{\partial t} + (0)\frac{\partial f'}{\partial t} - \frac{1}{2}f\frac{\partial f''}{\partial t}. \end{aligned}$$

Letting $z = \partial f / \partial t$, gives

$$z''' = -\frac{1}{2} f'' z - \frac{1}{2} f z''$$
(B.15)

with the boundary conditions $z(0) = 0$, $z'(0) = 0$, and $z''(0) = 1$.

Now, $m = \partial f' / \partial t = z'$ and $m' = z''$. The following system of equations must therefore be solved:

$$\begin{bmatrix} \frac{dh_1}{d\eta} \\ \frac{dh_2}{d\eta} \\ \frac{dh_3}{d\eta} \\ \frac{dh_4}{d\eta} \\ \frac{dh_5}{d\eta} \\ \frac{dh_6}{d\eta} \end{bmatrix} = \begin{bmatrix} h_2 \\ h_3 \\ -\frac{1}{2} h_1 h_3'' \\ h_5 \\ h_6 \\ -\frac{1}{2} h_3 h_4 - \frac{1}{2} h_1 h_6'' \end{bmatrix} \left(= \begin{bmatrix} f' \\ f'' \\ f''' \\ z' \\ z'' \\ z''' \end{bmatrix} \right)$$
(B.16)

with the boundary conditions

$$\begin{aligned} h_1(0) &= 0 & h_2(0) &= u_s/U_\infty & h_3(0) &= t_n \\ h_4(0) &= 0 & h_5(0) &= 0 & h_6(0) &= 1, \end{aligned}$$
(B.17)

where t_n is iteratively modified using $t_{n+1} = [h_2(\infty) - 1]/h_5(\infty)$ until $h_2(\infty) = 1$.

The resulting u- and v-velocities are plotted versus η at the top of figure B.1 for various slip velocities u_s (given as a percentage of the free stream velocity U_∞). The plots can be thought of as showing the velocity profiles for a given x-location, in which case Re_x is constant (thus the x-axis is corresponds to velocity only) and η is a function of y only (thus the y-axis corresponds to y only).

As the slip velocity increases, the u-velocity profile become more uniform as expected and the v-velocity approaches zero. The effect this has on the vorticity at the wall can be determined, where the vorticity is defined as

$$\begin{aligned} \omega|_{y=0} &\equiv \left(\nabla \times \vec{u} \right)|_{y=0} \\ &= \left(\frac{\partial v}{\partial x} - \frac{\partial u}{\partial y} \right)|_{y=0} \hat{z}, \end{aligned}$$

where

$$\frac{\partial u}{\partial y}\Big|_{y=0} = \left(U_\infty \frac{df'}{d\eta}\frac{\partial \eta}{\partial y}\right)\Big|_{y=0}$$

$$= \sqrt{\frac{U_\infty^3}{\nu x}}f''(0)$$

and

$$\frac{\partial v}{\partial x}\Big|_{y=0} = \frac{1}{2}U_\infty\left(\frac{\partial}{\partial x}Re^{-1/2}[\eta f'(\eta) - f(\eta)] + Re^{-1/2}\frac{d}{d\eta}[\eta f'(\eta) - f(\eta)]\frac{\partial \eta}{\partial x}\right)\Big|_{y=0}$$

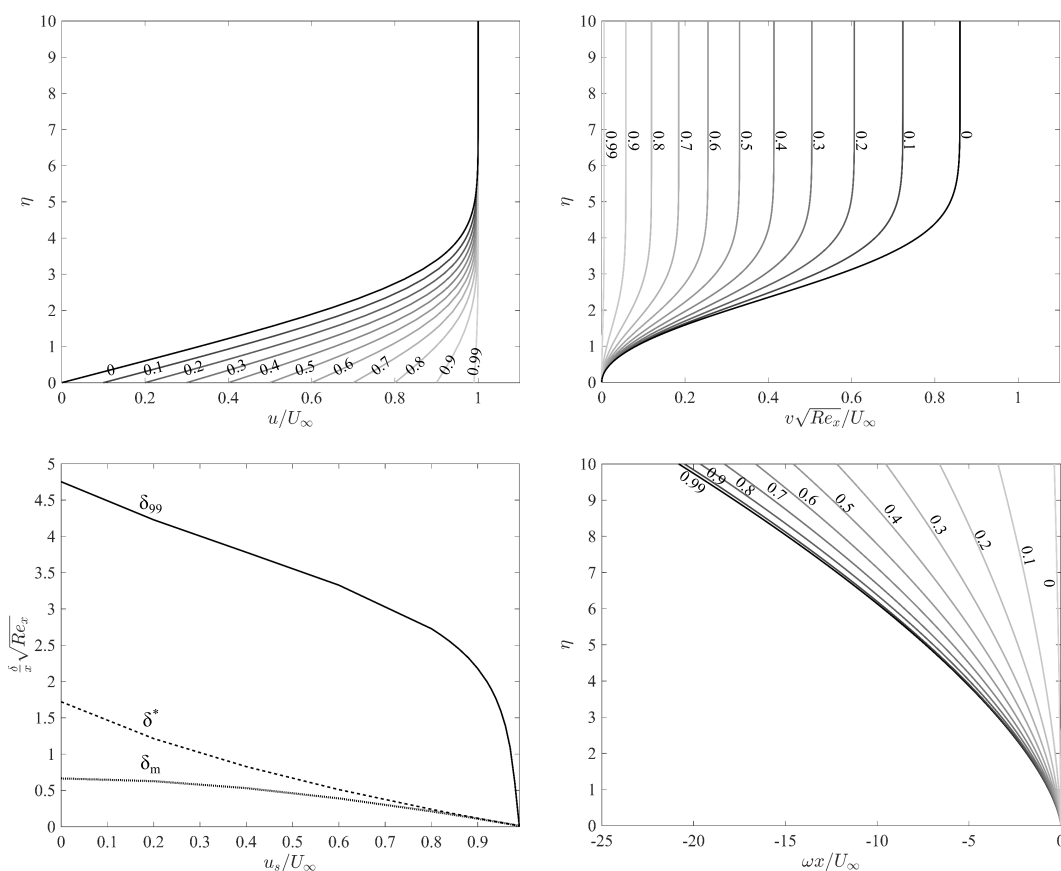$$= \frac{1}{4}\sqrt{\frac{\nu U_\infty}{x^3}}f(0).$$

Figure B.1: Theoretical boundary layer over a flat plate. The non-dimensionalized u- and v-velocities are plotted versus the self-similarity variable η (top row) for increasing u_s/U_∞, as indicated on the curves. The non-dimensionalized displacement (δ^*), momentum (δ_m) and $0.99U_\infty$ (δ_{99}) boundary layer thicknesses are plotted as functions of the slip velocity on the lower left. The vorticity $\omega = (\frac{\partial v}{\partial x} - \frac{\partial u}{\partial y})\hat{z}$ is plotted versus Reynolds number for varying u_s on the lower right.

Recall that $f(0) = 0$ from the non-permeability condition and that $f''(\eta)$ is given by h_3 in the numerical scheme. Thus,

$$\omega|_{y=0} = -\sqrt{\frac{U_\infty^3}{\nu x}} h_3(0). \tag{B.18}$$

The vorticity, plotted on the lower right in figure B.1, is found to approach zero with increasing slip. The vorticity is also found to be negative for all η. However, the derivative of vorticity ($\partial^2 u/\partial^2 y$), which goes like $f'''(0) = -0.5 f(0) f''(0)$, is zero at the wall. Thus the flow is neither accelerating ($\partial^2 u/\partial^2 y < 0$) nor decelerating ($\partial^2 u/\partial^2 y > 0$), which would lead to flow separation. The point of separation occurs when

$$\frac{\partial u}{\partial y}|_{y=0} = 0,$$

which is never the case for the theoretical flat plate studied here.

Note that while the pressure term $\partial p/\partial x$ was dropped when deriving Blasius's equation for a flat plate, the reality is that the vorticity at the wall is influenced by (and proportional to) the pressure gradient. If a wall is curved, a decrease in pressure ($\partial p/\partial x < 0$) is expected upstream of the highest point and an increase in pressure ($\partial p/\partial x > 0$) is expected downstream of the highest point. Thus, a favorable pressure gradient (lending itself to accelerating flow) exists upstream and an adverse pressure gradient (contributing to decelerating flow and thus flow separation) exists downstream of the highest point.

In the case of the hydrofoil experiment presented in this thesis, the trailing edge of the hydrofoil is downstream of the highest point. Thus, the flow is decelerating over the hydrofoil's trailing edge and an adverse pressure gradient is present. However, as introducing greater slip at the wall reduces gradients in u, it can be concluded that slip would delay this flow separation in the face of adverse pressure gradients. That is, flow separation would occur later (further downstream) for hydrophobic surfaces than hydrophilic surfaces. This is indeed what was found in the experiments conducted in section 3.5.3.

In order to determine the boundary layer thickness, the expressions B.1 and B.2 are integrated. First note that $dy = \sqrt{\nu x/U_\infty} d\eta$, thus the integrals can be expressed as

$$\sqrt{\frac{U_\infty}{\nu x}}\delta^* = \int_0^\infty \left(1 - \frac{u}{U_\infty}\right) d\eta \tag{B.19}$$

$$\sqrt{\frac{U_\infty}{\nu x}}\delta_m = \int_0^\infty \frac{u}{U_\infty}\left(1 - \frac{u}{U_\infty}\right) d\eta. \tag{B.20}$$

The δ_{99} boundary layer thickness is obtained by finding η at which $u(\eta) = 0.99U_\infty$ and then using the definition of η to determine the corresponding y-value $(=\delta_{99})$ at a given x-location. The resulting thicknesses as a function of the slip velocity are presented on the lower left of figure B.1. As the slip velocity increases, the boundary layer thickness non-linearly decreases (no matter how the thickness is defined).

The boundary layer thicknesses at $x = c = 30.5$ cm with $u_s = 0$ m/s (no-slip condition corresponding to the uniformly hydrophilic case) for the hydrofoil experiments are presented in table B.1. These boundary layer thicknesses represent the maximum theoretical values (as δ decreases with increasing u_s and increases with x). Similarly, the maximum boundary layer thicknesses for the wall jet experiments at the end of the inclined plate are presented in table B.2, where $U = Q/A_{\text{jet}}$ is the average jet velocity and $A_{\text{jet}} = 1.6$ cm^2 is the jet nozzle cross-sectional area.

Re (10^5)	δ_{99} [mm]	δ^* [mm]	δ_m [mm]
0.4	7.9	2.8	1.1
0.7	5.6	2.0	0.77
1.0	4.6	1.6	0.63
1.4	4.0	1.4	0.55
1.7	3.6	1.3	0.50
2.0	3.3	1.2	0.45
2.4	3.0	1.1	0.41
2.8	2.8	1.0	0.38
3.1	2.7	0.94	0.36

Table B.1: Maximum boundary layer thicknesses as given by the Blasius solution for the hydrofoil experiments.

Q [cm^3/s]	δ_{99} [μm]	δ^* [μm]	δ_m [μm]
4.5	15.2	2.5	5.3
110	3.1	0.4	1.1

Table B.2: Maximum laminar boundary layer thicknesses as given by the Blasius solution for the wall jet experiments.

The theoretical boundary layer thicknesses can be compared to the radius of curvature of the upper and lower surfaces of the hydrofoil in order to determine if approximating the the hydrofoil as a flat plate is valid.

The radius of curvature of a curve $y = f(x)$ is given by

$$r(x) = \frac{\left[1 + \left(\frac{dy}{dx}\right)^2\right]^{3/2}}{\left|\frac{d^2y}{dx^2}\right|}.$$

The curve for a NACA0012 is given by

$$y(x) = 0.6c\left[0.2969\sqrt{\frac{x}{c}} - 0.1260\left(\frac{x}{c}\right) - 0.3516\left(\frac{x}{c}\right)^2 + 0.2843\left(\frac{x}{c}\right)^3 - 0.1015\left(\frac{x}{c}\right)^4\right],$$

as reported by Abbott and Doenhoff (1959). Figure B.2 shows the radius of curvature along the hydrofoil cross-section as given using the equations above. The minimum radius of curvature is 5.8 cm, which is one order of magnitude greater than the maximum theoretical boundary layer thickness. Thus, the hydrofoil may be roughly approximated as flat plate.
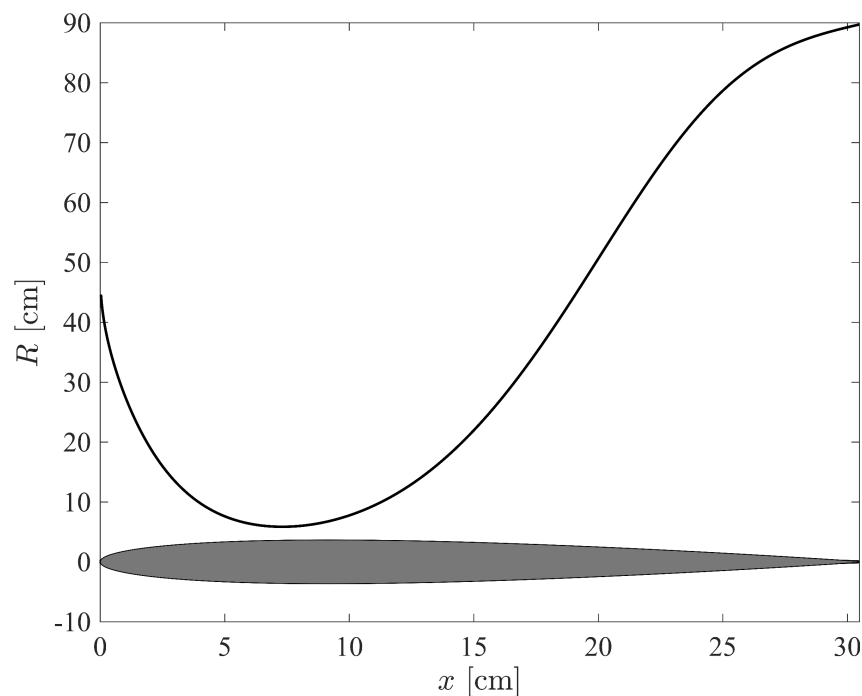

Figure B.2: The radius of curvature for the upper and lower surfaces of the NACA0012 hydrofoil cross-section (shown in grey).

A p p e n d i x   C

COATING THICKNESS EFFECTS

The plates and hydrofoil used for this body of work are naturally hydrophilic. In order to introduce hydrophobic properties, the surfaces are coated with Rust-Oleum's commercially available NeverWet Multi-Surface hydrophobic coating. Thus, the patterned surfaces will have protrusions wherever there are hydrophobic bands. The thickness of these bands is measured using a Bruker DekTakXT stylus profilometer (1Å resolution reported) at Caltech's Molecular Materials Research Center, the results of which are presented in figure C.1.
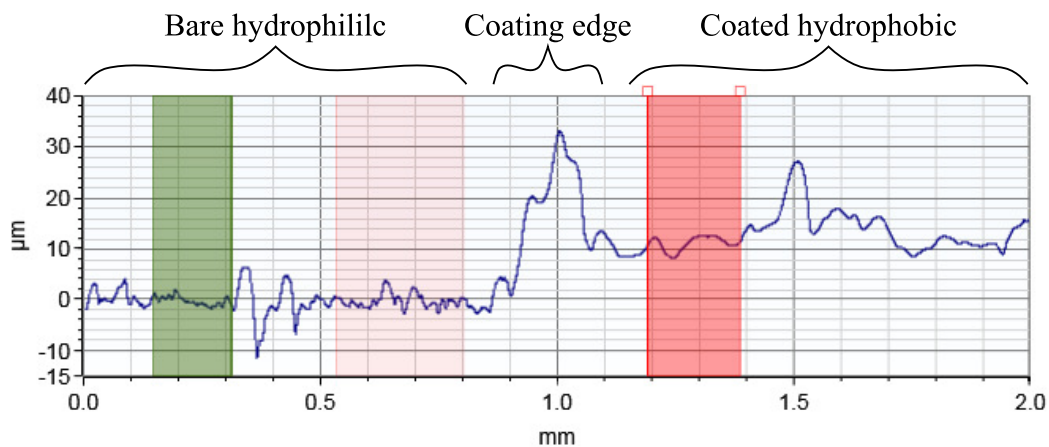

Figure C.1: Coating thickness and surface roughness as measured by a Bruker DekTakXT stylus profilometer.

The coating is 9 - 14 μm thick on average, with an increased thickness ($< 40\mu$m) at the edges of the band. This increased thickness at the edges is due to particles building up at the edge of the vinyl mask during the coating process.

For the thin film experiments, the coating is less than 3% of the jet nozzle height h_{jet} at the band edges and less than 0.9% of h_{jet} away from the band edges. The roughness is also two orders of magnitude smaller than the band widths (d) studied in those experiments. For the hydrofoil experiments, the coating is about 1.5% of the minimum estimated boundary layer (δ_{99} = 2.7 mm for Re = 3.1 × 10^5; see appendix B) at the band edges and about 0.5% of it away for the band edges.

In order to further qualify the effects of the coating thickness, two hydrophilic plates were milled to have approximately 40 ± 12 μm high steps oriented at an angle $\beta = 90°$ with respect to the flow direction. One of these milled plates was then hydrophobically coated. The result is one plate with uniform hydrophilic wettability but small steps and one plate with uniform hydrophobic wettability and small steps, as shown in schematic C.2. The behavior of a thin (1.6 mm) film flowing over these plates is presented in figures C.3 and C.4. (Note that the flow rate and plate inclination angle α were not recorded in these tests. However, from images, the plate inclination angle is observed to range from $10° - 17°$. Additionally, the flow regimes correspond to the film and braided regimes observed at higher flow rates in the experiments discussed in chapter 2).
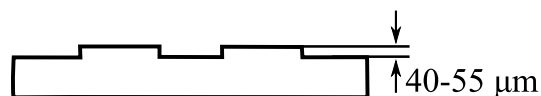

Figure C.2: Schematic of milled plates resulting in surfaces with uniform wettability and small steps.

Although capillary waves arise whenever there is an increase or decease in height, there is no corresponding change in the film thickness. The scales and roller structures observed for thin film flow on the $\beta = 90°$ patterned wettability plate in chapter 2, which have raised heights approximately 1-3 mm greater than the initial sheet thickness, are not observed in the absence of wettability gradients. Thus, those flow structures are indeed due to patterned wettability and not flow over obstacles (i.e., the step introduced by the hydrophobic coating thickness).

Similarly, it can be concluded that the modulated contact line observed in the hydrofoil experiments of chapter 3 are also due to wettability effects. As the resulting free-surface waves in these experiments are directly tied to the modulated contact line (troughs due to the concave contact line on hydrophobic bands, crests due to the convex contact line on hydrophilic bands), the standing waves can also be attributed to wettability effects rather than coating thickness effects.

The hydrofoil experiments in chapter 3 are conducted for $Re = 4 \times 10^4 - 3.1 \times 10^5$, which should be below the critical Reynolds number for transition to turbulent boundary layers. In any case, Jiménez (2004) reports that the effect of roughness elements of size k extends across the turbulent boundary layer if $\delta_{99}/k \lesssim 50$, at which point the flow is effectively flow over obstacles. In the hydrofoil experiments, $\delta_{99}/k > 67$ using the minimum estimated boundary layer thickness and maximum

coating thickness of 40 μm. So even if close to the transitional Reynolds number, the effect of the coating thickness should not extend far into the flow field, affirming the fact that the free-surface waves observed in these experiments can be attributed to wettability changes rather than flow over obstacles.
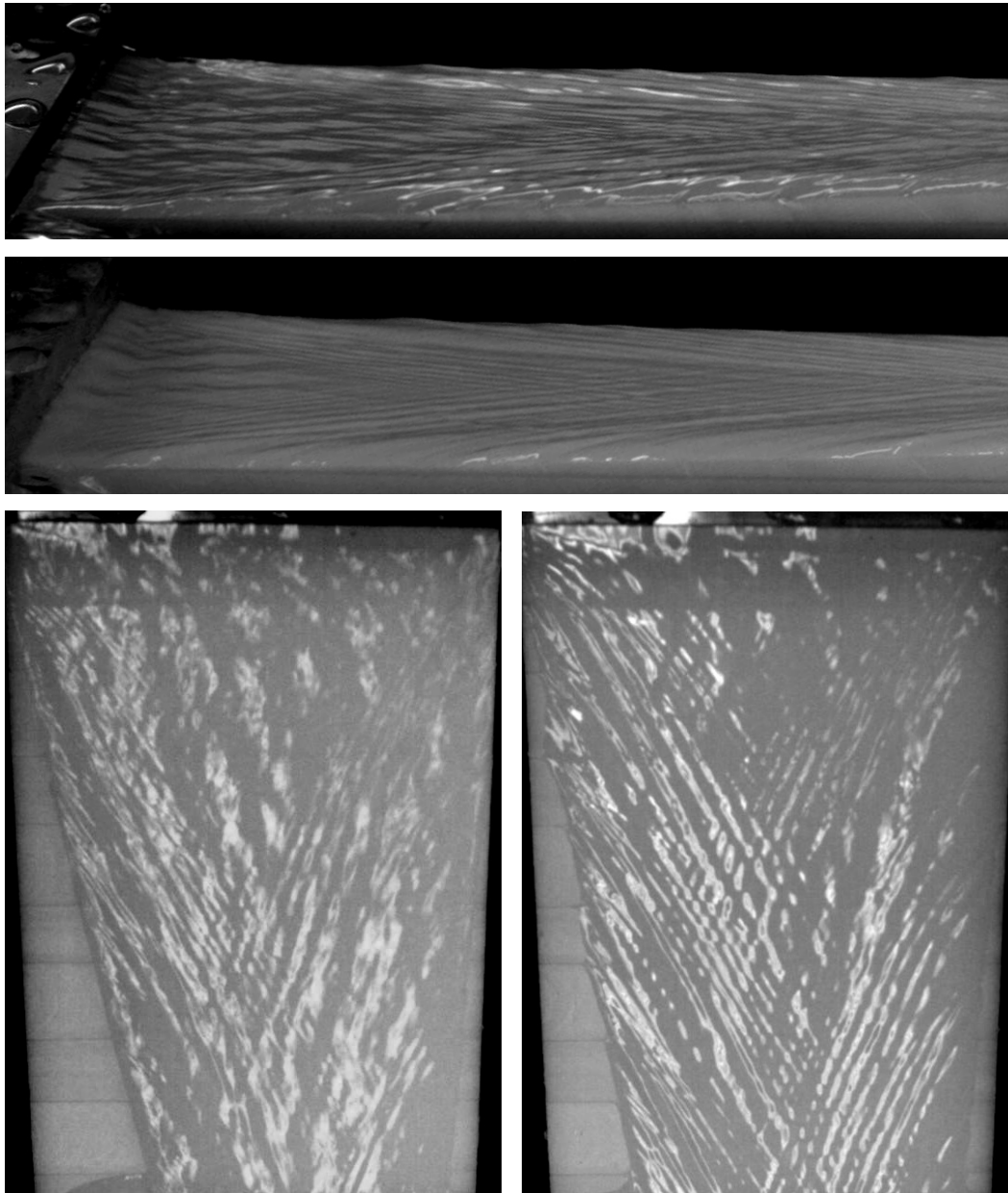

Figure C.3: Thin film flow on a uniformly hydrophilic surface with approximately 40 ± 12 μm high steps as seen from the side (top two images with flow left to right) and from the top (bottom two images with flow top to bottom).
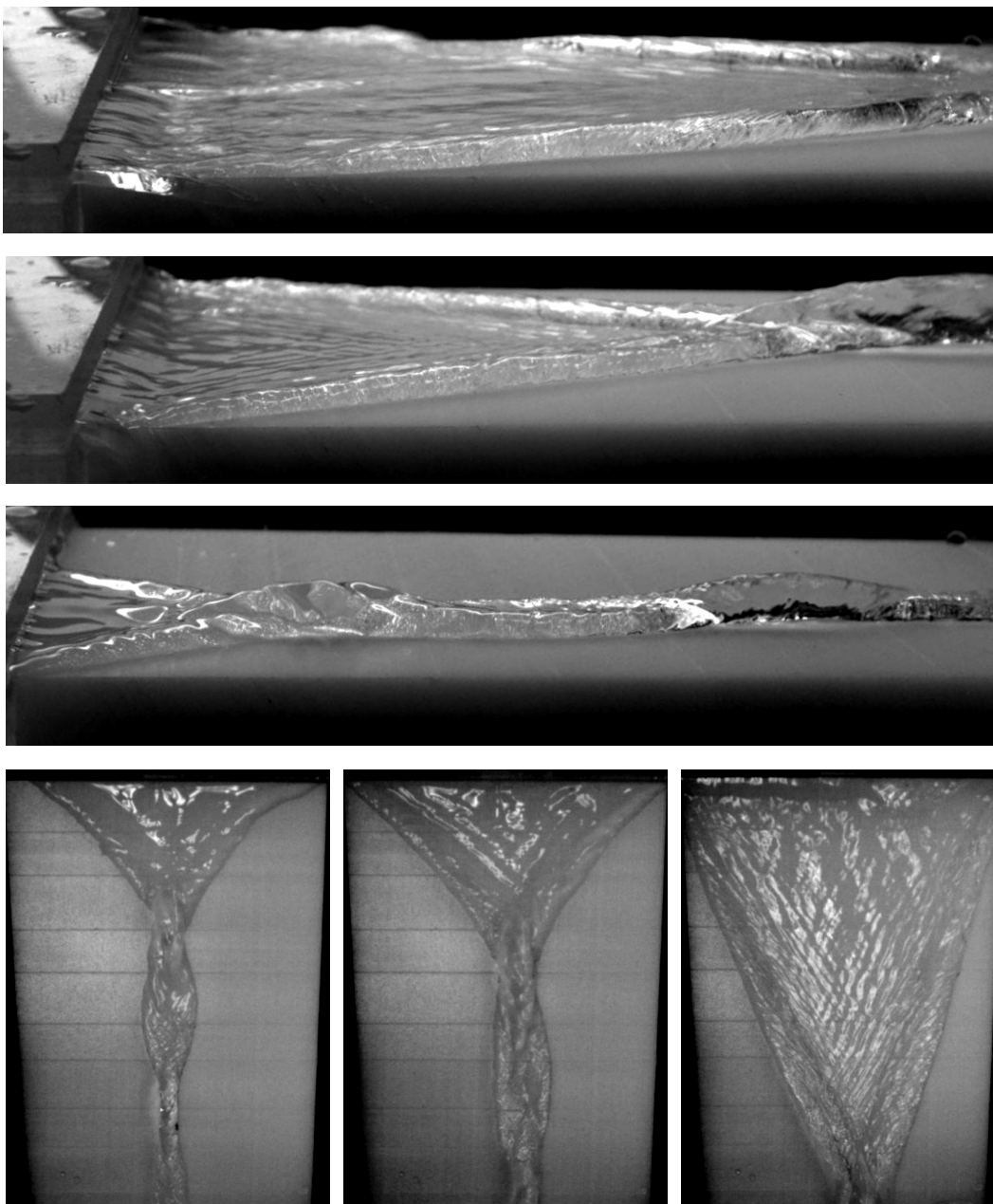
Figure C.4: Thin film flow on a uniformly hydrophobic surface with approximately 40 ± 12 μm high steps as seen from the side (top three images with flow left to right) and from the top (bottom three images with flow top to bottom).

NAVAL SHIP DESIGN

D.1 Basic Ship Terms

A schematic of the basic dimensions and nomenclature of a general ship hull are presented in figure D.1. The front of a ship is called the bow while the back is called the stern. The overall or total length of the ship is given by L_{OA}. In most ships, the overall length is greater than the length of the ship at the waterline. This wetted length, L_{WL}, is the relevant length scale for drag (termed "resistance" in reference to ship motion) and other force calculations. The submerged depth of the ship, termed the draft T, is measured from the lowest part of the ship to the waterline. The draft varies along the ship due to the presence of waves. The draft measurements reported in subsequent sections refers to the mean draft. The width of the ship also varies along the body. The maximum width of the ship at the waterline is called the beam B.
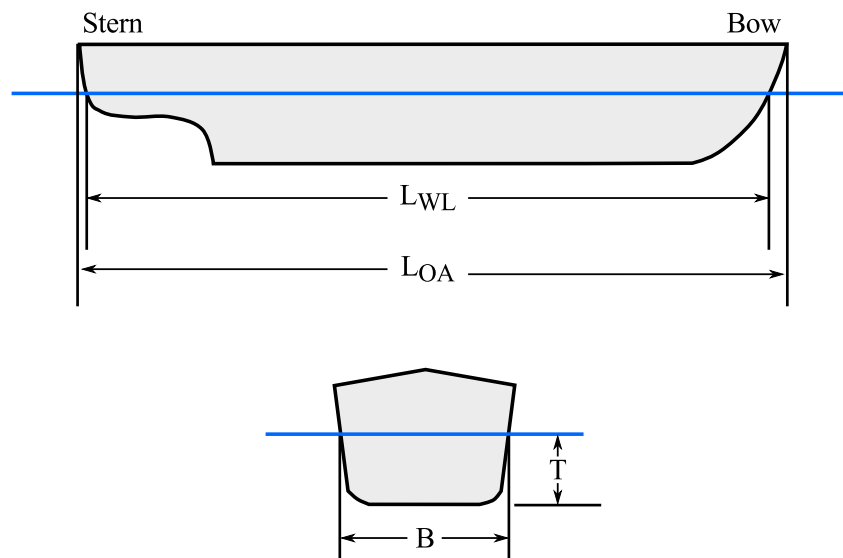

Figure D.1: Schematic of ship dimensions.

The analogous terms for the hydrofoil experiments are as follows: L_{OA} and L_{WL} both equal the chord c of the hydrofoil; B equals the thickness d of the hydrofoil; and T equals the submerged height h of the hydrofoil. Note that h is taken to be constant and equal to the submerged depth in still water, which does not take into

account the change in water height due to waves as T does.

D.2 Typical Dimensions and Flow Conditions

Typical naval ship speeds and dimensions are presented in table D.1.

Type	Class	L_{OA} [m]	L_{WL} [m]	B [m]	T [m]	Max. U [m/s]
Aircraft Carrier	Nimitz	332.85	316.99	40.84	12.19	15.43+
Aircraft Carrier	Ford	332.85	316.99	40.84	11.89	15.43+
Cruiser	Ticonderoga	172.82	161.24	16.76	10.06	15.43+
Littoral Combat	Freedom	118.1	98.76	17.6	4.3	20.58+
Littoral Combat	Independent	128.5	-	31.6	4.6	-
Destroyer	Arleigh Burke	155.29	142.04	18	9.45	15.43+
Destroyer	Zumwalt	185.93	-	24.60	8.53	15.43

Table D.1: Typical naval ship dimensions and speeds (*America's Navy: U.S. Navy Ships*; *Naval Vessel Register*).

Note that only a lower-bound maximum speed is given as the exact speed is not publicly available for active ships. In addition, most ships will cruise at lower speeds (typically around 9 to 12m/s) for fuel efficiency. The resulting non-dimensional parameters as well as aspect ratios are presented in table D.2, where the Froude number and Reynolds number are defined using L_{WL} as the length scale (expect in cases where L_{WL} is not given, in which case L_{OA} is used).

Type	Class	B/L_{WL} [10^{-1}]	T/L_{WL} [10^{-2}]	B/T	Re [10^9]	Fr [10^{-1}]
Aircraft Carrier	Nimitz	1.29	3.85	3.35	5.50	2.77
Aircraft Carrier	Gerald R. Ford	1.29	3.75	3.43	5.50	2.77
Cruiser	Ticonderoga	1.04	6.24	1.67	2.80	3.88
Littoral Combat	Freedom	1.78	4.35	4.09	2.28	6.61
Littoral Combat	Independence	2.46	3.58	6.87	-	-
Destroyer	Arleigh Burke	1.27	6.65	1.90	2.46	4.13
Destroyer	Zumwalt	1.32	4.59	2.88	3.22	3.61

Table D.2: Typical naval ship aspect ratios and non-dimensional parameters based on values from table D.1.

The experimental parameters (presented in table D.3, where Re and Fr use the chord length c as the length scale) can be compared to that of typical naval ships.

d/c	h/c	d/h	Re [10^5]	Fr [10^{-1}]
0.12	0.25	0.48	0.353 - 3.10	0.596 - 5.23

Table D.3: Hydrofoil's aspect ratios and non-dimensional parameters.

The higher Reynolds number experiments match the Froude number of typical naval ships, which is important for scaling up forces. In addition, experiments match the waterline beam-to-length ratio (d/c) of typical naval ships. The waterline draft-to-length ratio (given by h/c), however, is between three to seven times greater, and the beam-to-draft ratio (d/h) is 3-14 times smaller. The experimental Reynolds numbers is also four orders of magnitude smaller.

The inability to match Reynolds number along with Froude number is expected. A test model must be geometrically similar to the full scale ship, fixing the length scale L_1 of the model. Say that $100L_1 = L_2$, the full scale length of the ship. In order to match $Fr \sim U/\sqrt{L}$, U_2 would have to be ten times U_1. But, in order to match $Re \sim UL$, U_1 would have to equal $100U_2$, which is impractical. Thus, Froude scaling is used for ship modeling applications. In addition, if the model were geometrically similar to the full scale ship, having the same Froude number would ensure that the wave patterns generated are similar between the two cases.

D.3 Typical Hull Form

The hull designs of several naval ships are presented in figure D.2. As seen in the images, ships are designed with a fine bow cross section at the waterline. The reason for doing so is to minimize the wave-breaking phenomenon and the corresponding wave-breaking resistance. This is especially important for fast ships (Carlton, 2007). The photos also show stern views of the naval vessels. The stern is not as fine as the bow at the waterline and is typically square with a flat or slightly curved surface.

Figure D.2: Typical hull designs of U.S. Navy ships. (a) Stern view of the USS Enterprise (CVN 65) aircraft carrier in the Atlantic Ocean. U.S. Navy photo by Photographer's Mate 3rd Class Rob Gaston (*America's Navy: USS Enterprise (CVN 65)*).(b) Bow view of the USS Nimitz (CVN 68) aircraft carrier at the Naval Air Station North Island. U.S. Navy photo by Mass Communication Specialist Seaman Jake Berenguer (*America's Navy: USS Nimitz (CVN 68)*). (c) Bow view of the USS Spruance (DD 963) destroyer, left, and the guided-missile cruiser USS Ticonderoga (CG 47), right, moored at the Naval Operating Base Norfolk. Navy Photo DN-ST-85-11657 by Don S. Montgomery (*NavSource Naval History: USS Ticonderoga (CG 47)*). (d) Ariel view of the USS Bunker Hill (CG 52) cruiser during Operation Desert Shield. U.S. Navy Photo (*NavSource Naval History: USS Bunker Hill (CG 52)*). (e) Bow view of the Momsen (DDG 92) destroyer pulling into Panama City. U.S. Navy photo by Photographer's Mate 1st Class Dawn C. Montgomery (*America's Navy: Momsen (DDG 92)*). (f) Ariel view of the littoral combat ship USS Freedom (LCS 1) in the Pacific Ocean. DoD photo by Petty Officer 1st Class James R. Evans, U.S. Navy (*U.S. Department of Defense: USS Freedom (LCS 1)*). (g) Bow view of littoral combat ship USS Freedom (LCS 1) at the Cleveland Municipal Pier. U.S. Navy photo by Mass Communication 3rd Class Specialist Kenneth R. Hendrix (*America's Navy: USS Freedom (LCS 1)*).